Phytoplankton's role in the biological pump during the growth season across the Atlantic Southern Ocean

Raquel Francesca Flynn

A thesis presented for the degree of

Doctor of Philosophy



Department of Oceanography

Faculty of Science

University of Cape Town

Supervisor: Associate Professor Sarah E. Fawcett

June 2023

University of Cape Town

The copyright of this thesis vests in the author. No quotation from it or information derived from it is to be published without full acknowledgement of the source. The thesis is to be used for private study or non-commercial research purposes only.

Published by the University of Cape Town (UCT) in terms of the non-exclusive license granted to UCT by the author.

University of Cape Town

I dedicate this thesis to my parents; they nurtured my inquisitive mind since the beginning and have always supported my love for science and the ocean.

"The Sea, once it cases its spell, holds one in its net of wonder forever" – Jacques-Yves Cousteau

Plagiarism declaration

I know the meaning of plagiarism and declare that all work present in this dissertation is my own work. The contents of this dissertation have not been submitted for the consideration of any other degree or qualification.

Signed by candidate

Raquel Flynn

19 June 2023

Date

I confirm that I have been granted permission by the University of Cape Town's Doctoral Degrees Board to include the following publication(s) in my PhD thesis, and where co-authorships are involved, my co-authors have agreed that I may include the publication:

Flynn R.F., Bornmann T.G., Burger J.M., Smith S., Spence K.A.M., and Fawcett S.E. (2021) Summertime productivity and carbon export potential in the Weddell Sea, with a focus on the waters adjacent to Larsen C Ice Shelf. *Biogeosciences* 18, 6031-6059. https://doi.org/10.5194/bg-18-6031-2021.

Thesis Abstract

Southern Ocean phytoplankton growth is seasonally co-limited by light and iron availability. In winter, iron and macronutrients such as nitrate are supplied to surface waters during deep mixing events. Sea-ice melt and increased solar radiation in spring drive rapid stratification of surface waters, alleviating phytoplankton from light limitation and allowing them to consume the nutrients supplied in winter. In the framework of the "new production paradigm", phytoplankton growth fuelled by upwelled nitrate ("new production") can be equated to atmospheric CO_2 removal, while growth fuelled by ammonium and urea ("regenerated production") results in no net CO_2 drawdown. As such, once phytoplankton begin assimilating the nitrate supplied from the subsurface, the upper Southern Ocean ecosystem starts removing atmospheric CO_2. As the spring/summer growth season progresses, mixed-layer iron concentrations decline, leading to phytoplankton growth being predominantly fuelled by regenerated nutrients, with a concomitant decrease in CO_2 removal.

The role of phytoplankton in the Southern Ocean's CO_2 sink remains poorly understood, particularly early in the growth season (i.e., spring) and in regions where thick sea-ice conditions persist year-round (e.g., Larsen C Ice Shelf; LCIS). For the research described in this thesis, field sampling was undertaken near the LCIS during summer 2018/2019 and across the Atlantic Southern Ocean in spring 2019. Rates of net primary production (NPP) and nitrogen (N; as nitrate, ammonium, and urea) uptake were measured in both seasons to determine the dominant N source supporting phytoplankton growth and to quantify carbon export potential. In spring, coincident rates of iron uptake were also measured, allowing for an assessment of the iron requirements of different phytoplankton size classes. In contrast to expectations that large diatoms dominate the open Southern Ocean spring bloom, the biomass and rates of NPP and N uptake were dominated by nanoplankton (2.7-20 μm), particularly the diatom *Chaetoceros* spp., which employs a "boom-and-bust" life-cycle. It appears that *Chaetoceros* were able to grow so rapidly because of their low iron and light requirements, as well as their ability to form long spiney chains that reduce grazing pressure. The *Chaetoceros* bloom was relatively short-lived (a few weeks) and its senescence, driven by iron limitation and increased grazing pressure, drove a massive export event that accounted for roughly a third of the carbon exported over the entire spring/summer growth season.

In contrast to spring, the late-summer phytoplankton community in the Weddell Sea relied strongly on regenerated N, with ammonium and urea consumption fuelling 53 ± 8% of their growth at LCIS. These high rates of regenerated production coincided with an elevated ammonium supply rather than low iron availability as sea-ice melt led to non-limiting iron concentrations in surface waters. The high ammonium concentrations partially inhibited nitrate uptake and thus, biological carbon export, particularly near LCIS. Here, the phytoplankton community shifted from *Phaeocystis Antarctica*- to diatom-dominated as the growth season progressed, coincident with an increase in upper water-column

stratification. This shift may have further decreased carbon export as *P. Antarctica* can fix up to 50% more carbon per mole of phosphate consumed than diatoms.

To further investigate the role of small (<20 μm) phytoplankton in nutrient and carbon cycling in the summertime Weddell Sea, the $^{15}N/^{14}N$ of four groups sorted by flow cytometry (*Synechococcus,* picoeukaryotes, nanoeukaryotes, and cryptophytes) was measured. Phytoplankton growth fuelled by subsurface nitrate produces particulate organic N (PON) that is high in $^{15}N/^{14}N$ relative to growth fuelled by ammonium. Using biomass $^{15}N/^{14}N$ as a measure of new- versus regenerated N dependence, the contribution of each phytoplankton group to carbon export potential can be estimated. *Synechococcus* generally relied on nitrate less than the other phytoplankton groups although interestingly, its nitrate dependence was highest at LCIS and increased with increasing seawater temperatures and ammonium concentrations. Conversely, the high LCIS ammonium concentrations may have partially inhibited nitrate consumption by the picoeukaryotes, nanoeukaryotes, and cryptophytes. These groups relied most heavily on nitrate at the Antarctic Peninsula and in the Weddell Gyre even though total productivity was significantly lower in these regions than at LCIS. The flow cytometry-$^{15}N/^{14}N$ data yield a higher (although still overlapping) mean estimate of new- relative to total production (i.e., the proportion of exportable carbon) than the ^{15}N-tracer-derived uptake rates (56 ± 18% versus 47 ± 15% of productivity fuelled by nitrate). This discrepancy is likely due to the different time-scales captured by the two methods, with PON isotopes integrating over days to weeks and the rate experiments quantifying N uptake at the time of sampling only. Additionally, flow cytometric sorting may have excluded certain phytoplankton groups that relied more heavily on regenerated N (e.g., *P. Antarctica*). It is thus important that the results of either method be interpreted in the appropriate context.

The work presented in this thesis shows how seasonal shifts in the phytoplankton community drive changes in biological carbon export in the Southern Ocean. In contrast to previous suggestions, the novel measurements described herein indicate that although summer is the period of maximum biomass accumulation in the Southern Ocean, it may not be the season of highest carbon export. This finding can be explained by the increasing reliance of phytoplankton on regenerated N as the season progresses. In ice-adjacent waters, this shift is largely due to elevated ammonium availability rather than iron limitation, which may (partially) inhibit nitrate uptake. By contrast, in the open Southern Ocean, iron limitation drives the seasonal shift towards regenerated production because of the high iron requirement of nitrate uptake. The work detailed in this thesis also indicates that different phytoplankton groups are better adapted to different physicochemical conditions (e.g., *P. Antarctica* to deep mixed-layers versus diatoms to recently-stratified waters), with the dominance of one group over another acting to strengthen or weaken the Southern Ocean's biological pump. Understanding the drivers of phytoplankton community composition is essential if we are to predict how phytoplankton will respond to a changing climate, and the implications of their response for the Southern Ocean's biological pump.

Acknowledgements

This Ph.D. has been an incredible journey, filled with once in a lifetime opportunities and experiences that have made me want to continue in the pursuit of knowledge, and have grown my love for the ocean and science.

To Sarah Fawcett, I was truly lucky to meet you all those years ago. Thank you for convincing me that an Honours in Oceanography was the way to go. It was indeed the right decision, and the seven years that followed have proved that. Sarah, you have not only been my supervisor, but you are my mentor and without you this Ph.D. would not have been possible. You have guided me and taught me to always dig deeper, that there is always more to be uncovered from the data. I will forevermore try to get as much out of a dataset as possible, even if it means I never manage to write a paper that does not consist of over 10 figures with multiple panels! I look forward to our future collaborations, and continuing to nerd out about nitrogen isotopes.

I thank Captain Knowledge Bengu, Captain Freddie Ligthelm, and the exceptional crew of the RV SA Agulhas II. Without this beautiful polar research vessel and the amazing crew that make sure all operations run smoothly, none of the work presented in this thesis would have been possible. I spent a total of six months on the SA Agulhas II during the first year of my Ph.D. and it became my second home. To team nitrogen cycle: Riesna Audh, Tommy Bornmann, Jessica Burger, Heather Forrer, Lumi Haraguchi, Eesaa Harris, Tahlia Henry, Katherine Hutchinson, Hermann Luyt, Ruan Parrot, Eleonora Puccinelli, Kurt Spence, Luca Stirnimann, Sina Wallschuss, Sive Xolashe. Thank you to each and everyone of you for your help with collecting and measuring samples during either the 58th South African National Antarctic Expedition (SANAE58), Weddell Sea Expedition 2019, and the winter and spring Southern oCean seAsonaL Experiment (SCALE) 2019. I wish to thank the scientific teams on the Weddell Sea Expedition 2019, and the winter and spring SCALE 2019 for their support throughout the expeditions.

I acknowledge Ronnie Dreyer, Kate Pecsok Ewert, Patricia Groenewald, Brett Kuyper, Julie Luyt, Ian Newton, Tim Reid Raymond Roman and the Stable Isotope Laboratory at the University of Cape Town for their assistance during the analysis of my samples.

To Jessica Burger, my partner in crime. Thank you for keeping me sane on our multiple expeditions and for always helping me with my uptake rate experiments. Without you filtering would have been a tedious task but somehow, we managed to make it enjoyable. I could not have asked for a better person to have spent countless hours filtering what has amounted to thousands of litres of seawater. Also, thank

you for always reminding me that “slow and steady wins the race”, it is definitely what got me through all those incubation experiments.

Luca Stirnmann and Sina Wallschuss, you two have taught me to not take life so seriously. Thank you for both being a welcome distraction from work and for the endless chats, series watching and saunas.

Thank you to Hazel Little and Pieter Truter, you have both been so understanding and dealt with my last-minute requests in prepping for sea. Pieter, thank you for always coming up with new and innovative ways to make my experiments work that much better. And of course, for fuelling my coffee addiction! Hazel, without you the lab cannot function. More importantly, thank you for being my friend and always listening to me trying to figure out my issues, whether it be why the bacteria weren’t doing what I wanted or checking my calculations. It would have been a far more boring journey without you!

To Lumi Haraguchi and Eleonora Puccinelli, thank you both for always be willing to give me advice and for showing me that a career in academia is worth it. Lumi, thank you for teaching me everything you know about phytoplankton and for guiding me through what seemed like a small but amounted to a huge dataset. I cannot wait for the world to see the importance of nanoplankton for carbon export in the Southern Ocean!

I wish to thank the Fawketieri Lab group (now known as the UCT Marine Biogeochemistry Lab). To every member, thank you for always listening to me speak about the new production paradigm and why urea may or may not be an important source of regenerated nitrogen. I have enjoyed every moment of being part of this lab group, and will cherish the moments we have all spent together.

To the staff and students of the Oceanography Department, particularly to Cashifa Karriem and Isabelle Ansorge. Cashifa, thank you for always being willing to help and sort out any issue I might have. Isabelle, I could not have asked for a more supportive head of department.

This may be bit strange, but I need to acknowledge my incubator, the denitrifying bacteria and the mass spec. The incubator was put through its paces, but it still managed to cope with freezing temperatures and ensured that my experiments were a success. I never imagined that the incubator I built in my Honours year would be with me throughout this journey. I was also truly privileged to be able to complete every step of the analysis of my FACS samples in the UCT Marine Biogeochemistry Lab. Thank you to the denitrifying bacteria for sacrificing their lives (albeit unwillingly) for my science.

To my family, thank you for whole-heartedly supporting me through this journey. You were there for it all, and always supported and encouraged me.

Finally, to Jason Dionysopoulos, my number one human. I do not know how I would have done this Ph.D. without you. Thank you for encouraging me to go on my adventures, looking after me and always being there. I truly appreciate everything that you do for me, even if I sometimes forget to tell you.

















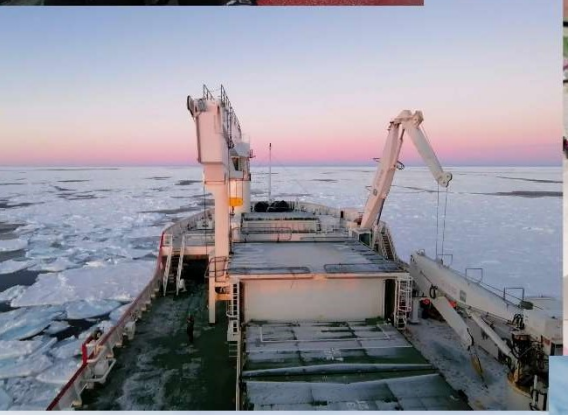









Table of Contents

Plagiarism declaration ii
Thesis Abstract iii
Acknowledgements v
Chapter 1: Introduction and Literature Review 1
1.1. The marine nitrogen cycle and biological carbon pump 1
1.2. Broad hydrography and biogeochemistry of the Southern Ocean 3
1.3. Phytoplankton diversity in the Southern Ocean 7
1.3.1. Picophytoplankton 8
1.3.2. Eukaryotes 9
1.3.3. Dinoflagellates 12
1.4. Quantifying the nitrogen cycle using nitrogen isotopes 13
1.4.1. ^{15}N-labelled tracer incubation experiments 13
1.4.2. Natural abundance nitrogen isotopes 14
1.4.3. Coupling flow cytometry with nitrogen isotope analysis 20
1.5. Scope of thesis 20
1.6. References 24
Chapter 2: Nanoplankton: the dominant vector for carbon export across the springtime Southern Ocean 43
Abstract 43
2.1. Introduction 45
2.2. Results 48
2.2.1. Hydrographic and biogeochemical context 48
2.2.2. Phytoplankton biomass and distributions 49
2.2.3. Primary production and nutrient uptake rates 52
2.2.4. Fe:C and Fe:N uptake ratios 54
2.2.5. Carbon export potential 54
2.3. Discussion 57
2.3.1. Nanoplankton dominate biomass and productivity across the springtime Southern Ocean 57
2.3.2. The springtime nanoplankton community is dominated by *Chaetoceros* spp. 59
2.3.3. Implications of the boom-and-bust lifestyle for carbon export 62
2.3.4. Implications of the spring *Chaetoceros* bloom for phytoplankton community composition and carbon export potential in summer 64
2.4. Materials and Methods 71
2.4.1. Study region and hydrography 71
2.4.2. Sample collection 72

2.4.3. Nutrient and chlorophyll *a* concentrations ... 72
2.4.4. Phytoplankton and zooplankton taxonomy ... 73
2.4.5. Rates of NPP and nitrogen and iron uptake ... 74
2.4.6. Total carbon export potential and NCP estimates ... 76
2.5. References ... 78
Appendix A: Nanoplankton: the dominant vector of carbon export across the springtime Southern Ocean ... 90
A1. Surface chlorophyll a concentrations throughout the growth season ... 90
A2. Size-fractionated rates of NPP, and N and Fe uptake ... 91
Chapter 3: Summertime productivity and carbon export potential in the Weddell Sea, with a focus on the waters adjacent to Larsen C Ice Shelf ... 96
Abstract ... 96
3.1. Introduction ... 98
3.2. Methods ... 101
3.2.1. Field collections ... 101
3.2.2. Uptake rates ... 104
3.2.3. NO_2^- oxidation rates ... 105
3.2.4. Phytoplankton taxonomy and carbon biomass ... 106
3.3. Results ... 107
3.3.1. Water column hydrography ... 107
3.3.2. Nutrient concentrations ... 109
3.3.3. Upper ocean biomass, NPP and N uptake rates ... 113
3.4.1. Drivers of NPP and N uptake in the Weddell Sea ... 122
3.4.2. Carbon export potential across the Weddell Sea ... 129
3.4.3. Broader biogeochemical implications at LCIS ... 132
3.5. Conclusions ... 133
3.6. References ... 135
Appendix B: Summertime productivity and carbon export potential in the Weddell Sea, with a focus on the waters adjacent to Larsen C Ice Shelf ... 148
B1. Carbon content of the identified Antarctic diatom species ... 148
B2. Flow cytometric identification of phytoplankton populations ... 150
B3. Including urea uptake in estimates of total N uptake ... 152
B4. Multiple dimension statistical analyses ... 153
B5. Apparent effect of temperature on NPP and N uptake ... 154

Chapter 4: Phytoplankton group-specific contributions to carbon export potential across the summertime Weddell Sea ... 158
Abstract ... 158
4.1. Introduction ... 161
4.2. Methods ... 163
4.2.1. Study site and hydrography ... 163
4.2.2. Nutrient analysis ... 166
4.2.3. Seawater nitrate isotopes ... 166
4.2.4. Seawater ammonium isotopes ... 167
4.2.5. Phytoplankton taxonomy ... 167
4.2.6. Bulk and size-fractionated PON concentration and $\delta^{15}N$ ... 167
4.2.7. Phytoplankton group-specific concentration and $\delta^{15}N$ ... 168
4.2.8. Size-fractionated ρNO_3^-, ρNH_4^+, and ρurea uptake rates ... 171
4.2.9. Phytoplankton group-specific and total community nitrate dependence ... 171
4.2.10. Bulk, size-fractionated, and flow-sorted phytoplankton community f-ratios and potential contributions to carbon export ... 175
4.3. Results ... 176
4.3.1. Hydrography and biogeochemical conditions ... 176
4.3.2. Phytoplankton biomass and community composition ... 179
4.3.3. $\delta^{15}N$ of PON and phytoplankton populations ... 182
4.3.4. Size-fractionated N uptake ratios ... 185
4.3.5. NO_3^- dependence of the different phytoplankton size-classes and groups ... 186
4.4. Discussion ... 189
4.4.1. Phytoplankton community composition in the summertime Weddell Sea ... 189
4.4.2. The role of community composition in modulating carbon export ... 191
4.4.3. The nitrate dependence of *Synechococcus*: biogeochemical implications at LCIS ... 198
4.5. Conclusion ... 200
4.6. References ... 201
Appendix C: Phytoplankton group-specific contributions to carbon export potential across the summertime Weddell Sea ... 214
C1: Flow cytometric identification of phytoplankton populations ... 214
C2: Size-fractionated rates of N uptake ... 215
Chapter 5: Conclusions ... 217
5.1. References ... 222

Table of Figures

Figure 1. 1. A schematic of the new production paradigm as originally conceptualised by Dugdale and Goering (1967). Over annual time scales, phytoplankton productivity fuelled by "new" N sources (e.g., NO3- supplied to the euphotic zone during deep winter mixing), termed "new production", can be equated to export production (orange dashed lines). In contrast, productivity fuelled by "regenerated" N sources (e.g., NH_4^+, urea, and NO_3^- produced via nitrification in the euphotic zone), termed "regenerated production", equates to no net export in a mass balance sense. [Figure adapted from Plumbago, 2006]. 2

Figure 1. 2. a) Map of Southern Ocean showing the annual mean positions of the hydrographic fronts (Subtropical Front – STF, Subantarctic Front – SAF, Polar Front – PF, southern Antarctic Circumpolar Current Front - SACCF, southern Antarctic Circumpolar Current boundary (SB)) and zones, and b) section plot across the Southern Ocean showing the approximate circulation of the intermediate and deep water masses (Subantarctic Mode Water – SAMW, Antarctic Intermediate Water – AAIW, Circumpolar Deep Water – CDW, Upper Circumpolar Deep Water – UCDW, Lower Circumpolar Deep Water – LCDW, Antarctic Bottom Water - AABW) in each hydrographic zone (Subantarctic Zone – SAZ, Polar Frontal Zone – PFZ, Open Antarctic Zone – OAZ, Marginal Ice Zone – MIZ, Coastal and Continental Shelf Zone – CCSZ). The general flow-path of the Antarctic Circumpolar Current (ACC) is denoted by the black arrows in panel (a). The size of the arrows in panel (b) indicates the proportion of silica export in each hydrographic zone. [Panel (a) taken from Talley et al. (2011) and panel (b) modified from Tréguer (2014)]. 6

Figure 1.3. Illustration of the simple models (Rayleigh and steady-state) often used to interpret N isotope data. The evolution of the $\delta^{15}N$ of the reactant (solid lines) and product (dashed lines) pools as a function of reactant pool concentrations is shown based on the Rayleigh (black lines) and steady-state models (green lines). The fraction of reactant remaining (f) is calculated as the [reactant]/[reactant]initial. A constant isotope effect (ε) of 5‰ was assumed for both models. [Figure taken from Sigman and Fripiat (2019)]. 16

Figure 1. 4. The theoretical evolution of the $\delta^{15}N$ of NO_3^- (i.e., the reactant pool) as a function of the NO_3^- concentration according to the Rayleigh model (solid line), steady-state model (dotted line) and the mixing of the Rayleigh model end-members (dashed line; i.e., to demonstrate the effect on the NO_3^- $\delta^{15}N$/concentration relationship of a mixing event that violates the Rayleigh model assumption of a closed system). The panels also show how the $\delta^{15}N$ of the reactant pool differs for the Rayleigh and steady-state models assuming a) 35% utilisation of the initial reactant pool (i.e., f = 0.65) and b) 70% utilisation of the initial reactant pool (i.e., f = 0.3). [Figure taken from Sigman et al. (1999)]. 17

Figure 2.1. a) Map of the Atlantic sector of the Southern Ocean showing the sampling stations overlayed on the monthly averaged sea surface temperature (SST) for November 2019 (https://oceancolor.gsfc.nasa.gov/l3/). Section plots of b) nitrate concentration ($[NO_3^-]$), c) silicate concentration ($[Si(OH)_4]$), d) ammonium concentration ($[NH_4^+]$), e) urea-N concentration ([urea]), f) dissolved iron concentration ([dFe]), and a bar plot showing g) the relative contribution of each phytoplankton size-class to chlorophyll a (colours, primary y-axis), along with the total surface chlorophyll a concentration (white dots, secondary y-axis) measured for samples collected along the Good Hope line. The fronts are identified in panel (a) by the grey lines (Subtropical Front (STF), Subantarctic Front (SAF), Polar Front (PF), and southern boundary of the Antarctic Circumpolar Current Front (sACCF)) and the hydrographic zones are indicated to the right of the map by the coloured rectangles (grey – Subtropical Zone (STZ), yellow – Subantarctic Zone (SAZ), orange – Polar Frontal Zone (PFZ), pink – Open Antarctic Zone (OAZ), purple – Marginal Ice Zone (MIZ). Together, the OAZ and MIZ constitute the Antarctic Zone). The station positions are shown in panels (a-f), with the coloured circles denoting the experimental stations and the grey circles the ancillary stations. The different water masses are identified in panels (b-c) by the density contours (ASW – Antarctic Surface Water, LCDW – Lower Circumpolar Deep Water, UCDW – Upper Circumpolar Deep Water, AAIW – Antarctic Intermediate Water, SAMW – Subantarctic Mode Water). The mixed layer depth is indicated

on panels (b-f) by the white filled circles. In panel (g), the black outlined bars indicate the four experimental stations, the different coloured bars represent the different hydrographic zones, and the shading of the bars shows the different plankton size-classes (white – picoplankton, opaque – nanoplankton, solid colour – microplankton). The stars in panel (g) indicate surface chlorophyll a concentrations that were higher than the secondary y-axis (3.0 μg L^{-1} and 1.8 μg L^{-1} at 55.5ºS and 55ºS, respectively). 47
Figure 2.2. Bar plots of a) size-fractionated particulate organic carbon (POC) concentration, b) relative phytoplankton cell abundance and total cell counts between 5 m and 125 m, c) relative and total phytoplankton biovolume between 5 m and 125 m, and d) relative and total mesozooplankton cell counts from Bongo net collections (integrated surface to 200 m). Panel (e) shows images taken by CytoSense flow cytometer of the dominant Chaetoceros spp. chains present at the experimental stations. The stations are labelled by zone on the right-hand y-axes of all the panels. The black dashed line in panel (a) indicates the euphotic zone depth (Z_{eu}) and the blue dashed line the mixed layer depth (MLD) at the four experimental stations and the shading denotes the different plankton size-classes (white – picoplankton, opaque – nanoplankton, solid colour – microplankton). At the depths where size-fractionated POC concentrations were not measured, only the bulk values are shown (striped bars). The white dots in panels (b) and (d) indicate the total cell counts and in panel (c), the total biovolume. The different bars in panel (d) show the different mesozooplankton life-stages and main groups identified at the four experimental stations. 51
Figure 2.3. Bar plots showing the mixed-layer integrated rates of a) net primary production (NPP), b) nitrate uptake (ρNO_3^-), c) ammonium uptake (ρNH_4^+), d) urea uptake (ρurea), e) dissolved inorganic iron uptake (Fe' uptake) normalized to POC, and f) organically-complexed iron uptake (Fe(FOB) uptake) normalized to POC. The shading denotes the different plankton size-classes (white – picoplankton, opaque – nanoplankton, solid colour – microplankton). 53
Figure 2.4. Scatter plots of a) inorganic iron (Fe') uptake versus net primary production (NPP), b) the iron-to-carbon (Fe:C) uptake ratio versus the f-ratio, and c) the Fe:C uptake ratio versus the iron-to-nitrogen (Fe:N) uptake ratio. The shapes in all panels indicate the size-classes (circle – picoplankton, square – nanoplankton, diamond – microplankton). The colours in panels (a) and (c) denote the stations (MIZ – purple, OAZ – pink, PFZ – orange, SAZ – yellow) and in panel (b), the Fe:N uptake ratios. The black dashed lines in panel (a) show literature-based average Fe:C uptake ratios (cyanobacteria – 250:1, dinoflagellates – 60:1, haptophytes – 20:1, diatoms – 7:1) and the grey dashed lines show the literature-based minimum Fe:C uptake ratios (cyanobacteria – 200:1, dinoflagellates – 15:1, haptophytes – 6:1, diatoms – 2:1) for the main phytoplankton groups identified in this study (Marchetti and Maldonado, 2016). The black dashed line in panel (c) shows the Redfield C:N ratio (6.63:1) and the blue shaded area shows the data points associated with coincident luxury iron and NO_3^- uptake. 54
Figure 2.5. a) Bar plot of the f-ratio (i.e., proportion of total production fueled by NO_3^- uptake) for each size-class, b) bar plot showing mixed-layer integrated total carbon export potential (eq. 6), and c) carbon export estimated from mixed-layer integrated NO_3^- depletion (pink dotted line; eq. 9), mixed-layer integrated particulate organic nitrogen (PON) and regenerated N (i.e., NH_4^+ + urea) converted to carbon (i.e., (PON + NH_4^+ + urea) × C:N ratio (Johnson et al., 2022); black dashed line), estimated carbon export associated with the spring bloom (blue dash-dotted line; eq. 8), and the percent (%) of annual net community production (NCP, a measure of carbon export) measured previously (Johnson et al., 2017) that can be attributed to the spring bloom (grey shaded area). The different zones are indicated by the different colours (MIZ – purple, OAZ – pink, PFZ – orange, SAZ – yellow). The shading in panels (a) and (b) shows the different size-classes (white – picoplankton, opaque – nanoplankton, solid colour – microplankton, striped – bulk community), with the striped bars in panel (a) indicating to bulk community estimates. 56
Figure 2.6. Schematics showing the seasonal physicochemical changes and associated shifts in the phytoplankton community in a) the Subantarctic Zone (SAZ), b) the Polar Frontal Zone (PFZ), c) the Open Antarctic Zone (OAZ), and d) the Marginal Ice Zone (MIZ) of the Southern Ocean developed using our new springtime data and the available observations from the other seasons (see text for

references). The pink rectangle indicates our sampling period when the mixed layer was dominated by a Chaetoceros bloom. The different phytoplankton groups and their qualitative importance (smaller – less dominant, bigger – more dominant) are shown in each panel. The gradient in mixed-layer silicate ($Si(OH)_4$) availability is represented by the bar to the left of the schematic (high (dark purple) to low (white) silicate availability). The relative rate (number of arrows) and magnitude (size of circles) of iron and nitrogen recycling are shown by the grey circles. The dashed blue line indicates the mixed layer depth and the dotted black line shows the iron concentration. Figure created using BioRender.com.. 65
Figure A1.Monthly-averaged surface concentrations of chlorophyll a across the Atlantic Southern Ocean in a) September 2019, b) October 2019, c) November 2019, d) December 2019, e) January 2020, f) February 2020, and g) March 2020. The stations occupied during the cruise (9-13 November 2019) are denoted by the circles, with the colours indicating the stations where uptake rate experiments were conducted (purple – Marginal Ice Zone (MIZ), pink – Open Antarctic Zone (OAZ), orange – Polar Frontal Zone (PFZ), yellow – Subantarctic Zone (SAZ)) and the grey circles showing the ancillary stations. The chlorophyll a concentrations are monthly averages from MODIS-Aqua (10.5067/AQUA/MODIS/L3M/CHL/2022). 90
Figure A2. Size-fractionated rates of a) net primary production (NPP), b) nitrate uptake (ρNO_3^-), c) ammonium uptake (ρNH_4^+), d) urea uptake (ρurea), e) dissolved inorganic iron uptake (Fe' uptake), and f) organically-complexed iron uptake (Fe-FOB uptake) in the euphotic zone, shown as a function of light availability relative to surface photosynthetically active radiation (%PAR). The station locations are labelled on the right-hand side of the panels. The colour shading indicates the different size-classes (white – picoplankton, opaque – nanoplankton, solid colour – microplankton). Where there are no bars in panels (e-f), no data are available. 92
Figure A3. Specific uptake rates of a) nitrate ($V_{NO_3^-}$) and b) total regenerated nitrogen (i.e., $V_{N_{reg}} = V_{NH_4^+} + V_{urea}$) versus latitude at the four experimental stations. The symbols denote the different size-classes (circles– picoplankton, squares– nanoplankton, diamonds– microplankton) and the colours indicate the station locations (purple – Marginal Ice Zone (MIZ), pink – Open Antarctic Zone (OAZ), orange – Polar Frontal Zone (PFZ), yellow – Subantarctic Zone (SAZ))..... 93
Figure 3.1. Maps of the Weddell Sea, Larsen C Ice Shelf (LCIS; insert a) and Fimbul Ice Shelf (FIS; insert b) showing the position of the stations where rate experiments were conducted during the Weddell Sea Expedition in January/February 2019. The symbols represent the different regions of the Weddell Sea sampled during the expedition (circle – Antarctic Peninsula (AP); diamond – FIS; triangle – LCIS; square – Weddell Gyre (WG)). The general cyclonic circulation of the Weddell Gyre (dashed blue arrow) is illustrated on the central map, with the dashed black arrows indicating the input of modified water masses from Filchner-Ronne Ice shelf (FRIS) and LCIS (Gordon et al. 1993; Schröder et al. 2002; Schodlok et al. 2002). The hypothesized circulation at LCIS (Nicholls et al. 2004; Hutchinson et al. 2020) is shown by the dashed light-blue arrow in insert (a). The 3.125 km sea-ice concentration data from 31 January 2019 shown in the central panel were taken from ftp://ftp-projects.cen.uni-hamburg.de/seaice/AMSR2/3.125km and the bathymetry data (inserts a and b) were taken from ETOPO1 (NOAA National Geophysical Data Center 2009)..... 102
Figure 3.2. Depth profiles of (a) potential density (σ_θ), (b) potential temperature, (c) absolute salinity, and (d) photosynthetically active radiation (PAR) in the upper 150 m and (e) σ_θ, (f) potential temperature, and (g) absolute salinity in the upper 1500 m at all stations. The water masses present at each station, identified by their temperature and salinity characteristics, are denoted in panels (e-g) as follows: WSBW – Weddell Sea Bottom Water, WSDW – Weddell Sea Deep Water, WDW – Warm Deep Water, MWDW – Modified Warm Deep Water, ISW – Ice Shelf Water, HSSW – High Salinity Shelf Water, WW – Winter Water, ASW – Antarctic Surface Water. In panel (f), the dark yellow rectangle indicates HSSW. The general station locations are indicated by the different marker colours: red shades – Antarctic Peninsula, green shades – Larsen C Ice Shelf, blue shade –Weddell Gyre, light purple shades – early summer Fimbul Ice Shelf, and dark purple – late summer Fimbul Ice Shelf... 109

Figure 3.3. Depth profiles (0-500 m) of (a) NH_4^+, (b) urea-N, (c) NO_2^-, (d) NO_3^-, (e) $Si(OH)_4$, and (f) PO_4^{3-} concentrations. For all panels, the error bars represent ± 1 SD of replicate samples (n = 2-3). For NO_3^-, which was calculated as $NO_3^-+NO_2^- - NO_2^-$, error has been propagated according to standard statistical practices. Note that the x-axis scales in panels (d-f) do not start at zero. 111
Figure 3.4. Depth profiles (0-150 m) of (a) NO_3^- depletion, (b) $Si(OH)_4$ depletion, and (c) PO_4^{3-} depletion at each station. Also shown are scatterplots of (d) $Si(OH)_4$ depletion versus total N depletion (coloured symbols; see text for details) and $Si(OH)_4$ depletion versus NO_3^- depletion (grey symbols) and (e) PO_4^{3-} depletion versus total N depletion (coloured symbols) and PO_4^{3-} depletion versus NO_3^- depletion (grey symbols) at each station. The dashed line in panel (d) represents the 1:1 Si:N depletion ratio, expected for iron-replete diatoms (Ragueneau et al. 2000; Hutchins and Bruland 1998; Takeda 1998; Mosseri et al. 2008), while the dotted lines represent the 2:1 Si:N ratio, expected for iron-limited diatoms (Arrigo et al., 1999; Franck et al., 2000; Brzezinski et al., 2003; Green and Sambrotto, 2006; Mosseri et al., 2008; Weber and Deutsch, 2010a; Martiny et al., 2013), and the 1:2 Si:N ratio, indicative of enhanced activity of non-siliceous phytoplankton. The dashed line in panel (e) represents the 16:1 N:P depletion ratio (the Redfield ratio), while the dotted lines represent the 20:1 N:P ratio, expected for P. antarctica, and the 14:1 N:P ratio, expected for iron-replete diatoms (Hutchins and Bruland 1998; Takeda 1998; Arrigo et al. 1999; Ragueneau et al. 2000; Mosseri et al. 2008). 112
Figure 3.5. Bar plots of (a, d, g) POC concentrations, (b, e, h) PON concentrations, and (c, f, i) biomass C:N ratios measured at the 55% (a-c), 10% (d-f), and 1% light levels (g-i). The stations are labelled on the x-axis, and the general stations locations are indicated by the different colours: red shades – Antarctic Peninsula, green shades – Larsen C Ice Shelf, blue shade –Weddell Gyre, light purple shades – early summer Fimbul Ice Shelf, and dark purple – late summer Fimbul Ice Shelf. The dotted black horizontal line in panels (c), (f), and (i) shows the Redfield C:N ratio of 6.63. The purple star in panel (i) indicates the anomalously high C:N ratio estimated for the 1% PAR depth at station F2. The error bars represent ± 1 SD of replicate samples (n = 2-6). Where applicable, the error has been propagated according to standard statistical practices. 113
Figure 3.6. Daily rates of (a, e, i) NPP, (b, f, j) ρNO_3^-, (c, g, k) ρNH_4^+, and (d, h, l) ρurea for the 55% (a-d), 10% (e-h), and 1% light levels (i-l). Where there are no bars in panels (d), (h) and (l), no data are available. The stations are labelled on the x-axis, and the general station locations are indicated by the different colours: red shades – Antarctic Peninsula, green shades – Larsen C Ice Shelf, blue shade – Weddell Gyre, light purple shades – early summer Fimbul Ice Shelf, and dark purple – late summer Fimbul Ice Shelf. The error bars represent ± 1 SE of replicate experiments (n = 2). 115
Figure 3.7. Depth profiles of NO_2^- oxidation rates measured at each station (a) between the surface and 500 m, and (b) within the euphotic zone. 116
Figure 3.8. Euphotic zone-integrated f-ratios estimated for each station. The black-hashed and white bars show the difference between the $\text{f-ratio}_{(\text{excluding urea})}$ (higher value; eq. 3.4a) and the $\text{f-ratio}_{(\text{including urea})}$ (lower value; eq. 3.4b), with the black-hashed bars indicating the stations where urea uptake was measured and the white bars where it was estimated (see text for details). 117
Figure 3.9. The (a, d) cell counts, (b, e) relative cell abundances, (c) log-transformed biovolume, and (f) carbon biomass of all phytoplankton groups identified from (a-c) surface flow cytometry samples and (d-f) plankton net-tow samples. The stations are labelled on the x-axis. Where there are no bars in panels (d), (e), and (f), no data are available. Carbon biomass estimates in panel (f) are shown only for the prymnesiophyte, P. antarctica, and the diatom species. 119
Figure 3.10. Euphotic zone-averaged rates of (a) NPP versus SST, (b) ρNO_3^- versus euphotic zone depth (Z_{eu}), (c) N uptake (left y-axis) versus PON (bottom x-axis) and NPP (right y-axis) versus POC (top x-axis), (d) ρNH_4^+ versus NH_4^+ concentration, and (e) ρurea versus urea concentration, as well as (f) the concentrations of NH_4^+ (black outlined symbols; left y-axis) and urea (grey outlined symbols; right y-axis) versus PON at each station. The symbols in panel (a) are coloured by ρNO_3^-, in panel (b) by NO_3^- concentration, and in panel (c) by NPP (pink), ρNO_3^- (black), ρNH_4^+ (blue), and ρurea (grey). 124

Figure 3.11. Scatterplots of (a) the Si:N depletion ratio (i.e., $Si(OH)_4$-to-total N depletion) versus the % diatom abundance, (b) N:P depletion ratio (i.e., total N-to-PO_4^{3-} depletion) versus the % P. antarctica abundance, (c) % of total N (i.e., NO_3^- + NH_4^+ + urea) assimilated as NO_3^- versus the % diatom abundance, and (d) % of total N assimilated as regenerated N (i.e., NH_4^+ + urea) versus the % P. antarctica abundance at each station. 127
Figure 3.12. (a) NO_3^- uptake normalised to NH_4^+ uptake as a function of NH_4^+ concentration and b) NO_3^- depletion versus NH_4^+ concentration. The symbols in panel (a) are coloured by NH_4^+ uptake rate (ρNH_4^+) and in panel (b) by PON concentration. In panel (b), the symbol size indicates the incubation light level, NO_3^- depletion at LCIS corresponds with the left y-axis, and NO_3^- depletion at all other ("non-LCIS") stations corresponds with the right y-axis. 131
Figure B1. Example (a) histogram of relative cell size as inferred from forward scatter area (FSC-A) and (b) cytogram of phycoerythrin (PE) (i.e., orange) fluorescence versus chlorophyll-a (i.e., red) fluorescence, showing the Weddell Sea populations that were identified using flow cytometry. The populations identified the include: Synechococcus (Syn 1 and Syn 2), picoeukaryotes (PicoEuk), nanoeukaryotes (NanoEuk 1 and NanoEuk 2), and microeukaryotes (MicroEuk). Panel (c) shows the calibration curve generated from beads of various sizes that was used to infer the biovolume of the different phytoplankton groups. The grey vertical bars in panel (a) indicate the FSC-A of the 2.8 µm (light grey) and 20 µm beads (dark grey). The grey data in panel (b) show background noise and detritus. 151
Figure B2. Euphotic zone-integrated rates of NPP and total N uptake (ρN_x) × 6.63. The black symbols represent $\rho N_x = \rho NO_3^- + \rho NH_4^+$ and the grey symbols show $\rho N_x = \rho NO_3^- + \rho NH_4^+ + \rho$urea. The dashed line represents the 1:1 line on which the data points are expected to fall if all N sources supporting NPP are accounted for. Error (± 1 SE) has been propagated according to standard statistical practices. ... 152
Figure B3. (a) NMDS analysis of the variability in phytoplankton community composition among stations and (b) CCA ordination of phytoplankton species constrained by environmental variables, visualized as a biplot with sampling stations labeled (see Fig. 3.3.1 for station positions). 154
Figure B4. Average euphotic zone rates of (a) net primary production (NPP), (b) NO_3^- uptake (ρNO_3^-), (c) NH_4^+ uptake (ρNH_4^+), and (d) urea uptake (ρurea) as a function of sea surface temperature (SST), as well as the (e) specific rates of NPP, NO_3^-, NH_4^+, and urea uptake (V_X) and (f) concentrations of POC (black outline; left y-axis) and PON (grey outline; right y-axis) versus SST. The symbol outline colours in panel (e) denote the specific uptake rates of carbon (black), NO_3^- (blue), NH_4^+ (pink), and urea (grey). 155
Figure B5. Maps of (a) SST, (b) sea surface salinity, and (c) surface oxygen concentrations and (d) depth profiles of oxygen concentrations in the region of LCIS at the time of sampling. SST and salinity data were acquired from the underway (~7 m inflow) ferrybox, while the oxygen concentrations were measured via the oxygen sensor on the CTD profiler, calibrated against discrete seawater samples measured for dissolved oxygen by Winkler titration (Carpenter, 1965; Grasshoff et al., 1983; Hutchinson et al., 2020). The symbols in panel (d) are coloured by potential density (σ_θ), with the circles indicating the "non-upwelling" stations and the triangles the upwelling stations. The grey box in panel (d) indicates the average mixed layer depth (MLD) ± 1 SD across the stations at LCIS (n=10). The bathymetry data in panels (a-c) were taken from ETOPO1 (NOAA National Geophysical Data Center, 2009). 157
Figure 4.1. Maps of the Weddell Sea and Larsen C Ice Shelf (LCIS; insert) showing the position of the stations sampled during the Weddell Sea Expedition in January-February 2019. The symbols and colours represent the different regions of the Weddell Sea that were sampled (red circle – Antarctic Peninsula, green square – Larsen C Ice Shelf, purple diamond – Weddell Gyre). The symbols outlined in red indicate the stations where size-fractionated rates of nitrogen uptake were measured, in black where bulk rates of nitrogen uptake were measured (Chapter 3), and in grey where only samples for fluorescence-activated cell sorting (FACS) were collected (Table 4.1). At station WG2, denoted by the empty symbol, no FACS samples were collected. The dark blue cyclonic arrow in the main panel indicates the Weddell Gyre and the black dashed lines indicate the input of modified deep-water masses

from LCIS and Filchner-Rönne Ice Shelf (FRIS; Gordon et al., 1993; Schröder et al. , 2002; Schodlok et al., 2002). The hypothesized circulation at LCIS (Nicholls et al., 2004; Hutchinson et al., 2020) is represented by the light blue dashed arrow in the insert. The 3.125 km sea-ice concentration data from 31 January 2019 shown in the main panel were taken from ftp://ftp-projects.cen.uni-hamburg.de/seaice/AMSR2/3.125km (last access: 29 September 2021), and the bathymetry data (insert) were taken from ETOPO1 (NOAA National Geophysical Data Center, 2009)..... 164
Figure 4.2. Depth profiles (0-125 m) of a) sigma-theta (σ_θ), b) nitrate concentrations ([NO_3^-]), c) ammonium concentrations ([NH_4^+]), d) urea concentrations ([urea]), e) $\delta^{15}N_{NO_3^-}$, f) $\delta^{15}N_{NH_4^+}$ and g) $\delta^{15}N_{PON}$ of the bulk particulate organic nitrogen (PON) pool. The $\delta^{15}N_{NH_4^+}$ could not be measured at all stations and depths because the NH_4^+ concentrations were too low; in panel f, we show all available data. The different hydrographic regions are represented by different symbols and colours (red circles – Antarctic Peninsula, green square – Larsen C Ice Shelf, purple diamond – Weddell Gyre) and the stations are represented by different colours. Note the difference in the x-axis among panels. 178
Figure 4.3. Depth profiles (0-125 m) of the particulate organic nitrogen (PON) concentrations measured or estimated for the a) bulk phytoplankton community (PON_{bulk}), b) picoplankton ($PON_{picoplankton}$), c) nanoplankton ($PON_{nanoplankton}$), d) microplankton ($PON_{microplankton}$), e) cryptophytes (PON_{Crypto}), f) nanoeukaryotes ($PON_{N.euk}$), g) picoeukaryotes ($PON_{P.euk}$) and h) Synechococcus (PON_{Syn}). Note the difference in the x-axis among panels..... 180
Figure 4.4. The (a,d) cell counts, (b,e) relative abundance and (c,f) relative carbon contribution of all phytoplankton groups identified via (a-c) flow cytometric analysis of surface samples and (d-f) microscopic analysis of plankton net tow samples. The stations are labelled on the x-axis. Where there are no bars in panels (d-f), no data are available. The carbon biomass estimates in panel (f) are for Phaeocystis antarctica and the diatom species only. Note that this figure is a slightly amended version of Fig. 3.9 in Chapter 3 (Figure 9 in Flynn et al., 2021). 181
Figure 4.5. Boxplots showing the median mixed-layer $\delta^{15}N$ of the a) bulk PON ($\delta^{15}N_{bulk\ PON}$), b) picoplankton PON ($\delta^{15}N_{picoplankton}$), c) nanoplankton PON ($\delta^{15}N_{nanoplankton}$), d) microplankton PON ($\delta^{15}N_{microplankton}$), e) cryptophytes ($\delta^{15}N_{Crypto}$), f) nanoeukaryotes ($\delta^{15}N_{N.Euk}$), g) picoeukaryotes ($\delta^{15}N_{P.Euk}$) and h) Synechococcus ($\delta^{15}N_{Syn}$). The stations are labeled on the x-axis. The pink line indicates the average $\delta^{15}N_{NO_3^-\ WW}$ (i.e., the source NO_3^-) and the blue line shows the average $\delta^{15}N_{NH_4^+}$ used in our calculations. The grey dots indicate the theoretical $\delta^{15}N_{new}$ at each station, estimated using the Rayleigh model (eq. 4.14) 183
Figure 4.6. Euphotic-zone integrated size-fractionated uptake rates of a) nitrate uptake (ρNO_3^-), b) ammonium uptake (ρNH_4^+) and c) urea uptake (ρurea) at LCIS. The stations are labeled on the x-axis. The different shadings indicate the different phytoplankton size-classes (white – picoplankton, opaque – nanoplankton, solid – microplankton). 186
Figure 4.7. The estimated fraction of NO_3^- (versus regenerated nitrogen) dependence of a) the bulk phytoplankton community, b) picoplankton, c) nanoplankton, d) microplankton, e) cryptophytes, f) nanoeukaryotes, g) picoeukaryotes and h) Synechococcus. The stations are labeled on the x-axis. The dashed black line indicates a nitrate dependence of 50%. 188
Figure 4.8. Estimates of the f-ratio calculated using a) size-fractionated nitrogen uptake rate data (eq. 4.19) and bulk nitrogen uptake rate data (Chapter 3) and b) measurements of flow-sorted phytoplankton $\delta^{15}N$ (eq. 4.16). The stations are labeled on the x-axis. The dashed black line indicates a f-ratio of 0.5. In panel (a) the different shadings indicate the different phytoplankton size-class f-ratios (transparent – picoplankton, opaque – nanoplankton, solid – microplankton) and the grey bar denotes the bulk phytoplankton f-ratio. Where there are no bars in panel (a), no data are available. Note that this panel (a) is a slightly amended version of Figure 3.8 in Chapter 3 (Figure 8 in Flynn et al., 2021). 188
Figure 4.9. Principal component analysis (PCA) of the variability in the extent of NO_3^- dependence by the different flow-sorted phytoplankton groups constrained by various environmental variables and visualized as a biplot. The points are coloured by station (red – Antarctic Peninsula, green – Larsen C

Ice Shelf, purple – Weddell Gyre) and the different phytoplankton groups are denoted by symbols (circle – cryptophytes, square – nanoeukaryotes, diamond – picoeukaryotes, triangle – Synechococcus). The variables used in the PCA are as follows: MLD – mixed layer depth, Zeu – euphotic zone depth, NO3 – nitrate concentration, NH4 – ammonium concentration, d15N_FACS – $\delta^{15}N_{phyto}$, NO3_dep – the fraction of nitrate consumed (i.e., $[NO_3^-]_{measured}/[NO_3^-]_{ww}$), d15NO3 –$\delta^{15}N_{NO_3^-}$, PON_FACS – PON concentration of the different flow-sorted phytoplankton groups, Temperature – the measured temperature. 195
Figure 4.10. Scatterplots of a) mixed-layer NH_4^+ concentration versus mixed-layer temperature, NO_3^- dependence versus temperature for the b) cryptophytes, c) nanoeukaryotes, d) picoeukaryotes and e) Synechococcus, and euphotic-zone integrated NO_3^- dependence versus ρN_{reg} (i.e., integrated bulk rates of regenerated N uptake) versus of f) the cryptophytes, nanoeukaryotes and picoeukaryotes and g) Synechococcus. The symbols in panel (a) are coloured by the bulk PON concentration, in panels (b-e) by NH_4^+ concentration and in (f-g) by station. The symbols in panels (a-e) denote the different hydrographic regions (circle – Antarctic Peninsula, square – Larsen C Ice Shelf, diamond – Weddell Gyre) and in panel (f-g), the different phytoplankton groups (dark green circle – cryptophytes, light green square – nanoeukaryotes, light blue diamond – picoeukaryotes, dark blue triangle – Synechococcus). In panel (a), the NH_4^+ concentrations at LCIS corresponds with the left y-axis and the NH_4^+ concentrations at the other ("non-LCIS") stations corresponds with the right y-axis. 196
Figure C1. Example (a) histogram of relative cell size as inferred from forward scatter area (FSC-A) and (b) cytogram of phycoerythrin (PE) (i.e., orange) fluorescence versus chlorophyll a (i.e., red) fluorescence, showing the Weddell Sea populations that were identified using flow cytometry. The populations identified the include: Synechococcus, picoeukaryotes, nanoeukaryotes and cryptophytes. The grey vertical bars in panel (a) indicate the FSC-A of the 2.8 µm (light grey) and 20 µm beads (dark grey). The grey data in panel (b) show background noise and detritus. 214
Figure C2. The (a,d,g) cell counts, (b,e,h) relative abundance and (c,f,i) relative carbon contribution of all phytoplankton groups identified via flow cytometric analysis at the 55% (surface; a-c), 10% (d-f) and 1% (base of the euphotic zone; g-i) light levels. The stations are labelled on the x-axis. Where there are no bars in panels (d-i), no data are available. The carbon biomass estimates in panels (c,f,i) were calculated using the average biovolume of each group (Flynn et al., 2021) and converted to particulate organic carbon (POC) using phytoplankton group-specific carbon conversion factors (Table 4.2)... 215
Figure C3. Size-fractionates rates of (a,d,h) nitrate uptake (ρNO_3^-), (b,e,i) ammonium uptake (ρNH_4^+) and (c,f.j) urea uptake (ρurea) throughout the euphotic zone. The stations are labelled on the x-axis and the euphotic zone depth on the y-axis. The different shading the different size-classes (white – picoplankton, opaque – nanoplankton, solid colour – microplankton). 216

Table of Tables

Table A1. Euphotic-zone integrated rates of net primary production (NPP), nitrate uptake (ρNO_3^-), ammonium uptake (ρNH_4^+), urea uptake (ρurea), dissolved inorganic iron uptake (Fe' uptake), and organically-complexed iron uptake (Fe-FOB uptake), as well as the total iron (i.e., Fe' + Fe-FOB) to carbon uptake ratio. Values shown are averages ± 1 SD (n = 2 experiments), with error propagated according to standard statistical practices where appropriate. Where standard deviations are not included, the values were <0.01. "-" indicates no available data. 94
Table A2. Calculated labile iron concentrations ([Fe']) in the experimental bottles considering ambient light, temperature, and pH. pH was derived from measurements of total alkalinity (TA) and total dissolved carbon (TC). The steady state dissociation constant of the Fe(EDTA) chelate (log k' light) was acquired through linear regression of the data from Sunda and Huntsman (1995) where the temperature-specific dissociation constants are related via log k' = m (pH) + b. Fe[tot] is the sum of the ambient iron concentration and the iron added to the experimental bottles. Values are shown for all experimental depths at each station (listed according to light availability relative to surface photosynthetically active radiation (%PAR)), with the station locations indicated at the left of the Table (Subantarctic Zone (SAZ), Polar Frontal Zone (PFZ), Open Antarctic Zone (OAZ), Marginal Ice Zone (MIZ)). 95
Table 3.1. Euphotic zone-averaged nitrogen nutrient concentrations, nutrient depletions, and nutrient depletion ratios at each station occupied in the Weddell Sea in January/February 2019. Values shown are averages ± 1 SD (n ≥ 2), with error propagated according to standard statistical practices where appropriate. "–" indicates no available data. 120
Table 3.2. Euphotic zone-integrated and averaged rates at each station occupied in the Weddell Sea in January/February 2019. Values shown are averages ± 1 SD (n ≥ 2), with error propagated according to standard statistical practices where appropriate. "–" indicates no available data. The values shown in italics (i.e., ρurea) were estimated rather than measured (see text for details). 121
Table B1. Average carbon content (pg C $cell^{-1}$) assigned to the various diatom species identified via light microscopy, taken from Leblanc et al. (2012) for waters between 50 and 70°S. "–" indicates no available data. 148
Table B2. Average biovolumes assigned to the various phytoplankton populations identified using flow cytometry. Due to the anomalous FSC-A of the Synechococcus populations, the average Syn 1 and Syn 2 biovolumes were set to 1 μm^3 (Kana and Glibert, 1987; Paulsen et al., 2015). 151
Table 4.1. Station information for all stations occupied in the Weddell Sea in January-February 2019. The mixed layer depth (MLD) and euphotic zone depth (Z_{eu}; the 1% light level) measured at each station are also provided. The stations where FACS samples were collected, and nitrogen uptake experiments (as bulk and size-fractionated) were conducted at each station in this chapter and in Chapter 3 are indicated in the table. 165
Table 4.2. Average biovolume and carbon content assigned to the different phytoplankton populations identified using flow cytometry (Flynn et al., 2021). Due to the anomalous forward scatter of the Synechococcus populations, the average biovolume of Syn was set to 1 μm^3 (Kana and Glibert, 1987; Paulsen et al., 2015; Flynn et al., 2021; see Chapter 3 section B2 for details). The carbon content values for each population were taken from literature (as indicated in the "Reference" column). 170
Table 4.3. End-members used for the Rayleigh model. The $\delta^{15}N_{NO_3^-\,WW}$ is the average $\delta^{15}N_{NO_3^-}$ of winter water (WW; the source to the Weddell Sea mixed layer), $\delta^{15}N_{NH_4^+}$ is the average $\delta^{15}N_{NH_4^+}$ measured at the Antarctic Peninsula (AP) and Larsen C Ice Shelf (LCIS) stations, and εassimilation is the isotope effect associated with NO3- uptake (eq. 4.11). At LCIS, the same end-members were used for all stations as the $\delta^{15}N_{NO_3^-\,WW}$ was homogenous among stations and the phytoplankton community composition was similar among stations. 174
Table 4.4. Depth-weighted mixed-layer average PON concentrations, $\delta^{15}N$ and the estimated extent of NO_3^- dependence for the bulk and size-fractionated PON community, and flow-sorted phytoplankton

populations at each station. The values in the brackets are the SD of the regional averages.‘-‘ indicates where no data are available. 184
Table 4.5. Depth-weighted mixed-layer averaged f-ratios (i.e., the proportion of NO_3^- consumed by the phytoplankton) estimated for the bulk phytoplankton community using the PON_{bulk} measurements (f-$ratio_{PON\ bulk}$; eq. 4.7), all flow-sorted phytoplankton groups (f-$ratio_{phyto}$; eq. 4.16) and for the bulk phytoplankton community using the bulk nitrogen uptake rates (f-$ratio_{rates\ bulk}$; eq. 4.19) for each station, and contribution of each flow-sorted phytoplankton group to carbon export potential (eq. 4.18). 187

Chapter 1: Introduction and Literature Review

1.1. The marine nitrogen cycle and biological carbon pump

Nitrogen (N) is an important macronutrient for phytoplankton growth in the euphotic (sunlit surface) ocean. During the process of photosynthesis, phytoplankton fix carbon dioxide (CO_2), macronutrients (predominantly N and phosphorus) and micronutrients (e.g., iron) into organic biomass, and are thus essential to the ocean's carbon cycle. Across the global ocean, ~10% of the atmospheric CO_2 fixed by phytoplankton during photosynthesis is exported below 200 m via the sinking of particulate organic matter (POM); this mechanism of POM production and export is termed the "biological carbon pump" (Volk and Hoffert, 1985; Falkowski et al., 1998). In the deep ocean, the POM is either remineralised back to dissolved inorganic carbon (DIC) or reaches the sediments (Laws et al., 2000; Henson et al., 2011; Sigman et al., 2010). When the POM is remineralised to DIC, it is stored in intermediate and mode water masses for >100 years and will eventually be upwelled to the surface at lower latitudes (Laws et al., 2000; Henson et al., 2011; Sigman et al., 2010; Sigman and Hain, 2012). In contrast, POM that reaches the sediments will be buried thereby sequestering CO_2 (Laws et al., 2000; Henson et al., 2011; Sigman et al., 2010). The biological carbon pump is therefore one of the mechanisms by which atmospheric CO_2 is transferred and stored in the ocean interior on climate-relevant time scales.

N is supplied to phytoplankton as either "new" N (e.g., NO_3^- mixed up from below the euphotic zone) or "regenerated" N (e.g., ammonium (NH_4^+) produced by the degradation of PON within the euphotic zone) (Fig. 1.1; Dugdale and Goering, 1967). Phytoplankton growth supported by new N sources is termed "new production", while growth fuelled by regenerated N sources is termed "regenerated production" (Dugdale and Goering, 1967). Over appropriate time and space scales, new production must be balanced by the export of PON (and associated particulate organic carbon (POC)) into the ocean's interior, therefore allowing us to use new production as a proxy for carbon export potential (Dugdale and Goering, 1967), provided the C:N ratio of the sinking organic matter is known.

The proportion of new production relative to total production (i.e., new + regenerated production) is generally quantified using the f-ratio (shorthand for "flux ratio; Eppley and Peterson, 1979). The f-ratio therefore estimates the proportion of carbon produced via primary production that is potentially exported from the euphotic zone (i.e., export production; Dugdale and Goering, 1967). The f-ratio also indicates whether primary production is predominantly fuelled by new (i.e., f-ratio >0.5) or regenerated nitrogen (i.e., f-ratio <0.5), provided that various assumptions are not violated (Dugdale and Goering, 1967; Yool et al., 2007). For example, if primary production is fuelled by N_2 fixation, carbon export will be underestimated as N_2 fixation represents a new source of N to the euphotic zone. Since the focus of this thesis is the Southern Ocean, and most evidence suggests that N_2 fixation is not an important source of new nitrogen relative to the consumption of subsurface NO_3^- (Raes et al., 2020), its role in the N cycle and carbon export will be excluded. On the other hand, if NO_3^- is produced within the euphotic

zone via nitrification, carbon export may be overestimated. This is because euphotic zone nitrification provides a regenerated rather than new source of NO_3^- to the euphotic zone, with its assimilation thus contributing to regenerated rather than new production (Fig. 1.1; Dugdale and Goering, 1967; Eppley and Peterson, 1979; Dore and Karl, 1996; Raimbault et al., 1999; Diaz and Raimbault, 2000; Yool et al., 2007; Mdutyana et al., 2020). Nevertheless, if we can constrain euphotic zone nitrification, the relationship between new production and carbon export allows us to use measurements of the N cycle to investigate and quantify the oceanic carbon cycle.

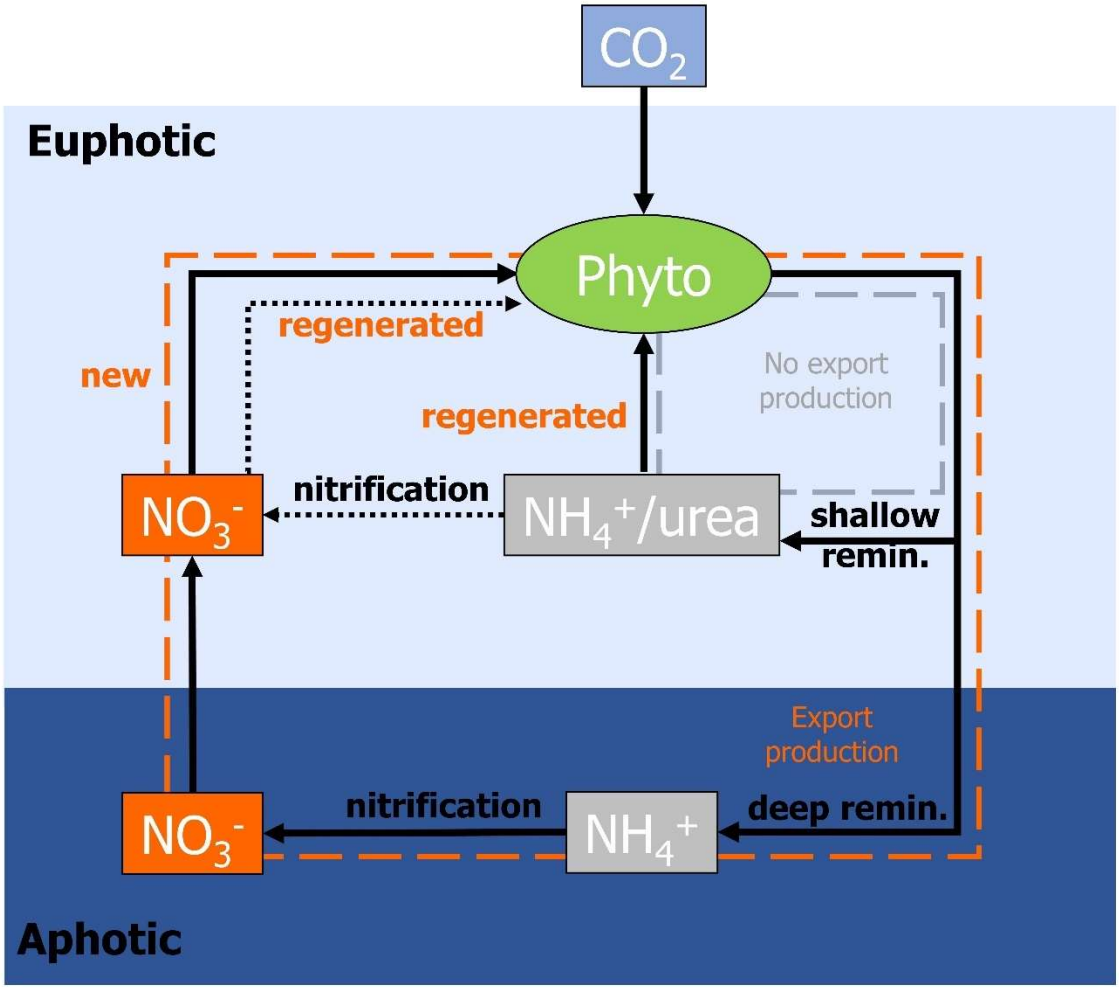


Figure 1. 1. A schematic of the new production paradigm as originally conceptualised by Dugdale and Goering (1967). Over annual time scales, phytoplankton productivity fuelled by "new" N sources (e.g., NO_3^- supplied to the euphotic zone during deep winter mixing), termed "new production", can be equated to export production (orange dashed lines). In contrast, productivity fuelled by "regenerated" N sources (e.g., NH_4^+, urea, and NO_3^- produced via nitrification in the euphotic zone), termed "regenerated production", equates to no net export in a mass balance sense. [Figure adapted from Plumbago, 2006].

1.2. Broad hydrography and biogeochemistry of the Southern Ocean

The Southern Ocean, defined here as the waters south of the Subtropical Front (STF; Fig. 1.2a), occupies ~20% of the global ocean (Schlitzer, 2002; Tréguer and Pondaven, 2002) and plays a disproportionate role in the oceanic carbon cycle (Sarmiento and Toggweiler, 1984; Sigman and Boyle, 2000; Schlitzer, 2002; Sigman et al., 2010). Annually, the Southern Ocean absorbs ~40% of the anthropogenic CO_2 taken up by the global ocean (Takahashi et al., 2012; DeVries, 2014; Frölicher et al., 2015; Gruber et al., 2019). It is estimated that without the Southern Ocean's biological pump atmospheric CO_2 concentrations could be up to 50% higher than current levels (Cox et al., 2000). Despite this, the Southern Ocean still represents a "leak" in the global ocean's biological carbon pump due to the incomplete consumption of the surface macronutrient inventory by phytoplankton (Sarmiento and Toggweiler, 1984; Weber and El-sayed, 1987; Priddle et al., 1998; Sigman and Boyle, 2000). Indeed, the Southern Ocean is the largest high-nutrient, low-chlorophyll (HNLC) region in the global ocean due to primary production (and thus macronutrient uptake) being limited by iron, silicate ($Si(OH)_4$; north of the Polar Front (PF) in summer) and light in winter (e.g., Martin et al., 1991; Morel et al., 1991; De Baar et al., 1995; Franck et al., 2000; Boyd and Law, 2001)

The dominant circulation feature of the Southern Ocean is the eastward-flowing Antarctic Circumpolar Current (ACC), which circumnavigates Antarctica. The ACC is comprised of various hydrographic fronts (Subantarctic Front (SAF), Polar Front (PF), southern ACC Front (sACCF)) that divide the Southern Ocean into distinct regions characterised by different physical, chemical and biological function (Orsi et al., 1993, 1995; Chapman et al., 2020). The Subantarctic Zone (SAZ) and Polar Frontal Zone (PFZ), sometimes referred to collectively as the "Subantarctic", and the Antarctic Zone (AZ), which consists of the Open Antarctic Zone (OAZ), Marginal Ice Zone (MIZ) and Coastal and Continental Shelf Zone (CCSZ) (Fig. 1.2). The northern boundary of the ACC is demarcated by the STF, while the southern boundary is defined by the upwelling of Upper Circumpolar Deep Water (UCDW), although not associated with a hydrographic front, and extends south of the sACCF (Talley et al., 2011). Although the dominant circulation of the ACC is eastward, surface waters are advected northwards from the Antarctic Slope Front (ASF) to the SAZ due to Ekman transport (Fig. 1.2b; Talley et al., 2011). The northward Ekman transport of southern-sourced waters across the frontal zones drives upwelling and subduction, leading to the formation and modification of water masses. Each hydrographic zone is thus characterised by different water masses with defined physicochemical properties (Talley et al., 2011; Chapman et al., 2020).

The Subantarctic (Subantarctic Zone and Polar Frontal Zone)

The Subantarctic encompasses >50% of the Southern Ocean and is bordered by the STF (at the northern extent) and the PF (at the southern extent). The Subantarctic comprises two hydrographic zones: the SAZ and the PFZ (Orsi et al., 1995). The water masses present in the SAZ are Subantarctic Surface

Water (SASW), Subantarctic Mode Water (SAMW), Antarctic Intermediate Water (AAIW), Upper Circumpolar Deep Water (UCDW), Lower Circumpolar Deep Water (LCDW) and Antarctic Bottom Water (AABW) (Fig. 1.2b). The PFZ contains Antarctic Surface Water (ASW), UCDW, LCDW and AABW. SAMW and AAIW are formed at the SAF and the PF, respectively, during the northward subduction of ASW, thereby forming the various intermediate water masses (Talley et al., 2011 and references therein).

The predominant mechanism of nutrient supply to the surface waters of the Subantarctic is deep winter mixing (De Baar et al., 1995; Moore et al., 2002; Boyd and Ellwood, 2010; Klunder et al., 2011; Tagliabue et al., 2012, 2014); however, this mechanism supplies disproportionate ratios of macro- versus micronutrients resulting in phytoplankton growth being iron limited (Croot et al., 2007; Boyd and Ellwood, 2010; Tagliabue et al., 2014). Iron is proportionally less abundant in upwelling waters because the depth of the ferricline (the depth with the steepest vertical gradient in iron concentration) is deeper than both the nutricline depth (the depth with the steepest gradient in the macronutrient concentrations) and the winter mixed layer depth, thereby limiting the supply of iron to surface waters (Croot et al., 2007; Boyd and Ellwood, 2010; Tagliabue et al., 2014). Iron is therefore perennially limited in regions of the Subantarctic where other supply mechanisms or sources (e.g., aeolian deposition, continental runoff) are restricted, such as the open Subantarctic (Boyd et al., 2004; Cassar et al., 2007; Pollard et al., 2009; Boyd and Ellwood, 2010; Doblin et al., 2011; Klunder et al., 2011; Tagliabue et al., 2014; Ryan-Keogh et al., 2018; Mtshali et al., 2019). The winter mixed layer reaches the depth of the nutricline, however, and winter mixing supplies high concentrations of macronutrients to Subantarctic surface waters. While mixed-layer NO_3^- and phosphate (PO_4^{3-}) concentrations remain elevated throughout the spring and summer growth season (Sarmiento et al., 2004; Nissen et al., 2021), $Si(OH)_4$ is rapidly depleted by silicifying phytoplankton (i.e., silicoflagellates and diatoms) resulting in $Si(OH)_4$ becoming limited by mid-summer (Trull et al., 2001; Salter et al., 2007; Pollard et al., 2009).

The iron limiting conditions of the Subantarctic drive deviations in the expected macronutrient uptake ratios and have global biogeochemical implications (Sarmiento et al., 2004; Arteaga et al., 2019; Fripiat et al., 2021; Nissen et al., 2021). For example, under iron replete conditions diatoms consume $Si(OH)_4$ and NO_3^- (hereafter referred to as Si:N) in a ratio of ~1:1 (Brzezinski, 1985; Ragueneau et al., 2000; Hutchins and Bruland, 1998; Takeda, 1998; Mosseri et al., 2008) while under iron deplete conditions, they consume disproportionately more Si than N (Si:N >>2:1) (Arrigo et al., 1999; Franck et al., 2000; Brzezinski et al., 2003; Green and Sambrotto, 2006; Mosseri et al., 2008; Weber and Deutsch, 2010a; Martiny et al., 2013). This behaviour depletes the mixed-layer $Si(OH)_4$ inventory more rapidly than NO_3^-, decoupling the N and silica cycles through the preferential export of $Si(OH)_4$ (Hoffmann et al., 2008; Assmy et al., 2013b, a; Boyd, 2013; Nissen et al., 2021). Furthermore, the northward Ekman transport of surface waters drives a north-to-south gradient in the macronutrient concentrations (i.e.,

elevated in the south and decreasing northwards), which controls the distribution of various phytoplankton groups (Hoffmann et al., 2008; Quéguiner, 2013; Weir et al., 2020). Heavily-silicified diatom species (e.g., *Fragilariopsis spp.*) are abundant in the $Si(OH)_4$-replete waters of the PFZ, with their distribution decreasing northwards (Salter et al., 2007; Assmy et al., 2013b; Rembauville et al., 2016). A shift towards smaller, less-silicified diatom species (e.g., *Thalassiosira spp.*) and non-silicified phytoplankton (e.g., nanoflagellates) occurs in the SAZ (Smetacek et al., 2004; Hoffmann et al., 2008; Assmy et al., 2013b; Quéguiner, 2013). The meridional $Si(OH)_4$ gradient thus controls the distribution of diatoms, with implications for N, carbon and silica export (Sigman et al., 1999; Lourey and Trull, 2001; Weir et al., 2020).

Antarctic Zone (including MIZ and CCSZ)

The AZ is defined as the region south of the PF, and is divided into the OAZ and the Polar AZ (PAZ) by the sACCF (Fig. 1.2; Talley et al., 2011). The OAZ is permanently ice-free while the PAZ experiences seasonal sea-ice cover (Whitworth and Nowlin, 1987; Orsi et al., 1995). The water masses present in the AZ are similar to those in the PFZ; however, the upwelling of UCDW at the sACCF indicates the southern extent of UCDW (Talley et al., 2011). As such, in the OAZ, UCDW underlies the surface waters while in the PAZ, the underlying water mass is LCDW (Talley et al., 2011 and references therein). Furthermore, the AZ is characterised by a distinct temperature minimum (T_{min}) layer of -1.5°C to 2°C that lies beneath the summer mixed layer. The T_{min} forms when the warming and freshening of surface waters causes the summer mixed layer to shoal, leaving the remnant of the winter mixed layer behind (Gordon et al., 1977; Talley et al., 2011 and references therein). The T_{min} can therefore be used as a summertime record of winter mixed layer conditions, providing an indication of the conditions from which the summer mixed layer evolved (Altabet and Francois, 2001; Difiore et al., 2010).

The largest distinction between the Subantarctic and AZ is that the more southerly latitude of the AZ means that its waters are subject to a high degree of seasonality, particularly in light availability, that influences biogeochemical cycling and phytoplankton community composition (Moore and Abbott, 2000). Similar to the Subantarctic, the predominant mechanism of nutrient supply to the AZ surface waters is deep winter mixing (Sigman et al., 1999; Dong et al., 2008; Henley et al., 2017, 2020). Moreover, iron limitation persists in AZ surface waters, albeit to varied extents across the region (Klunder et al., 2011, 2014; Tagliabue et al., 2012; De Jong et al., 2012). In contrast to the Subantarctic, $Si(OH)_4$ concentrations are perennially elevated in the AZ mixed layer, allowing for the proliferation of silicified phytoplankton species (predominantly diatoms) throughout the phytoplankton growth season (Smetacek et al., 2002; Assmy et al., 2013b; Quéguiner, 2013). Once these diatoms become iron-limited, they consume more $Si(OH)_4$ than NO_3^- (i.e., Si:N uptake ratio >>2:1), ultimately driving

a meridional nutrient gradient that is depleted in $Si(OH)_4$ relative to NO_3^- compared to the CDW source waters (Treguer and Jacques, 1992; Pollard et al., 2002; Henley et al., 2020)

The OAZ is characterised by perennial iron limitation as deep winter mixing supplies insufficient iron to surface waters, and the supply of iron by other mechanisms (e.g., iceberg melt) is scarce (Klunder et al., 2011; Tagliabue et al., 2012). The OAZ is therefore characterised by low productivity and carbon export (Quéguiner, 2013), with a phytoplankton community predominantly consisting of small diatoms and other small phytoplankton (e.g., nanoflagellates; (Quéguiner, 2013; Petrou et al., 2016). In contrast, the MIZ and CCSZ experience elevated iron availability, largely due to rapid sea-ice melt that can supply >2 nM of iron to surface waters (Klunder et al., 2011, 2014; Tagliabue et al., 2012). The MIZ and CCSZ therefore host large phytoplankton blooms, fuelled by the high iron supply and increased light availability associated with sea-ice melt-driven stratification, that are dominated by large (>20 μm) diatoms that contribute significantly to carbon and silica export (El-Sayed and Taguchi, 1981; Smith and Nelson, 1990; Quéguiner, 2013). The dynamics of the iron supply to the AZ therefore regulate the magnitude and duration of phytoplankton blooms in this region, with consequences for carbon and silica export, as well as the stoichiometry of the lateral nutrient supply to the Subantarctic (Takeda, 1998; Brzezinski et al., 2003; Sarmiento et al., 2004; Mosseri et al., 2008b; Tréguer et al., 2017; Nissen et al., 2021).

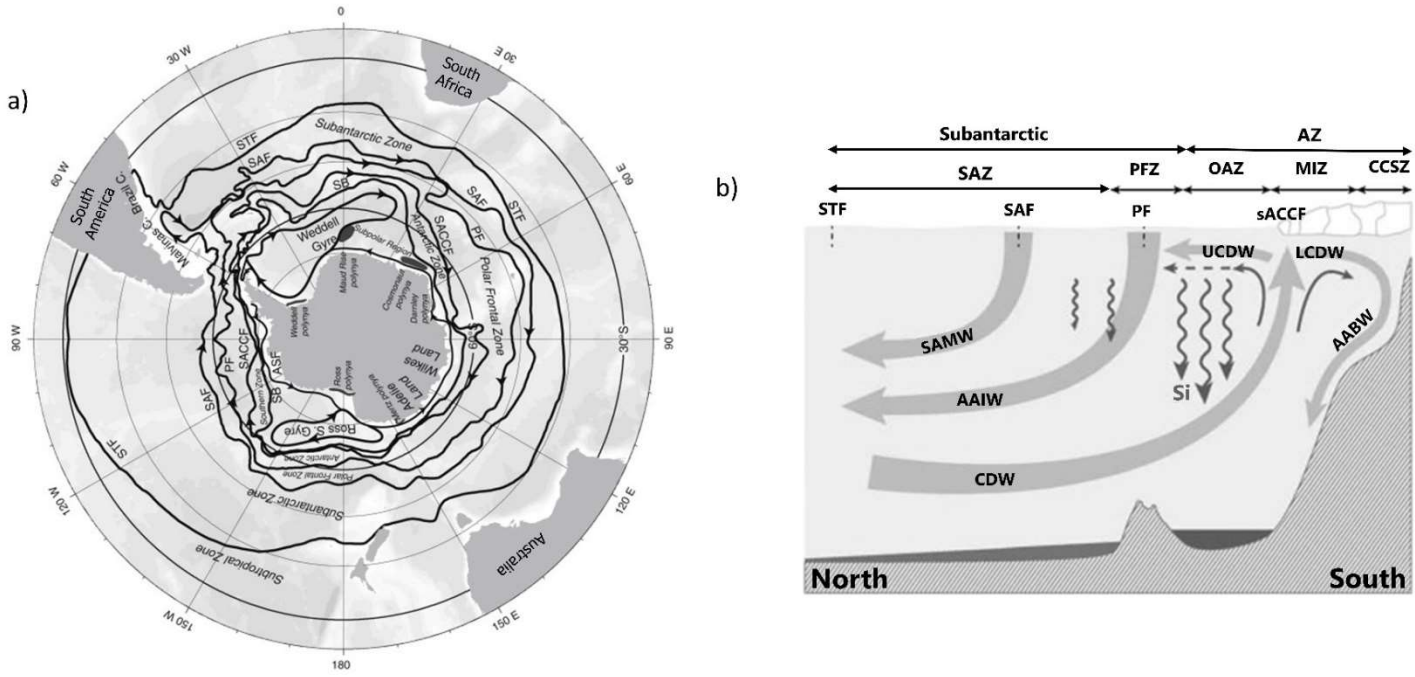


Figure 1. 2. a) Map of Southern Ocean showing the annual mean positions of the hydrographic fronts (Subtropical Front – STF, Subantarctic Front – SAF, Polar Front – PF, southern Antarctic Circumpolar Current Front - SACCF, southern Antarctic Circumpolar Current boundary (SB)) and

zones, and b) section plot across the Southern Ocean showing the approximate circulation of the intermediate and deep water masses (Subantarctic Mode Water – SAMW, Antarctic Intermediate Water – AAIW, Circumpolar Deep Water – CDW, Upper Circumpolar Deep Water – UCDW, Lower Circumpolar Deep Water – LCDW, Antarctic Bottom Water - AABW) in each hydrographic zone (Subantarctic Zone – SAZ, Polar Frontal Zone – PFZ, Open Antarctic Zone – OAZ, Marginal Ice Zone – MIZ, Coastal and Continental Shelf Zone – CCSZ). The general flow-path of the Antarctic Circumpolar Current (ACC) is denoted by the black arrows in panel (a). The size of the arrows in panel (b) indicates the proportion of silica export in each hydrographic zone. [Panel (a) taken from Talley et al. (2011) and panel (b) modified from Tréguer (2014)].

1.3. Phytoplankton diversity in the Southern Ocean

The phytoplankton community in the Southern Ocean is diverse, with the variability in community composition driven by a number of "bottom-up" (e.g., nutrients, light) and "top-down" (e.g., grazing pressure) controls (Quéguiner, 2013; Deppeler and Davidson, 2017; Arteaga et al., 2020). The efficiency with which the phytoplankton community exports carbon is dependent on numerous factors such as cell size, phytoplankton physiology, nutrient preference, and nutrient uptake ratios and strategies (Edwards et al., 2012 and references therein; Glibert et al., 2016 and references therein). The data presented throughout this thesis show that intermediate-to-large-sized cells are disproportionately important for carbon export in the Southern Ocean, with the dominance of one group over another, as well as the shifts in community composition over the spring/summer growth season, generally driven by various physicochemical factors (e.g., mixed-layer depth, iron availability) and grazing pressure. The main phytoplankton groups considered throughout this thesis will be discussed below.

1.3.1. Picophytoplankton

Picophytoplankton are the smallest phytoplankton size-class (defined as 0.3-2.7 μm in this thesis) and are generally the most abundant, resulting in their ubiquity across the global oceans (Buitenhuis et al., 2012). This size-class encompasses both prokaryotes and eukaryotes, with picoeukaryotes (0.8-2.7 μm) typically being larger than the prokaryotes *Synechococcus* (~1.0-1.6 μm) and *Prochlorococcus* (~0.6 μm) (Marie et al., 2005). The small size of picophytoplankton means that these cells have a high surface area-to-volume ratio, allowing them to be more efficient at utilising nutrients and light, as well as having a lower requirement for these resources compared to larger cells (Edwards et al., 2012). This physiological advantage is a major reason for the high abundance of picophytoplankton (Quere et al., 2005).

Little is known about the picophytoplankton in the Southern Ocean; however, two groups have been observed – picoeukaryotes and picoprokaryotes (mainly *Synechococcus*) (Doolittle et al., 2008; Buitenhuis et al., 2012). *Prochlorococcus* is generally thought to be limited to the tropical and temperate

oceans (i.e., north of the STF, the northern border of the Southern Ocean) due to its growth being inhibited by temperatures cooler than 15°C (Moore et al., 1995; Partensky et al., 1999b, a; Johnson et al., 2006; Flombaum et al., 2013). By contrast, *Synechococcus* is ubiquitous across the global ocean and due to the high physiological diversity of this group, it is able to thrive in polar waters (Moore et al., 1995; Zwirglmaier et al., 2008; Huang et al., 2012; Flombaum et al., 2013; Gilbert et al., 2022). In addition, the Southern Ocean hosts a diverse eukaryotic population, from diatoms to cryptophytes to *Phaeocystis antarctica*, with some of these groups occupying a broad size range including that of the picophytoplankton. The major phytoplankton groups identified and discussed in Chapters 2-4 of this thesis are described in detail below.

Synechococcus

Synechococcus is abundant in high-light, high-nutrient environments (such as the subtropical gyres and in the summertime Southern Ocean) (Shapiro and Haugen, 1988; Partensky et al., 1999; Treibergs et al., 2014; Flombaum et al., 2013; Gilbert et al., 2022). *Synechococcus* has been observed to utilise both oxidized (e.g., NO_3^-) and reduced N forms (e.g., NH_4^+; Glibert et al., 1986; Paerl, 1991; Lindell et al., 1998; Collier et al., 1999; Moore et al., 2002; Maranger et al., 1998; Glibert et al., 2016); however, culture and field studies have shown that *Synechococcus* prefers reduced N forms (Glibert and Ray, 1990; Lindell and Post, 2001; Fawcett et al., 2011, 2015; Treibergs et al., 2014). There are exceptions to this, with a some studies observing a positive relationship between the abundance of *Synechococcus* and the ambient NO_3^- concentration, with the inference being that *Synechococcus'* growth is strongly dependent on NO_3^- availability (Partensky et al., 1999; Durand et al., 2001). Furthermore, a recent study conducted by Forrer (2021) in the Indian sector of the Subantarctic showed that *Synechococcus* relied heavily on NO_3^- even under elevated NH_4^+ availability (>0.5 μM). Forrer (2021) concluded that the high NO_3^- dependence of *Synechococcus* was the result of various physicochemical drivers including nutrient availability (specifically, iron) and warm mixed-layer temperatures.

Synechococcus is distinct from other phytoplankton groups in that in addition to chlorophyll, it contains a high proportion of the light-harvesting pigment, phycoerythrin (Sunda and Huntsman, 2015). The high proportion of phycoerythrin in *Synechococcus* is thought to be the result of the high light requirement of *Synechococcus* due to its high ratio of photosystem I relative to photosystem II (Sunda and Huntsman, 2015). The high-light requirement of *Synechococcus* regulates its distribution, both geographically (limited to high-light environments) and throughout the water column (prevalent in surface waters with abundances decreasing towards the base of the euphotic zone) (Glover et al., 1987; Prezelinl et al., 1989; Moore et al., 1998; Sunda and Huntsman, 2015). Furthermore, photosystem I requires approximately four-times as much iron as photosystem II, resulting in *Synechococcus* also having a high iron requirement (Raven, 1990; Brand, 1991; Wilhelm et al., 1996). The high light and

iron requirements of *Synechococcus* may therefore limit its distribution in the Southern Ocean where light and iron are at times co-limiting (Sunda and Huntsman, 2015).

1.3.2. Eukaryotes

Diatoms

Diatoms account for ~20% of global primary productivity (Nelson et al., 1995) and due to their requirement for $Si(OH)_4$ to build their silica-frustules, regulate the ocean's silica cycle (Tréguer et al., 1995; Tréguer, 2014). In the Southern Ocean, diatoms generally dominate carbon and silica export (Tréguer et al., 2017), with their geographic distribution regulated by the availability of $Si(OH)_4$ in surface waters, particularly in the Subantarctic (Quéguiner, 2013). Diatoms can be divided into two main types: type 1 diatoms are small (5-25 μm; either nano- or micro-phytoplankton), weakly-silicified species that grow rapidly under conditions of high light and nutrient availability (e.g., *Chaetoceros* spp.) and type 2 diatoms are large (>20 μm; microphytoplankton), heavily-silicified species that are slow growing and able to persist in the mixed layer even under nutrient- and light-limited conditions (e.g., *Fragilariopsis* spp.) (Quéguiner, 2013). The ecology of type 1 diatoms leads to the dominance of this group early in the growth season, particularly in regions where there is a high supply of $Si(OH)_4$ and iron such as in the MIZ, CCSZ and in the vicinity of Southern Ocean fronts where upwelling occurs (e.g., at the PFZ; Quéguiner, 2013; Assmy et al., 2013). By contrast, type 2 diatoms generally dominate in the open Southern Ocean where iron is somewhat limiting, with the larger size of these cells allowing them to achieve higher maximum nutrient uptake rates and escape predation more effectively than the smaller phytoplankton (Smetacek, 2000; Smetacek et al., 2004; Edwards et al., 2012; Quéguiner, 2013; Assmy et al., 2013b).

The two different diatom types have distinct implications for carbon export, particularly since type 1 diatoms are carbon-rich relative to type 2 diatoms (Assmy et al., 2013b; Tréguer et al., 2017). This difference arises because type 2 diatoms inherently contain less carbon per mole of N and their persistence in the mixed layer throughout the growth season requires that they recycle their cellular contents, which ultimately leads to the export of carbon-poor frustules (Assmy et al., 2013b; Tréguer et al., 2017). Both diatom types are, however, important for export in the Southern Ocean, both directly (via their contribution to the sinking flux) and from a mass balance perspective. Southern Ocean diatoms are known to preferentially consume NO_3^- even when regenerated N concentrations are elevated (Probyn and Painting, 1985; Koike et al., 1986; Lomas and Glibert, 1999; Karsh et al., 2003), which means that they make a significant contribution to new production and by extension, carbon export potential and the biological carbon pump (Dugdale and Goering, 1967). In addition, diatoms have protective silica-frustules that allow their cells to remain intact within the zooplankton digestive tract, which inhibits the remineralisation of diatom cells in the mixed layer and increases the sinking velocities of the now silica-ballasted faecal pellets (Smetacek, 2000; Smetacek et al., 2004; Quéguiner, 2013;

Tréguer et al., 2017). These silica-frustules therefore enhance the export efficiency of diatom cells, strengthening the biological pump. Additionally, diatoms generally form long chains that collate PON as they sink out of the mixed layer, which further increases the export of PON from the surface into the mesopelagic (Smetacek, 2000). The large contribution of diatoms to the export flux in the Southern Ocean is evidenced by the high diatom abundance in sediment traps and the sediment record, which supports the notion that this phytoplankton group makes a disproportionate contribution to carbon export relative to other phytoplankton groups (Trull et al., 2001; Smetacek et al., 2002; Lourey et al., 2003; Rigual-Hernández et al., 2015, 2016; Rembauville et al., 2016).

The perennially low iron conditions of the Southern Ocean have implications for the diversity and nutrient stoichiometry of diatoms (Strzepek et al., 2011; Quéguiner, 2013; Tréguer et al., 2017). Under iron-deplete conditions, diatoms increase their consumption of $Si(OH)_4$ and phosphate (PO_4^{3-}) relative to N (uptake ratios of >2:1 and 12:1, respectively; Hutchins and Bruland, 1998; Takeda, 1998; Arrigo et al., 1999; Ragueneau et al., 2000; Mosseri et al., 2008). This leads to the iron limited surface waters where diatoms dominate (e.g., the AZ) having low(high) Si:N(:P) ratios, which in turn affects the ratio of the nutrients available to the succeeding phytoplankton community and of the mode and intermediate water masses that supply the lower latitudes (e.g., SAMW in the SAZ) (Sarmiento et al., 2004; Weber and Deutsch, 2010; Henley et al., 2020; Nissen and Vogt, 2021). Furthermore, the preferential consumption of $Si(OH)_4$ over N in the PFZ and AZ limits the availability of $Si(OH)_4$ in the SAZ (Fig. 1.2b), which limits the growth of diatoms, particularly large, heavily-silicified diatom species, and allows for the proliferation of other phytoplankton groups such as nanoflagellates (Hoffmann et al., 2006, 2008), with associated implications for carbon export.

Phaeocystis antarctica

P. antarctica exist either as single cells (~3-9 μm; nanophytoplankton) or as large, mucosal colonies (>20 μm; microphytoplankton) (Schoemann et al., 2005), with the formation of colonies catalysed by bottom-up (e.g., iron availability) and/or top-down drivers (e.g., increased grazing pressure) (Goffart et al., 2000; Schoemann et al., 2005; Nissen and Vogt, 2021). Blooms of *P. antarctica* are generally observed in the MIZ and CCSZ of the Southern Ocean, and their initiation appears to be driven by deep mixed layers coincident with high iron availability (Goffart et al., 2000; Schoemann et al., 2005; Nissen and Vogt, 2021). The proliferation of *P. antarctica* under these conditions occurs because they are low light specialists and are thus able to outcompete other phytoplankton groups in weakly-stratified waters such as coastal polynyas or in the late-summer MIZ following sea-ice melt and increased wind-mixing (Goffart et al., 2000; Schoemann et al., 2005; Strzepek et al., 2011). In these regions, iron is generally elevated early in the growth season (Klunder et al., 2014) and colonial *P. antarctica* store excess iron within their mucosal matrix, which allows them to persist later in the season when iron is depleted (Schoemann et al., 2005; Strzepek et al., 2011). Furthermore, the large mucosal *P. antarctica* colonies

(at times as large as 3 cm; Schoemann et al., 2005) are less palatable than smaller phytoplankton (e.g., diatoms; Dennett et al., 2001; Wright et al., 2010), mitigating their losses due to predation. These mechanisms therefore provide *P. antarctica* with a physiological advantage over other phytoplankton groups as iron becomes limiting and grazing pressure increases. The growth of *P. antarctica* is, however, inhibited in the open Southern Ocean where iron is perennially depleted (Klunder et al., 2011; Tagliabue et al., 2012), even in regions with deep mixed layers (e.g., the SAZ) because of their high iron requirement (Goffart et al., 2000; Nissen and Vogt, 2021). The distribution of *P. antarctica* is therefore predominantly regulated by iron availability, with this species generally present in the MIZ and CCSZ.

Cryptophytes

Cryptophytes are characterised as nanoeukaryotes (6-20 μm; Clay and Kugrens, 1999) and, along with diatoms and *P. antarctica*, are one of the most abundant phytoplankton groups present in the Antarctic CCSZ (Garibotti et al., 2005; Trimborn et al., 2015). Similarly to *Synechococcus,* cryptophytes evolved from red algae and therefore contain a high quantity of phycoerythrin (McFadden, 2001). They also contain photoprotective carotenoid pigments, which, combined with the phycoerythrin, allows them to thrive under both light-limited (i.e., in deep mixed layers) and high-light (i.e., in shallow mixed layers) conditions (Mendes et al., 2018a; Trimborn et al., 2019; Mendes et al., 2023).

In the Antarctic CCSZ, cryptophyte blooms are generally negatively correlated with diatoms blooms and cryptophytes typically succeed diatoms (Mendes et al., 2013, 2018b; Kerr et al., 2018). Cryptophytes blooms are generally initiated by rapid sea-ice- and/or glacial melt, which shoals the mixed layer and exposes the endemic phytoplankton community to high light (Mendes et al., 2012, 2013, 2023). However, cryptophytes have photoprotective carotenoids which allows this group to thrive under conditions that might otherwise be characterised as photoinhibitory (Mendes et al., 2018a, 2023). The shift from diatoms to cryptophytes in the Antarctic CCSZ may also be favoured by a decrease in iron availability, as cryptophytes have a lower iron requirement than diatoms (Koch and Trimborn, 2019). Furthermore, cryptophytes have been observed to decrease their cell size, thus increasing their surface area-to-volume ratio, under low iron conditions, which allows them to more efficiently access the lower concentrations of iron as smaller cells have a higher nutrient affinity (Raven and Kübler, 2002; Strzepek et al., 2011; Sunda, 2012). A shift in the phytoplankton community from diatoms to cryptophytes in the Antarctic CCSZ (such as along the Antarctic Peninsula) is therefore expected as the growth season progresses and iron becomes limiting.

1.3.3. Dinoflagellates

Dinoflagellates in the Southern Ocean are generally mixotrophic (facultatively autotrophic and heterotrophic) (Moorthi et al., 2009; Stoecker et al., 2016) and may switch between these strategies

based the availability of nutrients and light (Berge et al., 2016). Dinoflagellates have been observed to be associated with elevated concentration of regenerated N (Cochlan, 2008), although this may not be due to this group preferring regenerated N. Rather, the observed coincidence of dinoflagellates with elevated regenerated N concentrations may arise because later in the growth season after the spring and summer phytoplankton blooms have depleted the surface iron inventory, regenerated N concentrations increase due to heterotrophic consumption and remineralisation of bloom biomass (Goeyens et al., 1995; Semeneh et al., 1998). As iron becomes limiting, dinoflagellates shift towards heterotrophy, particularly since phagotrophy (i.e., the engulfing of phytoplankton cells) provides them with a direct iron source from the engulfed cells (Maranger et al., 1998; Stukel et al., 2011). Indeed, a recent modelling study found that dinoflagellates switch from autotrophy to phagotrophy as iron become limiting (Berge et al., 2016). The role of dinoflagellates in carbon and nutrient cycling across the Southern Ocean remains poorly understood (Stoecker et al., 2016); further studies are therefore required to investigate their importance for phytoplankton productivity and carbon export.

1.4. Quantifying the nitrogen cycle using nitrogen isotopes

The N cycle can be investigated using the stable isotopes of N, ^{14}N and ^{15}N. The different atomic masses of these isotopes renders them a useful tool for tracing biological and chemical processes because the light isotope (^{14}N) is often preferentially reacted over the heavier isotope (^{15}N; Mariotti et al., 1981; Sigman and Fripiat, 2019). The isotopes of N are generally applied using two different methods to assess the N cycle. ^{15}N-labelled tracers (e.g., $Na^{15}NO_3$ and $^{15}NH_4Cl$) are used to assess the instantaneous rate of N cycle processes (e.g., NO_3^- assimilation by phytoplankton), while measurements of the naturally occurring ratio of $^{15}N/^{14}N$ ($\delta^{15}N$) is often used to study the cycling of N over longer time-scales (weeks-to-years). Below, the difference between these two methods are discussed, along with how they are applied in this thesis to investigate the dominant N source(s) (i.e., new versus regenerated) utilised by phytoplankton.

1.4.1. ^{15}N-labelled tracer incubation experiments

^{15}N-labelled tracer additions can be used to investigate the rates of N cycle processes such as nitrification, denitrification and N_2 fixation as they allow for the direct quantification of the rates at which various N species are transformed. The tracer addition method has long been used to investigate the uptake of N by phytoplankton because PON is easily filtered from seawater (Lipschultz, 2008 and references therein). Improvements in the analytical tools used to measure ^{15}N (Lipschultz, 2008 and references therein) and advances in our ability to measure low concentrations (sub-micromolar) of inorganic and organic N (Garside, 1982; Holmes et al., 1999; McCarthy and Bronk, 2008 and references therein) have allowed for the quantification of almost all transformation pathways in the N cycle using the ^{15}N tracer approach (e.g., Bronk and Glibert, 1993; Jensen et al., 1996).

The most common application of the ^{15}N tracer approach is experiments aimed to quantify the rate of N uptake by phytoplankton (Dugdale and Wilkerson, 1986; Lipschultz, 2008). Here, ^{15}N-labelled substrate (e.g., NO_3^-, NH_4^+, urea) is added to seawater and the change in the ^{15}N enrichment of the substrate or the PON pool is monitored over a specific time period, ultimately allowing for the uptake rate of the substrate to be calculated. An experiment designed to quantify the *in situ* uptake rate is characterised by ^{15}N-labelled substrate additions at ~5-10% of the ambient concentration of the substrate (Lipschultz, 2008). Additions greater than this generally stimulate uptake of the substrate, and can therefore result in the overestimation of the uptake rate relative to that observed in the environment at ambient substrate concentrations.

A major consideration in designing ^{15}N tracer experiments is ensuring that mass balance is maintained and that all transformations of the ^{15}N-labelled substrate are accounted for (Lipschultz, 2008). Constraining all transformation processes may prove challenging. For example, during long incubations (~24 hours) the ^{15}N-labeled NH_4^+ pool may be diluted by the regeneration of ^{14}N-NH_4^+ (from the ^{14}N-PON originally present in the sample bottle) (i.e., isotope dilution; Gilbert et al., 1982; Harrison and Harris, 1986). Not accounting for NH_4^+ regeneration if this flux is significant would lead to an underestimation of the NH_4^+ uptake rate because the phytoplankton are assimilating an NH_4^+ pool that is lower in $^{15}N/^{14}N$ than it was when the ^{15}N-NH_4^+ was added at the start of the experiment (Lipschultz, 2008).

To ensure that tracer experiments are as robust and representative of environmental conditions as possible, zooplankton grazing and isotope dilution either need to be accounted for or mitigated. Limiting the effects of zooplankton grazing is fairly straightforward, and requires only that the seawater be filtered through a large mesh (generally >200 μm) prior to tracer addition (Lipschultz, 2008 and references therein). To mitigate isotope dilution, the experiments need to be short enough to prevent signification dilution of the substrate pool while also long enough to ensure that there is enough time for the phytoplankton to assimilate a sufficient quantity of the ^{15}N-labelled substrate that it alters their PON $^{15}N/^{14}N$ (Lipschultz, 2008). Advances in analytical methods (e.g., continuous flow-isotope ratio mass spectrometry) have greatly improved measurement sensitivity, allowing for much shorter incubation times (as short as 3 hours) and low concentrations of ^{15}N-labelled substrate to be added (the latter reducing the risk of stimulating uptake).

1.4.2. Natural abundance nitrogen isotopes

As previously stated, N has two stable isotopes, ^{14}N and ^{15}N. The ^{14}N is the most abundant isotope (accounting for 99.63% of all N on Earth), while only 0.37% exists as ^{15}N. Various biological, chemical and physical processes discriminate between the two isotopes, with the measurement of their ratio

(quantified as $\delta^{15}N$; eq. 1.1) providing us with a tool to track these processes. The $\delta^{15}N$ is quantified (in permil (‰) vs N_2 in air) as:

$$\delta^{15}\mathrm{N} = \left(\frac{(^{15}\mathrm{N}/^{14}\mathrm{N})_{\mathrm{sample}}}{(^{15}\mathrm{N}/^{14}\mathrm{N})_{\mathrm{standard}}} - 1\right) \mathrm{x}\ 1000 \quad (1.1)$$

Processes that affect the distribution of stable isotopes are either unidirectional, resulting in kinetic isotope fractionation, or bilateral, yielding an equilibrium isotope effect (Sharp, 2017). Biological nitrogen cycle processes (e.g., NO_3^- uptake) are often unidirectional (Mariotti et al., 1981). During NO_3^- uptake, phytoplankton preferentially consume ^{14}N-bearing NO_3^- as it is more energetically efficient to do so (Sigman and Casciotti, 2001). The PON (also known as the product) pool that is produced by NO_3^- assimilation is therefore lower in $\delta^{15}N$ than the substrate (also known as the reactant) pool (i.e., the NO_3^- pool). As phytoplankton consumption proceeds, both the reactant and product pools become increasingly enriched in ^{15}N, which increases the $\delta^{15}N$ of both pools. The extent of the isotope fractionation between the reactant and product pools is described by the isotope effect (ε), which is approximated as:

$$\varepsilon\ (‰) = (1 - {}^{15}\mathrm{k}/{}^{14}\mathrm{k})\ \mathrm{x}\ 1000 \quad (1.2)$$

where ^{15}k and ^{14}k are the rate coefficients of the heavily and light isotope of N, respectively (Mariotti et al., 1981).

The evolution of the $\delta^{15}N$ of the substrate and product pools undergoing kinetic isotope fractionation are frequently investigated using either the Rayleigh model or the steady-state model.

The Rayleigh model

The Rayleigh model is used to approximate a closed system (i.e., no inputs or outputs) where the initial supply of the reactant is transformed into the product via a unidirectional reaction with a constant ε (Fig. 1.3; Mariotti et al., 1981; Sigman et al., 1999, 2009). As the reaction progresses, the reactant pool is depleted and its $\delta^{15}N$ ($\delta^{15}N_{reactant}$; black line in Fig. 1.3) increases due to kinetic isotope fractionation (ε). The $\delta^{15}N_{reactant}$ in the framework of the Rayleigh model is defined as:

$$\delta^{15}\mathrm{N}_{\mathrm{reactant}} = \delta^{15}\mathrm{N}_{\mathrm{initital}} - \varepsilon \ln(f) \quad (1.3)$$

where $\delta^{15}N_{initial}$ is the $\delta^{15}N$ of the reactant at the beginning of the reaction and f is the fraction of the reactant remaining at any point during the reaction (i.e., $[reactant]/[reactant]_{initial}$).

As the reactant is transformed into the product (e.g., NO_3^- is transformed into PON), its $\delta^{15}N$ rises. The $\delta^{15}N$ of the product pool that is instantaneously produced ($\delta^{15}N_{instantaneous}$; black dotted-dashed line in Fig. 1.3) from the substrate is defined as:

$$\delta^{15}N_{instantaneous} = \delta^{15}N_{reactant} - \varepsilon \quad (1.4)$$

The $\delta^{15}N_{instantaneous}$ is therefore lower than the $\delta^{15}N_{reactant}$ by ε. The $\delta^{15}N$ of the accumulated product pool ($\delta^{15}N_{accumulated}$; black dashed line in Fig. 1.3) increases more gradually than that of the $\delta^{15}N_{instantaneous}$ as it represents the summed product pool over the entire reaction. The $\delta^{15}N_{accumulated}$ is defined as:

$$\delta^{15}N_{accumulated} = \delta^{15}N_{initial} + \varepsilon\left(\frac{f}{1-f}\right)\ln(f) \quad (1.5)$$

At the end of the reaction (i.e., when [reactant] = 0 and $f = 1$), the $\delta^{15}N_{accumulated}$ will be equal to the $\delta^{15}N_{initial}$ because the entire reactant pool has been converted into the product pool.

The Rayleigh model only holds if the system remains closed, which is a reasonable assumption for the summertime Southern Ocean, particularly the AZ (Sigman et al., 1999; Smart et al., 2015). However, there may be instances when a mixing event occurs during the period of NO_3^- consumption, thereby violating the Rayleigh model. Following such a mixing event, the reactant pool will have a concentration and $\delta^{15}N$ that falls between that of the newly supplied- and partially consumed reactant pools, along a mixing line (Fig. 1.4). The extent to which the mixing line deviates from the Rayleigh model is dependent on the fraction of the reactant pool that was consumed prior to mixing. The larger the fraction of the reactant pool consumed, the more the $\delta^{15}N$ and concentration of the mixed pool will differ from that predicted by the Rayleigh model (Fig. 1.4; Sigman et al., 1999).

The steady-state model

The steady-state model approximates an open system (i.e., the reactant is continuously supplied to balance the output, such that the net supply of the reactant is equal to the sum of the product and the exported reactant) (Sigman et al., 1999; Sigman and Fripiat, 2019). As per the Rayleigh model, as the steady-state reaction progresses and the reactant concentration declines, the $\delta^{15}N_{reactant}$ and $\delta^{15}N_{product}$ both increase (green lines Fig. 1.3). At the end of the reaction (i.e., when [reactant] = 0 and $f = 1$), the $\delta^{15}N_{product}$ will be equal to the $\delta^{15}N_{initial}$. The $\delta^{15}N$ of the reactant and product pools for a given ε and f are defined as:

$$\delta^{15}N_{reactant} = \delta^{15}N_{initital} - \varepsilon(1-f) \quad (1.6)$$

$$\delta^{15}N_{product} = \delta^{15}N_{initital} - \varepsilon(f) \quad (1.7)$$

At low degrees of NO_3^- consumption (f >0.65), the Rayleigh and steady-state models evolve similarly (Fig. 1.4; Sigman et al., 1999); therefore, in oceanic regions where <35% of the supplied NO_3^- is consumed (e.g., NO_3^- in the Southern Ocean), either model can be applied (Sigman et al., 1999). These models therefore provide us with a framework in which to interpret N isotope data and describe the biological, chemical and physical processes that influence the oceanic N cycle.

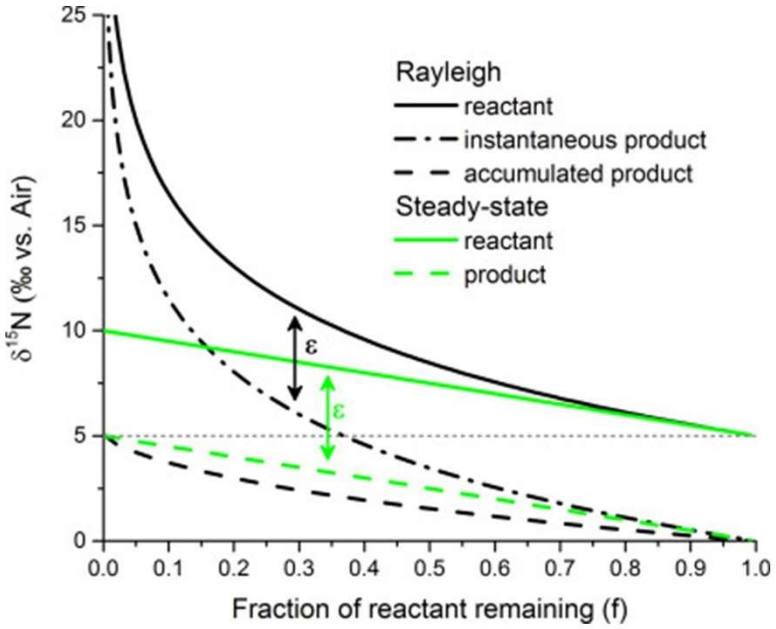


Figure 1.3. Illustration of the simple models (Rayleigh and steady-state) often used to interpret N isotope data. The evolution of the $\delta^{15}N$ of the reactant (solid lines) and product (dashed lines) pools as a function of reactant pool concentrations is shown based on the Rayleigh (black lines) and steady-state models (green lines). The fraction of reactant remaining (f) is calculated as the [reactant]/$[reactant]_{initial}$. A constant isotope effect (ε) of 5‰ was assumed for both models. [Figure taken from Sigman and Fripiat (2019)].

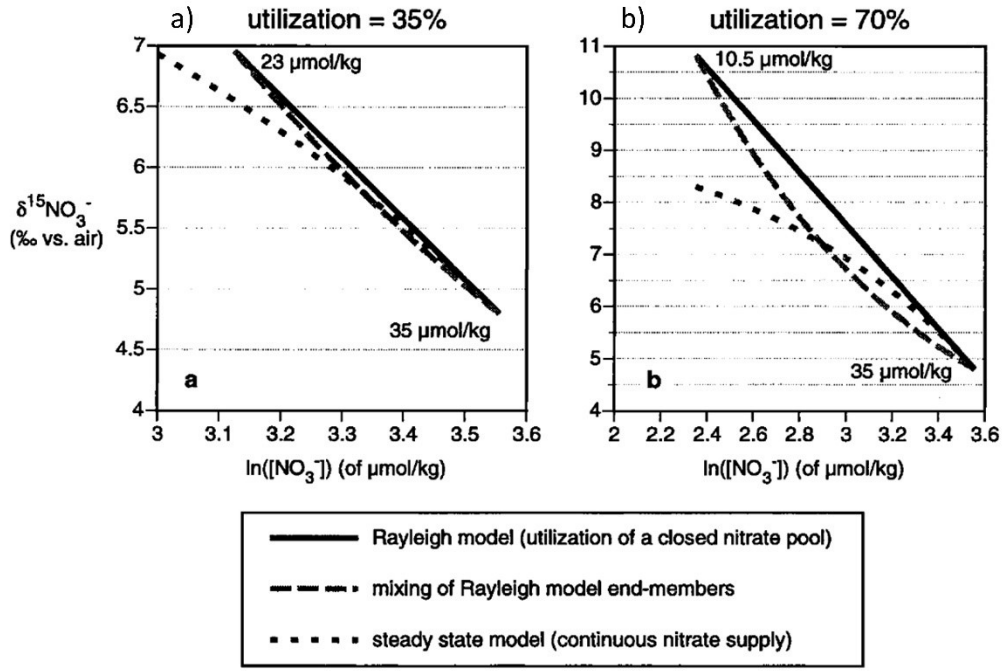


Figure 1. 4. The theoretical evolution of the $\delta^{15}N$ of NO_3^- (i.e., the reactant pool) as a function of the NO_3^- concentration according to the Rayleigh model (solid line), steady-state model (dotted line) and the mixing of the Rayleigh model end-members (dashed line; i.e., to demonstrate the effect on the NO_3^- $\delta^{15}N$/concentration relationship of a mixing event that violates the Rayleigh model assumption of a closed system). The panels also show how the $\delta^{15}N$ of the reactant pool differs for the Rayleigh and steady-state models assuming a) 35% utilisation of the initial reactant pool (i.e., f = 0.65) and b) 70% utilisation of the initial reactant pool (i.e., f = 0.3). [Figure taken from Sigman et al. (1999)].

Using nitrogen isotopes to estimate carbon export potential

N isotopes are used throughout this thesis to investigate the role of phytoplankton in the N cycle and the biological carbon pump of the Southern Ocean. To this end, the processes that affect the distribution and isotopic composition of N species in the ocean are discussed below. The isotopic fractionation of N isotopes reflects the biological processes that are active within the water column. The dominant biological process ongoing in the surface waters of the spring- and summertime Southern Ocean is phytoplankton assimilation (e.g., DiFiore et al., 2006; Difiore et al., 2009; Mdutyana et al., 2020; Flynn et al., 2021). During the assimilation of NO_3^-, phytoplankton preferentially consume ^{14}N relative to ^{15}N, coincidently increasing the $\delta^{15}N$ of the reactant NO_3^- and product (i.e., PON) pools. The $\delta^{15}N$ of the residual NO_3^- and PON pools is dependent on the degree of consumption (i.e., *f*) and the magnitude of ε. Field-based studies suggest that the ε of NO_3^- assimilation ranges from 4‰ to 10‰ (Sigman et al., 1999; DiFiore et al., 2006; Difiore et al., 2009, 2010; Sigman and Fripiat, 2019; Fripiat et al., 2019; Forrer, 2021). The ε is set by 1) the ε imparted during NO_3^- assimilation (which is generally small), and 2) the ε imparted during the intracellular reduction of NO_3^- to NO_2^- by NO_3^- reductase (which is significant 15-25‰; Needoba et al., 2004). The ε reflected in the in the environment is dependent on the quantity of unconsumed cellular NO_3^- that is effluxed from the cell (Francois et al., 1993; Needoba et al., 2004; Granger et al., 2004, 2010; Karsh et al., 2014).

In the Southern Ocean, NO_3^- is supplied to the mixed layer during deep winter mixing. Due to the perennially iron-, and at times, light-limited conditions of the Southern Ocean, NO_3^- is never fully consumed (Martin et al., 1991; Sunda and Huntsman, 1997). As a result, the $\delta^{15}N$ of the initial NO_3^- supply and the ε of NO_3^- uptake dictates the $\delta^{15}N$ of the residual NO_3^- pool and the PON produced during NO_3^- uptake (Sigman et al., 1999). The $\delta^{15}N_{NO_3^-}$ supplied to the mixed layer of the Southern Ocean is high (≥5‰; Sigman et al., 1999; Difiore et al., 2010; Fripiat et al., 2021) and phytoplankton growth fuelled by this NO_3^- yields biomass that is also relatively high in $\delta^{15}N_{PON}$ (0-5‰; Smart et al., 2020). In contrast, phytoplankton growth fuelled by NH_4^+ yields low $\delta^{15}N_{PON}$ (<0‰). This is because the $\delta^{15}N_{NH_4^+}$ is similarly low in the marine environment (~0‰) due to the process associated with NH_4^+ production (e.g., excretion by zooplankton and bacterial degradation of PON; Deniro and Epstein, 1981; Macko et al., 1986; Silfer et al., 1992; Checkley and Miller, 1989). Additionally, the ε associated with NH_4^+ uptake in the ocean is of little concern since its expression is concentration-dependent (Liu et al., 2013). At ambient NH_4^+ concentrations <5 μM, there appears to be no expression of an NH_4^+ assimilation ε. Additionally, even if there were a non-zero ε associated with NH_4^+ assimilation (given that our knowledge of the isotope systematics of NH_4^+ consumption are limited), the generally low mixed-layer NH_4^+ concentrations in the spring- and summertime Southern Ocean (Smith et al., 2022) and the preferential consumption of NH_4^+ over NO_3^- under iron limitation (El-Sayed and Taguchi, 1981; Dortch, 1990; Jacques, 1991; Goeyens et al., 1995) result in the (near-)complete consumption of mixed-

layer NH_4^+ (i.e., $f = 0$), which would yield no expression of ε (Hoch et al., 1993; Pennock et al., 1996; Waser et al., 1998a; Lourey et al., 2003). If some portion of regenerated N uptake was fuelled by urea, the $\delta^{15}N_{PON}$ produced would be low because urea has a low $\delta^{15}N$ (≤0‰) and the ε associated with urea uptake is small (<1‰; Waser et al., 1998b). The $\delta^{15}N_{PON}$ produced via the assimilation of regenerated N will therefore converge on the $\delta^{15}N_{NH_4^+}$, which is expected to be low (≤0‰).

The difference between the $\delta^{15}N_{PON}$ produced by new production ($\delta^{15}N_{PON}$ >>0‰) versus regenerated production ($\delta^{15}N_{PON}$ generally ≤0‰) therefore provides information about carbon export potential (e.g., Fawcett et al., 2011, 2014; Treibergs et al., 2014; Van Oostende et al., 2017; Forrer, 2021), even at low levels of NO_3^- consumption. This is based on the premise of the new production paradigm, whereby all NO_3^- consumed is assumed to be new to the mixed layer and must thus be balanced by an equal flux of organic N (and carbon) out of the mixed layer (Dugdale and Goering, 1967). The assumption that all NO_3^- is new to the mixed layer is appropriate for the summertime Southern Ocean where the predominant source of mixed layer NO_3^- is deep winter mixing (Sigman et al., 1999), with measurements from the summer revealing little to no contribution from mixed layer nitrification (Mdutyana et al., 2020; Flynn et al., 2021). However, if some portion of the NO_3^- consumed were produced in the mixed layer (e.g., as has been suggested to occur in the vicinity of Subantarctic Islands; (Cavagna et al., 2015; Dehairs et al., 2015), this NO_3^- would constitute a regenerated source of N and export would be overestimated (Yool et al., 2007). Not accounting for newly-nitrified NO_3^- is only an issue when estimating export production using ^{15}N-labelled tracer experiments because the $\delta^{15}N$ of new versus regenerated NO_3^- is different (Difiore et al., 2009; Fawcett et al., 2011; Smart et al., 2015). Phytoplankton biomass produced via the assimilation of regenerated NO_3^- has a low $\delta^{15}N$. This is because the nitrification of mixed layer NH_4^+ occurs coincident with NH_4^+ assimilation (Difiore et al., 2009). The nitrification of NH_4^+ occurs with a large ε (14-19‰; Mariotti et al., 1981; Yoshida, 1988; Casciotti et al., 2003; Santoro and Casciotti, 2011), while the assimilation occurs with no expressed ε (Hoch et al., 1993; Pennock et al., 1996; Waser et al., 1998; Lourey et al., 2003). The ^{14}N is therefore channelled into the regenerated NO_3^- pool (i.e., producing low $\delta^{15}N_{NO_3^-}$) while the ^{15}N is channelled into the PON pool (i.e., producing high $\delta^{15}N_{PON}$) (Difiore et al., 2009). However, in the summertime mixed layer, rates of nitrification are low and almost all of the NH_4^+ is assimilated rather than nitrified (Smart et al., 2015; Mdutyana et al., 2020; Flynn et al., 2021; Smith et al., 2022). As such, most of the mixed layer NH_4^+ is converted to PON rather than nitrified in the summertime so the $\delta^{15}N_{PON}$ produced via the assimilation of NH_4^+ is low (<0‰). As such, except in a few unusual cases, phytoplankton biomass with a high $\delta^{15}N$ was therefore produced from the assimilation of new N and is indicative of carbon export potential, while low-$\delta^{15}N_{PON}$ indicates phytoplankton growth fuelled by regenerated N (including NO_3^- produced via mixed layer nitrification), which results in no net carbon export (e.g., Fawcett et al., 2011, 2014; Treibergs et al., 2014; Van Oostende et al., 2017; Forrer, 2021).

Previous studies have used the $\delta^{15}N$ of bulk PON to investigate the photoautotrophic assimilation of new versus regenerated N in the Southern Ocean mixed layer (e.g., Karsh et al., 2003; Lourey et al., 2003). The bulk PON pool is, however, made-up of the active phytoplankton community, detritus and heterotrophic material (Fawcett et al., 2011) and integrates over longer time-scales (weeks to months) than the phytoplankton community (~days; Rau et al., 1991; Fawcett et al., 2011). The bulk PON pool is therefore susceptible to heterotrophic degradation and remineralisation, which may alter its isotopic composition (Trull et al., 2001; Lourey et al., 2003; Smart et al., 2020). These limitations in using the bulk PON pool to determine the dominant N source(s) to phytoplankton and estimate their relative contributions to carbon export potential motivated the work outlined in Chapter 4.

1.4.3. Coupling flow cytometry with nitrogen isotope analysis

To overcome the limitations inherent to bulk $\delta^{15}N_{PON}$ and to investigate how individual phytoplankton groups contribution to carbon export in the Southern Ocean, the photoautotrophic component of the bulk PON samples needs to be separated before the $\delta^{15}N_{PON}$ is measured (Fawcett et al., 2011, 2014; Treibergs et al., 2014). This can be achieved using flow cytometry, specifically via fluorescence-activated cell sorting (FACS). Flow cytometry has been used widely in ocean sciences to identify various phytoplankton populations (e.g., *Synechococcus*, *Prochlorococcus*), measure their abundances, and estimate cell size and biovolume (Chisholm et al., 1988; Olson et al., 1988; Marie et al., 2005). Briefly, phytoplankton cells are passed in front of a laser or lasers of specific wavelength and the light that scatters and fluoresces from the cells in response is then used to identify individual phytoplankton populations. For example, when excited by a blue laser (488 nm wavelength), cells containing chlorophyll-a will fluoresce red while cells containing phycoerythrin will fluoresce orange (Marie et al., 2005 and references therein). Once the different populations have been identified, they are sorted and the $\delta^{15}N$ of the specific phytoplankton populations ($\delta^{15}N_{phyto}$) is then measured using the persulfate-denitrifier method (Sigman et al., 2001; Knapp et al., 2005; Fawcett et al., 2011). This approach yields a measure of the $\delta^{15}N$ of specific phytoplankton populations (e.g., *Synechococcus*, picoeukaryotes, nanoeukaryotes, cryptophytes), from which their proportional contributions to new and regenerated production can be estimated (Fawcett et al., 2011, 2014; Treibergs et al., 2014)

1.5. Scope of thesis

The broad goal of this thesis was to investigate the role of phytoplankton community composition in the N cycle and biological carbon pump during the Southern Ocean growth season (i.e., spring and summer). The work described herein was conducted in the Atlantic sector of the Southern Ocean, with Chapter 2 focusing on all major frontal zones in the spring and Chapters 3 and 4 on the MIZ and CCSZ of the Weddell Sea in the summer.

In the literature review above (*Chapter 1: Introduction and literature review*), I have briefly introduced key concepts that are important for the entirety of the thesis. These include: the use of the new production paradigm to investigate the N cycle and carbon export, the role of iron in controlling primary production and nutrient dynamics in the Southern Ocean, the phytoplankton groups that dominate Southern Ocean biomass and productivity, and the methods used to quantify phytoplankton contributions to new production and carbon export. The content of the remaining chapters is briefly described below.

Chapter 2: Nanoplankton: the dominant vector of carbon export across the springtime Southern Ocean
The spring bloom in the open Southern Ocean is generally thought to be dominated by microplankton-sized diatoms, with their growth fuelled mainly by NO_3^- given the relatively high availability of iron in springtime surface waters (Smetacek, 2000; Smetacek et al., 2004; Quéguiner, 2013; Assmy et al., 2013b). Although N uptake has been extensively studied in the Southern Ocean, measurements are biased towards the summer and coincident measurements of N and iron uptake are scarce, particularly using tracer additions of 5-10% of ambient concentrations (i.e., representative of *in situ* conditions). Coincident experiments were conducted to quantify the size-fractionated (i.e., pico-, nano-, and microplankton) uptake rates of N (as NO_3^-, NH_4^+ and urea) and iron (as inorganic iron and siderophore-bound iron) at four stations located in each of the major hydrographic regions of the springtime Southern Ocean.

In contrast to expectations, biomass, net primary production (NPP) and N uptake were dominated by nanoplankton, primarily nanoplankton-sized *Chaetoceros* spp. The success of *Chaetoceros* appears to be due to this taxa employing a boom-and-bust lifecycle strategy. This strategy, possible because of its relatively smaller size, allowed *Chaetoceros* to grow rapidly and outcompete the microplankton-size diatoms (e.g., *Fragilariopsis*) for the available iron. Furthermore, *Chaetoceros* occupied a unique ecological niche because of its ability to form long (>50 μm), spiney chains. *Chaetoceros* was therefore able to concurrently act as microplankton (chains) and thus escape predation, in contrast to the picoplankton and other nanoplankton, and to act as nanoplankton (individual cells), which allowed *Chaetoceros* to access low concentrations of nutrients such as iron. *Chaetoceros* also had an apparently low iron requirement (iron:carbon uptake ratio of ~2:1), which did not increase with increasing reliance on NO_3^-. The inelasticity in the iron:carbon uptake ratio of *Chaetoceros* suggests that this taxa has adapted to the perennially low iron conditions of the open Southern Ocean, an adaptation that allows *Chaetoceros* to outcompete the other phytoplankton groups.

As the spring phytoplankton bloom progressed, grazing pressure increased and iron became depleted, leading to the senescence of the *Chaetoceros* bloom. We hypothesise that this senescence resulted in the rapid removal of *Chaetoceros* biomass from the mixed layer (i.e., as a large carbon export event).

We calculate that the spring bloom accounted for approximately one third of the annual rate of carbon export across the Atlantic Southern Ocean due largely to the boom-and-bust strategy employed by *Chaetoceros*. The spring bloom depleted mixed-layer iron, and to some extent $Si(OH)_4$ in the SAZ, thereby influencing the biogeochemical conditions (and thus phytoplankton community composition and associated carbon export potential) for the remainder the growth season. To conclude this chapter, the springtime data are placed into the context of the entire growth season and the potential effect(s) of the spring *Chaetoceros* bloom on the succeeding phytoplankton community are discussed.

Chapter 3: Summertime productivity and carbon export potential in the Weddell Sea, with a focus on the waters adjacent to Larsen C Ice Shelf

The Weddell Sea is a globally important region as its ice shelves, particularly Larsen C Ice Shelf (LCIS) and Filchner-Rönne Ice Shelf (FRIS), are areas of deep water mass formation (Gordon et al., 1993; Schröder et al., 2002; Schodlok et al., 2002), which sets the physicochemical conditions of much of the global ocean (Muench and Gordon, 1995; Talley et al., 2011). The surface waters adjacent to Antarctic ice shelves are unique in that they are perennially characterised by iron replete conditions (unlike the open Southern Ocean) due to sea-ice and glacial-melt and the resuspension of continental sediments (Klunder et al., 2014; Dinniman et al., 2020). The high iron availability in the vicinity of LCIS therefore drives large phytoplankton blooms (Lannuzel et al., 2008), driving changes in the chemical conditions of the deep water masses formed in this globally important region. To investigate the role of the Weddell Sea phytoplankton community in N and carbon cycling, we measured NPP, N (as NO_3^-, NH_4^+ and urea) uptake and nitrification and characterised the phytoplankton community via flow cytometry and microscopy in the western Weddell Sea along the Antarctic Peninsula and at LCIS, in the south-western Weddell Gyre, and at Fimbul Ice Shelf in the south-eastern Weddell Sea.

The phytoplankton community was dominated by colonial *P. antarctica* at LCIS and diatoms at all other stations. This finding is consistent with previous observations of *P. antarctica* dominating in deep mixed layers as they are well-adapted to low-light conditions, while diatoms proliferate in shallow mixed layers under high-light conditions (Goffart et al., 2000; Strzepek et al., 2011). Although the water column was well-stratified at LCIS at the time of sampling, it was likely characterised by deep mixed layers early in the growth season due to the mechanisms that initiate the formation of its coastal polynya, thus selecting for the dominance of *P. antarctica* over other phytoplankton groups. In contrast, the mixed layer at the other stations was shallow due to recent sea-ice melt, which caused rapid stratification of the upper water column, allowing diatoms to dominate.

At LCIS, the highest rates of NPP were measured coincident with the highest drawdown of nutrients. However, the lowest f-ratios were estimated at LCIS compared to the other stations, which we attribute to partial NH_4^+ inhibition of NO_3^- uptake driven by the elevated availability of NH_4^+ (average NH_4^+

concentration of 0.6 ± 0.4 μM). We hypothesise that the presence of diatoms at LCIS may have mitigated the effect of the high NH_4^+ concentrations on NO_3^- uptake, and therefore carbon export potential, because this phytoplankton group is known to preferentially consume NO_3^- even when NH_4^+ concentrations are inhibitory (Probyn and Painting, 1985; Koike et al., 1986; Lomas and Glibert, 1999; Karsh et al., 2003). However, as the season progressed and heterotrophy likely increased, further increasing the availability of NH_4^+, it is possibly that NO_3^- uptake was more strongly inhibited. Chapter 3 therefore shows how phytoplankton community composition across the Weddell Sea is controlled by a combination of physical, chemical, and biological factors, and yields insight into the implications of community composition for the biological carbon pump.

Chapter 4: Phytoplankton group-specific contributions to carbon export potential across the summertime Weddell Sea

Tracer-based rates of NPP and N uptake provide a snapshot of the role of phytoplankton in ocean productivity rather than an integrated (i.e., seasonal) view of phytoplankton ecology and carbon export potential. In addition, bulk (i.e., whole community) uptake rates (as presented in Chapter 3) provide information regarding the entire community only. To investigate the dominant N source(s) fuelling the growth of various important phytoplankton groups and quantify their contribution (in a mass balance sense) to carbon export potential in the Weddell Sea, the coupled flow cytometry-N isotope method was employed. The NO_3^- dependence of four flow-sorted phytoplankton groups (*Synechococcus,* picoeukaryotes, nanoeukaryotes and cryptophytes) was estimated along the Antarctic Peninsula, at LCIS and in the open Weddell Gyre during the summer, along with the relative contribution of each group to carbon export.

Synechococcus numerically dominated the phytoplankton community, while nanoplankton (predominately cryptophytes) made the largest contribution to biomass. The dominance of cryptophytes appears to have been due to this phytoplankton group having photoprotective carotenoids, which allowed the cryptophytes to persist in the extremely shallow mixed layers present across the Weddell Sea at the time of sampling (average mixed layer depth of 16 ± 7 m).

The $\delta^{15}N$ of all flow-sorted phytoplankton groups was highest at LCIS, indicating that the phytoplankton community here was the most productive, consistent with the bulk rates of NPP presented in Chapter 3. At the same time, the lowest proportional NO_3^- dependence was estimated for all phytoplankton groups, excluding *Synechococcus*, at LCIS, with the extent of their reliance on NO_3^- decreasing with increasing NH_4^+ availability. This trend is consistent with the findings described in Chapter 3 in which I concluded that NO_3^- uptake at LCIS was partially inhibited by NH_4^+. Although only ~50% of phytoplankton productivity was fuelled by NO_3^- at LCIS, because the phytoplankton community was highly productive here the net carbon flux was likely high. However, although the NH_4^+

concentrations at LCIS were elevated, the phytoplankton continued to consume NO_3^- and potentially contribute to carbon export. It is likely that carbon export is inhibited in other regions of the Weddell Sea and CCSZ of the Southern Ocean where elevated NH_4^+ concentrations persist.

Chapter 5: Conclusions and implications

Each data chapter (Chapters 2 through 4) of this thesis includes a detailed conclusions and implications section pertaining to the research presented therein. This concluding chapter will therefore not repeat these conclusions and implications in detail, but rather offer a summary of the main findings of each chapter and then place the findings of this thesis into a broader context by considering the implications of a changing climate for the nutrient cycling and carbon export in the Southern Ocean based on the results presented here.

1.6. References

Altabet, M. A. and Francois, R.: Nitrogen isotope biogeochemistry of the Antarctic polar frontal zone at 170°W, Deep. Res. Part II Top. Stud. Oceanogr., 48, 4247–4273, https://doi.org/10.1016/S0967-0645(01)00088-1, 2001.

Arrigo, K. R., Robinson, D. H., Worthen, D. L., Dunbar, R. B., DiTullio, G. R., VanWoert, M., and Lizotte, M. P.: Phytoplankton community structure and the drawdown of nutrients and CO2 in the Southern Ocean, Science (80-.)., 283, 365–367, https://doi.org/10.1126/science.283.5400.365, 1999.

Arteaga, L. A., Pahlow, M., Bushinsky, S. M., and Sarmiento, J. L.: Nutrient Controls on Export Production in the Southern Ocean, Global Biogeochem. Cycles, 33, 942–956, https://doi.org/10.1029/2019GB006236, 2019.

Arteaga, L. A., Boss, E., Behrenfeld, M. J., Westberry, T. K., and Sarmiento, J. L.: Seasonal modulation of phytoplankton biomass in the Southern Ocean, Nat. Commun. 2020 111, 11, 1–10, https://doi.org/10.1038/s41467-020-19157-2, 2020.

Assmy, P., Smetacek, V., Montresor, M., Klaas, C., Henjes, J., Strass, V. H., Arrieta, J. M., Bathmann, U., Berg, G. M., Breitbarth, E., Cisewski, B., Friedrichs, L., Fuchs, N., Herndl, G. J., Jansen, S., Krägefsky, S., Latasa, M., Peeken, I., Röttgers, R., Scharek, R., Schüller, S. E., Steigenberger, S., Webb, A., Wolf-Gladrow, D., Klaas, C., and Smetacek, V.: Mechanisms determining species dominance in a phytoplankton bloom induced by the iron fertilization experiment EisenEx in the Southern Ocean, Deep. Res. Part I Oceanogr. Res. Pap., 110, 20633–20638, https://doi.org/10.1073/pnas.1309345110, 2013

De Baar, H. J. W., Bathmannt, U., Smetacek, V., Löscher, B. M., and Veth, C.: Importance of iron for plankton blooms and carbon dioxide drawdown in the Southern Ocean, https://doi.org/10.1038/373412a0, 2 February 1995.

Berge, T., Chakraborty, S., Hansen, P. J., and Andersen, K. H.: Modeling succession of key resource-harvesting traits of mixotrophic plankton, ISME J. 2017 111, 11, 212–223,

https://doi.org/10.1038/ismej.2016.92, 2016.
Boyd, P. W.: Diatom traits regulate Southern Ocean silica leakage, Proc. Natl. Acad. Sci., 110, 20358–20359, https://doi.org/10.1073/pnas.1320327110, 2013.
Boyd, P. W. and Ellwood, M. J.: The biogeochemical cycle of iron in the ocean, Nat. Geosci., 3, 675–682, https://doi.org/10.1038/ngeo964, 2010.
Boyd, P. W. and Law, C. S.: The Southern Ocean Iron RElease Experiment (SOIREE)—introduction and summary, Deep Sea Res. Part II Top. Stud. Oceanogr., 48, 2425–2438, https://doi.org/10.1016/S0967-0645(01)00002-9, 2001.
Boyd, P. W., McTainsh, G., Sherlock, V., Richardson, K., Nichol, S., Ellwood, M., and Frew, R.: Episodic enhancement of phytoplankton stocks in New Zealand subantarctic waters: Contribution of atmospheric and oceanic iron supply, Global Biogeochem. Cycles, 18, https://doi.org/10.1029/2002GB002020, 2004.
Brand, L. E.: Minimum iron requirements of marine phytoplankton and the implications for the biogeochemical control of new production, Limnol. Oceanogr., 36, 1756–1771, https://doi.org/10.4319/LO.1991.36.8.1756, 1991.
Bronk, D. A. and Glibert, P. M.: Application of a 15N tracer method to the study of dissolved organic nitrogen uptake during spring and summer in Chesapeake Bay, Mar. Biol., 115, 501–508, https://doi.org/10.1007/BF00349849/METRICS, 1993.
Brzezinski, M. A.: The Si:C:N ratio of marine diatoms: interspecific variability and the effect of some environmental variables, https://doi.org/10.1111/j.0022-3646.1985.00347.x, 1985.
Brzezinski, M. A., Dickson, M. L., Nelson, D. M., and Sambrotto, R.: Ratios of Si, C and N uptake by microplankton in the Southern Ocean, Deep. Res. Part II Top. Stud. Oceanogr., 50, 619–633, https://doi.org/10.1016/S0967-0645(02)00587-8, 2003.
Buitenhuis, E. T., Li, W. K. W., Vaulot, D., Lomas, M. W., Landry, M. R., Partensky, F., Karl, D. M., Ulloa, O., Campbell, L., Jacquet, S., Lantoine, F., Chavez, F., MacIas, D., Gosselin, M., and McManus, G. B.: Picophytoplankton biomass distribution in the global ocean, Earth Syst. Sci. Data, 4, 37–46, https://doi.org/10.5194/ESSD-4-37-2012, 2012.
Casciotti, K. L., Sigman, D. M., and Ward, B. B.: Linking Diversity and Stable Isotope Fractionation in Ammonia-Oxidizing Bacteria, 20, 335–353, https://doi.org/10.1080/01490450303895, 2003.
Cassar, N., Bender, M. L., Barnett, B. A., Fan, S., Moxim, W. J., Levy, H., and Tilbrook, B.: The southern ocean biological response to aeolian iron deposition, Science (80-.)., 317, 1067–1070, https://doi.org/10.1126/SCIENCE.1144602/SUPPL_FILE/CASSAR.SOM.PDF, 2007.
Cavagna, A. J., Fripiat, F., Elskens, M., Mangion, P., Chirurgien, L., Closset, I., and Lasbleiz, M.: Production regime and associated N cycling in the vicinity of Kerguelen Island , Southern Ocean, 6515–6528, https://doi.org/10.5194/bg-12-6515-2015, 2015.
Chapman, C. C., Lea, M. A., Meyer, A., Sallée, J. B., and Hindell, M.: Defining Southern Ocean fronts and their influence on biological and physical processes in a changing climate, Nat. Clim. Chang., 10,

209–219, https://doi.org/10.1038/s41558-020-0705-4, 2020.

Checkley, D. M. and Miller, C. A.: Nitrogen isotope fractionation by oceanic zooplankton, Deep Sea Res. Part A. Oceanogr. Res. Pap., 36, 1449–1456, https://doi.org/10.1016/0198-0149(89)90050-2, 1989.

Chisholm, S. W., Olson, R. J., Zettler, E. R., Goericke, R., Waterbury, J. B., and Welschmeyer, N. A.: A novel free-living prochlorophyte abundant in the oceanic euphotic zone, Nat. 1988 3346180, 334, 340–343, https://doi.org/10.1038/334340a0, 1988.

Clay, B. L. and Kugrens, P.: Characterization of Hemiselmis amylosa sp. nov. and Phylogenetic Placement of the Blue-Green Cryptomonads H. amylosa and Falcomonas daucoides, Protist, 150, 297–310, https://doi.org/10.1016/S1434-4610(99)70031-3, 1999.

Cochlan, W. P.: Nitrogen Uptake in the Southern Ocean, Nitrogen Mar. Environ., 569–596, https://doi.org/10.1016/B978-0-12-372522-6.00012-8, 2008.

Collier, J. L., Brahamsha, B., and Palenik, B.: The marine cyanobacterium Synechococcus sp. WH7805 requires urease (urea amidohydrolase, EC 3.5.1.5) to utilize urea as a nitrogen source: Molecular-genetic and biochemical analysis of the enzyme, 145, 447–459, https://doi.org/10.1099/13500872-145-2-447/CITE/REFWORKS, 1999.

Cox, P. M., Betts, R. A., Jones, C. D., Spall, S. A., and Totterdell, I. J.: Acceleration of global warming due to carbon-cycle feedbacks in a coupled climate model, Nat. 2000 4086809, 408, 184–187, https://doi.org/10.1038/35041539, 2000.

Croot, P. L., Frew, R. D., Sander, S., Hunter, K. A., Ellwood, M. J., Pickmere, S. E., Abraham, E. R., Law, C. S., Smith, M. J., and Boyd, P. W.: Physical mixing effects on iron biogeochemical cycling: FeCycle experiment, J. Geophys. Res. Ocean., 112, https://doi.org/10.1029/2006JC003748, 2007.

De_Jong, J., Schoemann, V., Lannuzel, D., Croot, P., De Baar, H., and Tison, J. L.: Natural iron fertilization of the Atlantic sector of the Southern Ocean by continental shelf sources of the Antarctic Peninsula, J. Geophys. Res. Biogeosciences, 117, https://doi.org/10.1029/2011JG001679, 2012.

Dehairs, F., Fripiat, F., Cavagna, A. J., Trull, T. W., Fernandez, C., Davies, D., Roukaerts, A., Fonseca Batista, D., Planchon, F., and Elskens, M.: Nitrogen cycling in the Southern Ocean Kerguelen Plateau area: Evidence for significant surface nitrification from nitrate isotopic compositions, 12, 1459–1482, https://doi.org/10.5194/bg-12-1459-2015, 2015.

Deniro, M. J. and Epstein, S.: Influence of diet on the distribution of nitrogen isotopes in animals, Geochim. Cosmochim. Acta, 45, 341–351, https://doi.org/10.1016/0016-7037(81)90244-1, 1981.

Dennett, M. R., Mathot, S., Caron, D. A., Smith, W. O., and Lonsdale, D. J.: Abundance and distribution of phototrophic and heterotrophic nano- and microplankton in the southern Ross Sea, Deep Sea Res. Part II Top. Stud. Oceanogr., 48, 4019–4037, https://doi.org/10.1016/S0967-0645(01)00079-0, 2001.

Deppeler, S. L. and Davidson, A. T.: Southern Ocean phytoplankton in a changing climate, Front. Mar. Sci., 4, https://doi.org/10.3389/fmars.2017.00040, 2017.

DeVries, T.: The Oceanic Anthropogenic CO2 Sink: Storage, Air-Sea Fluxes, and Transports over the

Industrial Era, Global Biogeochem. Cycles, 28, 631–647, 2014.
Diaz, F. and Raimbault, P.: Nitrogen regeneration and dissolved organic nitrogen release during spring in a NW Mediterranean coastal zone (Gulf of Lions): implications for the estimation of new production, Mar. Ecol. Prog. Ser., 197, 51–65, https://doi.org/10.3354/MEPS197051, 2000.
Difiore, P. J., Sigman, D. M., Dunbar, R. B., Difiore, P. J., Sigman, D. M., and Dunbar, R. B.: Upper ocean nitrogen fluxes in the Polar Antarctic Zone: Constraints from the nitrogen and oxygen isotopes of nitrate, Geochemistry, Geophys. Geosystems, 10, https://doi.org/10.1029/2009GC002468, 2009.
Difiore, P. J., Sigman, D. M., Karsh, K. L., Trull, T. W., Dunbar, R. B., and Robinson, R. S.: Poleward decrease in the isotope effect of nitrate assimilation across the Southern Ocean, Geophys. Res. Lett., 37, 1–5, https://doi.org/10.1029/2010GL044090, 2010.
DiFiore, P. J., Sigman, D. M., Trull, T. W., Lourey, M. J., Karsh, K., Cane, G., and Ho, R.: Nitrogen isotope constraints on subantarctic biogeochemistry, J. Geophys. Res. Ocean., 111, 8016, https://doi.org/10.1029/2005JC003216, 2006.
Dinniman, M. S., St-Laurent, P., Arrigo, K. R., Hofmann, E. E., and Dijken, G. L. van: Analysis of Iron Sources in Antarctic Continental Shelf Waters, J. Geophys. Res. Ocean., 125, e2019JC015736, https://doi.org/10.1029/2019JC015736, 2020.
Doblin, M. A., Petrou, K. L., Shelly, K., Westwood, K., van den Enden, R., Wright, S., Griffiths, B., and Ralph, P. J.: Diel variation of chlorophyll-a fluorescence, phytoplankton pigments and productivity in the Sub-Antarctic and Polar Front Zones south of Tasmania, Australia, Deep Sea Res. Part II Top. Stud. Oceanogr., 58, 2189–2199, https://doi.org/10.1016/J.DSR2.2011.05.021, 2011.
Dong, S., Sprintall, J., Gille, S. T., and Talley, L.: Southern Ocean mixed-layer depth from Argo float profiles, J. Geophys. Res. Ocean., 113, 6013, https://doi.org/10.1029/2006JC004051, 2008.
Doolittle, D. F., Li, W. K. W., and Wood, A. M.: Wintertime abundance of picoplankton in the Atlantic sector of the Southern Ocean With 6 fi gures and 1 table, 133, 147–160, 2008.
Dore, J. E. and Karl, D. M.: Nitrification in the euphotic zone as a source for nitrite, nitrate, and nitrous oxide at Station ALOHA, Limnol. Oceanogr., 41, 1619–1628, https://doi.org/10.4319/LO.1996.41.8.1619, 1996.
Dortch, Q.: The interaction between ammonium and nitrate uptake in phytoplankton, Mar. Ecol. Prog. Ser., 61, 183–201, https://doi.org/10.3354/meps061183, 1990.
Dugdale, R. C. and Goering, J. J.: Uptake of New and Regenerated Forms of Nitrogen in Primary Productivity, Limnol. Oceanogr., 12, 196–206, https://doi.org/10.4319/lo.1967.12.2.0196, 1967a.
Dugdale, R. C. and Goering, J. J.: UPTAKE OF NEW AND REGENERATED FORMS OF NITROGEN IN PRIMARY PRODUCTIVITY ’, 196–206, 1967b.
Dugdale, R. C. and Wilkerson, F. P.: The use of 15N to measure nitrogen uptake in eutrophic experimental considerations1 t2, 3, 1986.
Durand, M. D., Olson, R. J., and Chisholm, S. W.: Phytoplankton population dynamics at the Bermuda Atlantic Time-series station in the Sargasso Sea, Deep Sea Res. Part II Top. Stud. Oceanogr., 48, 1983–

2003, https://doi.org/10.1016/S0967-0645(00)00166-1, 2001.

Edwards, K. F., Thomas, M. K., Klausmeier, C. A., and Litchman, E.: Allometric scaling and taxonomic variation in nutrient utilization traits and maximum growth rate of phytoplankton, Limnol. Oceanogr., 57, 554–566, https://doi.org/10.4319/LO.2012.57.2.0554, 2012.

El-Sayed, S. Z. and Taguchi, S.: Primary production and standing crop of phytoplankton along the ice-edge in the Weddell Sea, Deep Sea Res. Part A, Oceanogr. Res. Pap., 28, 1017–1032, https://doi.org/10.1016/0198-0149(81)90015-7, 1981.

Eppley, R. W., Peterson, B.: Particulate organic matter flux and planktonic new production in the deep ocean, Nature, 282, 677–680, 1979.

Falkowski, P. G., Barber, R. T., and Smetacek, V.: Biogeochemical controls and feedbacks on ocean primary production, Science (80-.)., 281, 200–206, https://doi.org/10.1126/SCIENCE.281.5374.200/ASSET/8DA24923-585D-4624-B7D5-1D2D74007006/ASSETS/GRAPHIC/SE298667504A.JPEG, 1998.

Fawcett, S. E., Lomas, M. W., Casey, J. R., Ward, B. B., and Sigman, D. M.: Assimilation of upwelled nitrate by small eukaryotes in the Sargasso Sea, Nat. Geosci., 4, 717–722, https://doi.org/10.1038/ngeo1265, 2011

Fawcett, S. E., Lomas, M. W., Ward, B. B., and Sigman, D. M.: Global Biogeochemical Cycles production in the Sargasso Sea, Global Biogeochem. Cycles, 28, 86–102, https://doi.org/10.1002/2013GB004579.Received, 2014.

Fawcett, S. E., Ward, B. B., Lomas, M. W., and Sigman, D. M.: Vertical decoupling of nitrate assimilation and nitrification in the Sargasso Sea, Deep. Res. Part I Oceanogr. Res. Pap., 103, 64–72, https://doi.org/10.1016/j.dsr.2015.05.004, 2015.

Flombaum, P., Gallegos, J. L., Gordillo, R. A., Rincón, J., Zabala, L. L., Jiao, N., Karl, D. M., Li, W. K. W., Lomas, M. W., Veneziano, D., Vera, C. S., Vrugt, J. A., and Martiny, A. C.: Present and future global distributions of the marine Cyanobacteria Prochlorococcus and Synechococcus, Proc. Natl. Acad. Sci. U. S. A., 110, 9824–9829, https://doi.org/10.1073/pnas.1307701110, 2013.

Flynn, R. F., Bornman, T. G., Burger, J. M., Smith, S., Spence, K. A. M., and Fawcett, S. E.: Summertime productivity and carbon export potential in the Weddell Sea, with a focus on the waters adjacent to Larsen C Ice Shelf, 18, 6031–6059, https://doi.org/10.5194/BG-18-6031-2021, 2021.

Forrer, H.: Toward an improved understanding of the Southern Ocean's biological pump: phytoplankton group-specific contributions to nitrogen and carbon cycling across the Subantarctic Indian Ocean, http://hdl.handle.net/11427/33675, 2021.

Franck, V. M., Brzezinski, M. A., Coale, K. H., and Nelson, D. M.: Iron and silicic acid concentrations regulate Si uptake north and south of the Polar Frontal Zone in the Pacific Sector of the Southern Ocean, Deep. Res. Part II Top. Stud. Oceanogr., 47, 3315–3338, https://doi.org/10.1016/S0967-0645(00)00070-9, 2000.

Francois, R., Bacon, M. P., Altabet, M. A., and Labeyrie, L. D.: Glacial/interglacial changes in sediment

rain rate in the SW Indian Sector of subantarctic Waters as recorded by 230Th, 231Pa, U, and δ15N, Paleoceanography, 8, 611–629, https://doi.org/10.1029/93PA00784, 1993.

Fripiat, F., Martínez-García, A., Fawcett, S. E., Kemeny, P. C., Studer, A. S., Smart, S. M., Rubach, F., Oleynik, S., Sigman, D. M., and Haug, G. H.: The isotope effect of nitrate assimilation in the Antarctic Zone: Improved estimates and paleoceanographic implications, Geochim. Cosmochim. Acta, 247, 261–279, https://doi.org/10.1016/J.GCA.2018.12.003, 2019.

Fripiat, F., Martínez-García, A., Marconi, D., Fawcett, S., Kopf, S., Luu, V., Rafter, P., Zhang, R., Sigman, D., and Haug, G.: Nitrogen isotopic contraints on nutrient transport to the upper ocean, Nat. Geosci., 2021.

Frölicher, T. L., Sarmiento, J. L., Paynter, D. J., Dunne, J. P., Krasting, J. P., and Winton, M.: Dominance of the Southern Ocean in anthropogenic carbon and heat uptake in CMIP5 models, J. Clim., 28, 862–886, 2015.

Garibotti, I. A., Vernet, M., Smith, R. C., and Ferrario, M. E.: Interannual variability in the distribution of the phytoplankton standing stock across the seasonal sea-ice zone west of the Antarctic Peninsula, J. Plankton Res., 27, 825–843, https://doi.org/10.1093/PLANKT/FBI056, 2005.

Garside, C.: A chemiluminescent technique for the determination of nanomolar concentrations of nitrate and nitrite in seawater, Mar. Chem., 11, 159–167, https://doi.org/10.1016/0304-4203(82)90039-1, 1982.

Gilbert, N. E., LeCleir, G. R., Strzepek, R. F., Ellwood, M. J., Twining, B. S., Roux, S., Pennacchio, C., Boyd, P. W., and Wilhelm, S. W.: Bioavailable iron titrations reveal oceanic Synechococcus ecotypes optimized for different iron availabilities, ISME Commun. 2022 21, 2, 1–12, https://doi.org/10.1038/s43705-022-00132-5, 2022.

Gilbert, P. M., Lipschultz, F., McCarthy, J. J., and Altabet, M. A.: Isotope dilution models of uptake and remineralization of ammonium by marine plankton1, Limnol. Oceanogr., 27, 639–650, https://doi.org/10.4319/LO.1982.27.4.0639, 1982.

Glibert, P. M. and Ray, R. T.: Different patterns of growth and nitrogen uptake in two clones of marine Synechococcus spp., Mar. Biol., 107, 273–280, https://doi.org/10.1007/BF01319826/METRICS, 1990.

Glibert, P. M., Kana, T. M., Olson, R. J., Kirchman, D. L., and Alberte, R. S.: Clonal comparisons of growth and photosynthetic responses to nitrogen availability in marine Synechococcus spp, J. Exp. Mar. Bio. Ecol., 101, 199–208, https://doi.org/10.1016/0022-0981(86)90050-X, 1986.

Glibert, P. M., Wilkerson, F. P., Dugdale, R. C., Raven, J. A., Dupont, C. L., Leavitt, P. R., Parker, A. E., Burkholder, J. M., and Kana, T. M.: Pluses and minuses of ammonium and nitrate uptake and assimilation by phytoplankton and implications for productivity and community composition, with emphasis on nitrogen-enriched conditions, Limnol. Oceanogr., 61, 165–197, https://doi.org/10.1002/lno.10203, 2016a.

Glibert, P. M., Wilkerson, F. P., Dugdale, R. C., Raven, J. A., Dupont, C. L., Leavitt, P. R., Parker, A. E., Burkholder, J. M., and Kana, T. M.: Pluses and minuses of ammonium and nitrate uptake and

assimilation by phytoplankton and implications for productivity and community composition, with emphasis on nitrogen-enriched conditions, Limnol. Oceanogr., 61, 165–197, https://doi.org/10.1002/lno.10203, 2016b.

Glover, H. E., Keller, M. D., and Spinrad, R. W.: The effects of light quality and intensity on photosynthesis and growth of marine eukaryotic and prokaryotic phytoplankton clones, J. Exp. Mar. Bio. Ecol., 105, 137–159, https://doi.org/10.1016/0022-0981(87)90168-7, 1987.

Goeyens, L., Tréguer, P., Baumann, M. E. M., Baeyens, W., and Dehairs, F.: The leading role of ammonium in the nitrogen uptake regime of Southern Ocean marginal ice zones, J. Mar. Syst., 6, 345–361, https://doi.org/10.1016/0924-7963(94)00033-8, 1995.

Goffart, A., Catalano, G., and Hecq, J. H.: Factors controlling the distribution of diatoms and Phaeocystis in the Ross Sea, J. Mar. Syst., 27, 161–175, https://doi.org/10.1016/S0924-7963(00)00065-8, 2000.

Gordon, A. L., Huber, B. A., Hellmer, H. H., & Ffield, A.: Deep and bottom water of the Weddell Sea's western rim., Science (80-.)., 265, 95–97, 1993.

Gordon, A. L., Georgi, D. T., and Taylor, H. W.: Antarctic Polar Front Zone in the Western Scotia Sea—Summer 1975, J. Phys. Oceanogr., 7, 309–328, https://doi.org/10.1175/1520-0485(1977)007<0309:APFZIT>2.0.CO;2, 1977.

Granger, J., Sigman, D. M., Needoba, J. A., and Harrison, P. J.: Coupled nitrogen and oxygen isotope fractionation of nitrate during assimilation by cultures of marine phytoplankton, Limnol. Oceanogr., 49, 1763–1773, https://doi.org/10.4319/LO.2004.49.5.1763, 2004.

Granger, J., Sigman, D. M., Rohde, M. M., Maldonado, M. T., and Tortell, P. D.: N and O isotope effects during nitrate assimilation by unicellular prokaryotic and eukaryotic plankton cultures, Geochim. Cosmochim. Acta, 74, 1030–1040, https://doi.org/10.1016/J.GCA.2009.10.044, 2010.

Green, S. E. and Sambrotto, R. N.: Plankton community structure and export of C, N, P and Si in the Antarctic Circumpolar Current, Deep. Res. Part II Top. Stud. Oceanogr., 53, 620–643, https://doi.org/10.1016/j.dsr2.2006.01.022, 2006.

Gruber, N., Landschützer, P., and Lovenduski, N. S.: The variable southern ocean carbon sink, https://doi.org/10.1146/annurev-marine-121916-063407, 3 January 2019.

Harrison, W. G. and Harris, L. R.: Isotope-dilution and its effects on measurements of nitrogen and phosphorus uptake by oceanic microplankton, 21, 253–261, 1986.

Henley, S. F., Tuerena, R. E., Annett, A. L., Fallick, A. E., Meredith, M. P., Venables, H. J., Clarke, A., and Ganeshram, R. S.: Macronutrient supply, uptake and recycling in the coastal ocean of the west Antarctic Peninsula, Deep. Res. Part II Top. Stud. Oceanogr., 139, 58–76, https://doi.org/10.1016/j.dsr2.2016.10.003, 2017.

Henley, S. F., Cavan, E. L., Fawcett, S. E., Kerr, R., Monteiro, T., Sherrell, R. M., Bowie, A. R., Boyd, P. W., Barnes, D. K. A., Schloss, I. R., Marshall, T., Flynn, R., and Smith, S.: Changing Biogeochemistry of the Southern Ocean and Its Ecosystem Implications, 1–31 pp.,

https://doi.org/10.3389/fmars.2020.00581, 2020.
Henson, S. A., Sanders, R., Madsen, E., Morris, P. J., Le Moigne, F., and Quartly, G. D.: A reduced estimate of the strength of the ocean's biological carbon pump, Geophys. Res. Lett., 38, https://doi.org/10.1029/2011GL046735, 2011.
Hoch, M. P., Fogel, M. L., and Kirchman, D. L.: Isotope fractionation during ammonium uptake by marine microbial assemblages, 12, 113–127, https://doi.org/10.1080/01490459409377977, 1993.
Hoffmann, L. J., Peeken, I., Lochte, K., Assmy, P., and Veldhuis, M.: Different reactions of Southern Ocean phytoplankton size classes to iron fertilization, Limnol. Oceanogr., 51, 1217–1229, https://doi.org/10.4319/lo.2006.51.3.1217, 2006.
Hoffmann, L. J., Peeken, I., and Lochte, K.: Iron, silicate, and light co-limitation of three Southern Ocean diatom species, Polar Biol., 31, 1067–1080, https://doi.org/10.1007/s00300-008-0448-6, 2008.
Holmes, R. M., Aminot, A., Kerouel, R., Hooker, B. A., and Peterson, B. J.: A simple and precise method for measuring ammonium in marine and freshwater ecosystems, https://doi.org/10.1139/cjfas-56-10-1801, 1999.
Huang, K., Ducklow, H., Vernet, M., Cassar, N., and Bender, M. L.: Export production and its regulating factors in the West Antarctica Peninsula region of the Southern Ocean, Global Biogeochem. Cycles, 26, 2005, https://doi.org/10.1029/2010GB004028, 2012.
Hutchins, D. A. and Bruland, K. W.: Iron-limited diatom growth and Si:N uptake ratios in a coastal upwelling regime, Nature, 393, 561–564, https://doi.org/10.1038/31203, 1998.
Jacques, G.: Is the concept of new production—regenerated production valid for the Southern Ocean?, Mar. Chem., 35, 273–286, https://doi.org/10.1016/S0304-4203(09)90022-6, 1991.
Jensen, K. M., Jensen, M. H., and Cox, R. P.: Membrane inlet mass spectrometric analysis of N-isotope labelling for aquatic denitrification studies, FEMS Microbiol. Ecol., 20, 101–109, https://doi.org/10.1111/J.1574-6941.1996.TB00309.X, 1996.
Johnson, Z. I., Zinser, E. R., Coe, A., McNulty, N. P., Woodward, E. M. S., and Chisholm, S. W.: Niche partitioning among Prochlorococcus ecotypes along ocean-scale environmental gradients, Science (80-.).,311,1737–1740, https://doi.org/10.1126/SCIENCE.1118052/SUPPL_FILE/JOHNSON.SOM.REV1.PDF, 2006.
Karsh, K. L., Trull, T. W., Lourey, M. J., and Sigman, D. M.: Relationship of nitrogen isotope fractionation to phytoplankton size and iron availability during the Southern Ocean Iron RElease Experiment (SOIREE), Limnol. Oceanogr., 48, 1058–1068, https://doi.org/10.4319/lo.2003.48.3.1058, 2003.
Karsh, K. L., Trull, T. W., Sigman, D. M., Thompson, P. A., and Granger, J.: The contributions of nitrate uptake and efflux to isotope fractionation during algal nitrate assimilation, Geochim. Cosmochim. Acta, 132, 391–412, https://doi.org/10.1016/j.gca.2013.09.030, 2014.
Kerr, R., Mata, M. M., Mendes, C. R. B., and Secchi, E. R.: Northern Antarctic Peninsula: a marine climate hotspot of rapid changes on ecosystems and ocean dynamics, Deep. Res. Part II Top. Stud.

Oceanogr., 149, 4–9, https://doi.org/10.1016/j.dsr2.2018.05.006, 2018.

Klunder, M. B., Laan, P., Middag, R., De Baar, H. J. W., and van Ooijen, J. C.: Dissolved iron in the Southern Ocean (Atlantic sector), Deep. Res. Part II Top. Stud. Oceanogr., 58, 2678–2694, https://doi.org/10.1016/j.dsr2.2010.10.042, 2011.

Klunder, M. B., Laan, P., De Baar, H. J. W., Middag, R., Neven, I., and Van Ooijen, J.: Dissolved Fe across the Weddell Sea and Drake Passage: impact of DFe on nutrient uptake, 11, 651–669, https://doi.org/10.5194/bg-11-651-2014, 2014a.

Klunder, M. B., Laan, P., De Baar, H. J. W., Middag, R., Neven, I., and Van Ooijen, J.: Dissolved Fe across the Weddell Sea and Drake Passage: Impact of DFe on nutrient uptake, 11, 651–669, https://doi.org/10.5194/bg-11-651-2014, 2014b.

Knapp, A. N., Sigman, D. M., and Lipschultz, F.: N isotopic composition of dissolved organic nitrogen and nitrate at the Bermuda Atlantic Time-series Study site, Global Biogeochem. Cycles, 19, 1–15, https://doi.org/10.1029/2004GB002320, 2005.

Koch, F. and Trimborn, S.: Limitation by fe, zn, co, and b12 results in similar physiological responses in two antarctic phytoplankton species, Front. Mar. Sci., 6, 514, https://doi.org/10.3389/FMARS.2019.00514/BIBTEX, 2019.

Koike, I., Holm-Hansen, O., and Biggs, D.: Inorganic nitrogen metabolism by Antarctic phytoplankton with special reference to ammonium cycling, Mar. Ecol. Prog. Ser., 30, 105–116, https://doi.org/10.3354/meps030105, 1986.

Lannuzel, D., Schoemann, V., de Jong, J., Chou, L., Delille, B., Becquevort, S., and Tison, J. L.: Iron study during a time series in the western Weddell pack ice, Mar. Chem., 108, 85–95, https://doi.org/10.1016/j.marchem.2007.10.006, 2008.

Laws, E. A., Falkowski, P. G., Smith, W. O., Ducklow, H., and McCarthy, J. J.: Temperature effects on export production in the open ocean, Global Biogeochem. Cycles, 14, 1231–1246, https://doi.org/10.1029/1999GB001229, 2000.

Lindell, D. and Post, A. F.: Ecological Aspects of ntcA Gene Expression and Its Use as an Indicator of the Nitrogen Status of Marine Synechococcus spp., Appl. Environ. Microbiol., 67, 3340–3349, https://doi.org/10.1128/AEM.67.8.3340-3349.2001/ASSET/DAB3DEE9-DB5F-4E2D-8676-112B2C13E39E/ASSETS/GRAPHIC/AM0810457008.JPEG, 2001.

Lindell, D., Padan, E., and Post, A. F.: Regulation of ntcA expression and nitrite uptake in the marine Synechococcus sp. strain WH 7803, J. Bacteriol., 180, 1878–1886, https://doi.org/10.1128/JB.180.7.1878-1886.1998/ASSET/17649FC6-11C6-4B93-947D-1C90A344D2A4/ASSETS/GRAPHIC/JB0781268009.JPEG, 1998.

Lipschultz, F.: Isotope Tracer Methods for Studies of the Marine Nitrogen Cycle, 1345–1384 pp., https://doi.org/10.1016/B978-0-12-372522-6.00031-1, 2008.

Liu, K. K., Kao, S. J., Chiang, K. P., Gong, G. C., Chang, J., Cheng, J. S., and Lan, C. Y.: Concentration dependent nitrogen isotope fractionation during ammonium uptake by phytoplankton under an algal

bloom condition in the Danshuei estuary, northern Taiwan, Mar. Chem., 157, 242–252, https://doi.org/10.1016/J.MARCHEM.2013.10.005, 2013.

Lomas, M. W. and Glibert, P. M.: Interactions between NH4/+ and NO3/- uptake and assimilation: Comparison of diatoms and dinoflagellates at several growth temperatures, Mar. Biol., 133, 541–551, https://doi.org/10.1007/s002270050494, 1999.

Lourey, M. J. and Trull, T. W.: Seasonal nutrient depletion and carbon export in the Subantarctic and Polar Frontal zones of the Southern Ocean south of Australia, J. Geophys. Res. Ocean., 106, 31463–31487, https://doi.org/10.1029/2000JC000287, 2001.

Lourey, M. J., Trull, T. W., and Sigman, D. M.: Sensitivity of δ15N of nitrate, surface suspended and deep sinking particulate nitrogen to seasonal nitrate depletion in the Southern Ocean, Global Biogeochem. Cycles, 17, 1–18, https://doi.org/10.1029/2002gb001973, 2003.

Macko, S. A., Estep, M. L. F., Engel, M. H., and Hare, P. E.: Kinetic fractionation of stable nitrogen isotopes during amino acid transamination, Geochim. Cosmochim. Acta, 50, 2143–2146, https://doi.org/10.1016/0016-7037(86)90068-2, 1986.

Maranger, R., Bird, D. F., and Price, N. M.: Iron acquisition by photosynthetic marine phytoplankton from ingested bacteria, Nat. 1998 3966708, 396, 248–251, https://doi.org/10.1038/24352, 1998.

Marie, D., Pierre, U., Curie, M., Simon, N., and Vaulot, D.: Algae Culturing Techniques Chapter 17: Phytoplankton Cell Counting by Flow Cytometry, 1–15, 2005.

Mariotti, A., Germon, J. C., Hubert, P., Kaiser, P., Letolle, R., Tardieux, A., and Tardieux, P.: Experimental determination of nitrogen kinetic isotope fractionation: Some principles; illustration for the denitrification and nitrification processes, Plant Soil, 62, 413–430, https://doi.org/10.1007/BF02374138/METRICS, 1981.

Martin, J. H., Gordon, R. M., and Fitzwater, S. E.: Iron Limitation, Limnol. Oceanogr., 36, 1793–1802, 1991.

Martiny, A. C., Pham, C. T. A., Primeau, F. W., Vrugt, J. A., Moore, J. K., Levin, S. A., and Lomas, M. W.: Strong latitudinal patterns in the elemental ratios of marine plankton and organic matter, Nat. Geosci., https://doi.org/10.1038/NGEO1757, 2013.

McCarthy, M. D. and Bronk, D. A.: ANALYTICAL METHODS FOR THE STUDY OF NITROGEN, Nitrogen Mar. Environ., 1219–1275, https://doi.org/10.1016/B978-0-12-372522-6.00028-1, 2008.

McFadden, G. I.: PRIMARY AND SECONDARY ENDOSYMBIOSIS AND THE ORIGIN OF PLASTIDS, J. Phycol., 37, 951–959, https://doi.org/10.1046/J.1529-8817.2001.01126.X, 2001.

Mdutyana, M., Thomalla, S. J., Philibert, R., Ward, B. B., and Fawcett, S. E.: The Seasonal Cycle of Nitrogen Uptake and Nitrification in the Atlantic Sector of the Southern Ocean, Global Biogeochem. Cycles, 34, 1–29, https://doi.org/10.1029/2019GB006363, 2020.

Mendes, C. R. B., de Souza, M. S., Garcia, V. M. T., Leal, M. C., Brotas, V., and Garcia, C. A. E.: Dynamics of phytoplankton communities during late summer around the tip of the Antarctic Peninsula, Deep. Res. Part I Oceanogr. Res. Pap., 65, 1–14, https://doi.org/10.1016/j.dsr.2012.03.002, 2012.

Mendes, C. R. B., Tavano, V. M., Leal, M. C., de Souza, M. S., Brotas, V., and Garcia, C. A. E.: Shifts in the dominance between diatoms and cryptophytes during three late summers in the Bransfield Strait (Antarctic Peninsula), Polar Biol., 36, 537–547, https://doi.org/10.1007/s00300-012-1282-4, 2013.

Mendes, C. R. B., Tavano, V. M., Kerr, R., Dotto, T. S., Maximiano, T., and Secchi, E. R.: Impact of sea ice on the structure of phytoplankton communities in the northern Antarctic Peninsula, Deep. Res. Part II Top. Stud. Oceanogr., 149, 111–123, https://doi.org/10.1016/j.dsr2.2017.12.003, 2018a.

Mendes, C. R. B., Tavano, V. M., Dotto, T. S., Kerr, R., de Souza, M. S., Garcia, C. A. E., and Secchi, E. R.: New insights on the dominance of cryptophytes in Antarctic coastal waters: A case study in Gerlache Strait, Deep. Res. Part II Top. Stud. Oceanogr., 149, 161–170, https://doi.org/10.1016/j.dsr2.2017.02.010, 2018b.

Mendes, C. R. B., Costa, R. R., Ferreira, A., Jesus, B., Tavano, V. M., Dotto, T. S., Leal, M. C., Kerr, R., Islabão, C. A., Franco, A. de O. da R., Mata, M. M., Garcia, C. A. E., and Secchi, E. R.: Cryptophytes: an emerging algal group in the rapidly changing Antarctic Peninsula marine environments, Glob. Chang. Biol., https://doi.org/10.1111/GCB.16602, 2023.

Moore, J. K. and Abbott, M. R.: Phytoplankton chlorophyll distributions and primary production in the Southern Ocean, J. Geophys. Res. Ocean., 105, 28709–28722, https://doi.org/10.1029/1999JC000043, 2000.

Moore, L., Goericke, R., and Chisholm, S.: Comparative physiology of Synechococcus and Prochlorococcus: influence of light and temperature on growth, pigments, fluorescence and absorptive properties on JSTOR, Mar. Ecol. Prog. Ser., 116, 259–275, 1995.

Moore, L. R., Rocap, G., and Chisholm, S. W.: Physiology and molecular phylogeny of coexisting Prochlorococcus ecotypes, Nat. 1998 3936684, 393, 464–467, https://doi.org/10.1038/30965, 1998.

Moore, L. R., Post, A. F., Rocap, G., and Chisholm, S. W.: Utilization of different nitrogen sources by the marine cyanobacteria Prochlorococcus and Synechococcus, Limnol. Oceanogr., 47, 989–996, https://doi.org/10.4319/LO.2002.47.4.0989, 2002.

Moorthi, S., Caron, D. A., Gast, R. J., and Sanders, R. W.: Mixotrophy: a widespread and important ecological strategy for planktonic and sea-ice nanoflagellates in the Ross Sea, Antarctica, Aquat. Microb. Ecol., 54, 269–277, https://doi.org/10.3354/AME01276, 2009.

Morel, F., Rueter, J., and Price, N.: Iron Nutrition of Phytoplankton and Its Possible Importance in the Ecology of Ocean Regions with High Nutrient and Low Biomass, 4, 56–61, https://doi.org/10.5670/oceanog.1991.03, 1991.

Mosseri, J., Quéguiner, B., Armand, L., and Cornet-Barthaux, V.: Impact of iron on silicon utilization by diatoms in the Southern Ocean: A case study of Si/N cycle decoupling in a naturally iron-enriched area, Deep Sea Res. Part II Top. Stud. Oceanogr., 55, 801–819, https://doi.org/10.1016/j.dsr2.2007.12.003, 2008a.

Mosseri, J., Quéguiner, B., Armand, L., and Cornet-Barthaux, V.: Impact of iron on silicon utilization by diatoms in the Southern Ocean: A case study of Si/N cycle decoupling in a naturally iron-enriched

area, Deep. Res. Part II Top. Stud. Oceanogr., 55, 801–819, https://doi.org/10.1016/j.dsr2.2007.12.003, 2008b.

Mtshali, T. N., van Horsten, N. R., Thomalla, S. J., Ryan-Keogh, T. J., Nicholson, S. A., Roychoudhury, A. N., Bucciarelli, E., Sarthou, G., Tagliabue, A., and Monteiro, P. M. S.: Seasonal Depletion of the Dissolved Iron Reservoirs in the Sub-Antarctic Zone of the Southern Atlantic Ocean, Geophys. Res. Lett., 46, 4386–4395, https://doi.org/10.1029/2018GL081355, 2019.

Muench, R. D. and Gordon, A. L.: Circulation and transport of water along the western Weddell Sea margin, J. Geophys. Res., 100, 18503–18515, https://doi.org/10.1029/95jc00965, 1995.

Needoba, J. A., Sigman, D. M., and Harrison, P. J.: THE MECHANISM OF ISOTOPE FRACTIONATION DURING ALGAL NITRATE ASSIMILATION AS ILLUMINATED BY THE 15 N/ 14 N OF INTRACELLULAR NITRATE 1, J. Phycol, 40, 517–522, https://doi.org/10.1111/j.1529-8817.2004.03172.x, 2004.

Nelson, D. M., Tréguer, P., Brzezinski, M. A., Leynaert, A., and Quéguiner, B.: Production and dissolution of biogenic silica in the ocean: Revised global estimates, comparison with regional data and relationship to biogenic sedimentation, Global Biogeochem. Cycles, 9, 359–372, https://doi.org/10.1029/95GB01070, 1995.

Nissen, C. and Vogt, M.: Factors controlling the competition between Phaeocystis and diatoms in the Southern Ocean in the Southern Ocean, Biogeosciences Discuss., 1–39, https://doi.org/10.5194/bg-2019-488, 2021.

Nissen, C., Gruber, N., Münnich, M., and Vogt, M.: Southern Ocean Phytoplankton Community Structure as a Gatekeeper for Global Nutrient Biogeochemistry, Global Biogeochem. Cycles, 35, e2021GB006991, https://doi.org/10.1029/2021GB006991, 2021.

Olson, R. J., Chisholm, S. W., Zettler, E. R., and Armbrust, E. V.: Analysis of Synechococcus pigment types in the sea using single and dual beam flow cytometry, Deep Sea Res. Part A, Oceanogr. Res. Pap., 35, 425–440, https://doi.org/10.1016/0198-0149(88)90019-2, 1988.

Van Oostende, N., Fawcett, S. E., Marconi, D., Lueders-Dumont, J., Sabadel, A. J. M., Woodward, E. M. S., Jönsson, B. F., Sigman, D. M., and Ward, B. B.: Variation of summer phytoplankton community composition and its relationship to nitrate and regenerated nitrogen assimilation across the North Atlantic Ocean, Deep Sea Res. Part I Oceanogr. Res. Pap., 121, 79–94, https://doi.org/10.1016/J.DSR.2016.12.012, 2017.

Orsi, A. H., Nowlin, W. D., and Whitworth, T.: On the circulation and stratification of the Weddell Gyre, Deep. Res. Part I, 40, 169–203, https://doi.org/10.1016/0967-0637(93)90060-G, 1993.

Orsi, A. H., Whitworth, T., and Nowlin, W. D.: On the meridional extent and fronts of the Antarctic Circumpolar Current, Deep. Res. Part I, 42, 641–673, https://doi.org/10.1016/0967-0637(95)00021-W, 1995.

Paerl, H. W.: Ecophysiological and Trophic Implications of Light-Stimulated Amino Acid Utilization in Marine Picoplankton, Appl. Environ. Microbiol., 57, 473–479,

https://doi.org/10.1128/AEM.57.2.473-479.1991, 1991.

Partensky, F., Hess, W. R., and Vaulot, D.: Prochlorococcus , a Marine Photosynthetic Prokaryote of Global Significance , Microbiol. Mol. Biol. Rev., 63, 106–127, https://doi.org/10.1128/MMBR.63.1.106-127.1999/ASSET/7FE3CCE3-E809-4013-B565-F53CDCDE20BB/ASSETS/GRAPHIC/MR0190005011.JPEG, 1999a.

Partensky, F., Blanchot, J., and Vaulot, D.: DifferentiaI distribution and ecology of Prochlorococcus and Synechococcus in oceanic waters: a review, Bull. l'Institut océanographique, 1999b.

Pennock, J. R., Velinsky, D. J., Ludlam, J. M., Sharp, J. H., and Fogel, M. L.: Isotopic fractionation of ammonium and nitrate during uptake by Skeletonema costatum: Implications for δ15N dynamics under bloom conditions, Limnol. Oceanogr., 41, 451–459, https://doi.org/10.4319/LO.1996.41.3.0451, 1996.

Petrou, K., Kranz, S. A., Trimborn, S., Hassler, C. S., Ameijeiras, S. B., Sackett, O., Ralph, P. J., and Davidson, A. T.: Southern Ocean phytoplankton physiology in a changing climate, J. Plant Physiol., 203, 135–150, https://doi.org/10.1016/j.jplph.2016.05.004, 2016.

Pollard, R. T., Lucas, M. I., and Read, J. F.: Physical controls on biogeochemical zonation in the Southern Ocean, Deep. Res. Part II Top. Stud. Oceanogr., 49, 3289–3305, https://doi.org/10.1016/S0967-0645(02)00084-X, 2002.

Pollard, R. T., Salter, I., Sanders, R. J., Lucas, M. I., Moore, C. M., Mills, R. A., Statham, P. J., Allen, J. T., Baker, A. R., Bakker, D. C. E., Charette, M. A., Fielding, S., Fones, G. R., French, M., Hickman, A. E., Holland, R. J., Hughes, J. A., Jickells, T. D., Lampitt, R. S., Morris, P. J., Nédélec, F. H., Nielsdóttir, M., Planquette, H., Popova, E. E., Poulton, A. J., Read, J. F., Seeyave, S., Smith, T., Stinchcombe, M., Taylor, S., Thomalla, S., Venables, H. J., Williamson, R., and Zubkov, M. V.: Southern Ocean deep-water carbon export enhanced by natural iron fertilization, Nat. 2009 4577229, 457, 577–580, https://doi.org/10.1038/nature07716, 2009.

Prezelinl, B. B., Glover2, H. E., Hovenl, D., and Steinbergl, H. A. ~: Blue-green light effects on light-limited rates of photosynthesis: relationship to pigmentation and productivity estimates for Synechococcus populations from the Sargasso Sea, 54, 121–136, 1989.

Priddle, J., Boyd, I. L., Whitehouse, M. J., Murphy, E. J., and Croxall, J. P.: Estimates of Southern Ocean primary production - Constraints from predator carbon demand and nutrient drawdown, in: Journal of Marine Systems, 275–288, https://doi.org/10.1016/S0924-7963(98)00043-8, 1998.

Probyn, T. A. and Painting, S. J.: Nitrogen uptake by size-fractionated phytoplankton populations in Antarctic surface waters1, Limnol. Oceanogr., 30, 1327–1332, https://doi.org/10.4319/LO.1985.30.6.1327, 1985.

Quéguiner, B.: Iron fertilization and the structure of planktonic communities in high nutrient regions of the Southern Ocean, Deep Sea Res. Part II Top. Stud. Oceanogr., 90, 43–54, https://doi.org/10.1016/j.dsr2.2012.07.024, 2013.

Quere, C. Le, Harrison, S. P., Colin Prentice, I., Buitenhuis, E. T., Aumont, O., Bopp, L., Claustre, H., Cotrim Da Cunha, L., Geider, R., Giraud, X., Klaas, C., Kohfeld, K. E., Legendre, L., Manizza, M.,

Platt, T., Rivkin, R. B., Sathyendranath, S., Uitz, J., Watson, A. J., and Wolf-Gladrow, D.: Ecosystem dynamics based on plankton functional types for global ocean biogeochemistry models, Glob. Chang. Biol., 0, 051013014052005-???, https://doi.org/10.1111/j.1365-2486.2005.1004.x, 2005.

Raes, E. J., van de Kamp, J., Bodrossy, L., Fong, A. A., Riekenberg, J., Holmes, B. H., Erler, D. V., Eyre, B. D., Weil, S. S., and Waite, A. M.: N2 Fixation and New Insights Into Nitrification From the Ice-Edge to the Equator in the South Pacific Ocean, Front. Mar. Sci., 7, 1–20, https://doi.org/10.3389/fmars.2020.00389, 2020.

Ragueneau, O., Tréguer, P., Leynaert, A., Anderson, R. F., Brzezinski, M. A., DeMaster, D. J., Dugdale, R. C., Dymond, J., Fischer, G., François, R., Heinze, C., Maier-Reimer, E., Martin-Jézéquel, V., Nelson, D. M., and Quéguiner, B.: A review of the Si cycle in the modern ocean: Recent progress and missing gaps in the application of biogenic opal as a paleoproductivity proxy, Glob. Planet. Change, 26, 317–365, https://doi.org/10.1016/S0921-8181(00)00052-7, 2000.

Raimbault, P., Slawyk, G., Boudjellal, B., Coatanoan, C., Conan, P., Coste, B., Garcia, N., Moutin, T., and Pujo-Pay, M.: Carbon and nitrogen uptake and export in the equatorial Pacific at 150°W: Evidence of an efficient regenerated production cycle, J. Geophys. Res. Ocean., 104, 3341–3356, https://doi.org/10.1029/1998JC900004, 1999.

Rau, G. H., Sullivan, C. W., and Gordon, L. I.: δ 13C and δ15N variations in Weddell Sea particulate organic matter, Mar. Chem., 35, 355–369, https://doi.org/10.1016/S0304-4203(09)90028-7, 1991.

Raven, J. A. and Kübler, J. E.: NEW LIGHT ON THE SCALING OF METABOLIC RATE WITH THE SIZE OF ALGAE, J. Phycol., 38, 11–16, https://doi.org/10.1046/J.1529-8817.2002.01125.X, 2002.

RAVEN, J. A.: Predictions of Mn and Fe use efficiencies of phototrophic growth as a function of light availability for growth and of C assimilation pathway, New Phytol., 116, 1–18, https://doi.org/10.1111/J.1469-8137.1990.TB00505.X, 1990.

Rembauville, M., Manno, C., Tarling, G. A., Blain, S., and Salter, I.: Strong contribution of diatom resting spores to deep-sea carbon transfer in naturally iron-fertilized waters downstream of South Georgia, Deep. Res. Part I Oceanogr. Res. Pap., 115, 22–35, https://doi.org/10.1016/J.DSR.2016.05.002, 2016.

Rigual-Hernández, A. S., Trull, T. W., Bray, S. G., Cortina, A., and Armand, L. K.: Latitudinal and temporal distributions of diatom populations in the pelagic waters of the Subantarctic and Polar Frontal zones of the Southern Ocean and their role in the biological pump, 12, 5309–5337, https://doi.org/10.5194/BG-12-5309-2015, 2015.

Rigual-Hernández, A. S., Trull, T. W., Bray, S. G., and Armand, L. K.: The fate of diatom valves in the Subantarctic and Polar Frontal Zones of the Southern Ocean: Sediment trap versus surface sediment assemblages, Palaeogeogr. Palaeoclimatol. Palaeoecol., 457, 129–143, https://doi.org/10.1016/J.PALAEO.2016.06.004, 2016.

Ryan-Keogh, T. J., Thomalla, S. J., Mtshali, T. N., Van Horsten, N. R., and Little, H. J.: Seasonal

development of iron limitation in the sub-Antarctic zone, 15, 4647–4660, https://doi.org/10.5194/BG-15-4647-2018, 2018.

Salter, I., Lampitt, R. S., Sanders, R., Poulton, A., Kemp, A. E. S., Boorman, B., Saw, K., and Pearce, R.: Estimating carbon, silica and diatom export from a naturally fertilised phytoplankton bloom in the Southern Ocean using PELAGRA: A novel drifting sediment trap, Deep Sea Res. Part II Top. Stud. Oceanogr., 54, 2233–2259, https://doi.org/10.1016/J.DSR2.2007.06.008, 2007.

Santoro, A. E. and Casciotti, K. L.: Enrichment and characterization of ammonia-oxidizing archaea from the open ocean: phylogeny, physiology and stable isotope fractionation, ISME J. 2011 511, 5, 1796–1808, https://doi.org/10.1038/ismej.2011.58, 2011.

Sarmiento, J., Toggweiler, J.: A new model for the role of the oceans in determining atmospheric P CO2., Nature, 308, 621–624, https://doi.org/https://doi.org/10.1038/308621a0, 1984.

Sarmiento, J. L., Gruber, N., Brzezinski, M. A., and Dunne, J. P.: High-latitude controls of thermocline nutrients and low latitude biological productivity, Nature, 427, 56–60, https://doi.org/10.1038/nature10605, 2004.

Schlitzer, R.: Carbon export fluxes in the Southern Ocean: results from inverse modeling and comparison with satellite-based estimates, Deep Sea Res. Part II Top. Stud. Oceanogr., 49, 1623–1644, https://doi.org/10.1016/S0967-0645(02)00004-8, 2002.

Schodlok, M. P., Hellmer, H. H.,&Beckmann, A.: On the transport, variability and origin of densewatermasses crossing the South Scotia Ridge.e, Deep Sea Res. II Trop. Stud. Oceanogr., 49, 4807–4825, 2002.

Schoemann, V., Becquevort, S., Stefels, J., Rousseau, V., and Lancelot, C.: Phaeocystis blooms in the global ocean and their controlling mechanisms: A review, J. Sea Res., 53, 43–66, https://doi.org/10.1016/j.seares.2004.01.008, 2005.

Schröder, M., Hellmer, H. H., and Absy, J. M.: On the near-bottom variability in the northwestern Weddell Sea, Deep. Res. Part II Top. Stud. Oceanogr., 49, 4767–4790, https://doi.org/10.1016/S0967-0645(02)00158-3, 2002.

Semeneh, M., Dehairs, F., Fiala, M., Elskens, M., and Goeyens, L.: Seasonal variation of phytoplankton community structure and nitrogen uptake regime in the Indian Sector of the Southern Ocean, Polar Biol., 20, 259–272, https://doi.org/10.1007/s003000050302, 1998.

Shapiro, L. P. and Haugen, E. M.: Seasonal distribution and temperature tolerance of Synechococcus in Boothbay Harbor, Maine, Estuar. Coast. Shelf Sci., 26, 517–525, https://doi.org/10.1016/0272-7714(88)90004-2, 1988.

Sharp, Z.: Principles of Stable Isotope Geochemistry, 2nd Edition, Open Textb., https://doi.org/ https://doi.org/10.25844/h9q1-0p82 , 2017.

Sigman, D. M. and Boyle[2], E. A.: Glacial/interglacial variations in atmospheric carbon dioxide, NATURE, 2000.

Sigman, D. M. and Casciotti, K. L.: Nitrogen Isotopes in the Ocean, Encycl. Ocean Sci., 1884–1894,

https://doi.org/10.1006/RWOS.2001.0172, 2001.
Sigman, D. M. and Fripiat, F.: Nitrogen isotopes in the ocean, in: Encyclopedia of Ocean Sciences, Elsevier Inc., 263–278, https://doi.org/10.1016/B978-0-12-409548-9.11605-7, 2019.
Sigman, D. M. and Hain, M. P.: The Biological Productivity of the Ocean, 2012.
Sigman, D. M., Bernard, C., Hastings, M. G., Sigman, D. M., Casciotti, K. L., Andreani, M., Barford, C., Galanter, M., and Bo, J. K.: A Bacterial Method for the Nitrogen Isotopic Analysis of Nitrate in Seawater and Freshwater A Bacterial Method for the Nitrogen Isotopic Analysis of Nitrate in Seawater and Freshwater, 73, 4145–4153, https://doi.org/10.1021/ac010088e, 2001.
Sigman, D. M., DiFiore, P. J., Hain, M. P., Deutsch, C., Wang, Y., Karl, D. M., Knapp, A. N., Lehmann, M. F., and Pantoja, S.: The dual isotopes of deep nitrate as a constraint on the cycle and budget of oceanic fixed nitrogen, Deep. Res. Part I Oceanogr. Res. Pap., 56, 1419–1439, https://doi.org/10.1016/j.dsr.2009.04.007, 2009.
Sigman, D. M., Hain, M. P., and Haug, G. H.: The polar ocean and glacial cycles in atmospheric CO 2 concentration, Nature, 466, https://doi.org/10.1038/nature09149, 2010.
Sigman, O. M., Altabet, M. A., McCorkle, D. C., Francois, R., and Fischer, G.: The δ15N of nitrate in the southern ocean: Consumption of nitrate in surface waters, Global Biogeochem. Cycles, 13, 1149–1166, https://doi.org/10.1029/1999GB900038, 1999.
Silfer, J. A., Engel, M. H., and Macko, S. A.: Kinetic fractionation of stable carbon and nitrogen isotopes during peptide bond hydrolysis: Experimental evidence and geochemical implications, Chem. Geol. Isot. Geosci. Sect., 101, 211–221, https://doi.org/10.1016/0009-2541(92)90003-N, 1992.
Smart, S. M., Fawcett, S. E., Thomalla, S. J., Weigand, M. a, Reason, C. J. C., and Sigman, D. M.: Global Biogeochemical Cycles, 1–19, https://doi.org/10.1002/2014GB005013.Received, 2015.
Smart, S. M., Fawcett, S. E., Ren, H., Schiebel, R., Tompkins, E. M., Martínez-García, A., Stirnimann, L., Roychoudhury, A., Haug, G. H., and Sigman, D. M.: The Nitrogen Isotopic Composition of Tissue and Shell-Bound Organic Matter of Planktic Foraminifera in Southern Ocean Surface Waters, Geochemistry, Geophys. Geosystems, 21, e2019GC008440, https://doi.org/10.1029/2019GC008440, 2020a.
Smart, S. M., Fawcett, S. E., Ren, H., Schiebel, R., Tompkins, E. M., Martínez-García, A., Stirnimann, L., Roychoudhury, A., Haug, G. H., and Sigman, D. M.: The Nitrogen Isotopic Composition of Tissue and Shell-Bound Organic Matter of Planktic Foraminifera in Southern Ocean Surface Waters, Geochemistry, Geophys. Geosystems, 21, 1–29, https://doi.org/10.1029/2019GC008440, 2020b.
Smetacek, V.: The giant diatom dump, Nat. 2000 4066796, 406, 574–575, https://doi.org/10.1038/35020665, 2000.
Smetacek, V., Klaas, C., Menden-Deuer, S., and Rynearson, T. A.: Mesoscale distribution of dominant diatom species relative to the hydrographical field along the Antarctic Polar Front, Deep Sea Res. Part II Top. Stud. Oceanogr., 49, 3835–3848, https://doi.org/10.1016/S0967-0645(02)00113-3, 2002.
Smetacek, V., Assmy, P., and Henjes, J.: The role of grazing in structuring Southern Ocean pelagic

ecosystems and biogeochemical cycles, Antarct. Sci., 16, 541–558, https://doi.org/10.1017/S0954102004002317, 2004.

Smith, S., Altieri, K. E., Mdutyana, M., Walker, D. R., Parrott, R. G., Gallie, S., Spence, K. A. M., Burger, J. M., and Fawcett, S. E.: Biogeochemical controls on ammonium accumulation in the surface layer of the Southern Ocean, 19, 715–741, https://doi.org/10.5194/BG-19-715-2022, 2022.

Smith, W. 0. and Nelson, D. M.: Phytoplankton growth and new production in the Weddell Sea marginal ice zone in the austral spring and autumn, Limnol. Oceanogr., 35, 809–821, https://doi.org/10.4319/lo.1990.35.4.0809, 1990.

Stoecker, D. K., Hansen, P. J., Caron, D. A., and Mitra, A.: Mixotrophy in the Marine Plankton, https://doi.org/10.1146/annurev-marine-010816-060617, 2016.

Strzepek, R. F., Maldonado, M. T., Hunter, K. A., Frew, R. D., and Boyd, P. W.: Adaptive strategies by Southern Ocean phytoplankton to lessen iron limitation: Uptake of organically complexed iron and reduced cellular iron requirements, Limnol. Oceanogr., 56, 1983–2002, https://doi.org/10.4319/lo.2011.56.6.1983, 2011.

Stukel, M. R., Landry, M. R., and Selph, K. E.: Nanoplankton mixotrophy in the eastern equatorial Pacific, Deep Sea Res. Part II Top. Stud. Oceanogr., 58, 378–386, https://doi.org/10.1016/J.DSR2.2010.08.016, 2011.

Sunda, W. G.: Feedback interactions between trace metal nutrients and phytoplankton in the ocean, Front. Microbiol., 3, 204, https://doi.org/10.3389/FMICB.2012.00204/BIBTEX, 2012.

Sunda, W. G. and Huntsman, S. A.: Interrelated influence of iron, light and cell size on marine phytoplankton growth, Nature, 390, 389–392, https://doi.org/10.1038/37093, 1997.

Sunda, W. G. and Huntsman, S. A.: High iron requirement for growth, photosynthesis, and low-light acclimation in the coastal cyanobacterium Synechococcus bacillaris, Front. Microbiol., 6, 561, 2015.

Tagliabue, A., Mtshali, T., Aumont, O., Bowie, A. R., Klunder, M. B., Roychoudhury, A. N., and Swart, S.: A global compilation of dissolved iron measurements: Focus on distributions and processes in the Southern Ocean, 9, 2333–2349, https://doi.org/10.5194/bg-9-2333-2012, 2012.

Tagliabue, A., Sallée, J. B., Bowie, A. R., Lévy, M., Swart, S., and Boyd, P. W.: Surface-water iron supplies in the Southern Ocean sustained by deep winter mixing, Nat. Geosci., 7, 314–320, https://doi.org/10.1038/ngeo2101, 2014.

Takahashi, T., Sweeney, C., Hales, B., Chipman, D. W., Goddard, J. G., Newberger, T., Iannuzzi, R. A., and Sutherland, S. C.: The changing carbon cycle in the southern ocean, 25, 26–37, https://doi.org/10.5670/oceanog.2012.71, 2012.

Takeda, S.: Influence of iron availability on nutrient consumption ratio, Nature, 393, 774–777, 1998.

Talley, L. D., Pickard, G. L., Emery, W. J., and Swift, J. H.: Southern Ocean, Descr. Phys. Oceanogr., 437–471, https://doi.org/10.1016/b978-0-7506-4552-2.10013-7, 2011.

Treguer, P. and G, J.: Review Dynamics of nutrients and phytoplankton, and fluxes of carbon, nitrogen and silicon in the Antarctic Ocean, edited by: Hempel, G., Springer Berlin Heidelberg, 1992.

Tréguer, P. and Pondaven, P.: Climatic changes and the carbon cycle in the Southern Ocean: a step forward, Deep Sea Res. Part II Top. Stud. Oceanogr., 49, 1597–1600, https://doi.org/10.1016/S0967-0645(02)00002-4, 2002.

Tréguer, P., Nelson, D. M., Van Bennekom, A. J., Demaster, D. J., Leynaert, A., and Quéguiner, B.: The Silica Balance in the World Ocean: A Reestimate, Science (80-.)., 268, 375–379, https://doi.org/10.1126/SCIENCE.268.5209.375, 1995.

Tréguer, P., Bowler, C., Moriceau, B., Dutkiewicz, S., Gehlen, M., Aumont, O., Bittner, L., Dugdale, R., Finkel, Z., Iudicone, D., Jahn, O., Guidi, L., Lasbleiz, M., Leblanc, K., Levy, M., and Pondaven, P.: Influence of diatom diversity on the ocean biological carbon pump, Nat. Geosci., https://doi.org/10.1038/s41561-017-0028-x, 2017.

Tréguer, P. J.: The Southern Ocean silica cycle, Comptes Rendus Geosci., 346, 279–286, https://doi.org/10.1016/J.CRTE.2014.07.003, 2014.

Treibergs, L. A., Fawcett, S. E., Lomas, M. W., and Sigman, D. M.: Nitrogen isotopic response of prokaryotic and eukaryotic phytoplankton to nitrate availability in Sargasso Sea surface waters, Limnol. Oceanogr., 59, 972–985, https://doi.org/10.4319/lo.2014.59.3.0972, 2014.

Trimborn, S., Hoppe, C. J. M., Taylor, B. B., Bracher, A., and Hassler, C.: Physiological characteristics of open ocean and coastal phytoplankton communities of Western Antarctic Peninsula and Drake Passage waters, Deep Sea Res. Part I Oceanogr. Res. Pap., 98, 115–124, https://doi.org/10.1016/J.DSR.2014.12.010, 2015.

Trimborn, S., Thoms, S., Karitter, P., and Bischof, K.: Ocean acidification and high irradiance stimulate the photo-physiological fitness, growth and carbon production of the Antarctic cryptophyte Geminigera cryophila, 16, 2997–3008, https://doi.org/10.5194/BG-16-2997-2019, 2019.

Trull, T., Rintoul, S. R., Hadfield, M., and Abraham, E. R.: Circulation and seasonal evolution of polar waters south of Australia: implications for iron fertilization of the Southern Ocean, Deep Sea Res. Part II Top. Stud. Oceanogr., 48, 2439–2466, https://doi.org/10.1016/S0967-0645(01)00003-0, 2001.

Volk, T. and Hoffert, M. I.: Ocean Carbon Pumps: Analysis of Relative Strengths and Efficiencies in Ocean-Driven Atmospheric CO2 Changes, in: Geophysical Monograph Series, edited by: Sundquist, E. T. and Broecker, W. S., 1985.

Waser, N. A., Yin, K., Yu, Z., Tada, K., Harrison, P. J., Turpin, D. H., and Calvert, S. E.: Nitrogen isotope fractionation during nitrate, ammonium and urea uptake by marine diatoms and coccolithophores under various conditions of N availability, Mar. Ecol. Prog. Ser., 169, 29–41, https://doi.org/10.3354/MEPS169029, 1998a.

Waser, N. A. D., Harrison, P. J., Nielsen, B., Calvert, S. E., and Turpin, D. H.: Nitrogen isotope fractionation during the uptake and assimilation of nitrate, nitrite, ammonium, and urea by a marine diatom, Limnol. Oceanogr., 43, 215–224, https://doi.org/10.4319/LO.1998.43.2.0215, 1998b.

Weber, L. H. and El-sayed, S. Z.: Contributions of the net, nano- and picoplankton to the phytoplankton standing crop and primary productivity in the Southern Ocean, J. Plankton Res., 9, 973–994,

https://doi.org/10.1093/PLANKT/9.5.973, 1987.

Weber, T. S. and Deutsch, C.: Ocean nutrient ratios governed by plankton biogeography, https://doi.org/10.1038/nature09403, 2010a.

Weber, T. S. and Deutsch, C.: Ocean nutrient ratios governed by plankton biogeography, Nature, 467, 550–554, https://doi.org/10.1038/nature09403, 2010b.

Weir, I., Fawcett, S., Smith, S., Walker, D., Bornman, T., and Fietz, S.: Winter biogenic silica and diatom distributions in the Indian sector of the Southern Ocean, Deep. Res. Part I Oceanogr. Res. Pap., 166, 103421, https://doi.org/10.1016/j.dsr.2020.103421, 2020.

Whitworth, T. and Nowlin, W. D.: Water Masses and Currents of the Southern Ocean at the Greenwich Meridian, JOURNAL OF GEOPHYSICAL RESEARCH, 6462–6476 pp., https://doi.org/10.1029/JC092iC06p06462, 1987.

Wilhelm, S. W., Maxwell, D. P., and Trick, C. G.: Growth, iron requirements, and siderophore production in iron-limited Synechococcus PCC 72, Limnol. Oceanogr., 41, 89–97, https://doi.org/10.4319/LO.1996.41.1.0089, 1996.

Wright, S. W., van den Enden, R. L., Pearce, I., Davidson, A. T., Scott, F. J., and Westwood, K. J.: Phytoplankton community structure and stocks in the Southern Ocean (30–80°E) determined by CHEMTAX analysis of HPLC pigment signatures, Deep Sea Res. Part II Top. Stud. Oceanogr., 57, 758–778, https://doi.org/10.1016/J.DSR2.2009.06.015, 2010.

Yool, A., Martin, A. P., Fernández, C., and Clark, D. R.: The significance of nitrification for oceanic new production, https://doi.org/10.1038/nature05885, 2007.

Yoshida, N.: 15 N-depleted N 2 O as a product of nitrification, Nature, 335, 528–529, 1988.

Zwirglmaier, K., Jardillier, L., Ostrowski, M., Mazard, S., Garczarek, L., Vaulot, D., Not, F., Massana, R., Ulloa, O., and Scanlan, D. J.: Global phylogeography of marine Synechococcus and Prochlorococcus reveals a distinct partitioning of lineages among oceanic biomes, Environ. Microbiol., 10, 147–161, https://doi.org/10.1111/J.1462-2920.2007.01440.X, 2008.

Chapter 2: Nanoplankton: the dominant vector for carbon export across the springtime Southern Ocean

This chapter is formatted for submission to Science Advances; therefore, the methods section is at the end of the chapter after the discussion.

Abstract

Across the Southern Ocean, large (≥20 μm) diatoms are generally assumed to be the primary vector for carbon export, although this assumption derives mainly from summertime observations. Here, we investigate carbon production and export during the Southern Ocean's spring bloom from size-fractionated measurements of net primary production (NPP), nitrogen (nitrate, ammonium, urea) and iron (labile inorganic iron and organically-complexed iron) uptake, and a high-resolution characterization of phytoplankton community composition. The nanoplankton-sized (2.7-20 μm) diatom, *Chaetoceros* spp., dominated biomass, NPP, and nitrate uptake across the basin (40-56ºS), which we attribute to their low iron requirement, rapid response to increased light availability, and ability to escape grazing when aggregated into chains. We estimate that the spring *Chaetoceros* bloom accounted for >30% of annual export production across the Southern Ocean, a finding consistent with recent studies from other ocean regions highlighting the central role of the phytoplankton "middle class" in driving carbon export.

Table of Acronyms

Acronym (units)	Full description
STF	Subtropical Front
SAF	Subantarctic Front
PF	Polar Front
sACCF	southern Antarctic Circumpolar Current Front
SAZ	Subantarctic Zone
PFZ	Polar Frontal Zone
OAZ	Open Antarctic Zone
MIZ	Marginal Ice Zone
AZ	Antarctic Zone (jointly the OAZ and MIZ)
CCSZ	Coastal and Continental Shelf Zone
OOZ	Open Ocean Zone
MLD (m)	Mixed layer depth
Z_{eu} (m)	Euphotic zone depth
POC (µM)	Particulate Organic Carbon
PON (µM)	Particulate Organic Nitrogen
NPP (mmol m^{-2} d^{l})	Euphotic zone integrated rate of absolute carbon fixation (also termed net primary production)
ρNO_3^- (mmol m^{-2} d^{-1})	Euphotic zone integrated rate of absolute nitrate uptake
ρNH_4^+ (mmol m^{-2} d^{-1})	Euphotic zone integrated rate of absolute ammonium uptake
ρurea (mmol m^{-2} d^{-1})	Euphotic zone integrated rate of absolute urea uptake
ρN_{reg} (mmol m^{-2} d^{-1})	Euphotic zone integrated rate of absolute regenerated nitrogen (i.e., ρNH_4^+ + ρurea) uptake
V_c (hr^{-1})	Specific rate of carbon fixation
$V_{NO_3^-}$ (hr^{-1})	Specific rate of nitrate uptake
$V_{NH_4^+}$ (hr^{-1})	Specific rate of ammonium uptake
V_{urea} (hr^{-1})	Specific rate of urea uptake
V_{reg} (hr^{-1})	Specific rate of regenerated nitrogen uptake (i.e., $V_{NH_4^+} + V_{urea}$)
dFe'uptake (µmol Fe mol^{-1} C^{-1} m^{-2} d^{-1})	Euphotic zone integrated rate of inorganic iron uptake normalised to POC
dFe(FOB) uptake (µmol Fe mol^{-1} C^{-1} m^{-2} d^{-1})	Euphotic zone integrated rate of siderophore-bound iron uptake normalised to POC
Fe:C uptake ratio (µmol mol^{-1})	The ratio of total iron uptake (i.e., dFe' uptake + dFe(FOB) uptake) to carbon fixation (NPP)
Fe:N uptake ratio (µmol mol^{-1})	The ratio of total iron uptake (i.e., dFe' uptake + dFe(FOB) uptake) to total nitrogen uptake (i.e., ρNO_3^- + ρNH_4^+ + ρurea)
f-ratio	Flux ratio, equal to the proportion of primary productivity fuelled by NO_3^- uptake

2.1. Introduction

In the open Southern Ocean, primary production is strongly iron-limited (Martin et al., 1990; Boyd et al., 2000a). Phytoplankton require iron for various photosynthetic and metabolic processes, with the assimilation of nitrate (NO_3^-; the most oxidized form of bioavailable nitrogen (N)) requiring far more iron than the consumption of regenerated N (i.e., ammonium (NH_4^+) and urea) (Dortch, 1990; Priddle et al., 1998). Phytoplankton that rely on NO_3^- as their primary N source (e.g., diatoms) (Glibert et al., 2016a) are thus more sensitive to iron limitation than phytoplankton that mainly assimilate regenerated NH_4^+ (Dortch, 1990; Priddle et al., 1998). In the framework of the "new production paradigm", phytoplankton growth supported by new N (e.g., NO_3^- upwelled during deep winter mixing) must be balanced on an annual basis by the flux of organic matter out of the mixed layer (i.e., export production) (Dugdale and Goering, 1967; Eppley and Peterson, 1979). The low-iron state of the upper Southern Ocean constrains the extent to which upwelled NO_3^- can be drawn down by phytoplankton, thus limiting biological carbon export (Sarmiento and Toggweiler, 1984; Martin et al., 1990).

For over four decades, ecological theory has suggested that across the global ocean, large phytoplankton (typically diatoms >20 μm) proliferate under nutrient-replete conditions, an idea based on the assumption that maximum nutrient uptake rates generally increase with cell volume (Edwards et al., 2012). These large phytoplankton are responsible for high rates of primary and new production, with their eventual senescence yielding large sinking fluxes, thus driving elevated carbon export (Eppley and Peterson, 1979). In contrast, small cells are typically associated with nutrient-deplete conditions, low rates of productivity, and enhanced nutrient recycling (i.e., the microbial loop) (Azam et al., 1983; Fenchel, 1988). They also contribute little to the sinking flux and by extension, carbon export (Legendre and Le Fevre, 1995; Michaels and Silver, 1988). This theoretical framework has been generally accepted, and to some extent observed, for the open Southern Ocean (Tremblay et al., 2002; Deppeler and Davidson, 2017). However, recent studies from other ocean regions have shown that the phytoplankton "middle-class" (i.e., the nanoplankton; ~3-20 μm) is also important for primary productivity and carbon export, even in high-nutrient waters, with the idea that they predominantly contribute to the microbial loop being an oversimplification (Cassar et al., 2015; Leblanc et al., 2018; Juranek et al., 2020; Burger et al., 2020). These recent studies suggest that top-down factors (e.g., zooplankton grazing) control nanoplankton production and carbon export both directly via grazing and indirectly by driving changes in nutrient availability (e.g., N recycling) and phytoplankton community composition (Cassar et al., 2015; Leblanc et al., 2018).

The surface waters of the open Southern Ocean are replenished with iron during deep winter mixing, with additional (smaller) inputs via diapycnal diffusion and Ekman upwelling that occur year-round (Klunder et

al., 2011; Tagliabue et al., 2014; Mtshali et al., 2019). In spring, phytoplankton are released from light limitation as daylight hours increase and the mixed layer shoals; along with the iron supplied during winter, the resultant elevated light availability favours the initiation of a bloom as phytoplankton begin to consume the available macronutrients (i.e., NO_3^-, phosphate, and silicate) (Martin et al., 1990; Llort et al., 2015). Consistent with the ecological theory outlined above, large diatoms are generally thought to dominate the open Southern Ocean spring bloom as they can achieve high maximum nutrient uptake rates and are resistant to grazing by microzooplankton (Edwards et al., 2012; Smetacek, 2000; Smetacek et al., 2004; Quéguiner, 2013; Assmy et al., 2013). These diatoms are also considered the major vectors for carbon export because of their biogenic silica (bSi) frustules, which cause them to sink rapidly out of the mixed layer and increase their resistance to bacterial degradation (Quéguiner, 2013; Tréguer et al., 2017). As the spring/summer growth season progresses and iron is depleted, the Southern Ocean phytoplankton community is thought to shift towards smaller taxa (e.g., nanoflagellates) that preferentially consume regenerated N (Lomas and Glibert, 1999; Karsh et al., 2003). This shift decreases the potential for carbon export, both directly, as the unballasted small phytoplankton sink less rapidly and are generally remineralised within the upper 200 m (Feinberg and Dam, 1998), and indirectly, as regenerated N uptake supports no net CO_2 removal in a mass balance sense(Dugdale and Goering, 1967a; Eppley and Peterson, 1979).

Studies based on satellite observations and Argo float measurements of chlorophyll *a* indicate that the seasonal modulation of phytoplankton blooms in the Southern Ocean is the result of a tight coupling between bottom-up (mainly iron and light) and top-down (grazing pressure and viral lysis) processes (Behrenfeld et al., 2016; Arteaga et al., 2020). Recently, Arteaga et al. (2020) showed that the Southern Ocean's annual cycle of phytoplankton productivity includes a period of rapid growth in spring as light limitation is alleviated, with phytoplankton initially outpacing their grazers. Indeed, the authors found that phytoplankton achieve their maximum growth rates in early spring, well before the peak in photoautotrophic biomass that characterizes the summer. We hypothesize that this spring bloom (i.e., the period of rapid phytoplankton growth) should be associated with elevated carbon export in addition to high rates of primary production, made possible by the non-limiting iron- (and in some regions, silicate-) and light conditions, as well as slow zooplankton grazing. To investigate this hypothesis, we measured the rates of net primary production (NPP) and N (as NO_3^-, NH_4^+, and urea) and iron (as labile inorganic iron and organically-complexed iron) uptake by three phytoplankton size-classes (0.3-2.7 μm – picoplankton, 2.7-20 μm – nanoplankton, and 20-200 μm – microplankton). Simulated *in situ* experiments were conducted at four stations representative of each of the major hydrographic zones of the open Southern Ocean (i.e., the Subantarctic Zone, Polar Frontal Zone, Open Antarctic Zone, and Marginal Ice Zone). We interpret the

uptake rates in the context of coincident measurements (from the four experimental stations plus eight ancillary stations) of macronutrient and iron concentrations, as well as phyto- and zooplankton community composition. Ultimately, we place our springtime observations into a broader temporal context by synthesizing the existing observations available for all seasons, with the goal of understanding the biogeochemical implications of the spring bloom for the succeeding phytoplankton community.

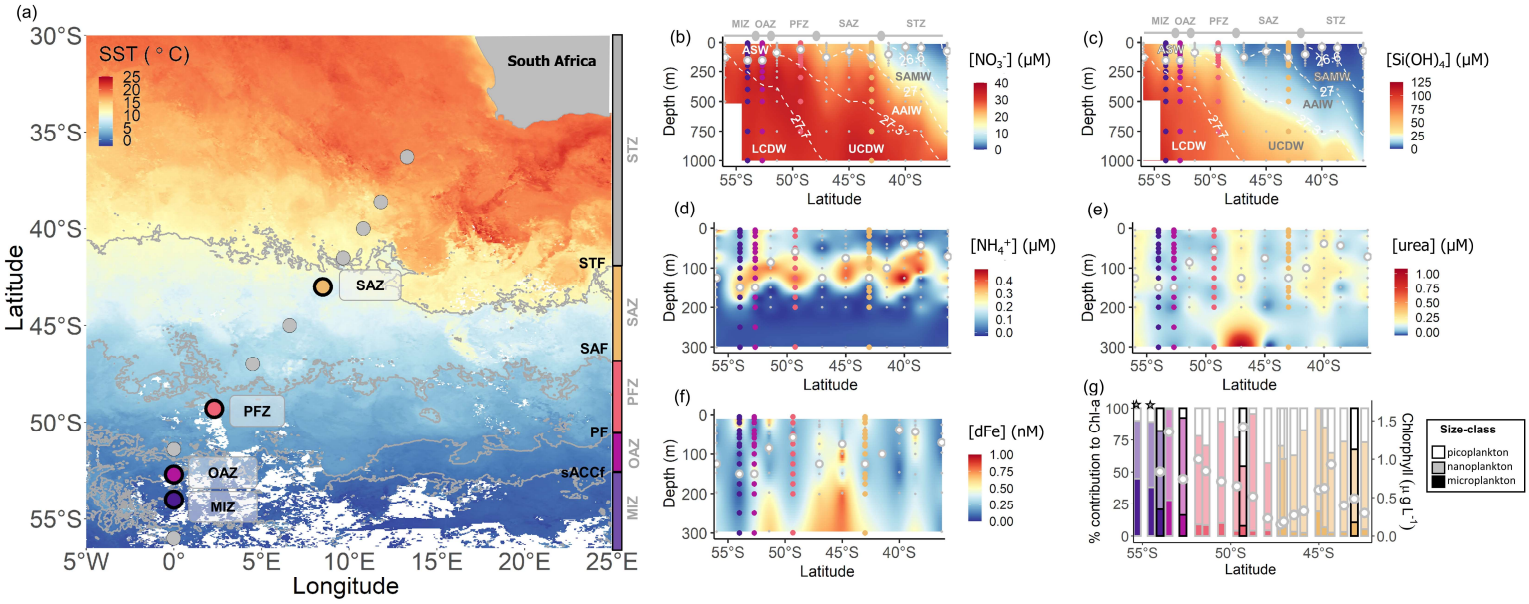


Figure 2.1. a) Map of the Atlantic sector of the Southern Ocean showing the sampling stations overlayed on the monthly averaged sea surface temperature (SST) for November 2019 (https://oceancolor.gsfc.nasa.gov/l3/). Section plots of b) nitrate concentration ($[NO_3^-]$), c) silicate concentration ($[Si(OH)_4]$), d) ammonium concentration ($[NH_4^+]$), e) urea-N concentration ([urea]), f) dissolved iron concentration ([dFe]), and a bar plot showing g) the relative contribution of each phytoplankton size-class to chlorophyll *a* (colours, primary y-axis), along with the total surface chlorophyll *a* concentration (white dots, secondary y-axis) measured for samples collected along the Good Hope line. The fronts are identified in panel (a) by the grey lines (Subtropical Front (STF), Subantarctic Front (SAF), Polar Front (PF), and southern boundary of the Antarctic Circumpolar Current Front (sACCF)) and the hydrographic zones are indicated to the right of the map by the coloured rectangles (grey – Subtropical Zone (STZ), yellow – Subantarctic Zone (SAZ), orange – Polar Frontal Zone (PFZ), pink – Open Antarctic Zone (OAZ), purple – Marginal Ice Zone (MIZ). Together, the OAZ and MIZ constitute the Antarctic Zone). The station positions are shown in panels (a-f), with the coloured circles denoting the experimental stations and the grey circles the ancillary stations. The different water masses are identified in panels (b-c) by the density contours (ASW – Antarctic Surface Water, LCDW – Lower Circumpolar Deep Water,

UCDW – Upper Circumpolar Deep Water, AAIW – Antarctic Intermediate Water, SAMW – Subantarctic Mode Water). The mixed layer depth is indicated on panels (b-f) by the white filled circles. In panel (g), the black outlined bars indicate the four experimental stations, the different coloured bars represent the different hydrographic zones, and the shading of the bars shows the different plankton size-classes (white – picoplankton, opaque – nanoplankton, solid colour – microplankton). The stars in panel (g) indicate surface chlorophyll *a* concentrations that were higher than the secondary y-axis (3.0 μg L^{-1} and 1.8 μg L^{-1} at 55.5ºS and 55ºS, respectively).

2.2. Results

2.2.1. Hydrographic and biogeochemical context

Along a transect of the Atlantic Southern Ocean between South Africa and the Marginal Ice Zone (MIZ) (the Good Hope line (Ansorge et al., 2005); 36-56ºS, occupied in early spring; Fig. 2.1a) surface-water density was highest at the southernmost station (56ºS), decreasing towards the lower latitudes (Fig. 2.1b-c) due to warming and salinification of Antarctic Surface Waters (ASW) during northward Ekman transport. The Subtropical Front (STF), Subantarctic Front (SAF), Polar Front (PF), and southern Antarctic Circumpolar Current Front (sACCF), which divide the Southern Ocean into its major hydrographic zones, were located at approximately 41°S, 47°S, 52°S, and 53°S, respectively.

The mixed layer depth (MLD) was predominantly controlled by salinity at all stations and was always deeper than the euphotic zone depth (Z_{eu}; Table A1). The deepest mixed layer was observed in the MIZ (160 m) and the shallowest in the PFZ (75 m), while Z_{eu} was similar at all stations (37.5-45 m). The rates of NPP and N and iron uptake were thus trapezoidally-integrated to the MLD rather than the Z_{eu}.

The concentrations of NO_3^- and silicate ($Si(OH)_4$) were lower in the mixed layer than the subsurface due to assimilation by phytoplankton (Fig. 2.1b-c). As expected, the surface concentrations of NO_3^- and $Si(OH)_4$ decreased northwards, consistent with a latitudinal decline in the upward nutrient supply during winter mixing, and the northward advection of surface waters and coincident assimilation of nutrients by phytoplankton(Henley et al., 2020). The highest mixed-layer NO_3^- concentrations were observed in the OAZ and MIZ (regional average of 27.4 ± 0.7 μM; n = 3 stations) while $Si(OH)_4$ was highest in the MIZ (regional average of 51.3 ± 14.4 μM; n = 2 stations). The lowest mixed-layer concentrations of NO_3^- and $Si(OH)_4$ were observed in the SAZ (regional average of 20.5 ± 1.1 μM and 5.9 ± 0.7 μM, respectively; n = 3 stations). The concentrations of regenerated N (i.e., NH_4^+ and urea-N, with the latter hereafter referred to as urea) were low in the surface, increasing with depth to reach a maximum just below Z_{eu} (Fig. 2.1d-e). Mixed-layer concentrations of NH_4^+ were highest in the OAZ (regional average of 0.26 ± 0.05 μM; n = 1

station) and lowest in the SAZ (regional average of 0.12 ± 0.09 μM; n = 3 stations), while urea concentrations were highest in the MIZ (regional average of 0.14 ± 0.05 μM; n = 2 stations) and lowest in the OAZ (regional average of 0.05 ± 0.02 μM; n = 1 station).

Mixed-layer dissolved iron concentrations ([dFe]) were generally >0.2 nM (Fig. 2.1f) at all depths and stations across the transect. The highest dFe concentration was measured in the surface of the MIZ ([dFe] = 0.75 nM at 25 m) while the average mixed-layer dFe concentration was highest in the SAZ (regional average of 0.38 ± 0.1 nM; n = 3 stations) and lowest in the OAZ (regional average of 0.26 ± 0.15 nM; n = 1 station).

2.2.2. Phytoplankton biomass and distributions

Chlorophyll *a* concentrations were highest in the mixed layer of the MIZ (average of 2.7 ± 1.1 μg L^{-1}; n = 3 stations) and lowest in the SAZ (average of 0.4 ± 0.2 μg L^{-1}; n = 3 stations), particularly near the SAF (average of 0.2 ± 0.04 μg L^{-1}; Fig. 2.1g and S1). Across the transect, chlorophyll *a* was dominated by nanoplankton, which contributed an average of 65 ± 12%. The pico- and microplankton made a smaller contribution to chlorophyll *a* (average of 25 ± 14% and 10 ± 11%, respectively), with the microplankton contribution increasing in the MIZ to 34 ± 10%.

The physicochemical conditions within each hydrographic region were generally similar, as were the phytoplankton size distributions (Fig. 2.1). We thus take each of the experimental stations to be broadly representative of the hydrographic region in which it was located. At the experimental stations, the euphotic zone-average bulk particulate organic carbon (POC) concentrations ranged from 8.1 ± 0.8 μM in the MIZ to 6.5 ± 0.4 μM in the OAZ (Fig. 2.2a), while the bulk particulate organic nitrogen (PON) concentrations ranged from 1.2 ± 0.1 μM in the PFZ to 0.9 ± 0.1 μM in the SAZ (data not shown). Biomass was dominated by the nanoplankton, which contributed an average of 68 ± 7% to total POC and 64 ± 9% to total PON across the transect. The other size-classes contributed less to biomass, with the picoplankton constituting 13 ± 6% and 21 ± 8% of the total POC and PON, respectively, and the microplankton constituting 19 ± 6% and 13 ± 6%.

The mixed-layer phytoplankton community was numerically dominated by picoplankton at all experimental stations, with picoprokaryotes being the most abundant group in the SAZ (44 ± 27% of the total phytoplankton cells counted) while picoeukaryotes dominated at the other stations (52 ± 5%) (Fig. 2.2b). We observed a southward shift in community composition, with nanoflagellates increasing in abundance relative to picoplankton south of the SAF (nanoflagellates contributed 6 ± 3% of the phytoplankton cells

counted in the SAZ versus 30 ± 5% at the other stations). The highest cell abundances were observed in the SAZ (20 054 ± 10 966 cells mL^{-1}) while the highest total biovolume was derived for the MIZ. Although diatoms were the least abundant phytoplankton group (0.8 ± 0.6% of cells on average across the transect), they contributed most to biovolume (61 ± 9%; Fig. 2.2c). The MIZ diatoms were generally more heavily-silicified Antarctic species (e.g., *Fragillariopsis* spp.), while those encountered further north, particularly in the SAZ where mixed-layer $Si(OH)_4$ concentrations were low (5.2 ± 0.4 µM at the SAZ experimental station), were smaller, weakly-silicified pennate diatoms.

The microzooplankton community was partially characterized by flow cytometry, with known mixotrophic species (ciliates and dinoflagellates) and heterotrophs containing freshly ingested prey enumerated (Fig. 2.2b). The highest abundance of mixotrophs was observed in the PFZ (41 ± 15 cells mL^{-1}), coincident with elevated biomass and low surface iron concentrations (Fig. 2.1f, 2a, and S1). The lowest abundance of mixotrophs and heterotrophs was observed in the MIZ (8 ± 4 cell mL^{-1} and 12 ± 5 cells mL^{-1}, respectively), while heterotrophs were most abundant in the SAZ (35 ± 28 cells mL^{-1}). Although both groups were similarly abundant, the mixotrophs contributed more to biovolume (Fig. 2.2c) as they were ~2.5 times larger than the heterotrophs (average biovolume of 436 ± 391 μm^3 versus 167 ± 102 μm^3).

The mesozooplankton community, characterized via microscopy, was numerically dominated by copepods (90 ± 8%) at all the experimental stations, with most of the mesozooplankton (copepods and other groups) being mature adults (83 ± 4%; Fig. 2.2d). The *in situ* and satellite chlorophyll *a* data indicate that the phytoplankton bloom had progressed the furthest in the PFZ by the time of our sampling (surface chlorophyll *a* concentration of 1.4 ug L^{-1}; Fig. 2.1g and S1). Here, we observed the lowest relative abundance of copepods (79%) while in the OAZ where the phytoplankton bloom had not progressed as far (surface chlorophyll *a* concentration of 0.7 ug L^{-1}), copepods dominated the community (97%). Overall, mesozooplankton were most abundant in the MIZ (848 cells L^{-1}), with high abundances also observed in the PFZ and OAZ (783 cells L^{-1} and 669 cells L^{-1}, respectively), and least abundant in the SAZ (99 cells L^{-1}).

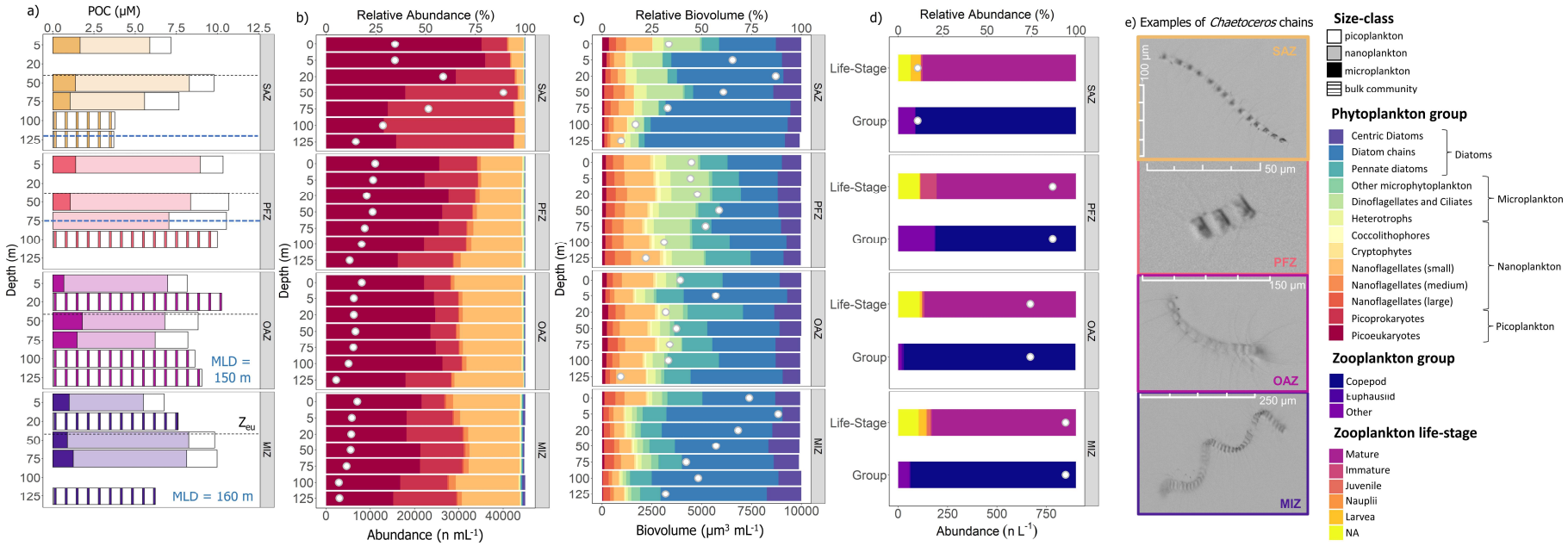


Figure 2.2. Bar plots of a) size-fractionated particulate organic carbon (POC) concentration, b) relative phytoplankton cell abundance and total cell counts between 5 m and 125 m, c) relative and total phytoplankton biovolume between 5 m and 125 m, and d) relative and total mesozooplankton cell counts from Bongo net collections (integrated surface to 200 m). Panel (e) shows images taken by CytoSense flow cytometer of the dominant *Chaetoceros* spp. chains present at the experimental stations. The stations are labelled by zone on the right-hand y-axes of all the panels. The black dashed line in panel (a) indicates the euphotic zone depth (Z_{eu}) and the blue dashed line the mixed layer depth (MLD) at the four experimental stations and the shading denotes the different plankton size-classes (white – picoplankton, opaque – nanoplankton, solid colour – microplankton). At the depths where size-fractionated POC concentrations were not measured, only the bulk values are shown (striped bars). The white dots in panels (b) and (d) indicate the total cell counts and in panel (c), the total biovolume. The different bars in panel (d) show the different mesozooplankton life-stages and main groups identified at the four experimental stations.

2.2.3. Primary production and nutrient uptake rates

The rates of NPP were similar at all experimental stations (average mixed-layer integrated rate of 66.5 ± 5.2 mmol m^{-2} d^{-1}; Fig. 2.3a and S2a; Table A1), with nanoplankton contributing most to total NPP (average of 73 ± 9% for all stations), while the picoplankton contributed 25 ± 9% and the microplankton contribution was low (2.4 ± 0.9%). The highest mixed-layer integrated rate of ρNO_3^- (i.e., new production) was measured in the MIZ (9.0 ± 0.01 mmol m^{-2} d^{-1}) and the lowest in the SAZ (4.7 ± 0.01 mmol m^{-2} d^{-1}) (Fig. 2.3b and S2b). As per NPP, the nanoplankton contributed most to total ρNO_3^- at all stations (67 ± 17%), while the average picoplankton contribution was 25 ± 16% and the microplankton contributed 8 ± 3%.

The rates of regenerated N uptake (i.e., ρNH_4^+ and ρurea) were ~1.4-times lower than ρNO_3^- (Fig. 2.3c-d and S2c-d), with ρNH_4^+ accounting for 63-93% (average of 80%) of regenerated N uptake across the transect. ρNH_4^+ and ρurea generally varied with the ambient NH_4^+ and urea concentrations, respectively. The highest mixed-layer integrated rates of ρNH_4^+ were observed in the OAZ (5.8 ± 0.04 mmol m^{-2} d^{-1}) and the lowest in the SAZ (2.7 ± 0.01 mmol m^{-2} d^{-1}). As for NPP and ρNO_3^-, the nanoplankton contributed most to total ρNH_4^+ (63 ± 12%), while the picoplankton contribution averaged 35 ± 12%, reaching a maximum in the SAZ (48 ± 13%) where picoplankton abundances were highest (Fig. 2.2b). The microplankton contribution to total ρNH_4^+ was low at all stations (2 ± 1%). In contrast to ρNO_3^- and ρNH_4^+, the highest rate of total ρurea was measured in the SAZ (1.5 ± 0.0 mmol m^{-2} d^{-1}) (Fig. 2.3d). Here, the picoplankton contributed most to urea uptake (98 ± 0.7%), with negligible contributions from the other size-classes. The lowest rates of ρurea were measured in the OAZ (0.65 ± 0.0 mmol m^{-2} d^{-1}), attributable to the nanoplankton (99 ± 0% of total ρurea). At the PFZ and MIZ stations, the nanoplankton dominated ρurea (62 ± 2.7%), with the pico– and microplankton contributing 36 ± 3% and 2 ± 0.4%, respectively.

The specific rates of carbon fixation (V_C) and N uptake ($V_{NO_3^-}, V_{NH_4^+}, V_{urea}$) were generally lowest in the SAZ and increased southwards for all size-classes (Fig. A3). As per the transport rates (NPP, ρNO_3^-, ρNH_4^+, ρurea), the specific uptake rates of regenerated N ($V_{reg\ N}$; = $V_{NH_4^+} + V_{urea}$) were lower than $V_{NO_3^-}$, and the highest specific uptake rates of all N species were associated with the picoplankton. The nano- and microplankton showed intermediate and low specific uptake rates, respectively.

The concentration of labile inorganic iron ([Fe′]) in the euphotic zone depends on the total dissolved iron concentration ([dFe]) and is also strongly affected by light, temperature, and pH (Johnson et al., 1994). The Fe′ uptake rates, determined using sub-saturating amendments of ^{55}Fe, generally tracked the Fe′ concentrations at each station and depth (Table A2). Uptake rates were highest at high light levels, consistent with enhanced photoreductive generation of Fe′ (Johnson et al., 1994), and the surface uptake

rates increased as sea surface temperatures decreased, consistent with the increased stability of reduced iron at lower seawater temperatures (Johnson et al., 1994) (Fig. A2). The highest Fe′ uptake rates were measured in the MIZ (1259.2 µmol Fe mol C^{-1} m^{-2} d^{-1}) and the lowest in the PFZ (140.5 µmol Fe mol C^{-1} m^{-2} d^{-1}) (Fig. 2.3e). In contrast to NPP and ρNO_3^-, Fe′ uptake was dominated by the picoplankton at all stations (61 ± 26%), while the nano- and microplankton contributed 19 ± 17% and 20 ± 12%, respectively.

In seawater, the concentration and composition of organically-complexed iron is generally unknown (Johnson et al., 1994). We amended seawater with the model iron siderophore Ferrioxamine-B (Fe-FOB) (1 nM final concentration) to probe saturated uptake rates. Despite this elevated concentration, the Fe-FOB uptake rates were 1-2 orders of magnitude lower than the rates of Fe′ uptake (Fig. 2.3f). The highest Fe-FOB uptake rates were measured in the SAZ (20.1 µmol Fe mol C^{-1} m^{-2} d^{-1}), coincident with the highest abundance of picoplankton and the largest biovolume of heterotrophs (Fig. 2.2b-c), while the lowest rates occurred in the PFZ (3.0 µmol Fe mol C^{-1} m^{-2} d^{-1}). The picoplankton contributed most to total Fe-FOB uptake (51 ± 32%), with the nano- and microplankton contributing 17 ± 10% and 32 ± 23%, respectively.

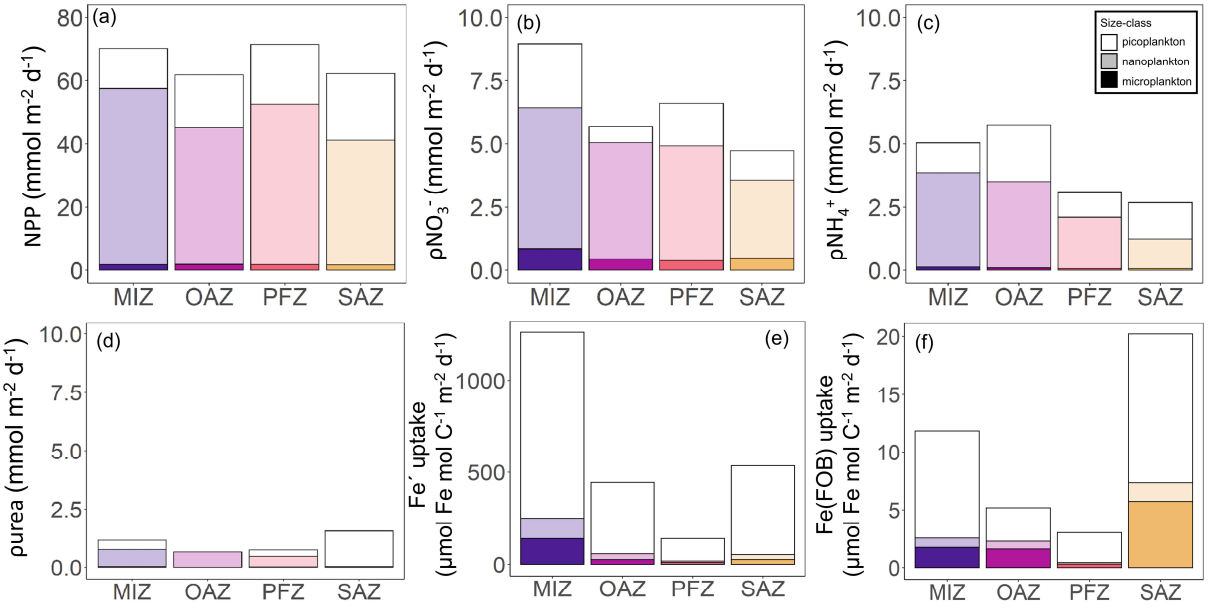


Figure 2.3. Bar plots showing the mixed-layer integrated rates of a) net primary production (NPP), b) nitrate uptake (ρNO_3^-), c) ammonium uptake (ρNH_4^+), d) urea uptake (ρurea), e) dissolved inorganic iron uptake (Fe' uptake) normalized to POC, and f) organically-complexed iron uptake (Fe(FOB) uptake) normalized to POC. The shading denotes the different plankton size-classes (white – picoplankton, opaque – nanoplankton, solid colour – microplankton).

2.2.4. Fe:C and Fe:N uptake ratios

Using the size-fractionated rates of NPP and total N (i.e., NO_3^- + NH_4^+ + urea) and iron (i.e., Fe' + Fe-FOB) uptake, we estimated the Fe:C and Fe:N uptake ratios for the three size-classes (eq. 5) (McKay et al., 2005; Strzepek et al., 2005). At all stations, the nanoplankton had the lowest Fe:C and Fe:N uptake ratios (average of 2.8 ± 2.7 µmol mol^{-1} and 18.8 ± 15.7 µmol mol^{-1}, respectively). The microplankton had the highest Fe:C uptake ratios (average of 26.4 ± 23.7 µmol mol^{-1}), while the picoplankton had the highest Fe:N uptake ratios (average of 77.8 ± 60.9 µmol mol^{-1}) (Fig. 2.4a; Table A1).

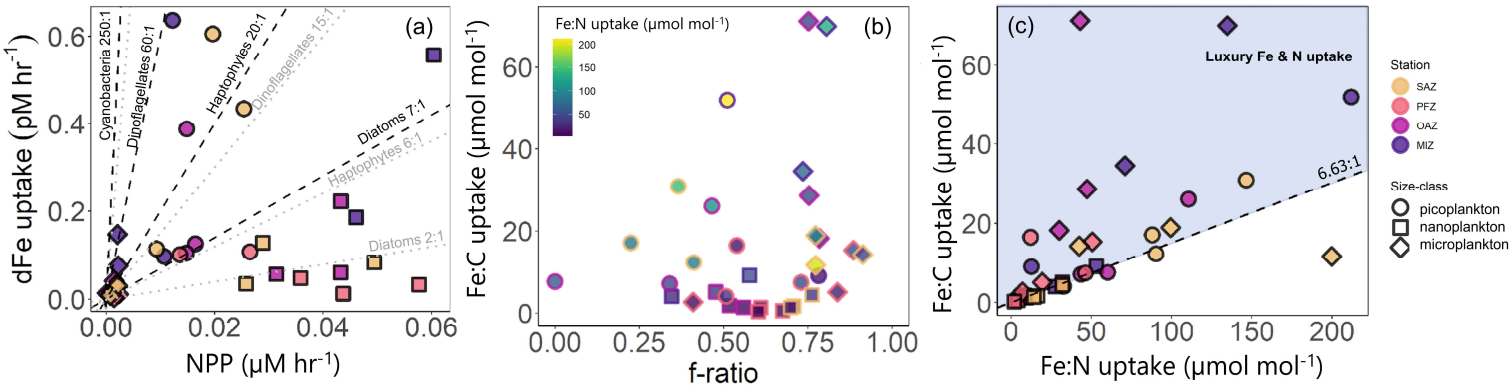


Figure 2.4. Scatter plots of a) inorganic iron (Fe') uptake versus net primary production (NPP), b) the iron-to-carbon (Fe:C) uptake ratio versus the f-ratio, and c) the Fe:C uptake ratio versus the iron-to-nitrogen (Fe:N) uptake ratio. The shapes in all panels indicate the size-classes (circle – picoplankton, square – nanoplankton, diamond – microplankton). The colours in panels (a) and (c) denote the stations (MIZ – purple, OAZ – pink, PFZ – orange, SAZ – yellow) and in panel (b), the Fe:N uptake ratios. The black dashed lines in panel (a) show literature-based average Fe:C uptake ratios (cyanobacteria – 250:1, dinoflagellates – 60:1, haptophytes – 20:1, diatoms – 7:1) and the grey dashed lines show the literature-based minimum Fe:C uptake ratios (cyanobacteria – 200:1, dinoflagellates – 15:1, haptophytes – 6:1, diatoms – 2:1) for the main phytoplankton groups identified in this study (Marchetti and Maldonado, 2016). The black dashed line in panel (c) shows the Redfield C:N ratio (6.63:1) and the blue shaded area shows the data points associated with coincident luxury iron and NO_3^- uptake.

2.2.5. Carbon export potential

We calculated the depth-integrated f-ratios (i.e., the proportion of total production fueled by NO_3^- uptake) at the experimental stations (eq. 6; Fig. 2.5a). The bulk community f-ratio was similar at all stations and averaged 0.55 ± 0.07 (range of 0.47-0.63), meaning that 55 ± 7% of the photoautotrophically produced organic carbon (NPP) was potentially exportable. The microplankton were associated with the highest f-

ratio (average of 0.75 ± 0.06; range of 0.70-0.85), while the nanoplankton f-ratio was 0.61 ± 0.08 (range of 0.52-0.71) and the picoplankton f-ratio, which varied most across the transect, averaged 0.41 ± 0.20 (range of 0.20-0.62).

To estimate the quantity of NPP that was potentially exported, we calculated total carbon export potential (i.e., mixed-layer integrated NPP × f-ratio; eq. 7; Fig. 2.5b), which was highest in the PFZ (45.0 ± 0.2 mmol m^{-2} d^{-1}) where the rates of NPP were highest and lowest in the OAZ (27.5 ± 0.1 mmol m^{-2} d^{-1}) where NPP was lowest (Fig. 2.1g, 2a, and 3a). Although the microplankton were associated with the highest f-ratios, they contributed least to carbon export potential (transect average of 4 ± 1%) because of their minor contribution to biomass and NPP. The nanoplankton contributed most to carbon export potential (transect average of 78 ± 4%) due to their large contribution to biomass and NPP.

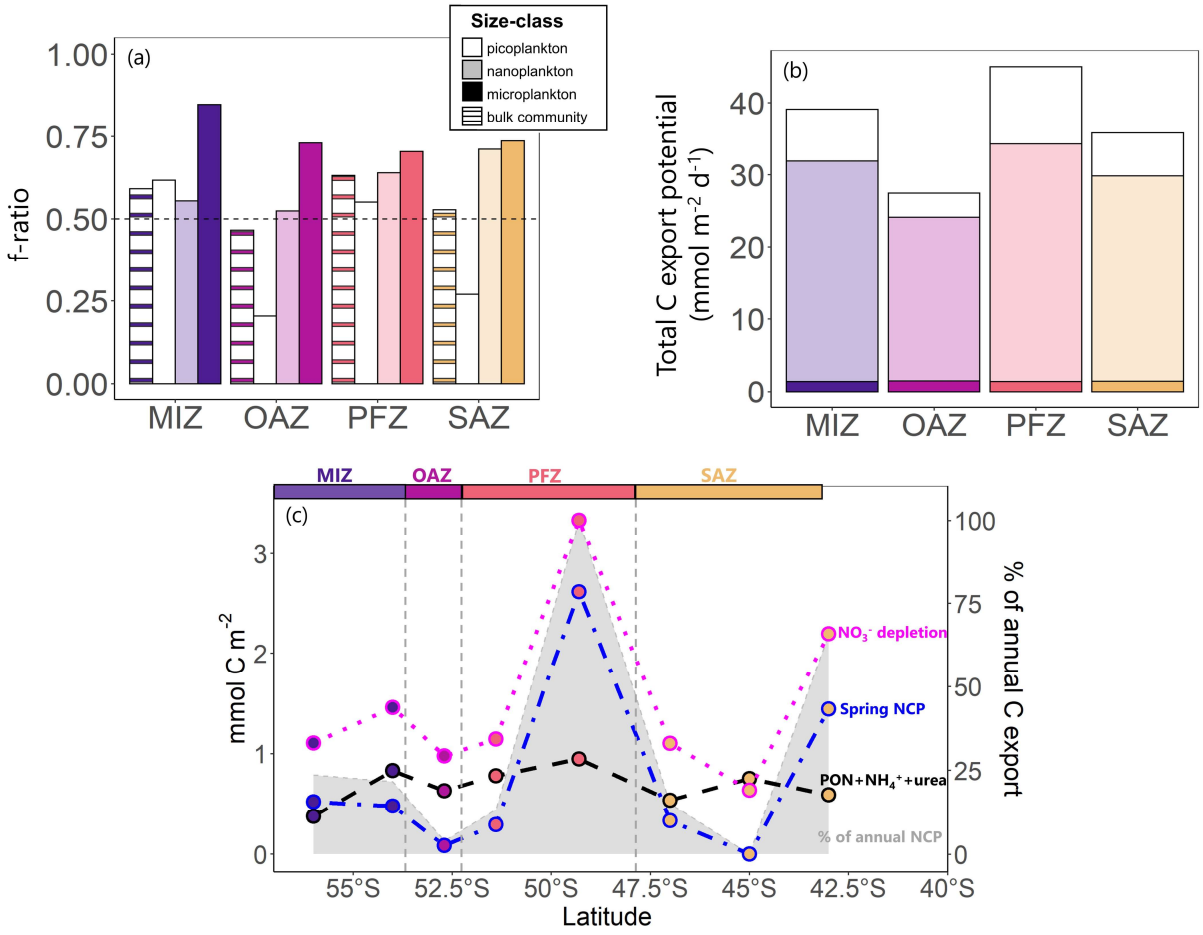


Figure 2.5. a) Bar plot of the f-ratio (i.e., proportion of total production fueled by NO_3^- uptake) for each size-class, b) bar plot showing mixed-layer integrated total carbon export potential (eq. 6), and c) carbon export estimated from mixed-layer integrated NO_3^- depletion (pink dotted line; eq. 9), mixed-layer integrated particulate organic nitrogen (PON) and regenerated N (i.e., NH_4^+ + urea) converted to carbon (i.e., (PON + NH_4^+ + urea) × C:N ratio (Johnson et al., 2022); black dashed line), estimated carbon export associated with the spring bloom (blue dash-dotted line; eq. 8), and the percent (%) of annual net community production (NCP, a measure of carbon export) measured previously (Johnson et al., 2017) that can be attributed to the spring bloom (grey shaded area). The different zones are indicated by the different colours (MIZ – purple, OAZ – pink, PFZ – orange, SAZ – yellow). The shading in panels (a) and (b) shows the different size-classes (white – picoplankton, opaque – nanoplankton, solid colour – microplankton, striped – bulk community), with the striped bars in panel (a) indicating to bulk community estimates.

2.3. Discussion

It is well-known that light and iron (and at times, $Si(OH)_4$) exert a strong control on productivity and biological carbon export across the Southern Ocean (Martin et al., 1990; Boyd et al., 2000b; Blain et al., 2007; Hoffmann et al., 2008; Sarmiento et al., 2011). In spring, the shoaling of the mixed layer alleviates light limitation, allowing phytoplankton to consume the macro- and micronutrients supplied during winter, thus initiating a bloom (Behrenfeld et al., 2016; Arteaga et al., 2020). In the open Southern Ocean, the spring bloom has been described as being dominated by large, heavily-silicified diatoms that are well-adapted to the low (albeit not limiting) iron conditions and are resistant to zooplankton grazing (Smetacek, 2000; Smetacek et al., 2004; Quéguiner, 2013; Assmy et al., 2013c). Our springtime data contradict this characterization. We observed nanoplankton (2.7-20 µm; predominantly the diatom, *Chaetoceros* spp.) dominating the phytoplankton biomass and rates of NPP and new production across all hydrographic zones of the Atlantic Southern Ocean in early spring. Below, we examine the mechanisms that allowed *Chaetoceros* to dominate the spring bloom, the implications for the seasonal and annual carbon export flux, and the consequences for the succeeding (i.e., summertime) phytoplankton communities.

2.3.1. Nanoplankton dominate biomass and productivity across the springtime Southern Ocean

Nanoplankton contributed >50% of the total phytoplankton biomass and rates of NPP and N uptake at all our experimental stations in early spring (Fig. 2.1g, 2a and 3a-d). The unequivocal dominance of this size-class was unexpected as microplankton (particularly large diatoms) have been reported to dominate Southern Ocean productivity and carbon export in spring and summer, particularly in the PFZ and Antarctic Zone (i.e., the combined OAZ and MIZ) (Tremblay et al., 2002; Deppeler and Davidson, 2017). Microplankton dominance is consistent with the basic tenets of phytoplankton ecophysiology – phytoplankton resource utilization traits typically depend on cell volume, with nutrient affinity and growth rates declining as cell volume increases (Eppley and Thomas, 1969; Finkel and Irwin, 2001; Finkel et al., 2004; Edwards et al., 2012). Large cells are thus expected to dominate when nutrients are readily available (i.e., early in the Southern Ocean growth season), while small cells should proliferate under nutrient-deplete conditions (e.g., in late summer and autumn) (Litchman, 2007; Marañón et al., 2013; Sommer et al., 2017). However, across the Atlantic Southern Ocean in spring, microplankton dominated neither biomass nor productivity.

We hypothesize that the low microplankton productivity was the consequence of two physiological constraints: 1) the greater effect of low light availability on large cells (Finkel and Irwin, 2001; Finkel et al., 2004) and 2) the fact that maximum potential growth rates generally decline with increasing cell size (Edwards et al., 2012). Across our transect, the mixed layer was always deeper than the Z_{eu} (Table A1),

often by >50 m. As such, the phytoplankton community would have experienced some degree of light limitation. The amount of light absorbed by phytoplankton decreases with increasing cell size (Sathyendranath et al., 1987; Babin et al., 1993); thus, microplankton are more prone to light limitation than pico- and nanoplankton. Light limitation likely hindered the proliferation of the microplankton, resulting in slower growth and nutrient uptake rates, and relatively low biomass (Fig. 2.1g, 2a, and S3). In addition, microplankton are physiologically unable to grow as rapidly as pico- and nanoplankton because of their larger cell volume(Edwards et al., 2012), which would have further impeded their success. By contrast, the intermediate size of the nanoplankton would have provided this group with a selective advantage, allowing them to grow more efficiently on the available resources (i.e., light and nutrients) and outcompete the microplankton. The nanoplankton also outcompeted the picoplankton, which we attribute to their capacity for high maximum nutrient uptake rates and immediate use of newly consumed nutrients for growth, by which they achieve high growth rates (Sommer, 1984; Litchman, 2007; Marañón et al., 2013). As such, the nanoplankton would have been able to rapidly consume the replete nutrients as soon as light limitation was alleviated. The physiological "sweet-spot" occupied by the nanoplankton has been hypothesized to explain their dominance across the global ocean under varying physicochemical conditions (Marañón et al., 2009; Cassar et al., 2015; Leblanc et al., 2018; Burger et al., 2020; Juranek et al., 2020) and appears to also underpin their success during the early development of the Southern Ocean spring bloom.

Nanoplankton dominance of biomass and productivity was likely also influenced by their apparently low iron requirement (average Fe:C uptake ratio of 2.8 ± 2.7 μmol mol^{-1}) relative to that of the pico- and microplankton (average Fe:C uptake ratios of 17.3 ± 14.2 μmol mol^{-1} and 26.4 ± 23.7 μmol mol^{-1}, respectively; Fig. 2.4a; Table A1). Iron availability (as inferred from iron concentration) was variable across the transect, with the highest concentrations measured in the MIZ and the lowest in the OAZ (Fig. 2.1f). However, the ratio in which iron is supplied to the surface layer relative to NO_3^- is more important than the absolute iron flux, with seawater Fe:NO_3^- ratios less than 10 μmol mol^{-1} thought to limit phytoplankton productivity (Croot et al., 2007; Janssen et al., 2020). Across our transect, the mixed layer seawater Fe:NO_3^- ratios ranged from 3 to 27 μmol mol^{-1}, indicating that the supply of iron at some stations (i.e., in the OAZ and MIZ) was insufficient to sustain NO_3^- uptake. Assuming balanced phytoplankton growth (i.e., a C:N uptake ratio of 6.7, 7.5, and 7.2 for the SAZ, PFZ and AZ, respectively, as has been recently inferred for phytoplankton biomass in the Atlantic sector (Johnson et al., 2022)), we can assess whether the mixed layer iron concentrations could sustain the Fe:C uptake ratios of the different phytoplankton size-classes. Multiplying our measured seawater Fe:NO_3^- ratios by the C:N ratios yields theoretical Fe:C uptake ratios of 0.4 to 4.2 μmol mol^{-1}. Based on the Fe:C uptake ratios derived for the different size-classes (Fig. 2.4a;

Table A1), the mixed-layer iron concentrations were sufficient to sustain nanoplankton growth but not pico- or microplankton productivity. This observation further explains why the nanoplankton were able to thrive at the onset of the spring bloom relative to the other phytoplankton size-classes.

Despite the overlapping size of the diverse nanoplankton cells present during spring (including nanoflagellates, coccolithophores, cryptophytes, and small diatoms; Fig. 2.2b-c), each group has distinctive functional traits, resulting in variable success under different physicochemical conditions (Edwards et al., 2012). For example, diatoms generally grow faster than other taxa and thrive under high-nutrient, turbulent conditions (Margalef, 1978; Edwards et al., 2012; Glibert et al., 2016b). By contrast, nanoflagellates are better adapted to low-nutrient, stable conditions, with some species even capable of mixotrophy (Flynn et al., 2013). Mixotrophy allows nanoflagellates to persist for the duration of phytoplankton blooms as they can alternate between autotrophy and heterotrophy depending on light and nutrient availability (Margalef, 1978; Berge et al., 2016; Ward and Follows, 2016). The grazers identified during our sampling were mostly microzooplankton and copepods (Fig. 2.2c-d), which preferentially graze on nanophytoplankton (Smetacek et al., 2004). Because microzooplankton and phytoplankton have similar lifespans (days), the former can regulate the biomass of the latter (Kiørboe, 1993). By contrast, mesozooplankton (the dominant grazers of microphytoplankton) have a more complex lifecycle and a significantly longer lifespan (weeks to months), such that large phytoplankton can initially out-grow them (Kiørboe, 1993; Cermeño et al., 2006). One might thus expect the nanophytoplankton biomass in the springtime Southern Ocean to have been regulated by the co-occurring microzooplankton, thereby favoring the proliferation of microphytoplankton, yet this is not what we observed. We propose that the diversity of the nanoplankton helped this size-class dominate the biomass and rates of NPP and new production, with some nanophytoplankton groups (e.g., nanoflagellates) being more readily grazed upon than others (e.g., small diatoms; Smetacek et al., 2004). Understanding the contribution to the nanoplankton of different phytoplankton groups, particularly that of the dominant species, will yield further insights into the success of this size-class during the Southern Ocean spring bloom.

2.3.2. The springtime nanoplankton community is dominated by *Chaetoceros* spp.

Phytoplankton biovolume was dominated by diatoms at all stations, with diatom chains contributing an average of 43 ± 22% of the total biovolume across the transect (Fig. 2.2c). These diatom chains largely comprised *Chaetoceros* spp., the individual cells of which generally fell into the nanoplankton size-class (i.e., <20 μm; Fig. 2.2e). *Chaetoceros* typically dominates in regions that experience unpredictable but rapid alleviation of macronutrient- (e.g., upwelling regions) (Fawcett and Ward, 2011; Burger et al., 2020) and/or micronutrient limitation (e.g., in the vicinity of Subantarctic Islands) (Assmy et al., 2013a), and is known

to employ a "boom-and-bust" growth strategy (Smetacek et al., 2004; Assmy et al., 2013c). This strategy involves a period of accelerated growth (boom) that is followed by a rapid decline in the population due to increased competition for diminishing resources and/or enhanced grazing pressure (bust) (Doebeli et al., 2021). When light limitation is alleviated, *Chaetoceros* responds rapidly and due to its relatively small size, is able to outcompete the slower-growing larger phytoplankton for nutrients (Litchman, 2007; Burger et al., 2020b). *Chaetoceros* can also outcompete the smaller phytoplankton because it is better adapted to withstand turbulent conditions and is less palatable to grazers (Margalef, 1978; Malone, 1980; Smetacek et al., 2004). Recent studies have suggested that the open Southern Ocean spring bloom is characterized by a period of rapid phytoplankton growth during which the community outpaces its dominant grazers, with the highest growth rates achieved before the biomass concentrations reach a maximum (Behrenfeld et al., 2016; Arteaga et al., 2020). The subsequent decline in the phytoplankton population is controlled by grazing pressure, with the period of maximum biomass accumulation also associated with declining growth rates (Arteaga et al., 2020). Our observations are consistent with this suggestion insofar as the *Chaetoceros* bloom involves a period of rapid growth during which potential grazers are outpaced, followed by a period of decline driven by increased grazing pressure (see section 2.3.3 below). We thus propose that the boom-and-bust behaviour of *Chaetoceros* controls the evolution of the Southern Ocean's spring bloom, with both bottom-up and top-down controls rendering this growth strategy favourable.

We suggest that the *Chaetoceros* boom was facilitated, at least in part, by the seemingly low iron requirement of these diatoms. Since *Chaetoceros* dominated total nanoplankton biovolume, we use the nanoplankton Fe:C uptake ratio as representative of *Chaetoceros*. The nanoplankton Fe:C uptake ratio was much lower than that of the pico- and microplankton (Fig. 2.4a; Table A1), which we take as evidence that *Chaetoceros* is well-adapted to the perennially-low iron conditions of the open Southern Ocean (Klunder et al., 2011; Tagliabue et al., 2012; Mtshali et al., 2019). Additionally, the nanoplankton Fe:C uptake ratios did not increase as the f-ratio increased (i.e., as the proportion of NO_3^- uptake relative to total N uptake increased; Fig. 2.4b). This finding is unexpected as NO_3^- assimilation requires considerably more iron than regenerated N consumption due to the high iron requirement of the nitrate and nitrite reductase enzymes (Morel et al., 1991; Cochlan, 2008). Moreover, NO_3^- assimilation has been shown to be associated with a Fe:C uptake ratio that is ~1.8 times higher than that of regenerated N consumption (Raven, 1988; Maldonado and Price, 1996). An increase in the f-ratio should thus have coincided with an increased iron requirement and consequently, an increase in the Fe:C uptake ratio.

The invariant nanoplankton Fe:C uptake ratios indicate that *Chaetoceros* was either using previously stored iron for NO_3^- assimilation and/or operating at a minimum Fe:C quota. Since vacuole-stored iron is generally

used by centric diatoms only when they are iron-limited (Cohen et al., 2017; Lampe et al., 2018), it is unlikely that the near-constant Fe:C ratios of *Chaetoceros* were due to their use of internally-stored iron. The idea that phytoplankton were not strongly iron-limited at the time of our sampling is supported by the observation that microplankton in the Antarctic Zone were engaging in luxury iron (and NO_3^-) uptake (Fig. 2.4c). Under balanced growth conditions, the Fe:C uptake ratio of phytoplankton should equal their Fe:N uptake ratio × C:N ratio (Johnson et al., 2022). However, the Antarctic microplankton Fe:C uptake ratios were roughly four-times higher than expected from the Fe:N uptake ratios (i.e., data falling above the dashed line in Fig. 2.4c), consistent with luxury iron and NO_3^- uptake. Phytoplankton consumption of iron in excess of their immediate metabolic requirements is only feasible when mixed-layer iron concentrations are not limiting. Co-occurring luxury iron and NO_3^- uptake has been observed for several Southern Ocean diatom species under conditions of elevated iron (Sunda and Huntsman, 1995; Hoffmann et al., 2006); the stored nutrients allow these species to continue growing later in the season when iron (and therefore NO_3^-) becomes severely limiting (Sunda and Huntsman, 1995; Hoffmann et al., 2006; Marchetti and Cassar, 2009) (see section 2.3.4 below).

The microplankton community in the Antarctic Zone was dominated by both pennate and centric diatoms (Fig. 2.2c). It is likely that both these groups were engaging in luxury iron and NO_3^- uptake as both possess a variety of iron and NO_3^- storage mechanisms (Sunda and Huntsman, 1995; Hoffmann et al., 2006). If the larger diatoms were consuming excess iron, coupled with the fact that the ambient iron concentrations were still relatively high at the time of sampling, it is highly unlikely that the nanoplankton-sized diatoms were using stored iron. Instead, we hypothesize that smaller diatoms are extremely well-adapted to low iron conditions and have therefore reduced their iron requirement, assimilating iron and fixing carbon in a particularly low ratio. Previous studies have shown that Southern Ocean *Chaetoceros* are plastic in their Fe:C uptake ratios, reducing them by up to 60% under low iron conditions akin to those observed here (Fig. 2.1f) (Petrou et al., 2014; Bozzato et al., 2021). The low measured Fe:C uptake ratios of the nanoplankton thus provide insights into the adaptation of Southern Ocean *Chaetoceros* to their environment. That they apparently do not increase their iron requirement during NO_3^- uptake, even when iron concentrations are relatively high, gives them a further competitive advantage over other Southern Ocean phytoplankton (including other diatoms) during the spring bloom.

We suggest that nanoplankton-sized *Chaetoceros* spp. occupy a unique ecological niche in the open Southern Ocean, as in other environments (Fawcett and Ward, 2011; Assmy et al., 2013c, a; Burger et al., 2020b). Individual *Chaetoceros* spp. cells have all the advantages inherent to being relatively small, while their ability to form long (>50 µm) spiny chains (Fig. 2.2e) also endows them with beneficial microplankton

characteristics. That they can occupy both size-classes further selects for *Chaetoceros* dominance during the spring bloom. The nanoplankton-sized cells were able to grow rapidly under low-light conditions, in contrast to the microplankton (Fig. A3). At the same time, chain formation allowed *Chaetoceros* to avoid losses due to grazing and mixing, unlike the picoplankton and non-colony-forming nanoplankton (Bergkvist et al., 2012). We suggest that this size duality helps to explain how *Chaetoceros* was able to dominate the biomass, productivity, and NO_3^- uptake rates across the large physicochemical gradients that characterized the Atlantic Southern Ocean in spring.

2.3.3. Implications of the boom-and-bust lifestyle for carbon export

Using NPP and the f-ratio estimates, we calculate a mixed layer-integrated total carbon export potential of 35.8 ± 0.09 mmol C m^{-2} d^{-1}, 45.0 ± 0.09 mmol C m^{-2} d^{-1}, 27.5 ± 0.08 mmol C m^{-2} d^{-1}, and 39.1 ± 0.06 mmol C m^{-2} d^{-1} for the SAZ, PFZ, OAZ and MIZ, respectively (eq. 6; Fig. 2.6b). These estimates are high compared to previous summertime values reported for the open Atlantic Southern Ocean derived using the same approach (summertime average of 16.9 ± 13.2 mmol C m^{-2} d^{-1}) (Mdutyana et al., 2020 and references therein), which indicates that spring is an important season for carbon export, as suggested by Takahashi et al. (2012) from measurements of Southern Ocean air-sea CO_2 fluxes.

At the time of our sampling, the mixed layer NO_3^- pool had declined by an average of 251.9 ± 134 mmol m^{-2} (range of 96.5-505.5 mmol m^{-2}) relative to that available following winter mixing (eq. 9). Assuming that the decrease in mixed-layer NO_3^- was entirely due to assimilation by phytoplankton, the amount of NO_3^- removed must equal the mixed layer PON and regenerated N concentrations plus the quantity of N exported from the mixed layer. We estimate that an average of 125.8 ± 120.3 mmol N m^{-2} was exported between the beginning of the growth season and our sampling. Using phytoplankton C:N ratios recently estimated (Johnson et al., 2022) for each zone, we calculate that 0-2.6 mol C m^{-2} (Fig. 2.6c; blue dashed-dotted line) had been exported by mid-November (~2.5 months since maximum mixed-layer NO_3^- recharge). If we instead use the Redfield C:N ratio of 6.6, our estimates decrease slightly to 0-2.3 mol C m^{-2}. Previous estimates of net community production (NCP) from seasonal NO_3^- depletion indicate that across the Atlantic Southern Ocean, 2.2 ± 1.6 mol C m^{-2} are exported annually and that interannual variability is low(Johnson et al., 2017). Comparing our springtime estimates to these annual values suggests that 30 ± 35% (0-100%) of the carbon export from the Atlantic Southern Ocean mixed layer occurred during the spring bloom (Fig. 2.6c; grey shaded area). We hypothesize that this elevated carbon export is largely driven by *Chaetoceros* spp., with their boom-and-bust lifestyle resulting in a large export event triggered by various bottom-up and top-down processes.

The senescence of *Chaetoceros* blooms can be initiated by bottom-up processes such as iron limitation and/or top-down processes such as viral-lysis and grazing by micro- (e.g., ciliates) and mesozooplankton (e.g., copepods and krill) (Smetacek et al., 2004; Tréguer et al., 2017). Senescence causes *Chaetoceros* chains to form large aggregates and/or resting spores that rapidly sink out of the upper water column, driving large carbon export events (Rembauville et al., 2016; Tréguer et al., 2017). The aftermath of *Chaetoceros* senescence was apparent at the PFZ experimental station where the *in situ* and satellite chlorophyll *a* data indicate that the bloom had progressed the furthest (Fig. 2.1g and S1). Here, the relative contribution of diatom chains to biovolume was lowest (mixed-layer average of 30.0 ± 6.9% versus 46.6 ± 14.9% at the other stations) and the community had shifted towards flagellates and mixotrophs (i.e., nanoflagellates, dinoflagellates, and mixotrophic ciliates; Fig. 2.2c). Additionally, the mesozooplankton community comprised proportionally more adults and late-stage juveniles than were present at the other stations (Fig. 2.2d), likely the result of prolonged food availability associated with a more developed plankton community. Furthermore, low mixed-layer iron concentrations and the lowest iron uptake rates were measured at the PFZ station (Fig. 2.1f and 3d-e), and mixed-layer NO_3^- had been most strongly depleted (by 506 mmol N m^{-2} versus 216 ± 94 mmol N m^{-2} at the other stations).

The satellite chlorophyll *a* data show that the spring bloom at the PFZ experimental station was initiated in October (Fig. A1). At the adjacent PFZ station (i.e., where rate experiments were not conducted; Fig. 2.1), the bloom had not progressed as far, evidenced by the lower mixed-layer chlorophyll *a* concentration that coincided with a deeper mixed layer and elevated mixed-layer iron concentration. Assuming a similarly high initial mixed-layer iron concentration at the PFZ experimental station, we estimate that *Chaetoceros* consumed the available iron to depletion in three weeks (i.e., October to the time of sampling). Moreover, we hypothesize that as soon as severe iron limitation set in (i.e., [dFe] ≤0.2 nM and seawater $Fe:NO_3^-$ ≤10 μmol mol^{-1}; the conditions observed at the time of sampling; Fig. 2.1f), the abundance of *Chaetoceros* declined and senescence was triggered. This decline is evidenced by the increased contribution of mixotrophs and flagellates at this station while the phytoplankton biomass at the adjacent PFZ station was still strongly dominated by diatoms. The contrast between the two PFZ stations demonstrates how rapidly *Chaetoceros* can consume the available iron and increase its biomass in response to the alleviation of light limitation.

The period of maximum phytoplankton biomass has long been (mis)interpreted as the period of maximum phytoplankton productivity in the Southern Ocean (Sverdrup, 1953; Uchida et al., 2019). Our study shows, in agreement with recent work (Arteaga et al., 2020), that although spring is not the season of maximum biomass accumulation (Fig. A1), it is nonetheless a period of elevated NPP and biological carbon export.

The bloom and subsequent senescence of *Chaetoceros* would have facilitated a large carbon export event (Assmy et al., 2013), after which the phytoplankton community likely shifted to one dominated by heavily-silicified large diatoms and flagellates (e.g., *Fragilariopsis* and dinoflagellates; as observed at the PFZ experimental station; Fig. 2.2c). The shift towards these taxa may inhibit carbon export. Heavily-silicified diatom species that persist in the mixed layer throughout the growth season sequester less carbon per mole of bSi than *Chaetoceros* (Assmy et al., 2013; Tréguer et al., 2017). Indeed, these large diatoms are considered bSi rather than carbon exporters as their persistence in the surface layer leads to *in situ* recycling of their cellular contents and ultimately, to the export of carbon-poor frustules(Assmy et al., 2013c; Tréguer et al., 2017). The shift to flagellate dominance also dampens carbon export potential as these phytoplankton preferentially assimilate regenerated N under iron-deplete conditions (which, in a mass balance sense, yields no net CO_2 removal (Dugdale and Goering, 1967)). These flagellates are also readily grazed by micro- and mesozooplankton (Smetacek et al., 2004), which enhances carbon (and nutrient) recycling in the mixed layer (Legendre and Le Fevre, 1995; Michaels and Silver, 1988). As such, the period of highest biomass accumulation in the Southern Ocean (i.e., mid- to late-summer; Fig. A1) may not be associated with the highest carbon export since the summertime export flux will comprise proportionally more large, heavily-silicified diatoms that are inefficient carbon exporters (Assmy et al., 2013; Tréguer et al., 2017). This scenario contrasts with the dynamics of the *Chaetoceros* bloom, where rapid biomass accumulation appears tightly coupled with carbon export.

2.3.4. Implications of the spring *Chaetoceros* bloom for phytoplankton community composition and carbon export potential in summer

The Southern Ocean phytoplankton community has been observed to change over the growth season in response to synergistic bottom-up and top-down controls (Quéguiner, 2013; Petrou et al., 2016). Below, we place our springtime data into a broader temporal context by synthesizing the existing observations available for all seasons (Fig. 2.6). For the Southern Ocean as a whole, our observations show that the springtime *Chaetoceros* bloom rapidly depletes mixed-layer iron, likely causing iron limitation of the succeeding summertime community. This limitation should favour phytoplankton groups capable of accessing iron by other means (e.g., stored intracellularly, via the consumption of organically-bound iron, and/or through phagotrophy) (Marchetti and Cassar, 2009; Nodwell and Price, 2001; Stukel et al., 2011). At the same time, the meridional gradient in $Si(OH)_4$ availability drives a divergent pattern in phytoplankton community succession north and south of the SAF (Hoffmann et al., 2006). In the SAZ, the already-low mixed layer $Si(OH)_4$ concentrations are rapidly exhausted by *Chaetoceros* in spring (Fig. 2.1c), resulting in the growth of non-siliceous phytoplankton such as flagellates and haptophytes, as well as small, weakly-silicified diatoms (e.g., *Pseudo-nitzschia*) (Hoffmann et al., 2006; Quéguiner, 2013). By contrast, south of

the SAF, $Si(OH)_4$ concentrations are perennially high, and the phytoplankton community shifts from *Chaetoceros* in spring to slow-growing, heavily-silicified diatoms (e.g., *Fragilariopsis*) in summer (Quéguiner, 2013). While $Si(OH)_4$ availability appears to dictate the post-spring-bloom geography of diatoms across the Southern Ocean (Hoffmann et al., 2006), other drivers (e.g., iron, light, grazing) will also structure the summertime phytoplankton community. Below, we address the apparent influence of these drivers in each hydrographic zone, then consider the effects of the resultant phytoplankton communities on the biological pump (both directly via the sinking flux and indirectly in the framework of the new production paradigm).

Subantarctic Zone

As the growth season progresses, the phytoplankton community in the SAZ shifts from centric diatoms to flagellates and haptophytes as a result of $Si(OH)_4$ limitation (Fig. 2.6a) (Hoffmann et al., 2006). This shift facilitates increased iron recycling as grazing on flagellates and haptophytes by copepods, the dominant grazers (Fig. 2.2d) (Smetacek et al., 2004), immediately releases up to 50% of their iron into the mixed layer (Møller et al., 2003). In addition, the faecal pellets produced by zooplankton grazing on flagellates and haptophytes sink more slowly than those produced from predation on diatoms, allowing the faecal pellets to be remineralised in the mixed layer and increasing the concentration of recycled iron (Feinberg and Dam, 1998). Nonetheless, iron still becomes limiting in the SAZ by mid- to late-summer (Tagliabue et al., 2014; Ryan-Keogh et al., 2018; Mtshali et al., 2019), driving a shift towards small cells (including the picoprokaryote, *Synechococcus*) and increased mixotrophy (Fig. 2.6a) (Smith et al., 2022). Although small cells appear to have a relatively high iron requirement (Fig. 2.3e-f and 4a) (Nodwell and Price, 2001; Marchetti and Maldonado, 2016), their success is the result of two ecological advantages: 1) their higher surface area-to-volume ratio, which enables them to access low concentrations of nutrients(Edwards et al., 2012), and 2) in the case of *Synechococcus*, the production of siderophores, which allows this taxa to acquire organically-bound iron (Fig. 2.3f) (Nodwell and Price, 2001; Marchetti and Maldonado, 2016). These factors select for picoplankton over larger cells when iron concentrations become severely limiting (Nodwell and Price, 2001). The concurrent shift towards mixotrophs occurs because this group can acquire iron directly via phagotrophy (Stukel et al., 2011). Indeed, Berge et al. (2014) modelled the effect of nutrient limitation on mixotrophs and showed a shift towards phagotrophy over autotrophy when light and prey are abundant but essential nutrients are limiting – conditions characteristic of the summertime Southern Ocean.

The shift towards smaller phytoplankton upregulates the microbial loop, increasing N (and carbon) recycling as these phytoplankton sink slowly and are generally remineralised within the mixed layer (Legendre and Le Fevre, 1995; Michaels and Silver, 1988). In addition, microzooplankton, the dominant

grazers of small phytoplankton, do not migrate below the mixed layer and produce slow-sinking faecal pellets (Stoecker, 1984) such that their excretions are also recycled within the mixed layer (Poulsen and Iversen, 2008). In contrast, a shift to mixotrophs may decrease mixed layer N (and carbon) recycling as they enhance the transfer of biomass (mainly that of bacteria and small phytoplankton) to higher trophic levels (Ward and Follows, 2016). Although this transfer lengthens the food chain, recent modelling studies have shown that accounting for mixotrophy can substantially enhance the sinking flux, particularly in oligotrophic regions (Ward and Follows, 2016). The contribution of mixotrophs to the total phytoplankton community across the open Southern Ocean is still unknown (Stoecker et al., 2016), yet even if they do increase carbon and N export, their contribution is likely small relative to the spring *Chaetoceros* bloom given their perennially low abundance (Edwards, 2019).

During spring and early-summer, large blooms in the SAZ provide organic matter that fuels enhanced remineralization in late-summer and autumn (El-Sayed, 1984). High fluxes of recycled N coincident with low iron availability favour regenerated production as phytoplankton NH_4^+ assimilation has no direct iron requirement (Raven, 1988). In the framework of the new production paradigm, this shift from NO_3^- to recycled N uptake decreases carbon export potential in the SAZ (Lourey et al., 2003). Furthermore, the dominance of small, slow-sinking phytoplankton directly decreases the export flux as these cells largely remain within the mixed layer (Legendre and Le Fevre, 1995; Michaels and Silver, 1988). The shift from *Chaetoceros* to small phytoplankton in the SAZ therefore weakens the biological pump over the summer, noting that the coincident increase in mixotrophy may partially offset this decline.

Polar Frontal Zone

The post-spring bloom phytoplankton community in the PFZ has been described as the most diverse of the Southern Ocean (Quéguiner, 2013). This elevated diversity occurs because the PFZ is hydrographically dynamic (Sokolov and Rintoul, 2007), which limits the dominance of one phytoplankton species or group over another since no single group can sustain elevated growth or nutrient uptake rates under such variable conditions (Hutchinson, 1961). In spring, the elevated mixed-layer iron and $Si(OH)_4$ concentrations may favour luxury iron uptake by large diatoms (Sunda and Huntsman, 1995; Marchetti et al., 2008), which, combined with the perennially high $Si(OH)_4$ concentrations, allows these diatoms to persist into late-summer and autumn(Hoffmann et al., 2008) (Fig. 2.6b). Coincidently, the PFZ hosts some of the largest spring and summer blooms of the open Southern Ocean (Quéguiner, 2013). The biomass thus produced fuels heterotrophy in late-summer, enhancing mixed-layer N recycling (Goeyens et al., 1995; Semeneh et al., 1998). The elevated NH_4^+ availability favours the proliferation of small phytoplankton (such as nanoflagellates), the grazing of which by zooplankton intensifies iron recycling (Møller et al., 2003), as in

the SAZ. Rapid recycling of both N and iron allows small phytoplankton to persist throughout the growth season and by its end, the PFZ hosts a mixed community of small phytoplankton, mixotrophs, and heavily-silicified diatoms (Quéguiner, 2013).

This mixed community facilitates two dominant export regimes: 1) elevated export associated with heavily-silicified diatoms (Assmy et al., 2013c; Quéguiner, 2013; Tréguer et al., 2017) and 2) low export (and f-ratios) due to enhanced mixed-layer recycling and the proliferation of small phytoplankton (Christaki et al., 2021). The PFZ is considered a region of high export, with the flux comprising mainly bSi from the large, heavily-silicified diatoms that dominate surface waters in late-summer and autumn (Fig. 2.6b) (Assmy et al., 2013b; Quéguiner, 2013; Tréguer et al., 2017). These diatoms are inherently more silicified than other species (bSi-to-carbon ratio of ~0.3:1, versus 0.15:1) and consume proportionally more $Si(OH)_4$ relative to the amount of carbon fixed under conditions of iron limitation (>>0.3:1) (Assmy et al., 2013b). Persisting in the mixed layer results in the loss of carbon from these cells (Assmy et al., 2013b). As such, while heavily-silicified diatoms dominate the bSi flux, their contribution to carbon export is low, particularly compared to carbon-rich diatom species such as *Chaetoceros* (Assmy et al., 2013a; Quéguiner, 2013; Tréguer et al., 2017). At the same time, small phytoplankton in the PFZ are associated with increased N and iron recycling, as in the SAZ, which decreases the regional f-ratio (Dugdale and Goering, 1967a; Lourey et al., 2003; Glibert et al., 2016b). Moreover, small phytoplankton are less ballasted, sink more slowly, and are more likely to be grazed than diatoms (Legendre and Le Fevre, 1995; Michaels and Silver, 1988), such that their direct contribution to carbon export is also low. Both of the major phytoplankton communities that emerge in the PFZ following the *Chaetoceros* bloom thus weaken carbon export, even though the heavily-silicified diatoms are still associated with a large sinking flux.

Antarctic Zone

The summertime phytoplankton community in the Antarctic Zone (OAZ and MIZ) is predominantly composed of large, heavily-silicified diatom species (Fig. 2.6c-d) (Quéguiner, 2013). These species persist from the spring (Fig. 2.2c) when they are able to consume iron in excess of their immediate requirements and store it for later use (Sunda and Huntsman, 1995; Hoffmann et al., 2006). Large diatoms such as *Fragilariopsis* and *Thalassiosira* are capable of substantial iron storage (Marchetti et al., 2008; Cohen et al., 2017; Lampe et al., 2019), although the two groups (i.e., pennates and centrics) employ different storage mechanisms. Pennate diatoms store excess iron intracellularly using the protein ferritin (Marchetti et al., 2008), while centric diatoms appear to store iron in their vacuoles (Cohen et al., 2017; Lampe et al., 2018). The varied iron storage mechanisms result in different cellular lifespans, with pennate diatoms outlasting centrics, in part because ferritin is a more effective iron storage mechanism (Twining et al., 2021). Indeed,

it has been suggested that ferritin allows for the storage of >4000 atoms of iron, which can support up to six cell divisions by pennate diatoms growing on NO_3^- (Twining et al., 2021). Using our maximum microplankton growth rate of 0.09 d^{-1} (average V_C determined for microplankton in the OAZ and MIZ), we calculate that it would take ~7.7 days for the microplankton to undergo one cell division (i.e., ln(2)/0.09 d^{-1} = 7.7 days). Assuming that the pennate diatoms were growing at this rate, then the iron stored in ferritin could have supported their growth for roughly 1.5 months (i.e., 7.7 days per cell division × six doublings = 46 days). We conclude that the iron storage mechanism employed by pennate diatoms explains their dominance over other phytoplankton groups in the late-summer Antarctic Zone (Quéguiner, 2013).

The dominance of diatoms in the Antarctic Zone (*Chaetoceros* in spring and pennate species in summer and autumn) impedes the growth of other phytoplankton groups during periods of iron limitation. Zooplankton grazing on diatoms, particularly heavily-silicified species, facilitates low rates of mixed-layer iron recycling because the bSi frustules remain intact as they pass through the zooplankton digestive system (Assmy et al., 2013c). As such, the iron in diatom frustules is efficiently exported from the mixed layer in rapidly sinking faecal pellets (Smetacek, 2000; Wright et al., 2010) instead of being recycled in situ, as occurs when zooplankton graze on non-silicified phytoplankton (e.g., nanoflagellates) (Feinberg and Dam, 1998). The Antarctic Zone is therefore characterized by low rates of mixed-layer iron recycling, which limits the growth of phytoplankton that are unable to store iron or consume organically-bound iron (Fig. 2.6c-d) (Marchetti and Maldonado, 2016).

While there are clear similarities in the phenology of the OAZ and MIZ, differences in the successional trends of their phytoplankton communities have also been observed. The MIZ is strongly influenced by the seasonal growth and melt of sea ice, in contrast to OAZ surface waters that remain ice-free year-round. Sea-ice melt introduces buoyancy that causes a rapid shoaling of the MIZ mixed layer, alleviating phytoplankton from light limitation and driving intense blooms such as the one we observed in spring (Fig. 2.1g and S1) (El-Sayed, 1984; Buesseler et al., 2003). As the season progresses, continued sea-ice decline exposes MIZ surface waters to enhanced wind-driven mixing that deepens the mixed layer into the late-summer, in contrast to the other Southern Ocean zones (Fig. 2.6 dashed blue lines) (Buesseler et al., 2003). Mixed layer deepening eventually causes light limitation of the MIZ phytoplankton community, driving a shift towards species adapted to low-light conditions such as *Phaeocystis antarctica* (Petrou et al., 2016). In addition to its low-light tolerance, *P. antarctica* can occur either as single cells or colonies. The colonies are generally more abundant later in the season as they can store iron within their mucosal matrix, allowing them to persist when ambient iron becomes limiting (Schoemann et al., 2005a). *P. antarctica* can also increase the size of their colonies when they experience grazing pressure and are thus less readily grazed upon than

other phytoplankton groups (Schoemann et al., 2005a). These adaptations allow *P. antarctica* colonies to survive in the MIZ following the decline of the diatom bloom (Fig. 2.6d) (Petrou et al., 2016). *P. antarctica* is rare in the other hydrographic zones where the mixed layer shoals rather than deepens from summer to early autumn, selecting for alternate phytoplankton groups (Petrou et al., 2016; Flynn et al., 2021). In addition, iron concentrations generally becoming limiting earlier in the open Southern Ocean, further inhibiting *P. antarctica* growth (Schoemann et al., 2005; Petrou et al., 2016).

The spring-to-late-summer shift from diatoms to *P. antarctica* in the MIZ (Schoemann et al., 2005; Petrou et al., 2016) may enhance carbon export. *P. antarctica* fix approximately twice as much carbon per mole of phosphate consumed than diatoms, and the colonies have been observed to sink rapidly out of the surface layer, thereby exporting large quantities of carbon (Arrigo et al., 1999). However, the large phytoplankton blooms that develop in the MIZ following sea-ice melt also yield elevated concentrations of biomass that enhance heterotrophic activity and NH_4^+ regeneration (Goeyens et al., 1995; Flynn et al., 2021). High NH_4^+ availability post-bloom, coincident with low iron, may shift the *P. antarctica*-dominated community towards regenerated N uptake, with the elevated NH_4^+ concentrations potentially even inhibiting NO_3^- uptake (Goeyens et al., 1995; Flynn et al., 2021). The shift from diatoms to *P. antarctica* may therefore decrease the f-ratio and biological carbon export in the MIZ.

The Atlantic OAZ is generally characterized by low iron conditions (Fig. 2.1f) because the winter mixed layer is shallower than the ferricline, which limits the amount of iron supplied during winter mixing (Klunder et al., 2011). These low mixed-layer iron concentrations limit productivity and phytoplankton growth is predominantly fueled by regenerated N following the spring bloom (Smetacek et al., 2004). This circumstance extends to the heavily-silicified diatoms that persist throughout the season. Although they have significant iron stores, large pennate diatoms will preferentially consume regenerated N over NO_3^- if the regenerated N flux is sufficient because of the lower iron requirement than that associated with NO_3^- consumption (Mengesha et al., 1998). This strategy allows them to persist in surface waters throughout the growth season, with the net consequence of the shift from *Chaetoceros* to heavily-silicified diatoms being a decrease in carbon export.

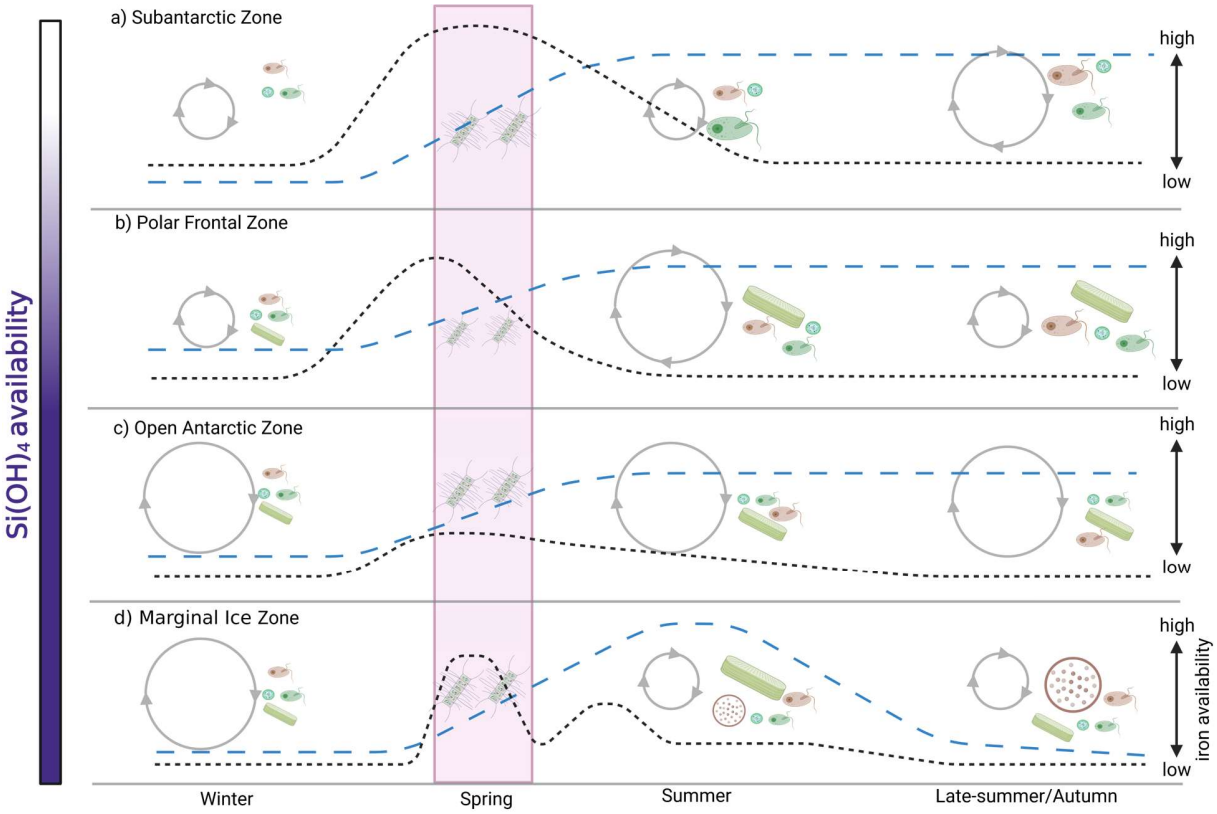


Figure 2.6. Schematics showing the seasonal physicochemical changes and associated shifts in the phytoplankton community in a) the Subantarctic Zone (SAZ), b) the Polar Frontal Zone (PFZ), c) the Open Antarctic Zone (OAZ), and d) the Marginal Ice Zone (MIZ) of the Southern Ocean developed using our new springtime data and the available observations from the other seasons (see text for references). The pink rectangle indicates our sampling period when the mixed layer was dominated by a Chaetoceros bloom. The different phytoplankton groups and their qualitative importance (smaller – less dominant, bigger – more dominant) are shown in each panel. The gradient in mixed-layer silicate ($Si(OH)_4$) availability is represented by the bar to the left of the schematic (high (dark purple) to low (white) silicate availability). The relative rate (number of arrows) and magnitude (size of circles) of iron and nitrogen recycling are shown by the grey circles. The dashed blue line indicates the mixed layer depth and the dotted black line shows the iron concentration. Figure created using BioRender.com.

In sum, although the evolution of the phytoplankton community following the *Chaetoceros* bloom differs in each hydrographic zone, biological carbon export potential declines over the growth season across the entire Southern Ocean. This decrease is principally due to rapid iron consumption by *Chaetoceros* in spring (as observed at the PFZ experimental station; Fig. 2.1f), which impacts iron availability later in the season.

In response, the phytoplankton community shifts towards regenerated N consumption, which decreases the f-ratio. At the same time, heterotrophic degradation of the spring- and summer phytoplankton blooms increases the supply of regenerated N as light availability declines, further reducing carbon export potential. This seasonal decline in carbon export potential underscores the importance of the spring *Chaetoceros* bloom for the Southern Ocean's seasonal (and annual) carbon flux.

Over the broad range of physicochemical conditions that characterize the Atlantic Southern Ocean in spring, we observed rates of productivity and carbon export potential that were remarkably similar. We attribute these observations to the dominance of nanoplankton-sized *Chaetoceros* spp. across all zones, with the boom-and-bust strategy employed by this taxon allowing it to outcompete all other phytoplankton groups. The *Chaetoceros* bloom is relatively short-lived (a few weeks), with its subsequent senescence accounting for roughly a third of the annual carbon export flux estimated previously for the Atlantic Southern Ocean (Fig. 2.6c). These rapid, short-lived blooms thus have large implications for Southern Ocean biogeochemistry and carbon export, along with influencing the conditions experienced by the succeeding phytoplankton community. With climate change, the Southern Ocean is predicted to become more stratified (Petrou et al., 2016; Deppeler and Davidson, 2017). In currently light-limited regions (e.g., the springtime MIZ), increased stratification will alleviate light limitation and potentially enhance NPP (Petrou et al., 2016; Deppeler and Davidson, 2017). However, stratification will coincidently decrease the upward iron supply, such that NPP in perennially iron-limited regions (e.g., the OAZ) may substantially decrease in response (Petrou et al., 2016; Deppeler and Davidson, 2017). The unique ecology of *Chaetoceros*, which can exist as both nanoplankton-sized individual cells and microplankton-sized chains, along with its boom-and-bust lifestyle and apparently low iron requirement, may allow this taxon to adapt to a changing climate. As such, the presence of *Chaetoceros* may (partly) mitigate the predicted negative effect of climate change on Southern Ocean carbon export.

2.4. Materials and Methods

2.4.1. Study region and hydrography

Samples were collected aboard the R/V *SA Agulhas II* during the 2019 Spring Cruise of the Southern oCean seAsonaL Experiment (SCALE) (http://scale.org.za/) along the Good Hope line(Ansorge et al., 2005) in the Atlantic sector of the Southern Ocean. The cruise involved four legs, with the final leg (9-13 November 2019) being the focus of this study. Sampling was conducted at 12 stations, including the four experimental stations that are central to this work, spanning the Marginal Ice Zone (MIZ), the Open Antarctic Zone (OAZ), the Polar Frontal Zone (PFZ), and the Subantarctic Zone (SAZ) (Fig. 2.1). Hereafter, all stations will be referred to by zone. The positions of the hydrographic fronts were determined from temperature and

salinity profiles (Orsi et al., 1995; Chapman et al., 2020) measured using a Seabird conductivity-temperature-depth (CTD) profiler. Mixed layer depth (MLD) was determined as the depth at which the Brunt-Väisälä frequency squared (N^2; a function of density) reached a maximum (Carvalho et al., 2017). The euphotic zone depth (Z_{eu}) was determined as the penetration depth of 1% of surface photosynthetically active radiation (PAR)(Kirk, 1994). In the instances where the PAR sensor was not deployed (n = 3 stations), the Z_{eu} was determined as follows:

$$E_z = E_0 \times e^{-kz} \quad (1)$$

Where E is irradiance, z is the euphotic zone depth (Z_{eu}), 0 is the surface, and k is the diffuse attenuation coefficient, extracted from satellite data for the sampling period (6-15 November 2019; doi: 10.5067/ORBVIEW-2/SEAWIFS/L3M/KD/2022).

2.4.2. Sample collection

Seawater samples were collected during three separate hydrocasts undertaken at each station. During the first hydrocast, seawater was collected in 12 L Teflon-coated GoFlo bottles attached to a powder-coated aluminium frame and CTD with titanium housings following GEOTRACES protocols (Cutter et al., 2020). Seawater was decanted from the GoFlo bottles inside a Class 100 clean container lab and processed under a laminar flow-hood. During the second and third casts, seawater was collected in 12 L Niskin bottles, with nutrient samples collected throughout the water column while samples for chlorophyll *a*, phytoplankton taxonomy, and rate experiments were collected from 3-6 depths in the mixed layer selected based on in situ profiles of temperature, fluorescence, and PAR.

2.4.3. Nutrient and chlorophyll *a* concentrations

Nitrate+nitrite (NO_3^-+NO_2^-) and silicate ($Si(OH)_4$) concentrations were analysed using a Lachat Quick-Chem flow injection autoanalyzer following standard colourimetric methods(Strickland and Parsons, 1968) in a configuration with a detection limit of 0.1 µM and standard deviation for duplicate samples of ≤0.5 µM. NO_3^- concentrations were determined by subtraction of NO_2^- from NO_3^-+NO_2^-. NO_2^- concentrations were measured shipboard by standard colourimetric methods (Strickland and Parsons, 1968) using a Thermo Scientific Genesis 30 Visible spectrophotometer with a detection limit of 0.05 µM and standard deviation for duplicate samples of ≤0.1 µM.

Ammonium (NH_4^+) concentrations were measured shipboard using the fluorometric method (Holmes et al., 1999) as described previously (Smith et al., 2022). The detection limit was <0.05 µM and the standard

deviation for duplicate samples was ≤0.1 µM. Urea-N concentrations were measured following the colourimetric method of Revilla et al. (2005) using a Thermo Scientific Genesis 30 Visible spectrophotometer equipped with a 10 cm path-length cell. The detection limit was 0.05 µM and the standard deviation for duplicate samples was ≤0.05 µM.

Dissolved iron (dFe) concentrations were measured using a quadrupole inductively coupled plasma mass spectrometer (Agilent 7900) connected to a seaFAST S3 inline preconcentration system (Elemental Scientific) (Samanta et al., 2021). The detection limit was 0.02 nM. GEOTRACES GSC, GSP, and in-house consensus/reference materials were included in all runs.

For bulk and size-fractionated chlorophyll *a* concentrations, seawater was filtered through 0.3 µm and 2.7 glass fibre filters (Sterlitech GF-75 and Grade D, respectively) and 20 µm nylon mesh filters (yielding bulk – ≥0.3 µm, picoplankton – 0.3-2.7 µm, nanoplankton – 2.7-20 µm, and microplankton – ≥20 µm chlorophyll *a*). Filters were immediately transferred to 20 mL glass scintillation vials to which 8 mL of 90% acetone was added before the vials were incubated at -20°C for 24 hours (Welschmeyer, 1994). Extracts were subsequently measured using a Turner Designs Trilogy fluorometer equipped with a chlorophyll *a* non-acidified module. The detection limit was 0.025 µg L^{-1}.

2.4.4. Phytoplankton and zooplankton taxonomy

Samples for phytoplankton taxonomy were collected at six mixed-layer depths in 50 mL centrifuge tubes and analyzed *in vivo* using a pulse-shape recording and imaging flow cytometer (CytoSense, Cytobuoy.com) fitted with a 488 nm laser, fluorescence sensors (yellow/green – 550 nm, orange – 600-650 nm, red – 650-700 nm) and two scatter sensors for light scattered parallel (forward scatter) and orthogonal (sideward scatter) to the laser beam. This technique yields phytoplankton counts (cell diameters of 1-1000 µm) comparable to those obtained with traditional microscopy, although with more reliable counts for cells <5 µm (Haraguchi et al., 2017). It also provides morphological information as the optical profile for each particle is recorded as it travels through the flow cell. Recorded cells were clustered by similarities in optical properties using CytoClus4 (Cytobuoy.com). Cells were assigned to one cluster only and the same clustering was used for all samples. Cluster identification was supported by high-resolution microphotographs taken by the instrument (e.g., Fig. 2.2e).

Samples for mesozooplankton taxonomy were collected using a Bongo net (200 µm) that was towed vertically from 200 m to the surface at a constant speed of 0.5 m s^{-1}. Samples were transferred to 1 L low density polyethylene (LDPE) bottles and immediately fixed with buffered formalin (final solution of 4%

v/v). Samples were analysed ashore using a ZEISS Stemi 508 stereo microscope and ZEISS Primo Star phase-contrast microscope(Boltovskoy et al., 1999). Individuals were grouped based on their life-stage and broadly categorized into three groups (copepod, euphausiid (or krill), and others).

2.4.5. Rates of NPP and nitrogen and iron uptake

Simulated *in situ* experiments were conducted to determine the bulk and size-fractionated (i.e., picoplankton – 0.3-2.7 µm, nanoplankton – 2.7-20 µm, and microplankton – >20 µm) rates of net primary production (NPP), N uptake (as NO_3^-, NH_4^+, and urea), and iron uptake (as labile inorganic iron (Fe') and organically-complexed iron (Fe-FOB)). Seawater was collected from three depths (typically surface, 50 m, and 75 m), then pre-screened through a 200 µm mesh to remove large grazers. Samples for NPP and N uptake were collected in Niskin bottles while those for iron uptake were collected in GoFlos. All experiments were performed in duplicate. For NPP and N uptake, isotope tracers were added at ~5-10% of the assumed ambient substrate concentrations, yielding final concentrations in the bottles of 100 µM $NaH^{13}CO_3$, 1 µM ^{15}N-NO_3^-, 0.05 µM ^{15}N-NH_4^+, and 0.05 µM ^{15}N-urea-N; for the rate calculations, tracer enrichments were calculated post-cruise from the measured nutrient concentrations. The bottles were incubated on deck for 4-6 hours in a custom-built incubator cooled with continuously-running surface seawater and equipped with neutral density filters to simulate the relevant light levels. Experiments were terminated via filtration onto 0.3 µm and 2.7 µm combusted (450°C for 8 hours) glass fibre filters (Sterlitech GF-75 and Grade D, respectively) and Milli Q rinsed 20 µm nylon mesh. The 20 µm samples were resuspended in 0.2 µm filtered seawater, then re-filtered onto combusted 2.7 µm glass fibre filters. All filters were stored frozen in combusted (500°C for 5 hours) foil envelopes at -80˚C pending analysis.

Ashore, filters were oven-dried for 24 hours at 40°C, then folded into tin cups. Filters were analysed using a Flash elemental analyser 1112 Series coupled to a Delta V Plus isotope ratio mass spectrometer (EA-IRMS) in a configuration with a detection limit of 2 µg C and 1 µg N. Blanks (combusted unused filters) and laboratory running standards (Merck gel, Choc, and Valine) calibrated to certified IAEA reference materials were run after every five samples and used to calibrate the sample measurements. Due to the low concentration of particulate organic matter on the 20 µm filters (often below the EA-IRMS detection limit for N), 0.06 µM of reagent grade urea (product code U5128, Sigma-Aldrich) was added to increase the organic content. Blank Grade D filters were treated in the same way to determine the $\delta^{15}N$ and $\delta^{13}C$ (where $\delta^{15}N$, in permil (‰) vs. N_2 in air, $= \left(\frac{(^{15}N/^{14}N)_{sample}}{(^{15}N/^{14}N)_{standard}} - 1\right) \times 1000$, and $\delta^{13}C$, in permil (‰) vs. Vienna Pee Dee Belemnite, $= \left(\frac{(^{13}C/^{12}C)_{sample}}{(^{13}C/^{12}C)_{standard}} - 1\right) \times 1000$) of the added urea ("urea blank"). The measured carbon (POC) and nitrogen (PON) content, $\delta^{15}N$, and $\delta^{13}C$ of the 20 µm samples were corrected for the urea blank

following Montoya (2008):

$$\delta^{15}N_{corrected} = \frac{(\delta^{15}N_{sample} - N\ content_{sample}) - (\delta^{15}N_{urea\ blank} - N\ content_{urea\ blank})}{N\ content_{sample} - N\ content_{urea\ blank}} \quad (2)$$

$$N\ content_{corrected} = N\ content_{sample} - N\ content_{urea\ blank} \quad (3)$$

Where $\delta^{15}N$ can be substituted for $\delta^{13}C$ and N content (µg N) can be substituted for C content (µg C).

The rates of NPP and N uptake were determined following Dugdale and Goering (1967) and Dugdale and Wilkerson (1986). POC, PON, NPP, N and iron uptake (see below) were determined for each filter fraction, with the rates attributable to the different phytoplankton size-classes then calculated by subtraction, with error propagated according to standard practices.

For the inorganic iron uptake experiments, to maintain the labile iron concentrations near ambient, we pre-complexed 0.5 nM ^{55}Fe with 10 µM of ultra-clean EDTA, which allowed us to calculate the labile iron amendment. [Fe'] was calculated following Sunda and Huntsman (2003), adjusting for the in situ particulate iron concentration ([pFe]), temperature, pH, and irradiance (Table A2). pH was derived from total alkalinity (TA) and total carbon (TC) measurements, and the conditional dissociation constants were derived using the values at 10°C and 20°C from Sunda and Huntsman (2003), extrapolated to colder temperatures as per Strzepeck (2011). Calculated dark [Fe'] was 3.4 to 6.5 pM, or < 1% of ambient dFe, but increased under higher irradiance and lower temperatures. To measure the community uptake rates of organically-complexed siderophore iron, we incubated 1 µM ^{55}Fe with 1.2 µM desferrioxamine-B (FOB) in lightly acidified (pH = 3) Milli-Q water, before amending to reach a final concentration of 1 nM ^{55}Fe-FOB.

All seawater manipulations were carried out using trace-metal clean procedures and in a particle- and metal-free environment. Seawater was collected in Go-Flo bottles at the same depths as for the NPP and N uptake experiments, transferred to 4L acid-cleaned polycarbonate bottles, and amended with either ^{55}Fe-EDTA or ^{55}Fe-FOB in a metal-free laminar flow hood. Bottles were incubated for 24 hours in a light- and temperature-controlled incubator with incubations terminated by filtration onto 0.2 µm, 2.7 µm, and 20 µm polycarbonate filters (Millipore). Each filter was rinsed with an oxalate solution to remove adherent (but non-assimilated) iron (Tang and Morel, 2006), then rinsed with filtered seawater and stored in a scintillation vial with 10 mL scintillation cocktail (Ultima Gold, Perkin Elmer).

Ashore, counts per minute were determined using a scintillation counter (TriCarb 2900), then converted to disintegrations per minute taking into account radioactive decay (specific activity of ^{55}Fe is 113 mCi mg^{-1}; Perkin-Elmer) and using a custom quench curve. Iron uptake rates were calculated using the amended plus intrinsic iron concentrations as follows:

$$Fe_{uptake}\ (\mu mol\ Fe\ mol\ C\ L^{-1}\ day^{-1} = [Fe_{tot}] \times \frac{DPM-filte\ \ blank}{^{55}Fe\ Specific\ Activity} \times day^{-1} \times vol^{-1}) \times [POC] \quad (4)$$

Using the size-fractionated rates of NPP, total N (i.e., NO_3^- + NH_4^+ + urea) uptake, and total iron (i.e., Fe' + Fe-FOB) uptake, we estimated the Fe:C and Fe:N uptake ratios(McKay et al., 2005; Strzepek et al., 2005) for the three size-classes as follows:

$$Fe{:}X\ uptake\ ratio_{(size\text{-}class)} = \frac{Fe'_{(size-class)} + Fe-FOB_{(size-class)}}{X_{(size-class)}} \quad (5)$$

where X is either NPP or total N uptake and size-class refers to pico-, nano-, or microplankton.

2.4.6. Total carbon export potential and NCP estimates

To determine carbon export potential relative to NPP at each station, we calculated the f-ratio (short-hand for flux ratio; a measure of new production relative to total production) using the absolute N uptake rates (Eppley and Peterson, 1979):

$$f\text{-}ratio = \frac{\rho N\ \bar{}_3}{\rho NO_3^- + \rho NH_4^+ + \rho urea} \quad (6)$$

Total carbon export potential (mmol C m^{-2} d^{-1}) was then calculated as:

$$Total\ carbon\ export\ potential = f\text{-}ratio \times NPP \quad (7)$$

Where NPP was integrated over the mixed layer at each station.

Net community production (NCP; a measure of export production; mmol C m^{-2}) between the start of the growth season and the time of our sampling was estimated from the net depletion of mixed layer NO_3^- from its maximum winter concentration (i.e., following recharge) until our sampling as follows:

$$Spring\ NCP = (NO_3^-\ depletion - [PON] - [NH_4^+] - [urea]) \times C{:}N\ ratio \quad (8)$$

where the C:N ratio is that estimated by Johnson et al. (2022) for each zone of the Atlantic Southern Ocean, [PON], $[NH_4^+]$, and [urea] are the average measured mixed-layer concentrations, and NO_3^- depletion was estimated as:

$$NO_3^- \text{ depletion} = [NO_3^-]_{source} - [NO_3^-]_{measured} \quad (9)$$

where $[NO_3^-]_{source}$ is the average NO_3^- concentration below the mixed layer and $[NO_3^-]_{measured}$ is the average measured mixed-layer concentration(Goeyens et al., 1995; Flynn et al., 2021).

2.5. References

Ansorge, I. J., Speich, S., Lutjeharms, J. R. E., Göni, G. J., De, C. J., Rautenbach, W., Froneman, P. W., Rouault, M., and Garzoli, S.: Monitoring the oceanic flow between Africa and Antarctica: Report of the first GoodHope cruise, South African J. Antarct. Res., 101, https://doi.org/10.10520/EJC96351, 2005.

Arrigo, K. R., Robinson, D. H., Worthen, D. L., Dunbar, R. B., DiTullio, G. R., VanWoert, M., and Lizotte, M. P.: Phytoplankton community structure and the drawdown of nutrients and CO2 in the Southern Ocean, Science (80-.)., 283, 365–367, https://doi.org/10.1126/science.283.5400.365, 1999.

Arteaga, L. A., Boss, E., Behrenfeld, M. J., Westberry, T. K., and Sarmiento, J. L.: Seasonal modulation of phytoplankton biomass in the Southern Ocean, Nat. Commun. 2020 111, 11, 1–10, https://doi.org/10.1038/s41467-020-19157-2, 2020.

Assmy, P., Smetacek, V., Montresor, M., Klaas, C., Henjes, J., Strass, V. H., Arrieta, J. M., Bathmann, U., Berg, G. M., Breitbarth, E., Cisewski, B., Friedrichs, L., Fuchs, N., Herndl, G. J., Jansen, S., Krägefsky, S., Latasa, M., Peeken, I., Röttgers, R., Scharek, R., Schüller, S. E., Steigenberger, S., Webb, A., Wolf-Gladrow, D., Klaas, C., and Smetacek, V.: Mechanisms determining species dominance in a phytoplankton bloom induced by the iron fertilization experiment EisenEx in the Southern Ocean, Deep. Res. Part I Oceanogr. Res. Pap., 110, 20633–20638, https://doi.org/10.1073/pnas.1309345110, 2013a.

Assmy, P., Smetacek, V., Montresor, M., Klaas, C., Henjes, J., Strass, V. H., Arrieta, J. M., Bathmann, U., Berg, G. M., Breitbarth, E., Cisewski, B., Friedrichs, L., Fuchs, N., Herndl, G. J., Jansen, S., Krägefsky, S., Latasa, M., Peeken, I., Röttgers, R., Scharek, R., Schüller, S. E., Steigenberger, S., Webb, A., and Wolf-Gladrow, D.: Thick-shelled, grazer-protected diatoms decouple ocean carbon and silicon cycles in the iron-limited Antarctic Circumpolar Current., Proc. Natl. Acad. Sci. U. S. A., 110, 20633–8, https://doi.org/10.1073/pnas.1309345110, 2013b.

Assmy, P., Smetacek, V., Montresor, M., Klaas, C., Henjes, J., Strass, V. H., Arrieta, J. M., Bathmann, U., Berg, G. M., Breitbarth, E., Cisewski, B., Friedrichs, L., Fuchs, N., Herndl, G. J., Jansen, S., Krägefsky, S., Latasa, M., Peeken, I., Röttgers, R., Scharek, R., Schüller, S. E., Steigenberger, S., Webb, A., and Wolf-Gladrow, D.: Thick-shelled, grazer-protected diatoms decouple ocean carbon and silicon cycles in the iron-limited Antarctic Circumpolar Current, Proc. Natl. Acad. Sci., 110, 20633–20638, https://doi.org/10.1073/pnas.1309345110, 2013c.

Azam, F., Fenchel, T., Field, J. G., Gray, J. S., Meyer-Reil, L. A., and Thingstad, F.: The ecological role of water-column microbes in the sea, in: Classic Papers with Commentaries, edited by: Miller, T. E. and Travis, J., University of Chicago Press, 384–390, https://doi.org/doi:10.7208/chicago/9780226125534-024, 1983.

Babin, M., Therriault, J. -C, Legendre, L., and Condal, A.: Variations in the specific absorption coefficient for natural phytoplankton assemblages: Impact on estimates of primary production, Limnol. Oceanogr., 38,

154–177, https://doi.org/10.4319/LO.1993.38.1.0154, 1993.

Behrenfeld, M. J., Hu, Y., O'Malley, R. T., Boss, E. S., Hostetler, C. A., Siegel, D. A., Sarmiento, J. L., Schulien, J., Hair, J. W., Lu, X., Rodier, S., and Scarino, A. J.: Annual boom–bust cycles of polar phytoplankton biomass revealed by space-based lidar, Nat. Geosci. 2017 102, 10, 118–122, https://doi.org/10.1038/ngeo2861, 2016.

Berge, T., Chakraborty, S., Hansen, P. J., and Andersen, K. H.: Modeling succession of key resource-harvesting traits of mixotrophic plankton, ISME J. 2017 111, 11, 212–223, https://doi.org/10.1038/ismej.2016.92, 2016.

Bergkvist, J., Thor, P., Jakobsen, H. H., Wängberg, S. Å., and Selander, E.: Grazer-induced chain length plasticity reduces grazing risk in a marine diatom, Limnol. Oceanogr., 57, 318–324, https://doi.org/10.4319/LO.2012.57.1.0318, 2012.

Blain, S., Quéguiner, B., Armand, L., Belviso, S., Bombled, B., Bopp, L., Bowie, A., Brunet, C., Brussaard, C., Carlotti, F., Christaki, U., Corbière, A., Durand, I., Ebersbach, F., Fuda, J. L., Garcia, N., Gerringa, L., Griffiths, B., Guigue, C., Guillerm, C., Jacquet, S., Jeandel, C., Laan, P., Lefèvre, D., Lo Monaco, C., Malits, A., Mosseri, J., Obernosterer, I., Park, Y. H., Picheral, M., Pondaven, P., Remenyi, T., Sandroni, V., Sarthou, G., Savoye, N., Scouarnec, L., Souhaut, M., Thuiller, D., Timmermans, K., Trull, T., Uitz, J., Van Beek, P., Veldhuis, M., Vincent, D., Viollier, E., Vong, L., and Wagener, T.: Effect of natural iron fertilization on carbon sequestration in the Southern Ocean, Nature, 446, 1070–1074, https://doi.org/10.1038/nature05700, 2007.

Boltovskoy, D., Gibbons, M. J., Hutchings, L., and Binet, D.: General biological features of the South Atlantic, South Atl. Zooplankt., 1, 1–42, 1999.

Boyd, P. W., Watson, A. J., Law, C. S., Abraham, E. R., Trull, T., Murdoch, R., Bakker, D. C. E., Bowie, A. R., Buesseler, K. O., Chang, H., Charette, M., Croot, P., Downing, K., Frew, R., Gall, M., Hadfield, M., Hall, J., Harvey, M., Jameson, G., LaRoche, J., Liddicoat, M., Ling, R., Maldonado, M. T., McKay, R. M., Nodder, S., Pickmere, S., Pridmore, R., Rintoul, S., Safi, K., Sutton, P., Strzepek, R., Tanneberger, K., Turner, S., Waite, A., and Zeldis, J.: A mesoscale phytoplankton bloom in the polar Southern Ocean stimulated by iron fertilization, Nature, 407, 695–702, https://doi.org/10.1038/35037500, 2000a.

Boyd, P. W., Watson, A. J., Law, C. S., Abraham, E. R., Trull, T., Murdoch, R., Bakker, D. C. E., Bowie, A. R., Buesseler, K. O., Chang, H., Charette, M., Croot, P., Downing, K., Frew, R., Gall, M., Hadfield, M., Hall, J., Harvey, M., Jameson, G., LaRoche, J., Liddicoat, M., Ling, R., Maldonado, M. T., McKay, R. M., Nodder, S., Pickmere, S., Pridmore, R., Rintoul, S., Safi, K., Sutton, P., Strzepek, R., Tanneberger, K., Turner, S., Waite, A., and Zeldis, J.: A mesoscale phytoplankton bloom in the polar Southern Ocean stimulated by iron fertilization, Nat. 2000 4076805, 407, 695–702, https://doi.org/10.1038/35037500, 2000b.

Bozzato, D., Jakob, T., Wilhelm, C., and Trimborn, S.: Effects of iron limitation on carbon balance and photophysiology of the Antarctic diatom Chaetoceros cf. simplex, Polar Biol., 44, 275–287, https://doi.org/10.1007/s00300-020-02785-1, 2021.

Buesseler, K. O., Barber, R. T., Dickson, M. L., Hiscock, M. R., Moore, J. K., and Sambrotto, R.: The effect of marginal ice-edge dynamics on production and export in the Southern Ocean along 170°W, Deep Sea Res. Part II Top. Stud. Oceanogr., 50, 579–603, https://doi.org/10.1016/S0967-0645(02)00585-4, 2003.

Burger, J. M., Moloney, C. L., Walker, D. R., Parrott, R. G., and Fawcett, S. E.: Drivers of short-term variability in phytoplankton production in an embayment of the southern Benguela upwelling system, J. Mar. Syst., 208, 103341, https://doi.org/10.1016/j.jmarsys.2020.103341, 2020a.

Burger, J. M., Moloney, C. L., Walker, D. R., Parrott, R. G., and Fawcett, S. E.: Drivers of short-term variability in phytoplankton production in an embayment of the southern Benguela upwelling system, J. Mar. Syst., 208, 103341, https://doi.org/10.1016/j.jmarsys.2020.103341, 2020b.

Carvalho, F., Kohut, J., Oliver, M. J., and Schofield, O.: Defining the ecologically relevant mixed-layer depth for Antarctica's coastal seas, Geophys. Res. Lett., 44, 338–345, https://doi.org/10.1002/2016GL071205, 2017.

Cassar, N., Wright, S. W., Thomson, P. G., Trull, T. W., Westwood, K. J., De Salas, M., Davidson, A., Pearce, I., Davies, D. M., and Matear, R. J.: The relation of mixed-layer net community production to phytoplankton community composition in the Southern Ocean, Global Biogeochem. Cycles, 29, 446–462, https://doi.org/10.1002/2014GB004936, 2015.

Cermeño, P., Marañón, E., Pérez, V., Serret, P., Fernández, E., and Castro, C. G.: Phytoplankton size structure and primary production in a highly dynamic coastal ecosystem (Ría de Vigo, NW-Spain): Seasonal and short-time scale variability, Estuar. Coast. Shelf Sci., 67, 251–266, https://doi.org/10.1016/J.ECSS.2005.11.027, 2006.

Chapman, C. C., Lea, M. A., Meyer, A., Sallée, J. B., and Hindell, M.: Defining Southern Ocean fronts and their influence on biological and physical processes in a changing climate, Nat. Clim. Chang., 10, 209–219, https://doi.org/10.1038/s41558-020-0705-4, 2020.

Christaki, U., Skouroliakou, I. D., Delegrange, A., Irion, S., Courcot, L., Jardillier, L., and Sassenhagen, I.: Microzooplankton diversity and potential role in carbon cycling of contrasting Southern Ocean productivity regimes, J. Mar. Syst., 219, 103531, https://doi.org/10.1016/J.JMARSYS.2021.103531, 2021.

Cochlan, W. P.: Nitrogen Uptake in the Southern Ocean, Nitrogen Mar. Environ., 569–596, https://doi.org/10.1016/B978-0-12-372522-6.00012-8, 2008.

Cohen, N. R., Ellis, K. A., Lampe, R. H., McNair, H., Twining, B. S., Maldonado, M. T., Brzezinski, M. A., Kuzminov, F. I., Thamatrakoln, K., Till, C. P., Bruland, K. W., Sunda, W. G., Bargu, S., and Marchetti, A.: Diatom transcriptional and physiological responses to changes in iron bioavailability across ocean

provinces, Front. Mar. Sci., 4, 360, https://doi.org/10.3389/FMARS.2017.00360/BIBTEX, 2017.

Croot, P. L., Frew, R. D., Sander, S., Hunter, K. A., Ellwood, M. J., Pickmere, S. E., Abraham, E. R., Law, C. S., Smith, M. J., and Boyd, P. W.: Physical mixing effects on iron biogeochemical cycling: FeCycle experiment, J. Geophys. Res. Ocean., 112, https://doi.org/10.1029/2006JC003748, 2007.

Cutter, G., Casciotti, K., Croot, P., Geibert, W., Heimbürger, L.-E., Lohan, M., Planquette, H., and van de Flierdt, T.: Sampling and Sample-handling Protocols for GEOTRACES Cruises. Version 3, August 2017., https://doi.org/10.25607/OBP-2, 2020.

Deppeler, S. L. and Davidson, A. T.: Southern Ocean phytoplankton in a changing climate, Front. Mar. Sci., 4, https://doi.org/10.3389/fmars.2017.00040, 2017.

Doebeli, M., Jaque, E. C., and Ispolatov, Y.: Boom-bust population dynamics increase diversity in evolving competitive communities, Commun. Biol. 2021 41, 4, 1–8, https://doi.org/10.1038/s42003-021-02021-4, 2021.

Dortch, Q.: The interaction between ammonium and nitrate uptake in phytoplankton, Mar. Ecol. Prog. Ser., 61, 183–201, https://doi.org/10.3354/meps061183, 1990.

Dugdale, R. C. and Goering, J. J.: Uptake of New and Regenerated Forms of Nitrogen in Primary Productivity, Limnol. Oceanogr., 12, 196–206, https://doi.org/10.4319/lo.1967.12.2.0196, 1967a.

Dugdale, R. C. and Goering, J. J.: UPTAKE OF NEW AND REGENERATED FORMS OF NITROGEN IN PRIMARY PRODUCTIVITY ’, 196–206, 1967b.

Dugdale, R. C. and Wilkerson, F. P.: The use of 15N to measure nitrogen uptake in eutrophic experimental considerations1 t2, 3, 1986.

Edwards, K. F.: Mixotrophy in nanoflagellates across environmental gradients in the ocean, Proc. Natl. Acad. Sci. U. S. A., 116, 6211–6220, https://doi.org/10.1073/PNAS.1814860116/SUPPL_FILE/PNAS.1814860116.SD01.XLSX, 2019.

Edwards, K. F., Thomas, M. K., Klausmeier, C. A., and Litchman, E.: Allometric scaling and taxonomic variation in nutrient utilization traits and maximum growth rate of phytoplankton, Limnol. Oceanogr., 57, 554–566, https://doi.org/10.4319/LO.2012.57.2.0554, 2012.

El-Sayed, S.: Productivity of the Antarctic Waters — A Reappraisal, in: Marine Phytoplankton and Productivity. Lecture Notes on Coastal and Estuarine Studies., edited by: O., H.-H., L., B., and R., G., Springer Berlin Heidelberg, 19–34, 1984.

Eppley, R. W. and Peterson, B.: Particulate organic matter flux and planktonic new production in the deep ocean, Nature, 282, 677–680, 1979.

Eppley, R. W. and Thomas, W. H.: COMPARISON OF HALF-SATURATION CONSTANTS FOR GROWTH AND NITRATE UPTAKE OF MARINE PHYTOPLANKTON 2, J. Phycol., 5, 375–379, https://doi.org/10.1111/J.1529-8817.1969.TB02628.X, 1969.

Fawcett, S. E. and Ward, B. B.: Phytoplankton succession and nitrogen utilization during the development of an upwelling bloom, Mar. Ecol. Prog. Ser., 428, 13–31, https://doi.org/10.3354/meps09070, 2011.
Feinberg, L. R. and Dam, H. G.: Effects of diet on dimensions, density and sinking rates of fecal pellets of the copepod Acartia tonsa, Mar. Ecol. Prog. Ser., 175, 87–96, https://doi.org/10.3354/MEPS175087, 1998.
Fenchel, T.: MARINE PLANKTON FOOD CHAINS, Annu. Rev. Ecol. Syst., 19, 19–38, https://doi.org/10.1146/annurev.es.19.110188.000315, 1988.
Finkel, Z. V. and Irwin, A. J.: Light absorption by phytoplankton and the filter amplification correction: cell size and species effects, J. Exp. Mar. Bio. Ecol., 259, 51–61, https://doi.org/10.1016/S0022-0981(01)00225-8, 2001.
Finkel, Z. V., Irwin, A. J., and Schofield, O.: Resource limitation alters the 3/4 size scaling of metabolic rates in phytoplankton, Mar. Ecol. Prog. Ser., 273, 269–279, https://doi.org/10.3354/MEPS273269, 2004.
Flynn, K. J., Stoecker, D. K., Mitra, A., Raven, J. A., Glibert, P. M., Hansen, J., Li, E. G., and Burkholder, J. M.: HORIZONS Misuse of the phytoplankton-zooplankton dichotomy: the need to assign organisms as mixotrophs within plankton functional types, J. Plankt. Res, 35, 3–11, https://doi.org/10.1093/plankt/fbs062, 2013.
Flynn, R. F., Bornman, T. G., Burger, J. M., Smith, S., Spence, K. A. M., and Fawcett, S. E.: Summertime productivity and carbon export potential in the Weddell Sea, with a focus on the waters adjacent to Larsen C Ice Shelf, 18, 6031–6059, https://doi.org/10.5194/BG-18-6031-2021, 2021.
Glibert, P. M., Wilkerson, F. P., Dugdale, R. C., Raven, J. A., Dupont, C. L., Leavitt, P. R., Parker, A. E., Burkholder, J. M., and Kana, T. M.: Pluses and minuses of ammonium and nitrate uptake and assimilation by phytoplankton and implications for productivity and community composition, with emphasis on nitrogen-enriched conditions, Limnol. Oceanogr., 61, 165–197, https://doi.org/10.1002/lno.10203, 2016a.
Glibert, P. M., Wilkerson, F. P., Dugdale, R. C., Raven, J. A., Dupont, C. L., Leavitt, P. R., Parker, A. E., Burkholder, J. M., and Kana, T. M.: Pluses and minuses of ammonium and nitrate uptake and assimilation by phytoplankton and implications for productivity and community composition, with emphasis on nitrogen-enriched conditions, Limnol. Oceanogr., 61, 165–197, https://doi.org/10.1002/lno.10203, 2016b.
Goeyens, L., Tréguer, P., Baumann, M. E. M., Baeyens, W., and Dehairs, F.: The leading role of ammonium in the nitrogen uptake regime of Southern Ocean marginal ice zones, J. Mar. Syst., 6, 345–361, https://doi.org/10.1016/0924-7963(94)00033-8, 1995.
Haraguchi, L., Jakobsen, H. H., Lundholm, N., and Carstensen, J.: Monitoring natural phytoplankton communities: a comparison between traditional methods and pulse-shape recording flow cytometry, Aquat. Microb. Ecol., 80, 77–92, 2017.
Henley, S. F., Cavan, E. L., Fawcett, S. E., Kerr, R., Monteiro, T., Sherrell, R. M., Bowie, A. R., Boyd, P. W., Barnes, D. K. A., Schloss, I. R., Marshall, T., Flynn, R., and Smith, S.: Changing Biogeochemistry of

the Southern Ocean and Its Ecosystem Implications, 1–31 pp., https://doi.org/10.3389/fmars.2020.00581, 2020.

Hoffmann, L. J., Peeken, I., Lochte, K., Assmy, P., and Veldhuis, M.: Different reactions of Southern Ocean phytoplankton size classes to iron fertilization, Limnol. Oceanogr., 51, 1217–1229, https://doi.org/10.4319/LO.2006.51.3.1217, 2006.

Hoffmann, L. J., Peeken, I., and Lochte, K.: Iron, silicate, and light co-limitation of three Southern Ocean diatom species, Polar Biol., 31, 1067–1080, https://doi.org/10.1007/s00300-008-0448-6, 2008.

Holmes, R. M., Aminot, A., Kerouel, R., Hooker, B. A., and Peterson, B. J.: A simple and precise method for measuring ammonium in marine and freshwater ecosystems, https://doi.org/10.1139/cjfas-56-10-1801, 1999.

Hutchinson, G. E.: The Paradox of the Plankton, 95, 137–145, https://doi.org/10.1086/282171, 1961.

Janssen, D. J., Sieber, M., Ellwood, M. J., Conway, T. M., Barrett, P. M., Chen, X., de Souza, G. F., Hassler, C. S., and Jaccard, S. L.: Trace metal and nutrient dynamics across broad biogeochemical gradients in the Indian and Pacific sectors of the Southern Ocean, Mar. Chem., 221, 103773, https://doi.org/10.1016/J.MARCHEM.2020.103773, 2020.

Johnson, K. S., Coale, K. H., Elrod, V. A., and Tindale, N. W.: Iron photochemistry in seawater from the equatorial Pacific, Mar. Chem., 46, 319–334, https://doi.org/10.1016/0304-4203(94)90029-9, 1994.

Johnson, K. S., Plant, J. N., Coletti, L. J., Jannasch, H. W., Sakamoto, C. M., Riser, S. C., Swift, D. D., Williams, N. L., Boss, E., Haëntjens, N., Talley, L. D., and Sarmiento, J. L.: Biogeochemical sensor performance in the SOCCOM profiling float array, J. Geophys. Res. Ocean., 122, 6416–6436, https://doi.org/10.1002/2017JC012838, 2017.

Johnson, K. S., Mazloff, M. R., Bif, M. B., Takeshita, Y., Jannasch, H. W., Maurer, T. L., Plant, J. N., Verdy, A., Walz, P. M., Riser, S. C., and Talley, L. D.: Carbon to Nitrogen Uptake Ratios Observed Across the Southern Ocean by the SOCCOM Profiling Float Array, J. Geophys. Res. Ocean., 127, e2022JC018859, https://doi.org/10.1029/2022JC018859, 2022.

Juranek, L. W., White, A. E., Dugenne, M., Henderikx Freitas, F., Dutkiewicz, S., Ribalet, F., Ferrón, S., Armbrust, E. V., and Karl, D. M.: The Importance of the Phytoplankton "Middle Class" to Ocean Net Community Production, Global Biogeochem. Cycles, 34, e2020GB006702, https://doi.org/10.1029/2020GB006702, 2020.

Karsh, K. L., Trull, T. W., Lourey, M. J., and Sigman, D. M.: Relationship of nitrogen isotope fractionation to phytoplankton size and iron availability during the Southern Ocean Iron RElease Experiment (SOIREE), Limnol. Oceanogr., 48, 1058–1068, https://doi.org/10.4319/lo.2003.48.3.1058, 2003.

Kiørboe, T.: Turbulence, Phytoplankton Cell Size, and the Structure of Pelagic Food Webs, Adv. Mar. Biol., 29, 1–72, https://doi.org/10.1016/S0065-2881(08)60129-7, 1993.

Kirk, J.: Light and photosynthesis in aquatic ecosystems, Cambridge Univ. Press, 1994.

Klunder, M. B., Laan, P., Middag, R., De Baar, H. J. W., and van Ooijen, J. C.: Dissolved iron in the Southern Ocean (Atlantic sector), Deep. Res. Part II Top. Stud. Oceanogr., 58, 2678–2694, https://doi.org/10.1016/j.dsr2.2010.10.042, 2011.

Lampe, R. H., Cohen, N. R., Ellis, K. A., Bruland, K. W., Maldonado, M. T., Peterson, T. D., Till, C. P., Brzezinski, M. A., Bargu, S., Thamatrakoln, K., Kuzminov, F. I., Twining, B. S., and Marchetti, A.: Divergent gene expression among phytoplankton taxa in response to upwelling, Environ. Microbiol., 20, 3069–3082, https://doi.org/10.1111/1462-2920.14361, 2018.

Lampe, R. H., Wang, S., Cassar, N., and Marchetti, A.: Strategies among phytoplankton in response to alleviation of nutrient stress in a subtropical gyre, ISME J. 2019 1312, 13, 2984–2997, https://doi.org/10.1038/s41396-019-0489-6, 2019.

Leblanc, K., Quéguiner, B., Diaz, F., Cornet, V., Michel-Rodriguez, M., Durrieu De Madron, X., Bowler, C., Malviya, S., Thyssen, M., Grégori, G., Rembauville, M., Grosso, O., Poulain, J., De Vargas, C., Pujo-Pay, M., and Conan, P.: Nanoplanktonic diatoms are globally overlooked but play a role in spring blooms and carbon export, Nat. Commun. 2018 91, 9, 1–12, https://doi.org/10.1038/s41467-018-03376-9, 2018.

Legendre, L. and Le Fevre, J.: Microbial food webs and the export of biogenic carbon in oceans, Aquat. Microb. Ecol., 09, 69–77, https://doi.org/10.3354/AME009069, 1995.

Litchman, E.: Resource Competition and the Ecological Success of Phytoplankton, Evol. Prim. Prod. Sea, 351–375, https://doi.org/10.1016/B978-012370518-1/50017-5, 2007.

Llort, J., Lévy, M., Sallée, J.-B., and Tagliabue, A.: Onset, intensification, and decline of phytoplankton blooms in the Southern Ocean, J. Mar. Sci., 72, 1971–1984, https://doi.org/10.1093/icesjms/fsv053, 2015.

Lomas, M. W. and Glibert, P. M.: Interactions between NH4/+ and NO3/- uptake and assimilation: Comparison of diatoms and dinoflagellates at several growth temperatures, Mar. Biol., 133, 541–551, https://doi.org/10.1007/s002270050494, 1999.

Lourey, M. J., Trull, T. W., and Sigman, D. M.: Sensitivity of δ15N of nitrate, surface suspended and deep sinking particulate nitrogen to seasonal nitrate depletion in the Southern Ocean, Global Biogeochem. Cycles, 17, 1–18, https://doi.org/10.1029/2002gb001973, 2003.

Maldonado, M. T. and Price, N. M.: Influence of N substrate on Fe requirements of marine centric diatoms, Mar. Ecol. Prog. Ser., 141, 161–172, 1996.

Malone, T.: Size-fractionated primary productivity of marine phytoplankton, in: Environmental Science Research, 301–319, 1980.

Marañón, E., Steele, J., Thorpe, A., and Turekian, K.: Phytoplankton size structure, Elem. Phys. Oceanogr. A Deriv. Encycl. Ocean Sci., 85, 2009.

Marañón, E., Cermeño, P., López-Sandoval, D. C., Rodríguez-Ramos, T., Sobrino, C., Huete-Ortega, M.,

Blanco, J. M., and Rodríguez, J.: Unimodal size scaling of phytoplankton growth and the size dependence of nutrient uptake and use, Ecol. Lett., 16, 371–379, https://doi.org/10.1111/ELE.12052, 2013.

Marchetti, A. and Cassar, N.: Diatom elemental and morphological changes in response to iron limitation: A brief review with potential paleoceanographic applications, Geobiology, 7, 419–431, https://doi.org/10.1111/j.1472-4669.2009.00207.x, 2009.

Marchetti, A. and Maldonado, M. T.: The Physiology of Microalgae, https://doi.org/10.1007/978-3-319-24945-2, 2016.

Marchetti, A., Parker, M. S., Moccia, L. P., Lin, E. O., Arrieta, A. L., Ribalet, F., Murphy, M. E. P., Maldonado, M. T., and Armbrust, E. V.: Ferritin is used for iron storage in bloom-forming marine pennate diatoms, Nat. 2008 4577228, 457, 467–470, https://doi.org/10.1038/nature07539, 2008.

Margalef, R.: Life-forms of phytoplankton Life-forms Phytoplankton Turbulence Dia toms Dinoftagellates Types biologiques Phytoplancton Turbulence Diatomées Dinoftagellés as survival alternatives in an unstable environment ABSTRACT RÉSUMÉ, Oceanol. Acta, 1, 1978.

Martin, J. H., Gordon, R. M., and Fitzwater, S. E.: Iron in Antarctic waters, Nature, 345, 156–158, https://doi.org/10.1038/345156a0, 1990.

McKay, R. M. L., Wilhelm, S. W., Hall, J., Hutchins, D. A., Al-Rshaidat, M. M. D., Mioni, C. E., Pickmere, S., Porta, D., and Boyd, P. W.: Impact of phytoplankton on the biogeochemical cycling of iron in subantarctic waters southeast of New Zealand during FeCycle, Global Biogeochem. Cycles, 19, https://doi.org/10.1029/2005GB002482, 2005.

Mdutyana, M., Thomalla, S. J., Philibert, R., Ward, B. B., and Fawcett, S. E.: The Seasonal Cycle of Nitrogen Uptake and Nitrification in the Atlantic Sector of the Southern Ocean, Global Biogeochem. Cycles, 34, 1–29, https://doi.org/10.1029/2019GB006363, 2020.

Mengesha, S., Dehairs, F., Fiala, M., Elskens, M., and Goeyens, L.: Seasonal variation of phytoplankton community structure and nitrogen uptake regime in the Indian Sector of the Southern Ocean, Polar Biol., 20, 1998.

Michaels, A. F. and Silver, M. W.: Primary production, sinking fluxes and the microbial food web, Deep Sea Res. Part A. Oceanogr. Res. Pap., 35, 473–490, https://doi.org/10.1016/0198-0149(88)90126-4, 1988.

Møller, E. F., Thor, P., and Nielsen, T. G.: Production of DOC by Calanus finmarchicus, C. glacialis and C. hyperboreus through sloppy feeding and leakage from fecal pellets, Mar. Ecol. Prog. Ser., 262, 185–191, https://doi.org/10.3354/MEPS262185, 2003.

Montoya, J. P.: Nitrogen Stable Isotopes in Marine Environments, Nitrogen Mar. Environ., 1277–1302, https://doi.org/10.1016/B978-0-12-372522-6.00029-3, 2008.

Morel, F., Rueter, J., and Price, N.: Iron Nutrition of Phytoplankton and Its Possible Importance in the Ecology of Ocean Regions with High Nutrient and Low Biomass, 4, 56–61,

https://doi.org/10.5670/oceanog.1991.03, 1991.

Mtshali, T. N., van Horsten, N. R., Thomalla, S. J., Ryan-Keogh, T. J., Nicholson, S. A., Roychoudhury, A. N., Bucciarelli, E., Sarthou, G., Tagliabue, A., and Monteiro, P. M. S.: Seasonal Depletion of the Dissolved Iron Reservoirs in the Sub-Antarctic Zone of the Southern Atlantic Ocean, Geophys. Res. Lett., 46, 4386–4395, https://doi.org/10.1029/2018GL081355, 2019.

Nodwell, L. M. and Price, N. M.: Direct use of inorganic colloidal iron by marine mixotrophic phytoplankton, Limnol. Oceanogr., 46, 765–777, https://doi.org/10.4319/lo.2001.46.4.0765, 2001.

Orsi, A. H., Whitworth, T., and Nowlin, W. D.: On the meridional extent and fronts of the Antarctic Circumpolar Current, Deep. Res. Part I, 42, 641–673, https://doi.org/10.1016/0967-0637(95)00021-W, 1995.

Petrou, K., Trimborn, S., Rost, B., Peter, ·, Ralph, J., and Hassler, C. S.: The impact of iron limitation on the physiology of the Antarctic diatom Chaetoceros simplex, https://doi.org/10.1007/s00227-014-2392-z, 2014.

Petrou, K., Kranz, S. A., Trimborn, S., Hassler, C. S., Ameijeiras, S. B., Sackett, O., Ralph, P. J., and Davidson, A. T.: Southern Ocean phytoplankton physiology in a changing climate, J. Plant Physiol., 203, 135–150, https://doi.org/10.1016/j.jplph.2016.05.004, 2016.

Poulsen, L. K. and Iversen, M. H.: Degradation of copepod fecal pellets: key role of protozooplankton, Mar. Ecol. Prog. Ser., 367, 1–13, https://doi.org/10.3354/MEPS07611, 2008.

Priddle, J., Boyd, I. L., Whitehouse, M. J., Murphy, E. J., and Croxall, J. P.: Estimates of Southern Ocean primary production - Constraints from predator carbon demand and nutrient drawdown, in: Journal of Marine Systems, 275–288, https://doi.org/10.1016/S0924-7963(98)00043-8, 1998.

Quéguiner, B.: Iron fertilization and the structure of planktonic communities in high nutrient regions of the Southern Ocean, Deep Sea Res. Part II Top. Stud. Oceanogr., 90, 43–54, https://doi.org/10.1016/j.dsr2.2012.07.024, 2013.

Raven, J. A.: The iron and molybdenum use efficiencies of plant growth with different energy, carbon and nitrogen sources, New Phytol., 109, 279–287, https://doi.org/10.1111/J.1469-8137.1988.TB04196.X, 1988.

Rembauville, M., Manno, C., Tarling, G. A., Blain, S., and Salter, I.: Strong contribution of diatom resting spores to deep-sea carbon transfer in naturally iron-fertilized waters downstream of South Georgia, Deep. Res. Part I Oceanogr. Res. Pap., 115, 22–35, https://doi.org/10.1016/J.DSR.2016.05.002, 2016.

Revilla, M., Alexander, J., and Glibert, P. M.: Urea analysis in coastal waters: Comparison of enzymatic and direct methods, Limnol. Oceanogr. Methods, 3, 290–299, https://doi.org/10.4319/lom.2005.3.290, 2005.

Ryan-Keogh, T. J., Thomalla, S. J., Mtshali, T. N., Van Horsten, N. R., and Little, H. J.: Seasonal

development of iron limitation in the sub-Antarctic zone, 15, 4647–4660, https://doi.org/10.5194/BG-15-4647-2018, 2018.

Samanta, S., Cloete, R., Loock, J., Rossouw, R., and Roychoudhury, A. N.: Determination of trace metal (Mn, fe, ni, cu, zn, co, cd and pb) concentrations in seawater using single quadrupole icp-ms: A comparison between offline and online preconcentration setups, 11, 1289, https://doi.org/10.3390/MIN11111289/S1, 2021.

Sarmiento, J., Toggweiler, J.: A new model for the role of the oceans in determining atmospheric P CO2., Nature, 308, 621–624, https://doi.org/https://doi.org/10.1038/308621a0, 1984.

Sarmiento, J. L., Gruber, N., Brzezinski, M. A., and Dunne, J. P.: High-latitude controls of thermocline nutrients and low latitude biological productivity, Nature, 479, 56–60, https://doi.org/10.1038/nature10605, 2011.

Sathyendranath, S., Lazzara, L., and Prieur, L.: Variations in the spectral values of specific absorption of phytoplankton, Limnol. Ocean., 32, 15, 1987.

Schoemann, V., Becquevort, S., Stefels, J., Rousseau, V., and Lancelot, C.: Phaeocystis blooms in the global ocean and their controlling mechanisms: A review, J. Sea Res., 53, 43–66, https://doi.org/10.1016/j.seares.2004.01.008, 2005a.

Schoemann, V., Becquevort, S., Stefels, J., Rousseau, V., and Lancelot, C.: Phaeocystis blooms in the global ocean and their controlling mechanisms: A review, J. Sea Res., 53, 43–66, https://doi.org/10.1016/j.seares.2004.01.008, 2005b.

Semeneh, M., Dehairs, F., Elskens, M., Baumann, M. E. M., Kopczynska, E. E., Lancelot, C., and Goeyens, L.: Nitrogen uptake regime and phytoplankton community structure in the Atlantic and Indian sectors of the Southern Ocean, J. Mar. Syst., 17, 159–177, https://doi.org/10.1016/S0924-7963(98)00036-0, 1998.

Smetacek, V.: The giant diatom dump, Nat. 2000 4066796, 406, 574–575, https://doi.org/10.1038/35020665, 2000.

Smetacek, V., Assmy, P., and Henjes, J.: The role of grazing in structuring Southern Ocean pelagic ecosystems and biogeochemical cycles, Antarct. Sci., 16, 541–558, https://doi.org/10.1017/S0954102004002317, 2004.

Smith, S., Altieri, K. E., Mdutyana, M., Walker, D. R., Parrott, R. G., Gallie, S., Spence, K. A. M., Burger, J. M., and Fawcett, S. E.: Biogeochemical controls on ammonium accumulation in the surface layer of the Southern Ocean, 19, 715–741, https://doi.org/10.5194/BG-19-715-2022, 2022.

Sokolov, S. and Rintoul, S. R.: On the relationship between fronts of the Antarctic Circumpolar Current and surface chlorophyll concentrations in the Southern Ocean, J. Geophys. Res. Ocean., 112, 2007.

Sommer, U.: The paradox of the plankton: Fluctuations of phosphorus availability maintain diversity of phytoplankton in flow-through cultures1, Limnol. Oceanogr., 29, 633–636,

https://doi.org/10.4319/LO.1984.29.3.0633, 1984.

Sommer, U., Charalampous, E., Genitsaris, S., Moustaka-Gouni, M., Kiel, K., □□□□□ G., And, □, and □□□□□□ T.: Benefits, costs and taxonomic distribution of marine phytoplankton body size, J. Plankton Res., 39, 494–508, https://doi.org/10.1093/PLANKT/FBW071, 2017.

Stoecker, D. K.: Particle production by planktonic ciliates1, Limnol. Oceanogr., 29, 930–940, https://doi.org/10.4319/LO.1984.29.5.0930, 1984.

Stoecker, D. K., Hansen, P. J., Caron, D. A., and Mitra, A.: Mixotrophy in the Marine Plankton, https://doi.org/10.1146/annurev-marine-010816-060617, 2016.

Strickland, J. D. H. and Parsons, T. R.: A practical handbook of seawater analysis, Bull. Fish. Res. Board Canada, 167, 81–86, 1968.

Strzepek, R. F., Maldonado, M. T., Higgins, J. L., Hall, J., Safi, K., Wilhelm, S. W., and Boyd, P. W.: Spinning the "ferrous wheel": The importance of the microbial community in an iron budget during the FeCycle experiment, Global Biogeochem. Cycles, 19, https://doi.org/10.1029/2005GB002490, 2005.

Stukel, M. R., Landry, M. R., and Selph, K. E.: Nanoplankton mixotrophy in the eastern equatorial Pacific, Deep Sea Res. Part II Top. Stud. Oceanogr., 58, 378–386, https://doi.org/10.1016/J.DSR2.2010.08.016, 2011.

Sunda, W. G. and Huntsman, S. A.: Iron uptake and growth limitation in oceanic and coastal phytoplankton, Mar. Chem., 50, 189–206, https://doi.org/10.1016/0304-4203(95)00035-P, 1995.

Sverdrup, H. U.: On conditions for the vernal blooming of phytoplankton, J. Cons. Int. Explor. Mer, 18, 287–295, 1953.

Tagliabue, A., Mtshali, T., Aumont, O., Bowie, A. R., Klunder, M. B., Roychoudhury, A. N., and Swart, S.: A global compilation of dissolved iron measurements: Focus on distributions and processes in the Southern Ocean, 9, 2333–2349, https://doi.org/10.5194/bg-9-2333-2012, 2012.

Tagliabue, A., Sallée, J. B., Bowie, A. R., Lévy, M., Swart, S., and Boyd, P. W.: Surface-water iron supplies in the Southern Ocean sustained by deep winter mixing, Nat. Geosci., 7, 314–320, https://doi.org/10.1038/ngeo2101, 2014.

Takahashi, T., Sweeney, C., Hales, B., Chipman, D. W., Goddard, J. G., Newberger, T., Iannuzzi, R. A., and Sutherland, S. C.: The changing carbon cycle in the southern ocean, 25, 26–37, https://doi.org/10.5670/oceanog.2012.71, 2012.

Tréguer, P., Bowler, C., Moriceau, B., Dutkiewicz, S., Gehlen, M., Aumont, O., Bittner, L., Dugdale, R., Finkel, Z., Iudicone, D., Jahn, O., Guidi, L., Lasbleiz, M., Leblanc, K., Levy, M., and Pondaven, P.: Influence of diatom diversity on the ocean biological carbon pump, Nat. Geosci., https://doi.org/10.1038/s41561-017-0028-x, 2017.

Tremblay, J. E., Lucas, M. I., Kattner, G., Pollard, R., Strass, V. H., Bathmann, U., and Bracher, A.:

Significance of the Polar Frontal Zone for large-sized diatoms and new production during summer in the Atlantic sector of the Southern Ocean, Deep. Res. Part II Top. Stud. Oceanogr., 49, 3793–3811, https://doi.org/10.1016/S0967-0645(02)00111-X, 2002.

Twining, B. S., Antipova, O., Chappell, P. D., Cohen, N. R., Jacquot, J. E., Mann, E. L., Marchetti, A., Ohnemus, D. C., Rauschenberg, S., and Tagliabue, A.: Taxonomic and nutrient controls on phytoplankton iron quotas in the ocean, Limnol. Oceanogr. Lett., 6, 96–106, https://doi.org/10.1002/lol2.10179, 2021.

Uchida, T., Balwada, D., Abernathey, R., Prend, C. J., Boss, E., and Gille, S. T.: Southern Ocean Phytoplankton Blooms Observed by Biogeochemical Floats, J. Geophys. Res. Ocean., 124, 7328–7343, https://doi.org/10.1029/2019JC015355, 2019.

Ward, B. A. and Follows, M. J.: Marine mixotrophy increases trophic transfer efficiency, mean organism size, and vertical carbon flux, Proc. Natl. Acad. Sci. U. S. A., 113, 2958–2963, https://doi.org/10.1073/PNAS.1517118113/SUPPL_FILE/PNAS.201517118SI.PDF, 2016.

Welschmeyer, N. A.: Fluorometric analysis of chlorophyll a in the presence of chlorophyll b and pheopigments, Limnol. Oceanogr., 39, 1985–1992, https://doi.org/10.4319/LO.1994.39.8.1985, 1994.

Wright, S. W., van den Enden, R. L., Pearce, I., Davidson, A. T., Scott, F. J., and Westwood, K. J.: Phytoplankton community structure and stocks in the Southern Ocean (30–80°E) determined by CHEMTAX analysis of HPLC pigment signatures, Deep Sea Res. Part II Top. Stud. Oceanogr., 57, 758–778, https://doi.org/10.1016/J.DSR2.2009.06.015, 2010.

Appendix A: Nanoplankton: the dominant vector of carbon export across the springtime Southern Ocean

A1. Surface chlorophyll a concentrations throughout the growth season

Monthly satellite surface chlorophyll *a* data (Fig. A1; 10.5067/AQUA/MODIS/L3M/CHL/2022) were used to determine when the spring bloom was initiated across the open Atlantic Southern Ocean. Chlorophyll *a* concentrations were ubiquitously low (<0.2 μg L^{-1}) south of 40°S until October, when concentrations began to increase, particularly in the Polar Frontal Zone and Marginal Ice Zone. As the phytoplankton growth season progressed, surface chlorophyll *a* concentrations increased to reach a maximum in January/February 2020.

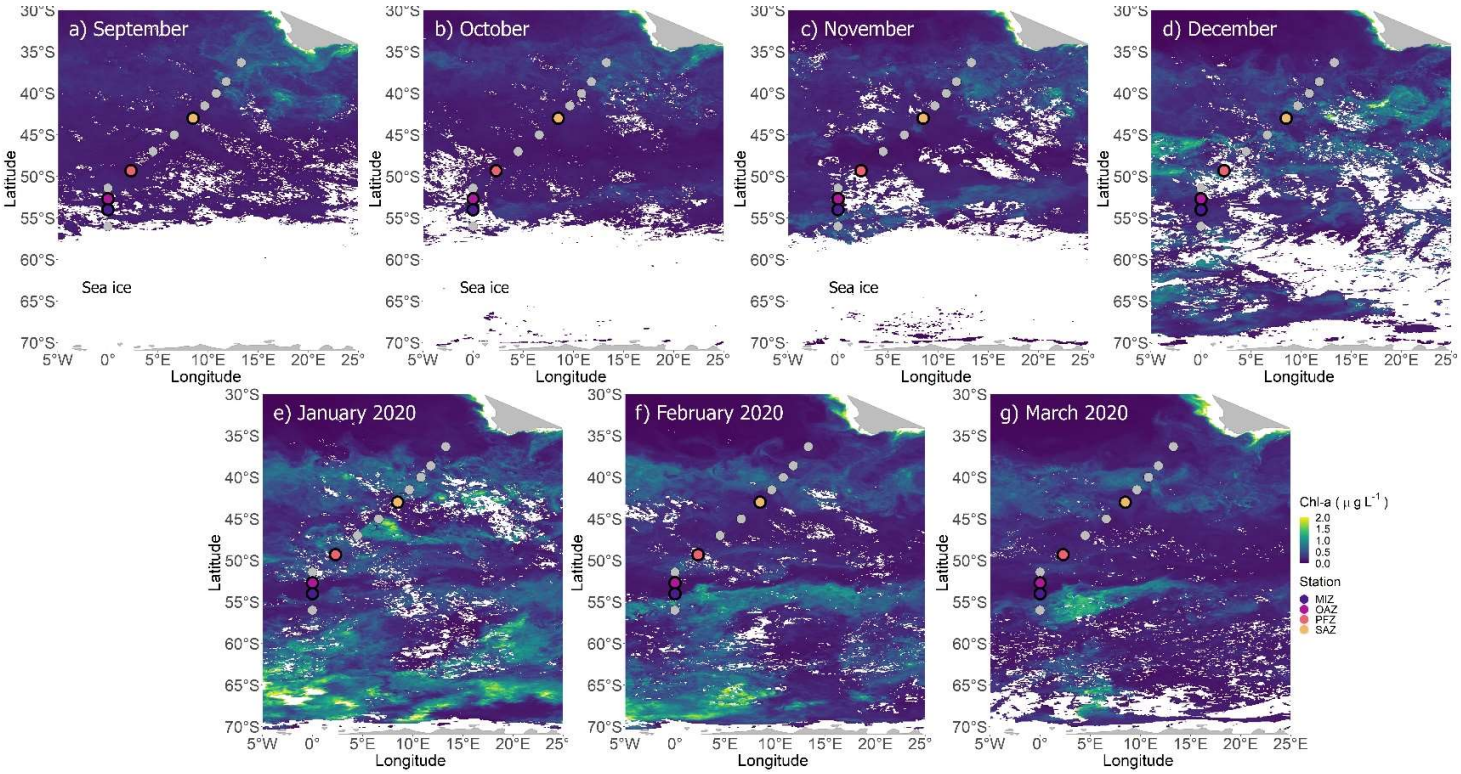


Figure A1.Monthly-averaged surface concentrations of chlorophyll a across the Atlantic Southern Ocean in a) September 2019, b) October 2019, c) November 2019, d) December 2019, e) January 2020, f) February 2020, and g) March 2020. The stations occupied during the cruise (9-13 November 2019) are denoted by the circles, with the colours indicating the stations where uptake rate experiments were conducted (purple – Marginal Ice Zone (MIZ), pink – Open Antarctic Zone (OAZ), orange – Polar Frontal Zone (PFZ), yellow – Subantarctic Zone (SAZ)) and the grey circles showing the ancillary stations. The chlorophyll a concentrations are monthly averages from MODIS-Aqua (10.5067/AQUA/MODIS/L3M/CHL/2022).

A2. Size-fractionated rates of NPP, and N and Fe uptake

Experiments to determine the size-fractionated rates of net primary production (NPP) and nitrogen (N; as nitrate (NO_3^-), ammonium (NH_4^+), and urea) and iron (Fe; as dissolved inorganic iron (Fe') and organically-

complexed iron (Fe-FOB)) uptake were conducted at four stations across the Atlantic Southern Ocean in spring (Fig. 2.1 and S2). At all stations, NPP and N uptake were dominated by the nanoplankton (2.7-20 μm), while the picoplankton (0.3-2.7 μm) dominated iron uptake. The rates of NPP and N uptake did not vary with depth, in contrast to the iron uptake rates (Fig. A2). The rates of Fe' and Fe-FOB uptake decreased between the surface (55% light level) and the base of the euphotic zone (Z_{eu}; 1% light level), although the decrease was much larger for Fe' uptake. This decrease in iron uptake with depth is likely because Fe(II), the most bioavailable form of iron, is produced by the photochemical reduction of Fe(III), the most thermodynamically stable form of iron in oxic waters (Johnson et al., 1994). The availability of Fe(II) is therefore higher in the surface ocean compared to at Z_{eu}, which explains the higher rates of Fe' uptake at the surface.

The specific rates of N uptake ($V_{NO_3^-}, V_{NH_4^+}, V_{urea}$) were generally lowest in the SAZ and increased southwards for all size-classes (Fig. A3). As per the transport rates (NPP, ρNO_3^-, ρNH_4^+, ρurea), the specific uptake rates of regenerated N ($V_{reg\ N}$; = $V_{NH_4^+} + V_{urea}$) were lower than $V_{NO_3^-}$. In contrast to the transport rates, the highest specific uptake rates of all N species were associated with the picoplankton, while the nano- and microplankton showed intermediate and low specific uptake rates, respectively.

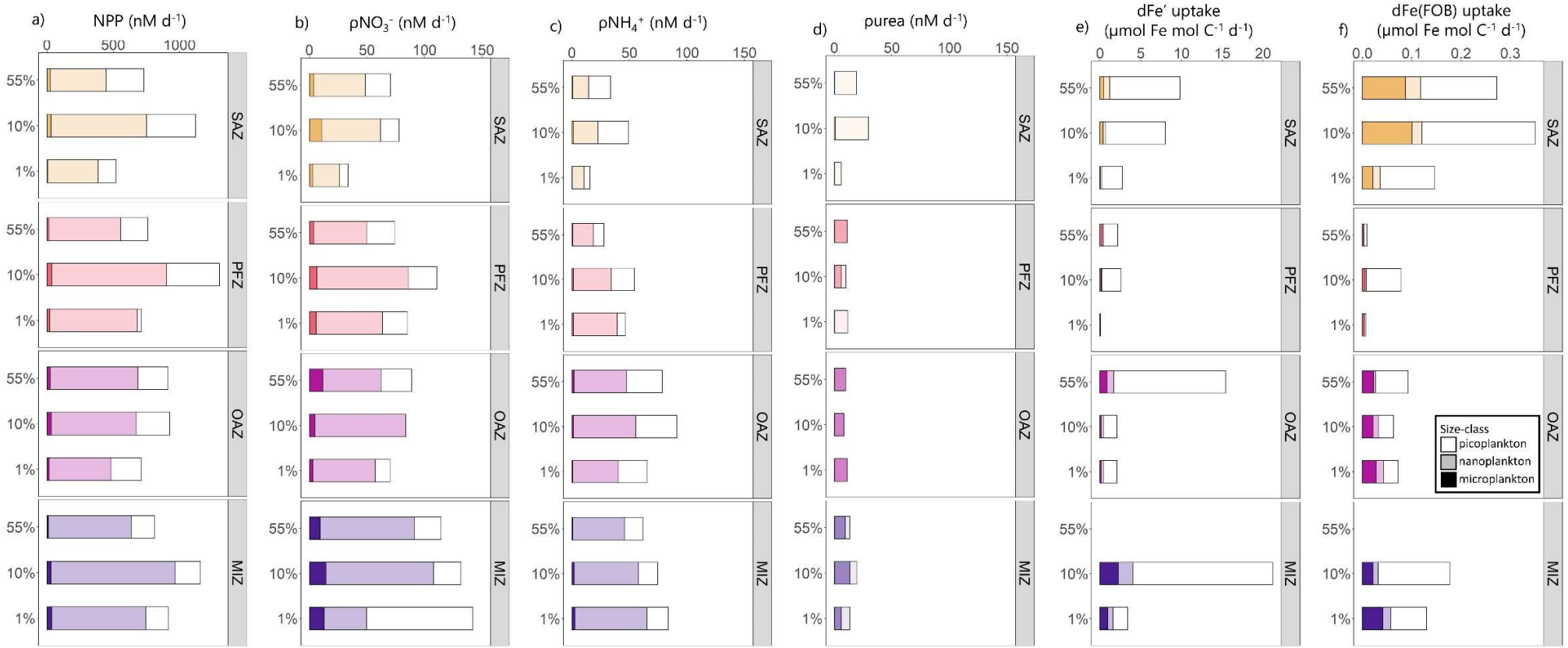


Figure A2. Size-fractionated rates of a) net primary production (NPP), b) nitrate uptake (ρNO_3^-), c) ammonium uptake (ρNH_4^+), d) urea uptake (ρurea), e) dissolved inorganic iron uptake (Fe' uptake), and f) organically-complexed iron uptake (Fe-FOB uptake) in the euphotic zone, shown as a function of light availability relative to surface photosynthetically active radiation (%PAR). The station locations are labelled on the right-hand side of the panels. The colour shading indicates the different size-classes (white – picoplankton, opaque – nanoplankton, solid colour – microplankton). Where there are no bars in panels (e-f), no data are available.

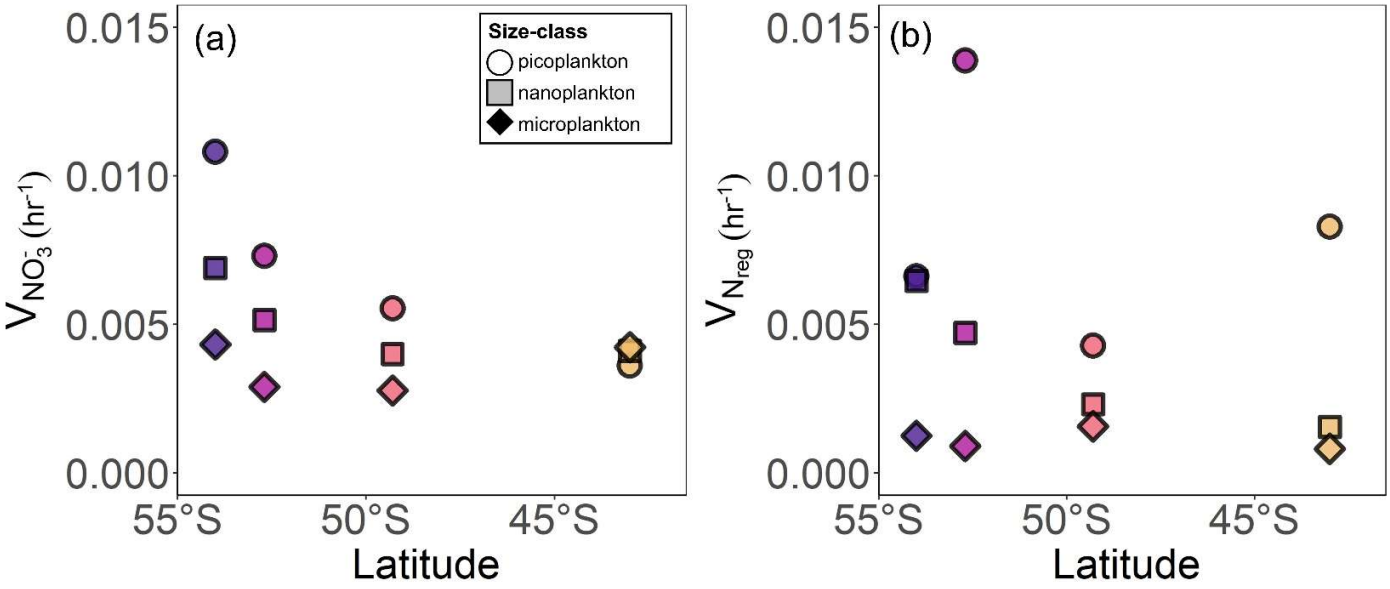


Figure A3. Specific uptake rates of a) nitrate ($V_{NO_3^-}$) and b) total regenerated nitrogen (i.e., $V_{N\ reg} = V_{NH_4^+} + V_{urea}$) versus latitude at the four experimental stations. The symbols denote the different size-classes (circles– picoplankton, squares– nanoplankton, diamonds– microplankton) and the colours indicate the station locations (purple – Marginal Ice Zone (MIZ), pink – Open Antarctic Zone (OAZ), orange – Polar Frontal Zone (PFZ), yellow – Subantarctic Zone (SAZ)).

Table A1. Euphotic-zone integrated rates of net primary production (NPP), nitrate uptake (ρNO_3^-), ammonium uptake (ρNH_4^+), urea uptake (ρurea), dissolved inorganic iron uptake (Fe' uptake), and organically-complexed iron uptake (Fe-FOB uptake), as well as the total iron (i.e., Fe' + Fe-FOB) to carbon uptake ratio. Values shown are averages ± 1 SD (n = 2 experiments), with error propagated according to standard statistical practices where appropriate. Where standard deviations are not included, the values were <0.01. "-" indicates no available data.

	MLD (m)	Z_{eu} (m)	Size-class	NPP (mmol m^{-2} d^{-1})	ρNO_3^- (mmol m^{-2} d^{-1})	ρNH_4^+ (mmol m^{-2} d^{-1})	ρurea (mmol m^{-2} d^{-1})	dFe' uptake (µmol Fe mol C^{-1} m^{-2} d^{-1})	dFe(FOB) uptake (µmol Fe mol C^{-1} m^{-2} d^{-1})	Fe:C uptake ratios (µmol Fe mol C^{-1})
SAZ	120	39	Bulk	62.2 ± 0.2	4.7 ± 0.01	2.7 ± 0.01	1.5	535.7	20.2	-
			Picoplankton	21.1 ± 0.2	1.2	1.4	1.5	482.5	12.9	20.1
			Nanoplankton	39.5 ± 0.1	3.1	1.2	0.0	27.3	1.6	2.5
			Microplankton	1.7	0.5	0.1	0.0	25.9	5.7	14.9
PFZ	75	37.5	Bulk	71.6 ± 0.1	6.6 ± 0.01	3.1 ± 0.01	0.7	140.5	3.0	-
			Picoplankton	19.0 ± 0.1	1.7	1.0	0.3	122.6	2.6	5.8
			Nanoplankton	50.8 ± 0.08	4.5	2.0	0.4	7.7	0.1	0.7
			Microplankton	1.8	0.4	0.1	0.0	10.3	0.3	7.7
OAZ	150	41	Bulk	61.9 ± 0.2	5.7 ± 0.02	5.8 ± 0.04	0.7	445.5	5.2	-
			Picoplankton	16.8 ± 0.2	0.6	2.3	0.0	387.8	2.9	13.6
			Nanoplankton	43.1 ± 0.07	4.6	3.4	0.6	32.2	0.7	2.8
			Microplankton	1.9 ± 0.02	0.5	0.1	0.0	25.6	1.6	39.4
MIZ	160	42.5	Bulk	70.3 ± 0.05	9.0 ± 0.01	5.0 ± 0.01	1.2	1259.2	11.8	-
			Picoplankton	12.8 ± 0.08	2.5	1.2	0.4	1008.2	9.3	30.5
			Nanoplankton	55.7 ± 0.07	5.6	3.7	0.7	111.5	0.8	6.6
			Microplankton	1.8 ± 0.01	0.9	0.1	0.0	139.5	1.8	52.3

Table A2. Calculated labile iron concentrations ([Fe']) in the experimental bottles considering ambient light, temperature, and pH. pH was derived from measurements of total alkalinity (TA) and total dissolved carbon (TC). The steady state dissociation constant of the Fe(EDTA) chelate (log k' light) was acquired through linear regression of the data from Sunda and Huntsman (1995) where the temperature-specific dissociation constants are related via log k' = m (pH) + b. Fe[tot] is the sum of the ambient iron concentration and the iron added to the experimental bottles. Values are shown for all experimental depths at each station (listed according to light availability relative to surface photosynthetically active radiation (%PAR)), with

the station locations indicated at the left of the Table (Subantarctic Zone (SAZ), Polar Frontal Zone (PFZ), Open Antarctic Zone (OAZ), Marginal Ice Zone (MIZ)).

		[Fe'] pmol L^{-1}	T.A. mmol kg^{-1}	T.C. mmol kg^{-1}	°C	pH	[^{55}Fe] nmol L^{-1}	$[Fe]_{tot}$ nmol L^{-1}	[EDTA] µmol L^{-1}	log k'_{light}	(m), $°C_{adj}$	(b), $°C_{adj}$	Light µmol m^{-2} s^{-1}
SAZ	55%PAR	**12.7**	2262.2	2120.6	6.5	8.021	0.5	0.88	10	-5.985	0.775	12.205	70
	10%PAR	**5.6**	2263.3	2120.7	6.5	8.032	0.5	0.88	10	-5.977	0.775	12.205	30
	1%PAR	**3.8**	2262.2	2120.6	6.5	8.022	0.5	0.88	10	-5.985	0.775	12.205	21
	DARK	**3.7**	2262.2	2120.6	6.5	8.022	0.5	0.88	10	-7.372	1.241	17.330	DARK
PFZ	55%PAR	**14.9**	2272.9	2137.3	3.4	8.055	0.5	0.82	10	-5.886	0.690	11.445	70
	10%PAR	**6.4**	2274.7	2137.9	3.4	8.055	0.5	0.82	10	-5.886	0.690	11.445	30
	1%PAR	**4.5**	2278.0	2141.0	3.4	8.055	0.5	0.82	10	-5.886	0.690	11.445	21
	DARK	**3.8**	2278.0	2141.0	3.4	8.055	0.5	0.82	10	-7.334	1.103	16.217	DARK
OAZ	55%PAR	**17.4**	2295.6	2168.7	0.8	8.043	0.5	0.76	10	-5.787	0.567	10.347	70
	10%PAR	**7.4**	2293.5	2171.0	0.8	8.042	0.5	0.76	10	-5.788	0.567	10.347	30
	1%PAR	**5.2**	2294.7	2169.9	0.8	8.043	0.5	0.76	10	-5.787	0.567	10.347	21
	DARK	**3.4**	2294.7	2169.9	0.8	8.043	0.5	0.76	10	-7.348	0.903	14.608	DARK
MIZ	10%PAR	**13.6**	2292.1	2172.4	-0.3	8.050	0.5	1.25	10	-5.742	0.520	9.925	30
	1%PAR	**9.5**	2293.2	2173.9	-0.3	8.046	0.5	1.25	10	-5.744	0.520	9.925	21
	DARK	**5.6**	2293.2	2173.9	-0.3	8.046	0.5	1.25	10	-7.346	0.826	13.989	DARK

Chapter 3: Summertime productivity and carbon export potential in the Weddell Sea, with a focus on the waters adjacent to Larsen C Ice Shelf

Abstract

The Weddell Sea represents a point of origin in the Southern Ocean where globally-important water masses form. Biological activities in Weddell Sea surface waters thus affect large-scale ocean biogeochemistry. During January/February 2019, we measured net primary production (NPP), nitrogen (nitrate, ammonium, urea) uptake, and nitrification in the western Weddell Sea at the Antarctic Peninsula (AP) and Larsen C Ice Shelf (LCIS), in the southwestern Weddell Gyre (WG), and at Fimbul Ice Shelf (FIS) in the south-eastern Weddell Sea. The highest average rates of NPP and greatest nutrient drawdown occurred at LCIS. Here, the phytoplankton community was dominated by colonial *Phaeocystis antarctica*, with diatoms increasing in abundance later in the season as sea-ice melted. At the other stations, NPP was variable, and diatoms known to enhance carbon export (e.g., *Thalassiosira* spp.) were dominant. Euphotic zone nitrification was always below detection, such that nitrate uptake could be used as a proxy for carbon export potential, which was highest in absolute terms at LCIS and the AP. Surprisingly, the highest f-ratios occurred near FIS rather than LCIS (average of 0.73 ± 0.09 versus 0.47 ± 0.08). We attribute this unexpected result to partial ammonium inhibition of nitrate uptake at LCIS (where ammonium concentrations were 0.6 ± 0.4 μM, versus 0.05 ± 0.1 μM at FIS), with elevated ammonium resulting from increased heterotrophy following the accumulation of nitrate-fuelled phytoplankton biomass in early summer. Across the Weddell Sea, carbon export appears to be controlled by a combination of physical, chemical, and biological factors, with the highest potential export flux occurring at the ice shelves and lowest in the central WG.

Table of Acronyms

Acronym (units)	Full description
AP	Antarctic Peninsula
FIS	Fimbul Ice Self
LCIS	Larsen C Ice Shelf
WG	Weddell Gyre
ASF	Antarctic Shelf Front
ACC	Antarctic Circumpolar Current
CCSZ	Coastal and Continental Shelf Zone
MIZ	Marginal Ice Zone
OOZ	Open Ocean Zone
ASW	Antarctic Surface Water
WW	Winter Water
MDWD	Modified Warm Deep Water
ISW	Ice Shelf Water
HSSW	High Salinity Shelf Water
WDW	Weddell Deep Water
WSDW	Weddell Sea Deep Water
WSBW	Weddell Sea Bottom Water
MLD (m)	Mixed layer depth
Z_{eu} (m)	Euphotic zone depth
PON (µM)	Particulate Organic Nitrogen
POC (µM)	Particulate Organic Carbon
NPP (µM d^{l})	Absolute rate of carbon fixation (also termed net primary production)
ρNO_3^- (µM d^{-1})	Absolute rate of nitrate uptake
ρNH_4^+ (µM d^{-1})	Absolute rate of ammonium uptake
ρurea (µM d^{-1})	Absolute rate of urea uptake
ρN_{reg} (µM d^{-1})	Absolute rate of regenerated nitrogen (i.e., ρNH_4^+ + ρurea) uptake
$V_{NO_2^-}$ (nM d^{-1})	Rate of nitrification
f-ratio	Flux ratio, equal to the proportion of primary productivity fuelled by NO_3^- uptake

3.1. Introduction

The Southern Ocean is an important driver of Earth's climate as it transports large quantities of heat and dissolved gases, and supplies 65-85% of the global ocean's nutrients (Keffer and Holloway, 1988; Sarmiento et al., 2004; Frölicher et al., 2015; Keller et al., 2016; Fripiat et al., 2021). Despite the Southern Ocean's central role in atmospheric CO_2 removal (DeVries, 2014; Frölicher et al., 2015; Gruber et al., 2019), the incomplete drawdown of surface-water nutrients (i.e., nitrate, phosphate, and silicic acid) due to iron and light limitation of phytoplankton (Martin et al., 1991; Sunda and Huntsman, 1997) represents a missed opportunity for CO_2 removal (Sarmiento and Toggweiler, 1984). The Weddell Sea constitutes a point of origin in the Southern Ocean where water masses form and communicate with the atmosphere before subducting (Muench and Gordon, 1995; Talley et al., 2011), thereby setting the initial physical and chemical conditions of the deep global ocean. Biogeochemical cycling in the surface Weddell Sea thus has implications for carbon transfer to and storage in the ocean interior (Hoppema et al., 2004; Kerr et al., 2018). The southern and western Weddell Sea are bounded by ice shelves, which promote high rates of summertime phytoplankton productivity, nutrient drawdown and carbon export (El-Sayed and Taguchi, 1981; Hoppema and Goeyens, 1999; Hoppema et al., 2000), largely because the surface ecosystem is less iron- and light-limited in the ice shelf-adjacent waters than in the open Weddell Sea (Klunder et al., 2014).

The Weddell Sea is separated from the Antarctic Circumpolar Current (ACC) and open Southern Ocean by the Weddell Sea fronts (Orsi et al. 1995). The general large-scale circulation takes the form of the cyclonic, wind-driven and topographically-steered Weddell Gyre (WG) (Fahrbach et al., 1994, 1995; Orsi et al., 1995). The production of bottom water is thought to occur at two sites in the Weddell Sea: at Filchner-Ronne Ice Shelf (FRIS) and Larsen C Ice Shelf (LCIS) (Gordon et al., 1993; Schröder et al., 2002; Schodlok et al., 2002). Here, Modified Warm Deep Water (MWDW) intrudes onto the continental shelf and mixes with Antarctic Surface Water (ASW), which alters its physical and chemical properties, ultimately resulting in the formation of dense bottom waters. Upon reaching the Antarctic Peninsula (AP), the transformed bottom waters either spill out over the shelf and re-enter the ACC or are entrained into the eastward flowing limb of the WG (Orsi et al., 1993; Locarnini et al., 1993).

The surface waters of the open Weddell Sea surface waters are warm and saline while those over the continental shelf are relatively cool and fresh (Nicholls et al,. 2004). These different waters are separated by the Antarctic Slope Front (ASF; Jacobs, 1986; 1991), a fast-flowing jet situated between the 500 m and 1000 m isobath that separates the Open Ocean Zone (OOZ) from the Coastal and Continental Shelf Zone (CCSZ; Jacobs, 1986; 1991; Muench and Gordon, 1995). The Antarctic CCSZ has been observed to host high rates of productivity in the summer (e.g., Smith and Nelson, 1990; Arrigo et al., 2008) as melting sea-ice supplies dissolved iron and increases water column stratification, yielding favourable conditions for phytoplankton growth (Lannuzel et al., 2008). Inputs of dissolved

iron from continental shelf sediments and coastal runoff further elevate the ambient iron concentrations, such that the CCSZ seldom experiences iron-depletion (Klunder et al., 2014; Dinniman et al., 2020). As a result, the large phytoplankton blooms of the CCSZ can at times almost completely deplete the surface nitrate concentrations (Jennings et al. 1984; Hoppema et al. 2000; Henley et al. 2017), supporting high rates of carbon export that fuel the benthic community on the underlying continental shelf (Isla et al., 2006, 2011; Pineda-Metz et al., 2019) and/or eventually lead to long-term storage of atmospheric CO_2 in newly-formed AABW (Arrigo et al., 2008). In contrast, the OOZ is far less productive due to persistent iron-deplete conditions, along with incidences of light limitation associated with high sea-ice concentrations (particularly in the central WG) and/or deep mixed layers (MLD) (Klunder et al., 2011; De Jong et al., 2012). Here, the co-limitation of productivity by iron and light typically yields low rates of biological carbon export (Boyd et al., 2008; Boyd and Ellwood, 2010; Klunder et al., 2011; De Jong et al., 2012).

On an annual basis, phytoplankton growth in the euphotic zone that is fuelled by nitrate supplied from below (i.e., "new production") must be balanced by the export of sinking organic matter into the ocean interior (i.e., "export production"), thus driving CO_2 removal (Dugdale and Goering, 1967; Eppley and Peterson, 1979). By contrast, phytoplankton growth supported by nitrogen (N) sources that are recycled within the euphotic zone, such as ammonium and urea (i.e., "regenerated production"), results in no net removal of CO_2 to the deep ocean. The biologically-driven flux of carbon from surface waters, termed the "biological carbon pump", transfers CO_2 to the isolated waters of the deep ocean, regulating the atmospheric concentration of this greenhouse gas (Volk and Hoffert, 1985). The high nutrient-low chlorophyll state of much of the Southern Ocean represents a "leak" in the ocean's biological carbon pump since by consuming mixed-layer nutrients more completely, phytoplankton could theoretically lower atmospheric CO_2 (Sarmiento and Toggweiler, 1984). Indeed, one hypothesis for the decrease in atmospheric CO_2 that characterized the ice ages is more complete consumption of surface nutrients (i.e., a more efficient biological carbon pump) in the open Southern Ocean (Sigman and Boyle, 2000; Sigman et al., 2010; Martínez-García et al., 2014).

Since phytoplankton in the CCSZ of the Weddell Sea consume much of the nitrate supplied to the surface (Jennings et al. 1984; Hoppema et al. 2000), they should, by mass balance, drive the export of a significant amount of atmospheric CO_2 ("fixed" as biomass) to depth, a significant portion of which will be subducted in newly-formed bottom waters to be sequestered for >1000 years (Ito et al. 2010). Understanding the controls on biological nutrient utilization in the Weddell Sea, particularly in the CCSZ, is thus central to our understanding of its contribution to the Southern Ocean's role in setting atmospheric CO_2. In general, phytoplankton growth in the Weddell Sea is regulated by the seasonal cycle of sea-ice, with the associated availability of light and iron imposing the main constraints (El-Sayed and Taguchi 1981). In winter, sea-ice formation and wind-driven mixing supply high

concentrations of nutrients to ASW (Hoppema et al. 2007; 2015) that remain largely unconsumed due to the deep mixed layers and short days (Cota et al., 1992; Scharek et al., 1994; Spiridonov et al., 1996). Relief from light limitation in spring and early summer following increased water-column stratification due to sea-ice melt combined with enhanced solar radiation leads to the development of phytoplankton blooms. The size and duration of these blooms is ultimately dependent on macro- (e.g., nitrate and silicate) and micronutrient (e.g., iron) availability (Martin et al. 1991; Boyd 2004; Boyd and Ellwood 2010; Llort et al. 2015), as well as zooplankton grazing (Smetacek et al., 2004 and references therein; Arteaga et al., 2020).

Observations suggest that Weddell Sea phytoplankton blooms are initially dominated by smaller species (e.g., *Phaeocystis antarctica*; 2-6 μm) that are well-adapted to the low-light conditions associated with deep springtime mixed layers (Moisan and Mitchell, 1999; Arrigo et al., 1999). As the season progresses, intensifying upper water-column stratification provides suitable growth conditions for larger phytoplankton such as diatoms (Goffart et al., 2000; Nissen and Vogt, 2021). Diatoms tend to rely heavily on nitrate as their dominant N source under high light and nutrient conditions, and are generally outcompeted by smaller phytoplankton for ammonium (Probyn and Painting, 1985; Koike et al., 1986; Lomas and Glibert, 1999; Karsh et al., 2003). Diatoms are also a major vector for carbon export due to their rapid sinking rates facilitated by their generally larger size and biogenic silica ballasting (Tréguer et al., 2017). The seasonal shift in the Weddell Sea community from small, non-silicified phytoplankton to larger, more heavily-silicified species is thus associated with a significant increase in carbon export (Assmy et al. 2013). Concomitantly, sea-ice melt supplies high concentrations of dissolved iron to surface waters (up to 7 nM in the western Weddell Sea; Lannuzel et al., 2008; Klunder et al., 2014), which helps to support nitrate drawdown (Klunder et al., 2011, 2014). Eventually, as surface iron (and occasionally, nitrate; Hoppema, et al. 2000) concentrations again become limiting, phytoplankton rely proportionally more on ammonium and other regenerated N sources that have become increasingly available due to heterotrophic processing of the accumulated (i.e., bloom) biomass (Goeyens et al., 1995; Semeneh et al., 1998). The phytoplankton community consequently shifts once more towards smaller species that are better adapted to low iron conditions and specialize in the consumption of regenerated N, ultimately leading to a decrease in carbon export (Goeyens et al., 1995).

The Weddell Sea is particularly understudied near LCIS where thick sea-ice conditions persist year-round. To our knowledge, the only biogeochemical study conducted in the vicinity of LCIS was undertaken in the austral summer of 1992/3. Using measurements of nutrient depletion, Hoppema et al. (2000) estimated primary production in the vicinity of LCIS to be 47.5-95 mmol C m^{-2} d^{-1}, while in the central Weddell Sea it was substantially lower at 8.3 mmol C m^{-2} d^{-1}. However, because the study did not characterize the phytoplankton community, the extent to which phytoplankton diversity may have influenced primary production and nutrient drawdown cannot be surmised. To evaluate the summertime

fertility of the Weddell Sea and the potential importance of different phytoplankton groups for carbon production and export, we directly measured the rates of total, new, and regenerated production in the western Weddell Sea (predominantly at LCIS), as well as at Fimbul Ice Shelf (FIS) in the south-eastern Weddell Sea. Rates of nitrification were also quantified to account for any nitrate regenerated within the euphotic zone at the time of sampling as this N flux supports regenerated rather than new production (e.g., Yool et al. 2007; Mdutyana et al. 2020). We interpret our rate data in the context of coincident measurements of regional hydrography, macronutrient concentrations and ratios, and phytoplankton community composition.

3.2. Methods

3.2.1. Field collections

Sampling was conducted in the January/February 2019 during the Weddell Sea Expedition onboard the R/V *SA Agulhas II* (Dowdeswell et al., 2019). A total of 19 stations were sampled across the Weddell Sea and are categorised based on their geographic position as Antarctic Peninsula (AP), Larsen C Ice Shelf (LCIS), Weddell Gyre (WG), or Fimbul Ice Shelf (FIS) stations (Table 3.1; Fig. 3.1). Hydrographic data were collected using a Seabird conductivity-temperature-depth (CTD) profiler equipped with a photosynthetically active radiation (PAR) sensor. Density (sigma-theta; σ_θ) was derived from CTD measurements of temperature, salinity, and pressure, and was used to identify the water mass distributions. The mixed layer depth (MLD) was determined as the depth at which the Brunt-Väisälä frequency squared (N^2; a function of σ_θ) reached a maximum (Schofield et al. 2015).

Seawater was collected from discrete depths using a rosette of twenty-four 12 L Niskin bottles. At each station, seawater samples for nutrient analysis were collected throughout the water column (typically at 15 discrete depths), while samples for phytoplankton taxonomy and rate experiments were taken from 3-6 depths (see below) that were selected based on profiles of temperature, chlorophyll-a fluorescence, and PAR measured during the CTD down-casts.

Simulated *in situ* experiments were conducted to determine the rates of net primary production (NPP), N uptake (as nitrate (NO_3^-), ammonium (NH_4^+), and urea-N), and nitrite (NO_2^-) oxidation (a measure of nitrification). For NPP and N uptake, seawater was collected from three depths coinciding with the 55%, 10%, and 1% PAR levels, then pre-screened through 200 µm mesh to remove large grazers and transferred to six 1 L and six 2 L polycarbonate bottles per depth. ^{15}N-labeled NO_3^-, NH_4^+, or urea-N was added to four of the twelve bottles (i.e., two 1 L and two 2 L bottles per N species) and $NaH^{13}CO_3$ was added to the bottles amended with ^{15}N-NH_4^+. The tracers were added at ~5-10% of the assumed ambient concentrations, yielding final concentrations in each bottle of approximately 100 µM $NaH^{13}CO_3$, 1 µM ^{15}N-NO_3^-, 0.05 µM ^{15}N-NH_4^+, and 0.1 µM ^{15}N-urea-N. Bottles were incubated on the deck for 4-6 hours in a custom-built incubator that was cooled with running surface (~7 m) seawater

and equipped with neutral density filters to simulate the relevant light levels. Experiments were terminated via filtration onto 0.3 µm combusted (450°C for 8 hours) glass fibre filters (Sterlitech GF-75) that were stored frozen in combusted (500°C for 5 hours) foil envelopes at -80˚C pending analysis.

Seawater samples for the NO_2^- oxidation experiments were collected from the 55%, 10%, and 1% light levels, just below the MLD, and at 200 m and 500 m. From each depth, seawater was transferred into duplicate 250 mL opaque high-density polyethylene (HDPE) bottles to which $^{15}N\text{-}NO_2^-$ was added to achieve a final tracer concentration of 0.1 µM. An initial 50 mL subsample ($T_{initial}$) was collected from each HDPE bottle immediately following tracer addition and frozen at -20°C until analysis ashore. The 55%, 10%, 1%, and MLD sample bottles were incubated in the on-deck incubator for 20-30 hours while the 200 m and 500 m samples were incubated in a ~2°C cold room. The experiments were terminated by collection and freezing of 50 mL T_{final} subsamples.

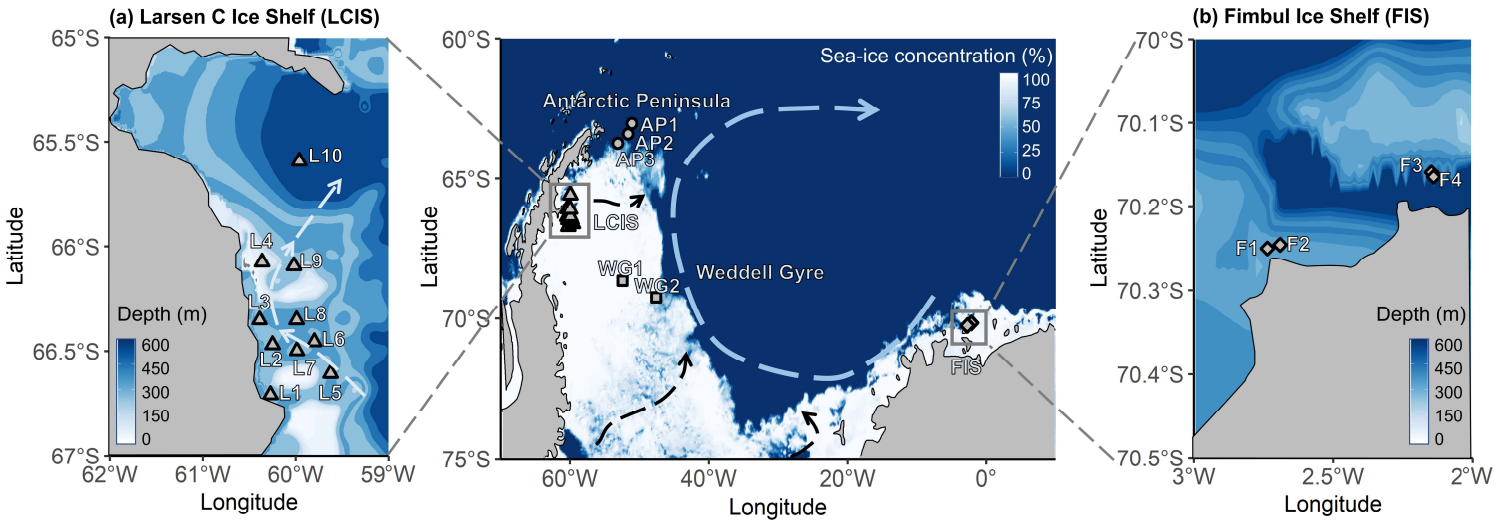


Figure 3.1. Maps of the Weddell Sea, Larsen C Ice Shelf (LCIS; insert a) and Fimbul Ice Shelf (FIS; insert b) showing the position of the stations where rate experiments were conducted during the Weddell Sea Expedition in January/February 2019. The symbols represent the different regions of the Weddell Sea sampled during the expedition (circle – Antarctic Peninsula (AP); diamond – FIS; triangle – LCIS; square – Weddell Gyre (WG)). The general cyclonic circulation of the Weddell Gyre (dashed blue arrow) is illustrated on the central map, with the dashed black arrows indicating the input of modified water masses from Filchner-Ronne Ice shelf (FRIS) and LCIS (Gordon et al. 1993; Schröder et al. 2002; Schodlok et al. 2002). The hypothesized circulation at LCIS (Nicholls et al. 2004; Hutchinson et al. 2020) is shown by the dashed light-blue arrow in insert (a). The 3.125 km sea-ice concentration data from 31 January 2019 shown in the central panel were taken from ftp://ftp-projects.cen.uni-hamburg.de/seaice/AMSR2/3.125km and the bathymetry data (inserts a and b) were taken from ETOPO1 (NOAA National Geophysical Data Center 2009).

3.2.2. Nutrients

3.2.2.1. Nutrient concentration analysis

NO_3^-+NO_2^- and silicic acid ($Si(OH)_4$) concentrations were measured using a Lachat QuickChem flow injection analysis platform following published auto-analysis protocols (Diamond, 1994; Grasshoff, 1976) in a configuration with a detection limit of 0.5 µM. Duplicate samples were measured for NO_3^- +NO_2^- and $Si(OH)_4$ on different days, and the standard deviation for duplicates was $\leq$0.5 µM, with a lower standard deviation for lower-concentration samples. NO_3^- concentrations were determined by subtraction of NO_2^- from NO_3^-+NO_2^-. Concentrations of phosphate (PO_4^{3-}) and NO_2^- were measured shipboard by standard benchtop colourimetric methods (Strickland and Parsons 1968; Bendschneider et al. 2020; Parsons et al. 1984) using a Thermo Scientific Genesis 30 Visible spectrophotometer. The detection limit was 0.05 µM and the standard deviation for duplicate samples was ≤0.05 µM. Aliquots of a certified reference material (JAMSTEC; Lot CG) were analysed during autoanalyzer and manual runs to ensure measurement accuracy.

NH_4^+ concentrations were measured shipboard following the fluorometric method of Holmes et al. (1999) using a Turner Designs Trilogy fluorometer equipped with a UV module. The detection limit was <0.05 µM and the standard deviation for duplicate samples was ≤0.05 µM. The matrix effect (ME) that results from the calibration of seawater samples with Milli-Q water standards was calculated using the standard addition method (Saxberg and Kowalski, 1979). All samples were corrected for the ME (Taylor et al., 2007), which was always <10% and typically ≤5%. Urea-N concentrations were measured via the colourimetric method of Revilla et al. (2005) using a Thermo Scientific Genesis 30 Visible spectrophotometer equipped with either a 1 cm- or 5 cm-pathlength cell. The detection limit was 0.05 µM and the standard deviation for duplicate samples was ≤0.05 µM. Hereafter, we use "urea" when referring to urea-N.

3.2.1.2. Estimating nutrient depletion

The net decrease in euphotic zone nutrient concentrations following nutrient recharge in winter (i.e., the extent of nutrient depletion due to consumption by phytoplankton), between the start of the growing season until the time of our sampling, can be estimated for each station as:

$$\text{X depletion} = [X]_{source} - [X]_{measured} \quad (3.1)$$

where $[X]_{source}$ is the average $[NO_3^-]$, $[Si(OH)_4]$ or $[PO_4^{3-}]$ in winter water (WW; a shallow temperature minimum layer underlying ASW that is the remnant of the winter mixed layer and considered representative of pre-bloom surface conditions) and $[X]_{measured}$ is the measured summertime nutrient concentration (Le Corre and Minas 1983; Jennings et al. 1984; Goeyens et al. 1995; Hoppema et al. 2007).

Seasonal melting of sea-ice in the Weddell Sea introduces low-salinity, low-nutrient waters that dilute the biogeochemistry of the mixed layer (Eicken, 1993), potentially leading to an overestimation of phytoplankton-driven nutrient depletion. We correct for the depletion in the surface $[NO_3^-]$, $[Si(OH)_4]$ or $[PO_4^{3-}]$ due to sea-ice melt (i.e., the dilution effect) as:

$$\text{X depletion}_{(\text{corrected})} = \text{X depletion} - \text{X depletion}_{(\text{melt water})} \quad (3.2a)$$

where $\text{X depletion}_{(\text{melt water})}$ is the decrease in surface $[NO_3^-]$, $[Si(OH)_4]$ or $[PO_4^{3-}]$ due to sea-ice melt, calculated as:

$$\text{X depletion}_{(\text{melt water})} = [X]_{\text{sea-ice}}\,(f_{\text{sea-ice}}) + [X]_{\text{source}}(1\text{-}f_{\text{sea-ice}}) \quad (3.2b)$$

Here, the nutrient concentrations in summertime sea-ice ($[X]_{\text{sea-ice}}$) are assumed to be: $[NO_3^-]_{\text{sea-ice}}$ = 1 µM, $[Si(OH)_4]_{\text{sea-ice}}$ = 5 µM, and $[PO_4^{3-}]_{\text{sea-ice}}$ = 0.3 µM (Fripiat et al., 2014, 2017), and:

$$f_{\text{sea-ice}} = \frac{\text{salinity}_{\text{measured}} - \text{salinity}_{\text{source}}}{\text{salinity}_{\text{sea-ice}} - \text{salinity}_{\text{source}}} \quad (3.2c)$$

with $\text{salinity}_{\text{sea-ice}}$ taken to be 5 based on sea-ice salinity measurements made during the cruise (Dowdeswell et al., 2019) and $\text{salinity}_{\text{source}}$ set to 34.2 at FIS and 34.4 at the other stations (the salinity of WW; Fig. 3.2g). On average, correcting for sea-ice melt changed the estimates of X depletion by 0.4 ± 0.9%. Hereafter, all references to nutrient depletion are to the computed values of $\text{X depletion}_{(\text{corrected})}$. The approach above for calculating $\text{X depletion}_{(\text{corrected})}$ assumes, following correction for sea-ice melt, that nutrient drawdown is due to phytoplankton assimilation only, a reasonable assumption in the Weddell Sea in summer.

3.2.2. Uptake rates

Filters containing the organic matter from the incubations were oven-dried for 24 hours at 40°C, then folded into tin cups. Samples were analysed using a Flash Elemental Analyser 1112 Series coupled to a Delta V Plus isotope ratio mass spectrometer (IRMS) in a configuration with a detection limit of 2 µg C and 1 µg N. Blanks (combusted unused filters + tin cups) and laboratory running standards, calibrated to certified IAEA reference materials, were run after every five samples.

The specific rates of carbon fixation (V_C) and NO_3^-, NH_4^+ and urea uptake ($V_{NO_3^-}$, $V_{NH_4^+}$, V_{urea}; d^{-1}) were calculated according to equation 2 in Dugdale and Wilkerson (1986). NPP and the absolute rates of NO_3^-, NH_4^+ and urea uptake (ρNO_3^-, ρNH_4^+ and ρurea; µM d^{-1}) were then determined by multiplying

V_C by the concentration of particulate organic carbon ([POC]) and $V_{NO_3^-}$, $V_{NH_4^+}$ and V_{urea} by the concentration of particulate organic nitrogen ([PON]) (Dugdale and Wilkerson 1986; eq. 3).

3.2.3. NO_2^- oxidation rates

The $T_{initial}$ and T_{final} samples from the NO_2^- oxidation incubations were measured for the $\delta^{15}N$ of NO_3^- ($\delta^{15}N_{NO3}$; where $\delta^{15}N = ((^{15}N_{sample}/^{14}N_{sample})/(^{15}N_{standard}/^{14}N_{standard}) - 1) \times 1000$) using the denitrifier method (Sigman et al. 2001; McIlvin and Casciotti 2011). Prior to isotopic analysis, all samples were treated with sulfamic acid to remove NO_2^- as the denitrifier method converts both NO_2^- and NO_3^- to N_2O gas (Granger and Sigman, 2009); the difference in $\delta^{15}N_{NO3}$ between the T_{final} and $T_{initial}$ samples was then taken as the $^{15}NO_3^-$ enrichment due to $^{15}NO_2^-$ oxidation (Peng et al. 2015). Results were referenced to atmospheric N_2 using certified reference materials (IAEA-NO-3, USGS-34, and USGS-32; Gonfiantini 1984; Böhlke and Coplen 1995; Böhlke et al. 2003). The rate of NO_2^- oxidation ($V_{NO_2^-}$; nM d^{-1}) was calculated following Peng et al. (2015) as:

$$V_{NO_2^-} = \frac{\Delta[^{15}NO_3^-]}{f_{NO_2^-}^{15} \times t} \tag{3.3}$$

where $\Delta[^{15}NO_3^-]$ is the difference in the concentration of $^{15}NO_3^-$ between the end and the start of the experiment (i.e., $T_{final} - T_{initial}$) due to NO_2^- oxidation, $f_{NO_2^-}^{15}$ is the fraction of $^{15}NO_2^-$ at the start of the incubation, and t is the length of the incubation (days). The detection limit for $V_{NO_2^-}$ ranged from 0.06-0.46 nM d^{-1} (calculated following Santoro et al. 2013). We take $V_{NO_2^-}$ as a measure of the nitrification rate given that NO_2^- oxidation is the step in the nitrification pathway that produces NO_3^-.

To determine relative carbon export potential at each station, we calculated the f-ratio (a measure of new production relative to total (i.e., new+regenerated) production) using the absolute N uptake and NO_2^- oxidation rates and a modified version of the Eppley and Peterson (1979) equation:

$$\text{f-ratio}_{(\text{excluding urea})} = \frac{\rho NO_3^- - V_{NO_2^-}}{\rho NO_3^- + \rho NH_4^+} \tag{3.4a}$$

$$\text{f-ratio}_{(\text{including urea})} = \frac{\rho NO_3^- - V_{NO_2^-}}{\rho NO_3^- + \rho NH_4^+ + \rho urea} \tag{3.4b}$$

Equation 3.4a and b account for euphotic zone nitrification (Mdutyana et al. 2020), which yields regenerated rather than new NO_3^- that is then available for phytoplankton to consume. Not accounting for $V_{NO_2^-}$ could result in the f-ratio being overestimated (Yool et al. 2007). Equation 3.4b accounts for

urea uptake, that was either measured (at the LCIS stations and WG1) or calculated (at the AP, FIS and WG2) (see section 3.3.3.4 below).

3.2.4. Phytoplankton taxonomy and carbon biomass

At all stations, microphytoplankton samples were collected between the surface and 30 m using a HYDROBIOS conical plankton net (r = 12.5 cm; h = 50 cm) with a mesh size of 55 µm. Samples were transferred to 50 mL centrifuge tubes, fixed with 10 µL of 25% glutaraldehyde, and stored at room temperature in the dark until later analysis via light and scanning electron microscopy. Additionally, samples for flow cytometry were collected in 50 mL centrifuge tubes from Niskin bottles fired at the 55%, 10%, and 1% PAR depths. These samples were fixed with 10 µL of 25% glutaraldehyde and stored in the dark at 4°C until analysis.

Onshore, each preserved net-sample was homogenized, and 40 µL was wet mounted on a slide. All the cells on the slide with intact chloroplasts (i.e., alive at the time of sampling) were counted at 400x or 630x magnification using a Zeiss AxioScope A1 light microscope (LM). The number of cells mL^{-1} was calculated as:

$$\text{cells mL}^{-1} = \left[\text{A}\left(\frac{1}{\text{mL}}\right)\left(\frac{\text{n}}{\text{V}}\right)\right] \tag{3.5}$$

where A is the number of cells per 40 µL, mL is the volume of water sampled (1470000 mL; computed using the volume of a cylinder, $\pi\, r^2\, h$, where r = 125 mm and h = 30000 mm depth), n is the total volume of concentrated sample, and V is 40 µL (the volume of concentrated sample analysed).

An aliquot of 5 mL from each preserved sample was cleaned by removing carbonate particles and organic matter using 10% hydrochloric acid and 37% hydrogen peroxide, respectively. After thorough rinsing with distilled water, permanent slides were prepared by pipetting the cleaned material onto acid-washed coverslips, air drying them overnight, and mounting the cover slips onto glass slides using Naphrax® mountant (refractive index = 1.7). The permanent slides were examined using a Zeiss AxioScope A1 LM equipped with differential interference contrast at 1000x magnification (under oil immersion) for identification of the diatom cells to the lowest taxonomic classification possible. Stubs were also prepared from the cleaned material for Scanning Electron Microscopy (SEM), with a JEOL JSM 7001F field emission SEM used to visualize the morphological features not evident under LM.

The average size (µm) and carbon content (pg C $cell^{-1}$) of each identified diatom species was taken from Leblanc et al. (2012) for high latitude locations (50 – 70°S) (Table A1), and the carbon content of colonial *P. antarctica* was estimated as 13.6 pg C $cell^{-1}$ (Mathot et al., 2000) for single cells within a

colony. Since the majority of *P. antarctica* were in spherical colony form, the total colony carbon biomass (C_{COL}) was calculated as:

$$C_{COL} = [13.60 \times N_C] + C_M \quad (3.6)$$

where N_C is the number of cells counted per litre, C_M is the mucus-related carbon calculated as $C_M = 0.213 \times V_{COL} + 4.58$, and V_{COL} is the volume of the spherical colony, calculated as $V_{COL} = 417 \times N_C^{1.67}$ (Mathot et al., 2000). The uncertainty of the C_{COL} is ± 20% at 95% significance level.

Flow cytometry samples were analyzed using a BD LSR II SORP flow cytometer with blue/red/green laser configuration. The size-class to which each cell belonged was defined based on its forward scatter area (FSC-A) relative to the FSC-A of 2.8 µm and 20 µm beads (Fig. B1a). Once categorized as either picoplankton (<2.8 µm), nanoplankton (2.8-20 µm), or microplankton (>20 µm), the cells were grouped into six populations based on their orange fluorescence (indicative of phycoerythrin; PE) relative to their red fluorescence (indicative of chlorophyll-a; chl-a): two *Synechococcus* populations (Syn 1 and Syn 2), one picoeukaryote population (PicoEuk), two nanoeukaryote populations (NanoEuk 1 and NanoEuk 2), and one microeukaryote population (MicroEuk; see section B2 in Appendix B for details of population identification). The biovolumes of the eukaryotic populations were estimated based on their FSC-A relative to that of six beads of known size and volume (Fig. B1c; Table B2). *Synechococcus* had an unrealistically high measured FSC-A, which is an artefact of the high ratio of photosystem I to photosystem II of the group compared to the other phytoplankton populations. This elevates electron chain activity, leading to an increase in the emission spectrum and low excitation of the *Synechococcus* populations (Kaprelyants and Kell 1993; Sunda and Huntsman 2015). The biovolume of *Synechococcus* was thus assumed to be 1 μm^3 (Kana and Glibert, 1987; Paulsen et al., 2015). Biovolume is used here as a proxy for biomass.

3.3. Results

3.3.1. Water column hydrography

Throughout the study region, relatively cool and fresh (-2 to 0°C and 33.0 to 34.5) ASW occurred between the surface and 135 m (Fig. 3.2). Through this layer and down to 200 m, salinity increased with depth while temperature decreased, reaching a local minimum (-1.6°C) at ~100 m. These hydrographic changes are characteristic of WW, which is considered a summertime record of winter conditions and a reflection of the initial state from which the mixed layer evolves over the spring/summer growing season (Altabet and Francois, 2001). Below WW at the AP and WG stations, salinity remained constant while temperature increased with depth, reaching a local maximum (0.5°C) at 500 m and 300 m for the AP and WG, respectively. This feature is characteristic of Warm Deep Water (WDW), a temperature maximum layer that is a modified form of Circumpolar Deep Water

(CDW) (Muench and Gordon, 1995; Fahrbach et al., 1995). Below WW at the LCIS and FIS stations, salinity increased, and temperature decreased with depth, reaching a local salinity maximum (34.6 at LCIS and 34.3 at FIS) and temperature minimum (≤ -1.8°C). The increase in salinity is characteristic of High Salinity Shelf Water (HSSW) produced by brine rejection during sea-ice formation, while the decrease in temperature is indicative of Ice Shelf Water (ISW) produced by the supercooling of ASW under the ice shelves (Fahrbach et al. 1995; Nicholls et al. 2009; Hutchinson et al. 2020). The densities of WW, WDW, HSSW, and ISW are contiguous, with the mixed product of these waters termed Modified Warm Deep Water (MWDW) (Fahrbach et al., 1995). Below WDW at the AP and WG stations, temperature decreased due to the presence of Weddell Sea Deep Water (WSDW; temperature range of -0.7 to 0°C) and Weddell Sea Bottom Water (WSBW; temperature ≤ -0.7°C) (Fahrbach et al., 1995; Muench and Gordon, 1995).

Variability in the density of ASW was observed among the stations (Fig. 3.2a). The surface density profiles at the AP, WG, and early-summer FIS stations were very similar, while the late-summer density profile at FIS revealed lower-density waters in the upper 100 m. At LCIS, the surface density profiles were highly variable, and no consistent pattern was observed, although the most northern stations (L9 and L10; Fig. 3.1) were characterised by the lowest densities. Stations L1 and L3, situated closest to the ice shelf, were characterised by the highest densities, contiguous with the underlying WW layer.

The MLD appeared most strongly controlled by salinity at all stations and was always shallower than the depth of the euphotic zone (Z_{eu}; Table 3.1; Fig. 3.2a-d), the latter defined as the depth to which 1% of surface PAR penetrated (Kirk 1994). The deepest MLD and Z_{eu} were observed at FIS in early summer (average MLD of 103.0 ± 36.6 m and Z_{eu} of 91.7 ± 14.4 m; n = 3), while the shallowest MLD and Z_{eu} were observed at LCIS (average MLD of 13.9 ± 5.9 m and Z_{eu} of 28.5 ± 9.1 m; n = 10) (Fig. 3.2d; Table 3.1). The rates of NPP, N uptake and nitrification were therefore trapezoidally-integrated to Z_{eu} rather than to the MLD since we assume that phytoplankton were active at least to the depth of 1% PAR.

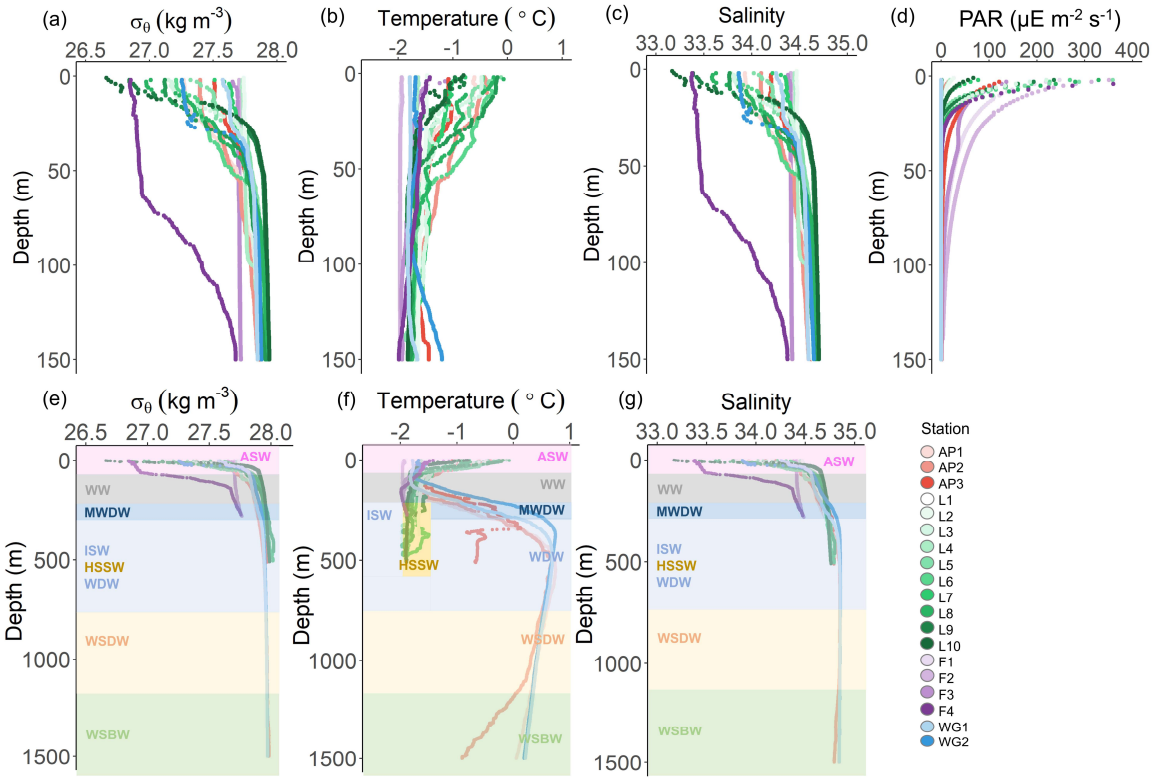


Figure 3.2. Depth profiles of (a) potential density (σ_θ), (b) potential temperature, (c) absolute salinity, and (d) photosynthetically active radiation (PAR) in the upper 150 m and (e) σ_θ, (f) potential temperature, and (g) absolute salinity in the upper 1500 m at all stations. The water masses present at each station, identified by their temperature and salinity characteristics, are denoted in panels (e-g) as follows: WSBW – Weddell Sea Bottom Water, WSDW – Weddell Sea Deep Water, WDW – Warm Deep Water, MWDW – Modified Warm Deep Water, ISW – Ice Shelf Water, HSSW – High Salinity Shelf Water, WW – Winter Water, ASW – Antarctic Surface Water. In panel (f), the dark yellow rectangle indicates HSSW. The general station locations are indicated by the different marker colours: red shades – Antarctic Peninsula, green shades – Larsen C Ice Shelf, blue shade –Weddell Gyre, light purple shades – early summer Fimbul Ice Shelf, and dark purple – late summer Fimbul Ice Shelf.

3.3.2. Nutrient concentrations

The concentrations of the regenerated N forms (i.e., NH_4^+ and urea) were generally low in the surface and increased with depth to reach a maximum in the shallow subsurface (Fig. 3.3a and b). A sharp maximum in the NH_4^+ concentration was observed near Z_{eu} at all stations, indicative of the depth of maximum net remineralisation. Urea concentrations were more variable, likely due to variability in the processes that produce this N form (e.g., bacterial excretion; Berges and Mulholland 2008). The highest average concentrations of regenerated N in the euphotic zone were observed at LCIS and FIS in late summer (0.62 ± 0.30 μM for NH_4^+ and 0.21 ± 0.07 μM for urea), while the lowest concentrations were observed at FIS in early summer (below detection for both NH_4^+ and urea). Elevated regenerated N

concentrations were also observed at the AP stations (euphotic zone average of 0.8 ± 0.3 μM for NH_4^+ and 0.2 ± 0.06 μM for urea), while low concentrations were observed at the WG stations (euphotic zone average of 0.3 ± 0.1 μM for NH_4^+ and 0.1 ± 0.0 μM for urea).

The concentrations of NO_2^- were generally low throughout the euphotic zone, and decreased to below detection by 120 m at the FIS, AP, and WG stations (with the exception of a single sample from the early-summer FIS), and by 500 m at LCIS (Fig. 3.3c). A high degree of variability was observed, with the highest surface-layer NO_2^- concentrations occurring in the WG and at FIS in late summer (average euphotic zone NO_2^- concentrations of 0.08 ± 0.06 μM and 0.12 ± 0.03 μM, respectively).

The euphotic zone concentrations of NO_3^-, $Si(OH)_4$ and PO_4^{3-} decreased towards the surface due to assimilation by phytoplankton (Fig. 3.3d-f). The lowest surface concentrations of NO_3^- and PO_4^{3-} were observed at LCIS (16.6 ± 3.8 μM and 1.3 ± 0.4 μM, respectively) and of $Si(OH)_4$ was observed at FIS in late summer (46.1 ± 0.8 μM). The highest surface concentrations of NO_3^-, PO_4^{3-} and $Si(OH)_4$ occurred in the WG (28.8 ± 2.4 μM, 2.0 ± 0.54 μM, and 70.1 ± 3.8 μM, respectively). Elevated $Si(OH)_4$ and PO_4^{3-} concentrations were observed between 200 and 500 m at the AP and WG stations due to the presence of WDW at these stations versus shelf waters (i.e., ISW and HSSW) at LCIS and FIS. The depth of maximum remineralisation in the open Weddell Sea is 300-500 m, the depth range occupied by WDW (Vernet et al. 2019, and references therein). The high rates of remineralisation, and therefore nutrient accumulation, in WDW account for the elevated nutrient concentrations observed in WDW relative to the shelf water masses (Whitworth and Nowlin, 1987). Estimates of NO_3^-, $Si(OH)_4$, and PO_4^{3-} depletion (i.e., X $depletion_{(corrected)}$; eq. 3,2) were highest at LCIS (average NO_3^- depletion of 8.3 ± 3.9 μM, $Si(OH)_4$ depletion of 8.3 ± 4.0 μM, and PO_4^{3-} depletion of 0.6 ± 0.3 μM), while the lowest nutrient depletions occurred in early summer at FIS (average NO_3^- depletion of 0.3 ± 0.3 μM, $Si(OH)_4$ depletion of 0.6 ± 0.6 μM, and PO_4^{3-} depletion of 0.00 ± 0.02 μM) (Fig. 3.4a-c; Table 3.1).

Variations in the depletion ratios of $Si(OH)_4$:NO_3^- and NO_3^-:PO_4^{3-} can be used as indicators of the nutrient status of the phytoplankton community, particularly diatoms. Under iron-replete conditions, diatoms have been observed to consume $Si(OH)_4$ and NO_3^- in a ratio of ~1:1, and NO_3^- and PO_4^{3-} in a ratio of ~14:1 (Hutchins and Bruland, 1998; Takeda, 1998; Ragueneau et al., 2000; Mosseri et al., 2008), while under conditions of limitation, the ratio of $Si(OH)_4$:NO_3^- uptake rises (to >2:1) and NO_3^-:PO_4^{3-} uptake decreases (to as low as 10:1) (Arrigo et al., 1999; Franck et al., 2000; Brzezinski et al., 2003; Green and Sambrotto, 2006; Mosseri et al., 2008; Weber and Deutsch, 2010a; Martiny et al., 2013). Additionally, the dominance of one phytoplankton species over another may cause deviations in the NO_3^-:PO_4^{3-} depletion ratio. For example, in regions dominated by *P. antarctica*, Arrigo et al. (1999) observed a NO_3^-:PO_4^{3-} depletion ratio of ~20:1, while in areas dominated by iron-deplete diatoms, this ratio was ~10:1. The NO_3^-:PO_4^{3-} depletion ratios can thus also yield insights into the dominant

phytoplankton species active in the upper water column. In our study, the average euphotic zone $Si(OH)_4$:NO_3^- depletion ratios ranged from 0.5 to 6.1 (Table 3.1), with the highest ratios estimated for the WG stations (average of 5.4 ± 5.5) and at FIS in late summer (average of 2.3 ± 0.5). The euphotic zone average NO_3^-:PO_4^{3-} depletion ratios were more variable, ranging from 3.7 ± 1.5 to 48.6 ± 11.5, with the lowest ratios computed for the WG stations (average of 4.1 ± 1.5) and the highest for FIS in early summer (average of 33.7 ± 3.6). In the latter case, the degree of $Si(OH)_4$ and PO_4^{3-} depletion was extremely low (Table 3.1), which likely accounts for the variable and anomalous $Si(OH)_4$:NO_3^- and NO_3^-:PO_4^{3-} depletion ratios computed for stations F1-F3.

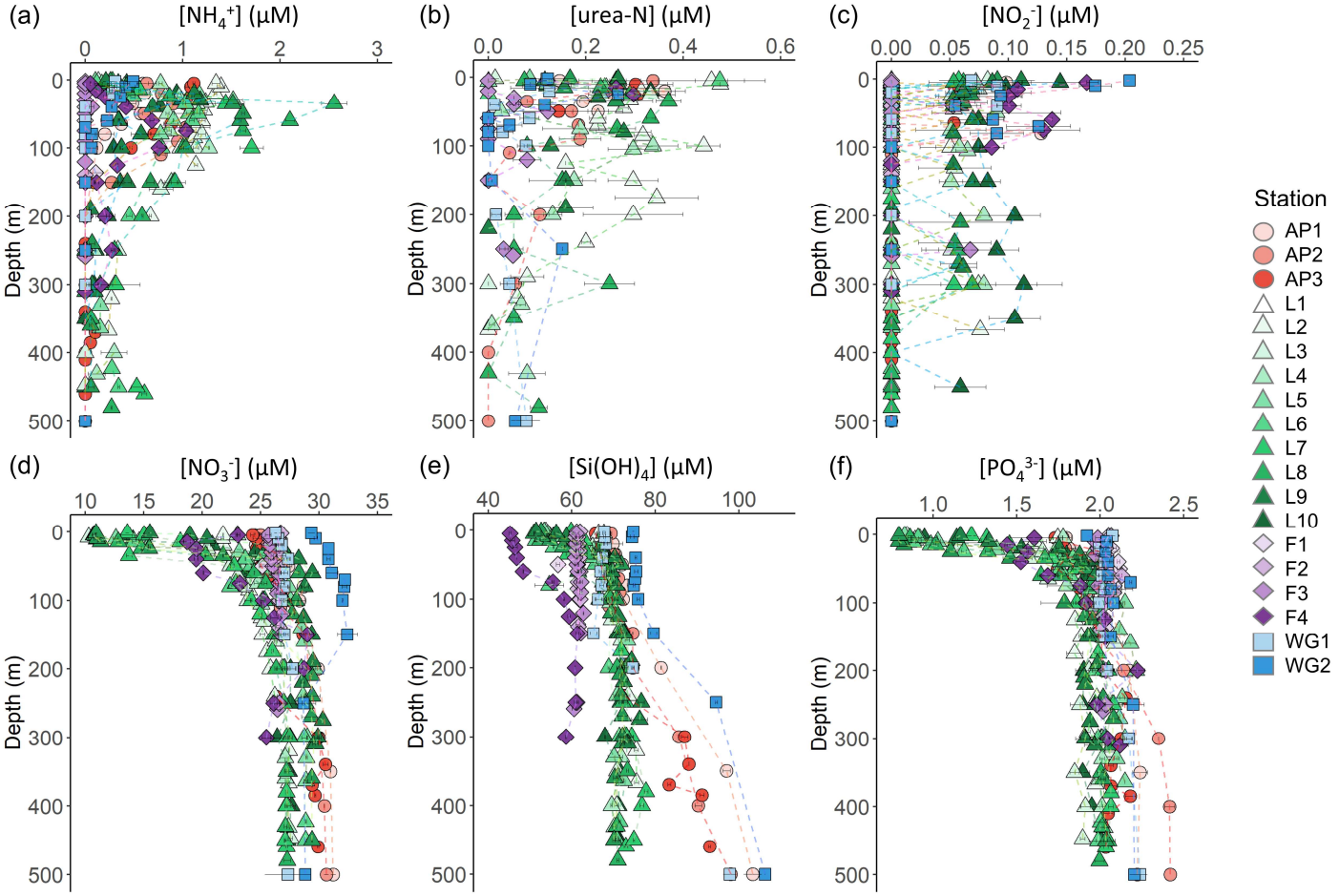


Figure 3.3. Depth profiles (0-500 m) of (a) NH_4^+, (b) urea-N, (c) NO_2^-, (d) NO_3^-, (e) $Si(OH)_4$, and (f) PO_4^{3-} concentrations. For all panels, the error bars represent ± 1 SD of replicate samples (n = 2-3). For NO_3^-, which was calculated as NO_3^-+NO_2^- – NO_2^-, error has been propagated according to standard statistical practices. Note that the x-axis scales in panels (d-f) do not start at zero.

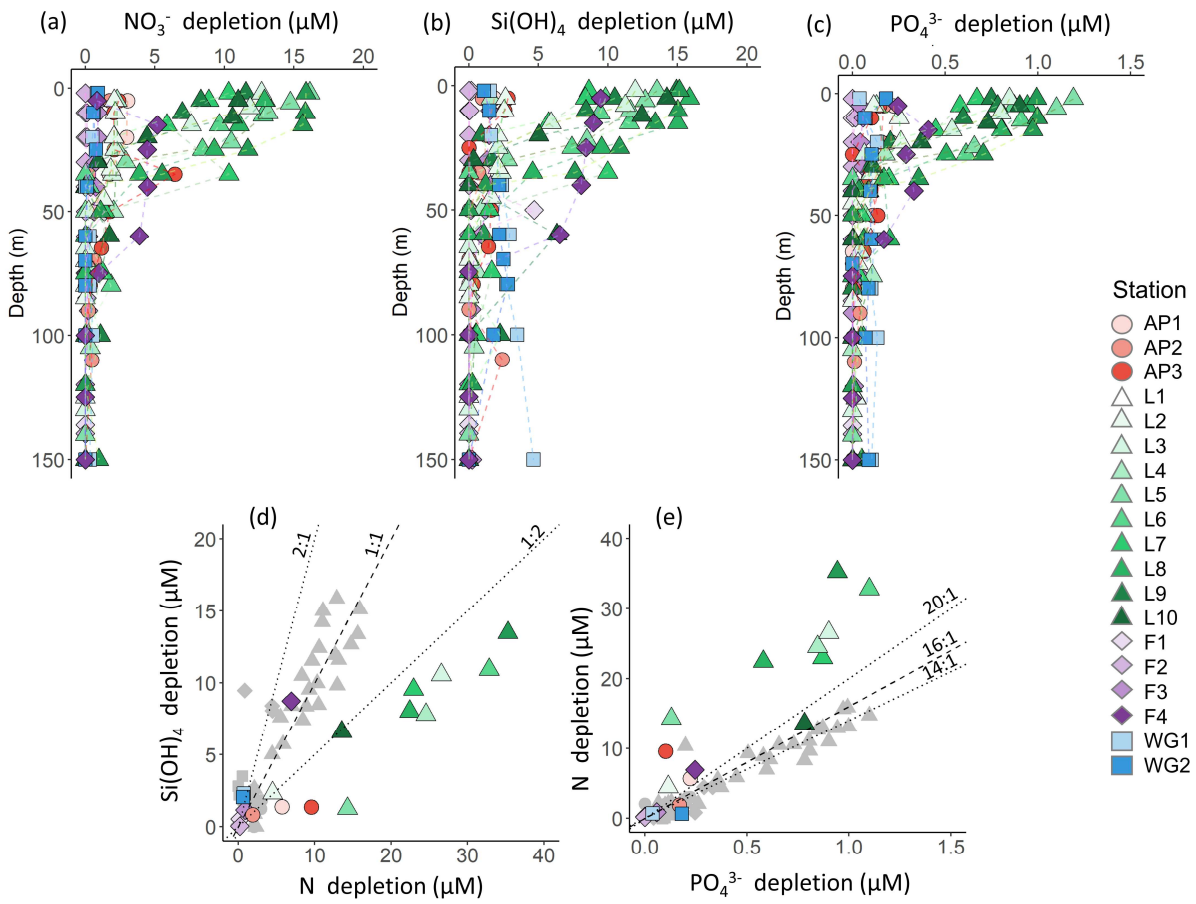


Figure 3.4. Depth profiles (0-150 m) of (a) NO_3^- depletion, (b) $Si(OH)_4$ depletion, and (c) PO_4^{3-} depletion at each station. Also shown are scatterplots of (d) $Si(OH)_4$ depletion versus total N depletion (coloured symbols; see text for details) and $Si(OH)_4$ depletion versus NO_3^- depletion (grey symbols) and (e) PO_4^{3-} depletion versus total N depletion (coloured symbols) and PO_4^{3-} depletion versus NO_3^- depletion (grey symbols) at each station. The dashed line in panel (d) represents the 1:1 Si:N depletion ratio, expected for iron-replete diatoms (Ragueneau et al. 2000; Hutchins and Bruland 1998; Takeda 1998; Mosseri et al. 2008), while the dotted lines represent the 2:1 Si:N ratio, expected for iron-limited diatoms (Arrigo et al., 1999; Franck et al., 2000; Brzezinski et al., 2003; Green and Sambrotto, 2006; Mosseri et al., 2008; Weber and Deutsch, 2010a; Martiny et al., 2013), and the 1:2 Si:N ratio, indicative of enhanced activity of non-siliceous phytoplankton. The dashed line in panel (e) represents the 16:1 N:P depletion ratio (the Redfield ratio), while the dotted lines represent the 20:1 N:P ratio, expected for *P. antarctica*, and the 14:1 N:P ratio, expected for iron-replete diatoms (Hutchins and Bruland 1998; Takeda 1998; Arrigo et al. 1999; Ragueneau et al. 2000; Mosseri et al. 2008).

3.3.3. Upper ocean biomass, NPP and N uptake rates

3.3.3.1. Particulate organic carbon and nitrogen

The highest concentrations of POC and PON were observed in the surface at all stations (Fig. 3.5a and b), decreasing towards Z_{eu} (Fig. 3.5g and h). Averaged over the euphotic zone, the lowest POC and PON concentrations occurred in early summer at FIS (4.6 ± 1.5 µM and 0.3 ± 0.1 µM, respectively) and the highest at LCIS (17.9 ± 7.3 µM and 2.5 ± 0.8 µM; Table 3.2). Across the region, the biomass C:N ratio was fairly uniform throughout the euphotic zone, except at stations F1, F2, WG1, and WG2 (Fig. 3.5c, f and i). In general, the FIS and WG stations were characterized by significantly higher C:N ratios than those expected from Redfield stoichiometry (C:N = 6.63:1), averaging 16.5 ± 8.8 and 12.3 ± 1.8, respectively. By contrast, at the LCIS stations, the biomass C:N ratios were close to the Redfield ratio (7.4 ± 1.9), while the AP stations were characterized by slightly higher C:N ratios (8.3 ± 2.5).

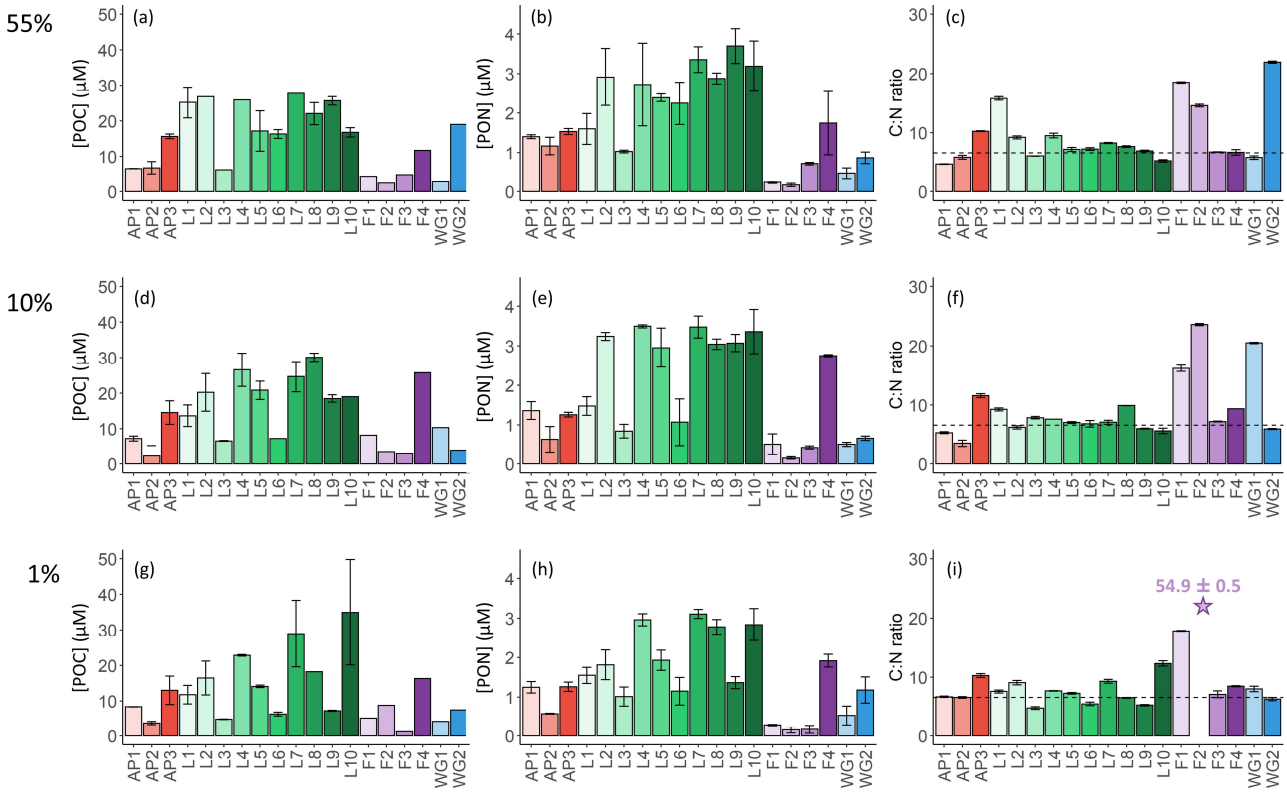


Figure 3.5. Bar plots of (a, d, g) POC concentrations, (b, e, h) PON concentrations, and (c, f, i) biomass C:N ratios measured at the 55% (a-c), 10% (d-f), and 1% light levels (g-i). The stations are labelled on the x-axis, and the general stations locations are indicated by the different colours: red shades – Antarctic Peninsula, green shades – Larsen C Ice Shelf, blue shade –Weddell Gyre, light purple shades – early summer Fimbul Ice Shelf, and dark purple – late summer Fimbul Ice Shelf. The dotted black horizontal line in panels (c), (f), and (i) shows the Redfield C:N ratio of 6.63. The purple star in panel (i) indicates the anomalously high C:N ratio estimated for the 1% PAR depth at station F2. The error bars represent ± 1 SD of replicate samples (n = 2-6). Where applicable, the error has been propagated according to standard statistical practices.

3.3.3.2. Rates of NPP and N uptake

At all stations, NPP was generally highest at the surface (Fig. 3.6a) and decreased towards Z_{eu} (Fig. 3.6i). The highest depth-specific (as opposed to integrated) rates were observed at LCIS (except at station L10 where the rates were very low), while the lowest rates occurred in early summer at FIS (with particularly low rates measured at station F1; Fig. 3.6a, e and i). At the WG stations and at FIS in late summer, the rates of NPP were comparable to the lower end of the rates observed at LCIS, while NPP along the AP increased shoreward (i.e., the lowest rates were observed at AP1 and the highest at AP3) to values similar to those observed at LCIS. The highest euphotic zone-integrated rates of NPP were observed at AP3 (65.0 ± 0.1 mmol m^{-2} d^{-1}) and L5 (61.0 ± 0.7 mmol m^{-2} d^{-1}), while the lowest occurred at L10 (1.8 ± 0.04 mmol m^{-2} d^{-1}) (Table 3.2).

As per NPP, the rates of ρNO_3^- decreased towards Z_{eu} at all stations (Fig. 3.6b, f and j), as did the extent of NO_3^- depletion (Fig. 3.4a). The depth-specific rates of ρNO_3^- were highest at LCIS and lowest in early summer at FIS. However, because the euphotic zone was generally shallower at LCIS than at the other stations, the euphotic zone-integrated rates of ρNO_3^- were fairly similar across the study region, with the largest variability observed at LCIS (Table 3.2). In late summer at FIS, integrated ρNO_3^- was on average higher than at LCIS (3.9 ± 0.03 mmol m^{-2} d^{-1} at F4 versus an average of 2.2 ± 1.1 mmol m^{-2} d^{-1} at LCIS), with depth-specific rates that were double those measured at FIS in early summer. The sea-ice at FIS had completely melted by late summer, which likely contributed to the increase in ρNO_3^- later in the season. The highest euphotic zone-integrated rates of ρNO_3^- were observed at stations F3 and L5 (4.8 ± 0.07 mmol m^{-2} d^{-1} and 4.7 ± 0.04 mmol m^{-2} d^{-1}, respectively). At L5, this elevated rate coincided with low euphotic zone NO_3^- concentrations (12.0 ± 1.9 µM; Fig. 3.3d) and a high degree of NO_3^- depletion (10.9 ± 2.3 µM; Fig. 3.4a). The lowest euphotic zone-integrated rates of ρNO_3^- occurred at station L10 (0.5 ± 0.0 mmol m^{-2} d^{-1}).

At all stations, rates of ρNH_4^+ increased with depth, reaching a maximum at Z_{eu} (Fig. 3.6c, g and k). The highest depth-specific rates of ρNH_4^+ were observed at LCIS and the lowest at FIS in early summer. Euphotic zone-integrated rates of ρNH_4^+ at the AP stations were comparable to those observed at LCIS (regional average of 3.3 ± 2.2 mmol m^{-2} d^{-1} and 2.5 ± 1.3 mmol m^{-2} d^{-1}, respectively), while the rates at the WG stations and at FIS in late summer were comparable to the lower end of the LCIS rates (average of 2.0 ± 0.2 mmol m^{-2} d^{-1} at WG and 1.9 ± 0.0 mmol m^{-2} d^{-1} at FIS). The early- to late-summer rise in the euphotic zone-integrated rates of ρNH_4^+ at FIS coincided with an increase in the average euphotic zone NH_4^+ concentration from below detection to 0.2 ± 0.1 µM (Fig. 3.3a). At the AP, LCIS, and WG stations, the rates of ρNH_4^+ were similar to the coincident rates of ρNO_3^-, while at FIS, ρNH_4^+ was less than half of ρNO_3^- (Table 3.2). The highest euphotic zone-integrated rates of ρNH_4^+ were observed at station AP3 (5.8 ± 0.0 mmol m^{-2} d^{-1}), coincident with a high average euphotic zone NH_4^+ concentration

(1.1 ± 0 µM). The lowest integrated ρNH_4^+ occurred at station F1 (0.4 ± 0.0 mmol m^{-2} d^{-1}) where the concentration of NH_4^+ in the euphotic zone was below detection.

Rates of ρurea were only measured at the LCIS stations and WG1 (Fig. 3.6d, h and l; Table 3.2). A high degree of variability in ρurea was observed at LCIS, with euphotic zone-integrated rates ranging from 0.2 to 1.1 mmol m^{-2} d^{-1} (average of 0.6 ± 0.3 mmol m^{-2} d^{-1}). This variability appears to be related to the urea concentrations, with the highest rates of ρurea coinciding with the highest ambient urea concentrations (e.g., station L5), and vice versa (e.g., station L4) (Fig. 3.3b). On average, the rates of ρurea in the WG were half the rates of ρNH_4^+, and urea concentrations were low (Fig. 3.3b; Table 3.2).

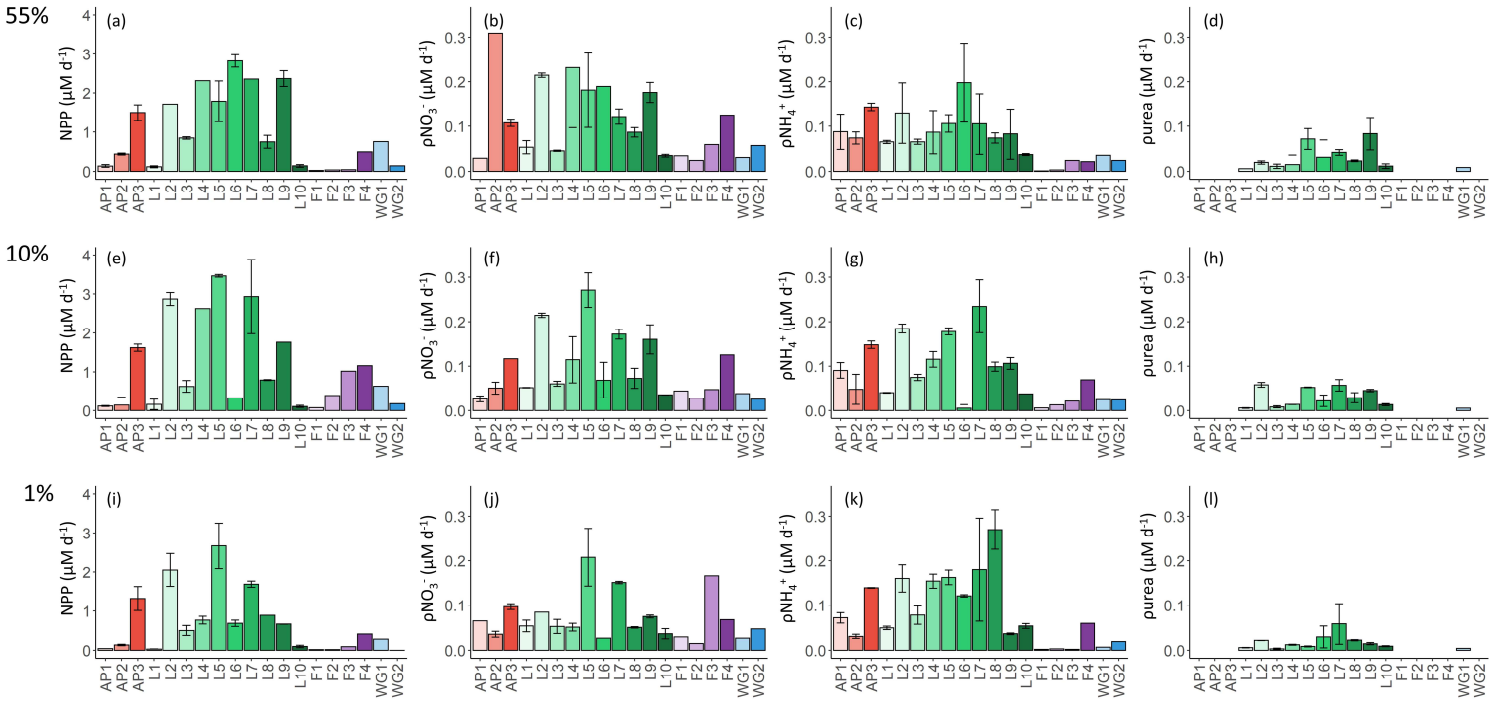


Figure 3.6. Daily rates of (a, e, i) NPP, (b, f, j) ρNO_3^-, (c, g, k) ρNH_4^+, and (d, h, l) ρurea for the 55% (a-d), 10% (e-h), and 1% light levels (i-l). Where there are no bars in panels (d), (h) and (l), no data are available. The stations are labelled on the x-axis, and the general station locations are indicated by the different colours: red shades – Antarctic Peninsula, green shades – Larsen C Ice Shelf, blue shade – Weddell Gyre, light purple shades – early summer Fimbul Ice Shelf, and dark purple – late summer Fimbul Ice Shelf. The error bars represent ± 1 SE of replicate experiments (n = 2).

3.3.3.3. Rates of nitrite oxidation

Rates of $V_{NO_2^-}$ were low throughout the euphotic zone across the study region (average euphotic zone-integrated rates of 20.8 ± 31.3 µmol m^{-2} d^{-1}), equivalent to 0 to 3.6% (average of 0.7 ± 1.1%) of ρNO_3^-, and increased rapidly below Z_{eu} (Fig. 3.7). The highest euphotic zone rates were observed at WG1 (depth-specific average of 6.3 ± 5.0 nM d^{-1}, integrated average of 113.6 ± 4.3 µmol m^{-2} d^{-1}), while the lowest rates occurred at the AP (depth-specific average of 0.0 ± 0.04 nM d^{-1}, integrated average of 0.8 ± 0.7 µmol m^{-2} d^{-1}).

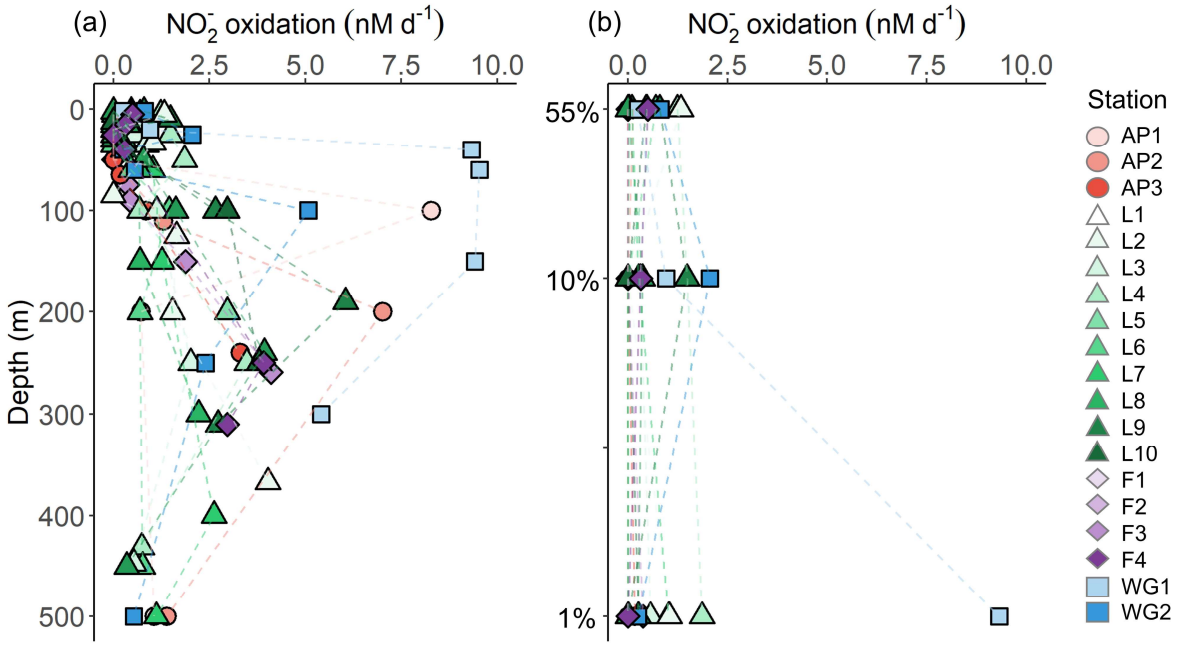


Figure 3.7. Depth profiles of NO_2^- oxidation rates measured at each station (a) between the surface and 500 m, and (b) within the euphotic zone.

3.3.3.4. f-ratio estimates

At the stations where urea uptake was measured (LCIS stations and WG1; 11 out of 19 stations; Fig. 3.6; Table 3.2), ρurea accounted for 8 ± 6% of total N uptake (i.e., $\rho NO_3^- + \rho NH_4^+ +$ ρurea). Excluding urea uptake when calculating the f-ratio would therefore overestimate the fraction of potentially exportable carbon by ~8%. We thus estimated urea uptake at the stations where it was not measured as:

$$\rho urea = (\rho NO_3^- + \rho NH_4^+) \times 0.08 \quad (3.7)$$

Eq. 3.7 may overestimate urea uptake at some of the stations, particularly where low urea concentrations were measured. Theoretically, ρurea can also be estimated by assuming that total N uptake should equal NPP/6.63, such that any difference between $\rho NO_3^- + \rho NH_4^+$ and NPP/6.63 is due to urea uptake. However, this approach underestimated urea uptake at all the stations where ρurea was directly

measured, probably because the use of a C:N ratio of 6.63:1 assumes balanced phytoplankton growth. We therefore chose to use eq. 3.7 to estimate urea uptake for the stations lacking ρurea measurements as this approach will yield a more conservative (i.e., lower) estimate of the fraction of potentially exportable carbon (section B3 in Appendix B for more details). Fig. 3.8 shows how including urea uptake affects the f-ratio throughout the sample region, with the white (no urea uptake measured) and hashed bars (urea uptake measured) indicating the amount by which the f-ratio decreased when urea uptake was included (i.e., eq. 3.4b versus eq. 3.4a).

The euphotic zone-integrated f-ratios were highest at FIS in early summer (average f-ratio$_{(\text{excluding urea})}$ of 0.79 ± 0.1 and f-ratio$_{(\text{including urea})}$ of 0.73 ± 0.09) and lowest at LCIS (average f-ratio$_{(\text{excluding urea})}$ of 0.50 ± 0.09 and f-ratio$_{(\text{including urea})}$ of 0.47 ± 0.08) (Fig. 3.8; Table 3.2). The variability in the f-ratios among stations appears to be largely related to the availability of NH_4^+. For example, at FIS in early summer there was no detectable NH_4^+ available to the phytoplankton and the highest f-ratios were observed (average f-ratio$_{(\text{excluding urea})}$ of 0.82 ± 0.08 and f-ratio$_{(\text{including urea})}$ of 0.76 ± 0.07), while in late summer, NH_4^+ concentrations were elevated (0.2 ± 0.1 μM) and the f-ratio declined (f-ratio$_{(\text{excluding urea})}$ of 0.68 ± 0.16 and f-ratio$_{(\text{including urea})}$ of 0.63 ± 0.15).

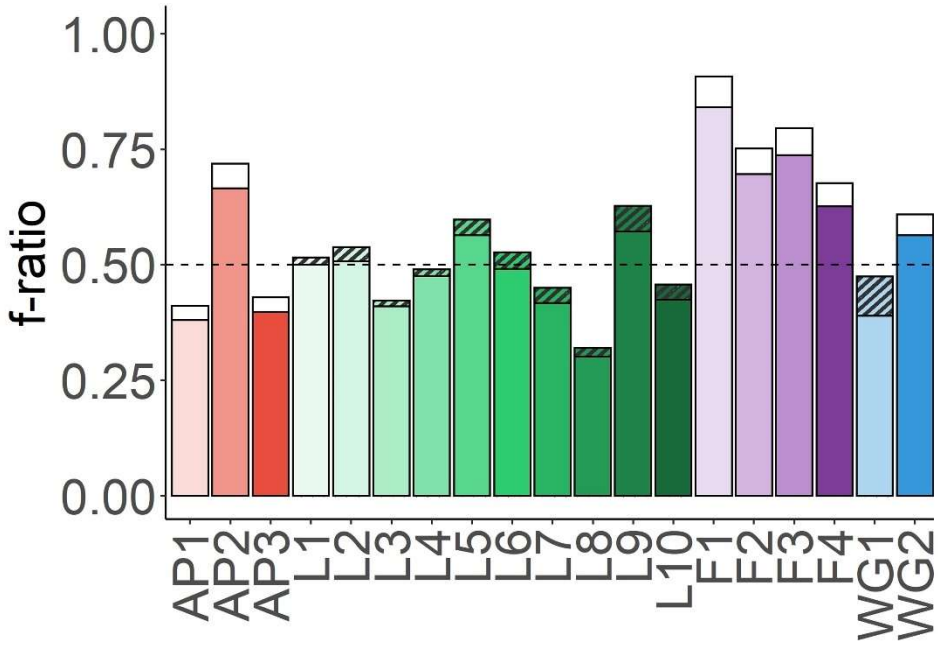


Figure 3.8. Euphotic zone-integrated f-ratios estimated for each station. The black-hashed and white bars show the difference between the f-ratio$_{(\text{excluding urea})}$ (higher value; eq. 3.4a) and the f-ratio$_{(\text{including urea})}$ (lower value; eq. 3.4b), with the black-hashed bars indicating the stations where urea uptake was measured and the white bars where it was estimated (see text for details).

3.3.3.5. Phytoplankton community composition

The flow cytometry data show that the phytoplankton community was numerically dominated by picoplankton at all stations, with *Synechococcus* emerging as the most abundant group (59 ± 19% of the total phytoplankton cells counted), except at stations L5 and L6 where picoeukaryotes were dominant (51 ± 1%; Fig. 3.9a-b). The microeukaryotes were the least abundant group at all stations (average abundance across the sampling region of 8 ± 3%); however, due to their large biovolume, they contributed most to the biomass (80 ± 7 %; Fig. 3.9c). In the configuration used here, flow cytometry is best suited for enumerating small cells (<15 μm; Dubelaar and Jonker 2000), such that the larger microplankton present at the time of sampling were likely underestimated via this technique. We thus take the phytoplankton net collections as more representative of the microplankton community and colonial nanoplankton groups.

From the samples collected using the phytoplankton net (i.e., single cells or colonies >55 μm), the dominant phytoplankton species at LCIS was the prymnesiophyte, *P. antarctica* (83 ± 17% of the total phytoplankton cells counted), while the phytoplankton community at the other stations was dominated by diatoms (mainly *Corethron pennatum, Chaetoceros* spp. (six species)*, Cylindrotheca closterium, Fragilariopsis ritscheri, Fragilariopsis curta, Fragilariopsis kerguelensis, Fragilariopsis rhombica, Leptocylindrus mediterraneus, Odontella weisflogii, Pseudo-nitzschia alanata* and several *Thalassiosira* spp., constituting 92 ± 6% of the phytoplankton cells counted; Fig. 3.9d-e). At LCIS, the stations sampled earlier in the season tended to be dominated by *P. antarctica* (e.g., station L3) while those sampled later hosted a more diatom-dominated community (e.g., station L8). In addition, the resident diatoms at LCIS (mainly *F. ritscheri, O. weisflogii*, and *Thalassiosira* spp.) were much larger than the numerically dominant *P. antarctica*. For example, at station L8, the 32 diatom species present (1.6 cells mL^{-1}) contributed 1.80 x 10^{-3} pg C mL^{-1} (Leblanc et al., 2012) compared to 0.14 x 10^{-3} pg C mL^{-1} resulting from the 7.8 cells mL^{-1} of *P. antarctica* (Mathot et al. 2000). The LCIS stations with the highest relative abundance of diatoms (e.g., station L8) were characterized by some of the highest rates of ρNO_3^- and greatest extent of NO_3^- depletion. More broadly, the LCIS stations with the lowest sea surface temperatures (SSTs) and nutrient uptake rates (i.e., stations L1 and L3) had the lowest phytoplankton counts, while those with the highest SSTs and nutrient uptake rates (i.e., station L5 and L7) had the highest phytoplankton counts (Fig. 3.9a and d; Table 3.1).

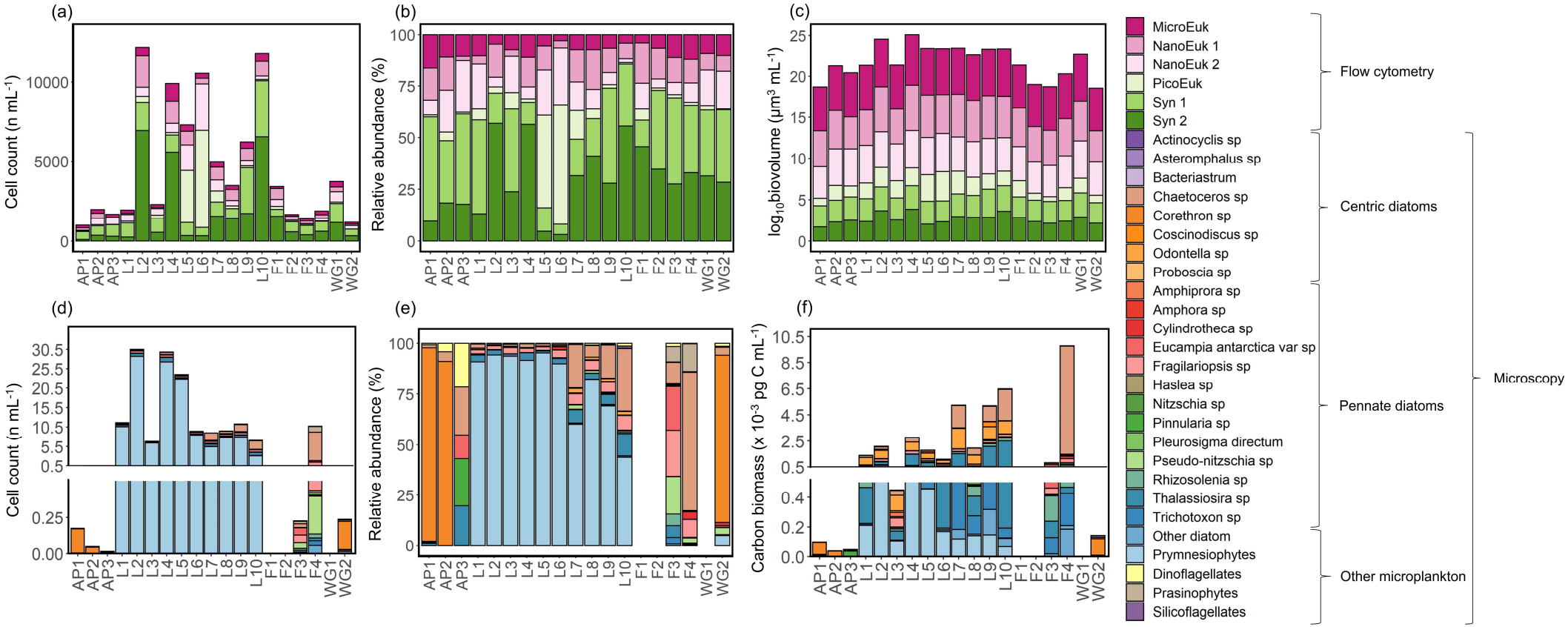


Figure 3.9. The (a, d) cell counts, (b, e) relative cell abundances, (c) log-transformed biovolume, and (f) carbon biomass of all phytoplankton groups identified from (a-c) surface flow cytometry samples and (d-f) plankton net-tow samples. The stations are labelled on the x-axis. Where there are no bars in panels (d), (e), and (f), no data are available. Carbon biomass estimates in panel (f) are shown only for the prymnesiophyte, P. antarctica, and the diatom species.

Table 3.1. Euphotic zone-averaged nitrogen nutrient concentrations, nutrient depletions, and nutrient depletion ratios at each station occupied in the Weddell Sea in January/February 2019. Values shown are averages ± 1 SD (n ≥ 2), with error propagated according to standard statistical practices where appropriate. "–" indicates no available data.

Station position	Station	Sampling date	Bottom depth (m)	MLD (m)	Z_{eu} (m)	NH_4^+ (μM)	Urea-N (μM)	NO_3^- (μM)	NO_3^- depletion (μM)	$Si(OH)_4$ depletion (μM)	PO_4^{3-} depletion (μM)	$Si(OH)_4$:NO_3^- depletion (μM:μM)	NO_3^-:PO_4^{3-} depletion (μM:μM)
FIS Average	**FIS**		**206 ± 83**	**82 ± 51**	**79 ± 28**	**0.1 ± 0.1**	**0.1 ± 0.1**	**25.0 ± 2.8**	**0.7 ± 1.4**	**1.6 ± 3.0**	**0.1 ± 0.1**	**2.0 ± 1.1**	**26.4 ± 19.8**
Fimbul	F1	01/01/19	130	135	100	0.0 ± 0.0	-	26.4 ± 0.5	0.2 ± 0.5	0.5 ± 1.6	0.0 ± 0.0	3.2 ± 3.9	-
Fimbul	F2	02/01/19	140	110	100	0.0 ± 0.0	-	26.5 ± 0.1	0.1 ± 0.1	0.0 ± 0.1	0.0 ± 0.0	0.5 ± 2.1	48.6 ± 11.5
Fimbul	F3	03/01/19	281	63	75	0.0 ± 0.0	0.0 ± 0.0	26.0 ± 0.3	0.7 ± 0.3	1.2 ± 0.5	0.0 ± 0.0	1.8 ± 0.6	18.8 ± 1.1
Fimbul	F4	20/02/19	274	20	40	0.2 ± 0.2	0.2 ± 0.1	20.2 ± 1.9	3.7 ± 2.0	8.7 ± 0.6	0.3 ± 0.1	2.3 ± 0.5	11.7 ± 0.6
AP Average	**AP**		**1451 ± 847**	**23 ± 8**	**45 ± 9**	**0.8 ± 0.2**	**0.3 ± 0.1**	**24.9 ± 0.6**	**2.5 ± 1.7**	**1.1 ± 0.8**	**0.1 ± 0.1**	**0.6 ± 0.2**	**19.8 ± 16.5**
Antarctic Peninsula	AP1	09/01/19	2155	23	35	0.6 ± 0.1	0.2 ± 0.1	25.6 ± 1.4	2.6 ± 0.7	1.4 ± 0.4	0.2 ± 0.1	0.5 ± 0.4	14.1 ± 0.4
Antarctic Peninsula	AP2	09/01/19	1686	30	50	0.7 ± 0.1	0.2 ± 0.1	25.9 ± 1.0	1.0 ± 1.1	0.8 ± 0.2	0.1 ± 0.0	0.8 ± 1.1	6.8 ± 1.1
Antarctic Peninsula	AP3	09/01/19	511	15	50	1.1 ± 0.0	0.3 ± 0.1	24.7 ± 0.3	3.2 ± 2.5	1.4 ± 1.5	0.1 ± 0.1	0.4 ± 1.4	38.4 ± 1.2
LCIS Average	**LCIS**		**434 ± 62**	**14 ± 6**	**29 ± 9**	**0.7 ± 0.4**	**0.2 ± 0.1**	**16.4 ± 4.7**	**8.2 ± 4.9**	**8.1 ± 4.9**	**0.6 ± 0.3**	**1.0 ± 0.2**	**14.7 ± 2.9**
Larsen C	L1	22/01/19	376	8.5	33	1.3 ± 0.1	0.4 ± 0.1	21.8 ± 0.1	2.0 ± 0.1	2.3 ± 0.3	0.2 ± 0.1	1.2 ± 0.1	11.2 ± 0.3
Larsen C	L2	20/01/19	451	14	25	0.4 ± 0.3	0.2 ± 0.2	13.7 ± 5.0	8.6 ± 4.8	7.8 ± 4.7	0.6 ± 0.4	0.9 ± 0.8	15.2 ± 1.0
Larsen C	L3	11/01/19	431	7	50	0.9 ± 0.1	0.2 ± 0.1	23.1 ± 0.2	2.2 ± 0.1	1.3 ± 0.8	0.1 ± 0.1	0.6 ± 0.6	17.7 ± 0.3
Larsen C	L4	14/01/19	368	24	22	0.5 ± 0.5	0.1 ± 0.1	12.1 ± 2.5	12.8 ± 2.1	10.9 ± 2.2	0.9 ± 0.2	0.9 ± 0.3	13.9 ± 0.2
Larsen C	L5	15/01/19	451	10	25	0.1 ± 0.0	0.4 ± 0.2	12.0 ± 1.9	10.9 ± 2.3	9.6 ± 1.7	0.8 ± 0.1	0.9 ± 0.3	13.7 ± 0.2
Larsen C	L6	13/01/19	475	17.5	30	0.7 ± 0.5	0.2 ± 0.1	15.1 ± 2.1	8.4 ± 2.1	8.0 ± 1.9	0.4 ± 0.1	1.0 ± 0.3	20.4 ± 0.3
Larsen C	L7	22/01/19	506	8.5	25	1.0 ± 1.1	0.2 ± 0.1	14.7 ± 4.1	11.1 ± 1.8	13.5 ± 3.4	0.8 ± 0.2	1.2 ± 0.3	14.8 ± 0.3
Larsen C	L8	23/01/19	450	22.5	35	0.3 ± 0.0	0.2 ± 0.0	12.2 ± 2.2	12.9 ± 4.5	12.4 ± 3.2	0.8 ± 0.3	1.0 ± 0.4	16.0 ± 0.5
Larsen C	L9	19/01/19	318	12.5	20	0.5 ± 0.4	0.2 ± 0.1	20.2 ± 4.3	5.8 ± 3.3	6.6 ± 5.1	0.5 ± 0.3	1.1 ± 1.0	11.0 ± 0.9
Larsen C	L10	24/01/19	510	14	20	0.7 ± 0.3	0.2 ± 0.1	18.2 ± 5.4	8.7 ± 3.7	10.6 ± 4.9	0.7 ± 0.3	1.2 ± 0.6	13.0 ± 0.6
WG Average	**WG**		**3565 ± 379**	**20 ± 0**	**90 ± 14**	**0.2 ± 0.2**	**0.1 ± 0.1**	**28.8 ± 2.4**	**0.4 ± 0.3**	**2.0 ± 0.9**	**0.1 ± 0.0**	**5.6 ± 0.7**	**4.1 ± 0.6**
Weddell Gyre	WG1	14/02/19	3297	20	100	0.2 ± 0.2	0.1 ± 0.1	26.7 ± 0.5	0.4 ± 0.3	2.3 ± 0.8	0.1 ± 0.0	5.1 ± 0.7	4.5 ± 0.7
Weddell Gyre	WG2	15/02/19	3833	20	80	0.4 ± 0.1	0.1 ± 0.1	30.2 ± 0.8	0.3 ± 0.4	2.0 ± 1.0	0.1 ± 0.1	6.1 ± 1.3	3.7 ± 1.5

Table 3.2. Euphotic zone-integrated and averaged rates at each station occupied in the Weddell Sea in January/February 2019. Values shown are averages ± 1 SD (n ≥ 2), with error propagated according to standard statistical practices where appropriate. "–" indicates no available data. The values shown in italics (i.e., ρurea) were estimated rather than measured (see text for details).

Station position	Station	[POC] (μM)	[PON] (μM)	C:N ratio	NPP (mmol m^{-2} d^{-1})	ρNO_3^- (mmol m^{-2} d^{-1})	ρNH_4^+ (mmol m^{-2} d^{-1})	ρurea (mmol m^{-2} d^{-1})	$V_{NO_2^-}$ (μmol m^{-2} d^{-1})	f-ratio$_{(excluding\ urea)}$	f-ratio$_{(including\ urea)}$
FIS Average	**FIS**	**8.0 ± 8.4**	**0.8 ± 0.9**	**16.5 ± 8.8**	**27.5 ± 26.6**	**3.7 ± 1.0**	**0.8 ± 0.4**	***0.5 ± 0.4***	**5.2 ± 0.7**	**0.80 ± 0.10**	**0.73 ± 0.09**
Fimbul	F1	5.9 ± 2.0	0.3 ± 0.2	21.6 ± 3.7	4.9 ± 0.0	3.8 ± 0.0	0.4 ± 0.0	*0.3 ± 0.0*	-	0.91	0.84
Fimbul	F2	4.9 ± 3.4	0.2 ± 0.0	26.3 ± 12.6	20.8 ± 0.2	2.4 ± 0.0	0.8 ± 0.0	*0.07 ± 0.0*	-	0.75	0.70
Fimbul	F3	3.1 ± 1.8	0.4 ± 0.2	8.8 ± 3.0	56.9 ± 0.6	4.8 ± 0.1	1.2 ± 0.0	*0.5 ± 0.0*	4.7 ± 1.6	0.80	0.74
Fimbul	F4	17.9 ± 7.2	2.1 ± 0.6	9.4 ± 0.5	28.3 ± 0.4	3.9 ± 0.0	1.9 ± 0.0	*0.9 ± 0.0*	5.7 ± 1.7	0.68	0.63
AP Average	**AP**	**8.7 ± 6.3**	**1.1 ± 0.3**	**8.3 ± 2.5**	**26.6 ± 33.5**	**3.4 ± 1.4**	**3.8 ± 2.0**	***0.5 ± 0.2***	**0.8 ± 0.7**	**0.52 ± 0.17**	**0.48 ± 0.16**
Antarctic Peninsula	AP1	7.4 ± 0.7	1.3 ± 0.1	6.1 ± 1.4	3.1 ± 0.1	1.8 ± 0.1	2.6 ± 0.0	*0.4 ± 0.0*	0.0 ± 3.3	0.41	0.38
Antarctic Peninsula	AP2	4.3 ± 3.5	0.8 ± 0.3	7.8 ± 2.7	11.8 ± 0.2	4.0 ± 0.2	2.1 ± 0.0	*0.4 ± 0.0*	1.0 ± 2.7	0.72	0.67
Antarctic Peninsula	AP3	14.4 ± 5.2	1.3 ± 0.2	11.0 ± 2.1	65.0 ± 0.1	4.4 ± 0.0	5.8 ± 0.0	*0.8 ± 0.0*	1.3 ± 1.3	0.43	0.40
LCIS Average	**LCIS**	**18.8 ± 22.1**	**2.4 ± 0.8**	**7.4 ± 1.9**	**28.6 ± 21.3**	**2.2 ± 1.1**	**2.6 ± 1.3**	**0.6 ± 0.3**	**17.3 ± 20.6**	**0.50 ± 0.09**	**0.47 ± 0.08**
Larsen C	L1	16.9 ± 5.9	1.5 ± 0.3	10.0 ± 3.4	2.2 ± 0.1	1.5 ± 0.0	1.4 ± 0.0	0.2 ± 0.0	16.7 ± 0.7	0.52	0.50
Larsen C	L2	21.2 ± 7.1	3.1 ± 0.5	6.3 ± 1.7	47.8 ± 0.5	1.5 ± 0.1	3.3 ± 0.0	0.8 ± 0.0	9.4 ± 0.6	0.54	0.51
Larsen C	L3	5.9 ± 0.1	2.6 ± 0.8	5.8 ± 1.4	32.0 ± 0.1	2.5 ± 0.0	3.3 ± 0.0	0.3 ± 0.0	-	0.42	0.41
Larsen C	L4	25.1 ± 4.7	1.0 ± 0.2	8.0 ± 0.5	32.2 ± 1.0	1.9 ± 0.1	2.1 ± 0.0	0.2 ± 0.0	69.0 ± 1.0	0.49	0.48
Larsen C	L5	17.3 ± 6.3	3.1 ± 0.6	7.4 ± 1.9	61.0 ± 0.7	4.7 ± 0.0	3.1 ± 0.0	0.9 ± 0.0	7.0 ± 0.5	0.60	0.56
Larsen C	L6	10.0 ± 1.3	2.4 ± 0.5	9.2 ± 5.3	25.9 ± 1.5	2.4 ± 0.1	2.2 ± 0.1	0.7 ± 0.0	23.0 ± 0.9	0.53	0.49
Larsen C	L7	27.1 ± 10.3	1.5 ± 0.7	8.2 ± 1.1	55.9 ± 1.0	3.1 ± 0.0	3.8 ± 0.1	1.1 ± 0.0	0.2 ± 0.9	0.45	0.42
Larsen C	L8	23.5 ± 3.3	3.3 ± 0.3	8.2 ± 1.3	17.3 ± 0.4	2.3 ± 0.0	4.8 ± 0.1	0.9 ± 0.0	8.7 ± 1.5	0.32	0.30
Larsen C	L9	17.1 ± 1.6	2.9 ± 0.2	3.4 ± 4.1	9.7 ± 1.3	2.0 ± 0.1	1.2 ± 0.0	0.6 ± 0.0	16.5 ± 2.3	0.63	0.57
Larsen C	L10	23.6 ± 14.9	2.7 ± 1.1	7.1 ± 0.4	1.8 ± 0.0	0.5 ± 0.0	0.6 ± 0.0	0.2 ± 0.0	5.2 ± 1.6	0.46	0.42
WG Average	**WG**	**8.0 ± 8.9**	**0.7 ± 0.3**	**12.3 ± 1.8**	**31.6 ± 31.3**	**3.2 ± 0.1**	**2.0 ± 0.2**	***0.5 ± 0.1***	**81.9 ± 44.7**	**0.54 ± 0.10**	**0.48 ± 0.12**
Weddell Gyre	WG1	5.8 ± 4.0	0.5 ± 0.2	13.6 ± 7.7	53.7 ± 0.2	3.3 ± 0.0	2.1 ± 0.0	0.6 ± 0.0	113.6 ± 4.3	0.47	0.39
Weddell Gyre	WG2	10.1 ± 7.9	0.9 ± 0.3	11.0 ± 7.5	9.5 ± 0.4	3.1 ± 0.0	1.8 ± 0.0	*0.4 ± 0.0*	50.3 ± 1.8	0.61	0.56

3.4. Discussion

For the regions of the Weddell Sea that we sampled in summer 2019, the euphotic zone-integrated rates of NPP and N uptake were generally lower at the OOZ stations than the CCSZ stations, with the highest depth-specific uptake rates observed in surface waters at LCIS (Fig. 3.6a-d; Table 3.2). The few studies that have previously measured summertime rates of NPP and N uptake in the Weddell Sea report similar results, with rates in the marginal ice zone (MIZ) and CCSZ that were up to five-times higher than in the OOZ (El-Sayed and Taguchi, 1981; Smith and Nelson, 1990; Park et al., 1999). The summertime CCSZ of the Weddell Sea can thus be broadly characterised as a highly productive region with elevated biomass accumulation driven by increased water-column stratification and iron-replete conditions, both the result of sea-ice melt (Semeneh et al., 1998; Lannuzel et al., 2008; Klunder et al., 2011). That said, we observed considerable variability in the biogeochemical rates measured in each region of the Weddell Sea, particularly at LCIS; we examine the possible drivers of and controls on the inter- and intra-regional differences below.

3.4.1. Drivers of NPP and N uptake in the Weddell Sea

Light and water column stability: Surface waters throughout the study region were generally well stratified, with MLDs ranging from 7 to 30 m, except at the early-summer FIS stations where the MLD ranged from 63 to 135 m (Table 3.1). These deep MLDs coincided with elevated sea-ice concentrations, while the shallowest MLDs at LCIS occurred in relatively ice-free waters (Table 3.1). Average euphotic zone rates of NPP typically increased with increasing SST and POC concentration (Fig. 3.10a and c), implicating water column stratification and biomass (which affects light penetration in addition to carbon production rate) as controls on NPP. By contrast, average euphotic zone rates of ρNO_3^- generally varied with MLD and Z_{eu} – they were highest (lowest) at the stations where Z_{eu} was shallowest (deepest) (Fig. 3.10b) - implicating light as a control on ρNO_3^-. At LCIS, the euphotic zone was shallow at all stations (<50 m, with an average Z_{eu} of 28.5 ± 9 m), yet ρNO_3^- varied by over an order of magnitude (Table 3.2). Here, we observed a positive relationship between the rates and SST, with ρNO_3^- increasing at higher SSTs, the latter indicative of increased water column stratification (Fig. 3.10a and S4b; see below).

Throughout the sampling region, the average euphotic zone rates of ρNH_4^+ and ρurea also varied with Z_{eu} which could be taken to indicate that these processes were also light dependent. However, such a finding would be unexpected, as the energy requirement associated with NH_4^+ and urea assimilation is low (El-Sayed and Taguchi 1981; Dortch 1990; Priddle et al. 1998). The observed relationship is more likely due to the *in situ* biomass, which i) attenuates light and ii) provides a source of organic matter for the production of NH_4^+ and dissolved organic N, including urea. Indeed, the stations with the deepest Z_{eu} were characterized by low concentrations of particulate organic matter and regenerated N (Fig. 3.3a-b and 3.5), leading us to conclude that ρNH_4^+ and ρurea were predominantly controlled by the

availability of regenerated N (Fig. 3.10d-e and B3b; section B4 in Appendix B). This conclusion is supported by the positive relationship observed between ρNH_4^+ or ρurea and the coincident NH_4^+ or urea concentrations (Fig. 3.10d-e).

The lowest regenerated N concentrations occurred at the stations with the lowest rates of NPP and ρNO_3^-, and the highest NO_3^- concentrations (e.g., station F1). This is probably because NH_4^+ and urea tend to accumulate only when biomass (and productivity) is sufficiently high to support elevated rates of heterotrophic activity (Semeneh et al., 1998). At the stations with low POC and PON concentrations, remineralisation rates were likely also low, limiting the flux of NH_4^+ and urea (Fig. 3.10f) and driving low rates of ρNH_4^+ and ρurea (Fig. 3.10d-e). At the stations where NH_4^+ and urea concentrations were elevated, rates of ρNH_4^+ and ρurea increased with depth, along with a decrease in NPP and ρNO_3^- (e.g., station L8). These observations further demonstrate the control of biomass on NPP, light on ρNO_3^-, and substrate availability on ρNH_4^+ and ρurea. That said, it is unlikely that the variability in NPP and N uptake among the stations was driven by biomass, light, and nutrient availability alone, and we hypothesize that hydrography, iron availability, and phytoplankton community composition also played a role.

At LCIS, the stations closest to the ice shelf were characterised by low SSTs and low rates of NPP and N uptake (stations L1 and L3; Fig. 3.1 , B4 and B5a ; Table 3.2). The low SSTs can be attributed either to the formation of sea-ice or to the upwelling of WW along the ice shelf. Sea-ice formation, in addition to decreasing SST, also increases the salinity of ASW due to brine rejection (Gill 1973). While the salinity of ASW at the low-SST stations was indeed elevated, the oxygen concentrations were relatively low (≤300 μM, which is below saturation; Fig. B5b-d). In surface waters and sea-ice, oxygen is typically saturated as it rapidly equilibrates with the atmosphere (Gleitz et al., 1995) and is produced by photosynthesizing phytoplankton and sea-ice algae. Sea-ice formation should not, therefore, drive a decrease in the oxygen content of ASW. The low oxygen concentrations at stations L1 and L3 were contiguous with those in the underlying WW (Fig. B5d), leading us to conclude that the cool, saline waters along the ice-shelf indicate recent upwelling of WW. Such upwelling could temporarily inhibit productivity by decreasing the stability of the water column and mixing phytoplankton below the euphotic zone. This mechanism can explain the low uptake rates and weak nutrient depletions observed at the low-SST stations.

Relatively cold, saline surface waters have previously been observed at the ice-edge off Larsen A and B Ice Shelves and shown to hinder NPP (Cape et al., 2014). In that case, the dense surface waters were surmised to result either from offshore wind stress at the inshore region that induced localised mixing, or from the advection of surface waters offshore by coastal upwelling. Both mechanisms would decrease water column stability, and by extension, productivity. Cape et al. (2014) observed an increase

in NPP with distance from the coast at Larsen A and B, a trend that we did not observe, likely because of the proximity of our LCIS stations to the ice shelf (within 75 km for all stations). Instead, our rates of NPP and N uptake were positively coupled with SST at the ice-edge (Fig. B4 and B5). We propose that surface SST at LCIS can be used as an indicator of water-mass age, with cooler SSTs indicating newly-upwelled WW and warmer SSTs designating older surface waters that have had time to absorb heat from the atmosphere. The higher rates of NPP and N uptake in the warmer surface waters occur because phytoplankton experience favourable growing conditions for an extended period, resulting in biomass accumulation. By contrast, persistent localised upwelling along LCIS inhibits productivity in the adjacent surface waters, with implications for the spatial distribution of biomass and the potential for organic carbon export.

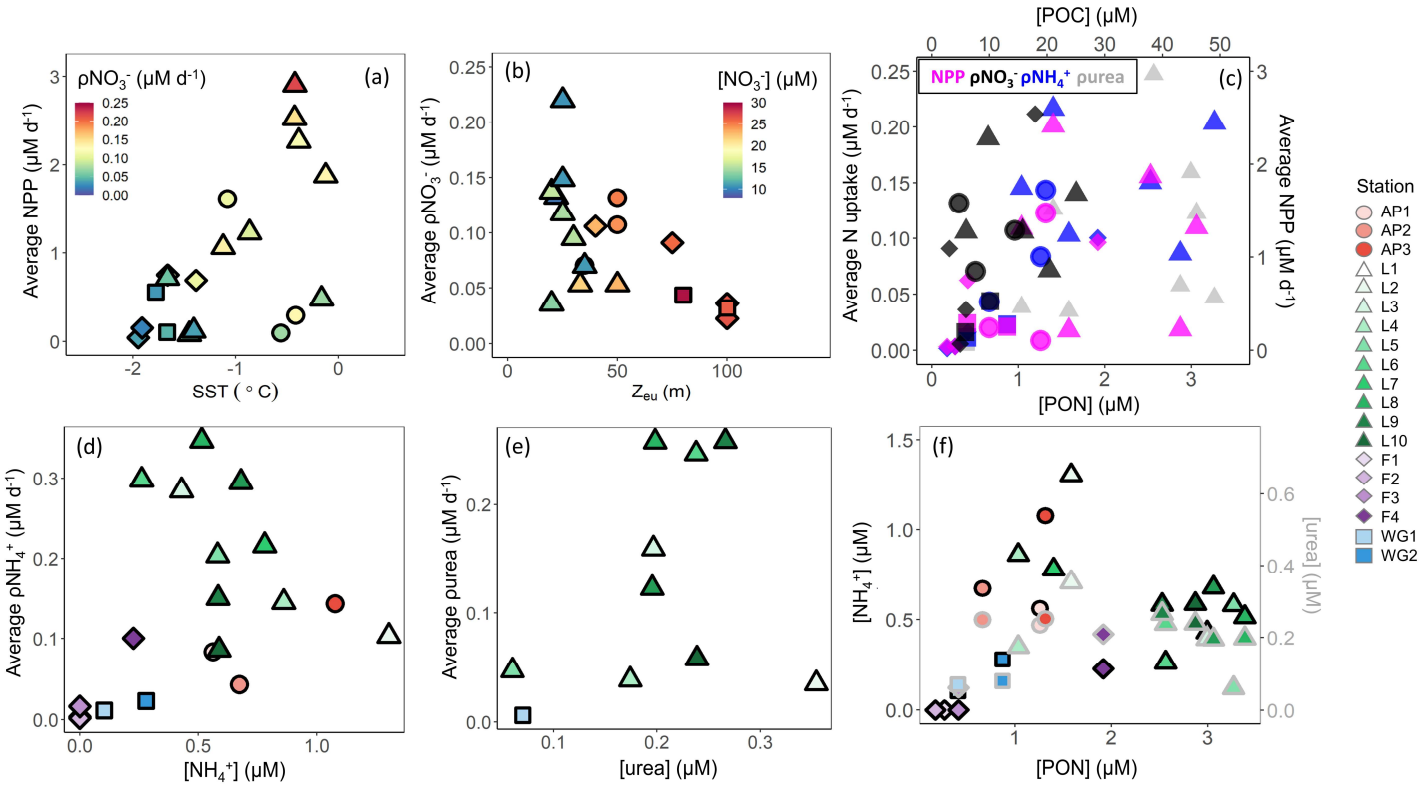


Figure 3.10. Euphotic zone-averaged rates of (a) NPP versus SST, (b) ρNO_3^- versus euphotic zone depth (Z_{eu}), (c) N uptake (left y-axis) versus PON (bottom x-axis) and NPP (right y-axis) versus POC (top x-axis), (d) ρNH_4^+ versus NH_4^+ concentration, and (e) ρurea versus urea concentration, as well as (f) the concentrations of NH_4^+ (black outlined symbols; left y-axis) and urea (grey outlined symbols; right y-axis) versus PON at each station. The symbols in panel (a) are coloured by ρNO_3^-, in panel (b) by NO_3^- concentration, and in panel (c) by NPP (pink), ρNO_3^- (black), ρNH_4^+ (blue), and ρurea (grey).

Nutrient and inferred iron conditions in Weddell Sea surface waters: Across our sampling region, ASW was depleted in NO_3^-, $Si(OH)_4$, and PO_4^{3-} relative to the underlying WW, with the greatest nutrient depletion occurring at LCIS and at FIS in late summer (Fig. 3.4a-c). Because diatoms and/or *P.*

antarctica were the dominant phytoplankton at all stations (Fig. 3.9d-f), we can use the Si:N:P depletion ratios (here used as shorthand for the $Si(OH)_4$:NO_3^-:PO_4^{3-} depletion ratios) to assess the iron conditions and N nutrition of these two phytoplankton groups. Under iron-replete conditions, diatoms consume Si:N:P in an approximate ratio of 1:1:0.07 (Ragueneau et al. 2000; Hutchins and Bruland 1998; Takeda 1998; Mosseri et al. 2008), while under iron-limitation, they increase their uptake of Si and decrease that of P relative to N, consuming nutrients in a ratio of ≥2:1:0.09 (Arrigo et al., 1999; Finkel et al., 2006; Green and Sambrotto, 2006; Mosseri et al., 2008; Weber and Deutsch, 2010; Martiny et al., 2013), with Si:N uptake ratios as high as 8:1 observed under conditions of extreme iron depletion (Franck et al., 2000; Brzezinski et al., 2003). At a first approximation, the Si:N:P depletion ratios estimated in our study suggest that the AP and LCIS stations were characterised by iron-replete conditions (ratio of 0.9:1:0.06) while phytoplankton community at the FIS and WG stations experienced iron limitation (ratios of 3.6:1:0.15; Fig. 3.4d-e; Table 3.1).

High iron concentrations have previously been measured in surface waters in the CCSZ and northern Weddell Sea (as high as 7 nM; Lannuzel et al. 2008; De Jong et al. 2012). Iron is supplied to the mixed layer in these regions via sea-ice melt, ice shelf melt, continental runoff, vertical and lateral advection, and resuspension of continental shelf sediments (Lannuzel et al., 2008; De Jong et al., 2012; Klunder et al., 2014). In contrast, the central WG is iron-limited as iron is supplied to surface waters mainly by wind-induced vertical mixing (Hoppema et al. 2015). During our sampling, sea-ice concentrations were high at the WG stations, which would have dampened the effect of wind stress on surface waters and thus hindered vertical mixing. At FIS in early summer, iron should have been replete as phytoplankton would not have had sufficient time to exhaust the surface reservoir. Here, the sea-ice concentrations were elevated, and the mixed layers were deep such that light, rather than iron, likely limited phytoplankton growth. Indeed, light-limited diatoms have been observed to consume Si:N:P in a ratio similar to that reported for conditions of iron depletion (Brzezinski, 1985). By late summer at FIS, the sea-ice had completely melted, which should have further alleviated iron limitation, yet the Si:N depletion ratios were high (average of 2.3 ± 0.5). These elevated ratios may be the result of only considering NO_3^- uptake and not accounting for regenerated N consumption. At FIS in late summer, NH_4^+ supported 32% of N uptake; accounting for this N source decreases the Si:N depletion ratio to 1.4:1, which is closer to expectations for iron-replete diatoms. Some diatom growth was likely also supported by urea, which would further decrease the Si:N depletion ratio. Additionally, it is plausible that the diatoms at station F4 were beginning to experience iron-limitation as sampling occurred late in the season.

Accounting for regenerated N uptake greatly alters the Si:N depletion ratios, particularly at LCIS, and provides insights into the behaviour of the dominant phytoplankton groups that were active in the mixed layer, both prior to and at the time of sampling. At the stations where diatoms dominated, the Si:NO_3^-

depletion ratios were elevated and ρNO_3^- was high (Fig. 3.11a and c). In contrast, at the stations where *P. antarctica* was dominant, the $Si:NO_3^-$ depletion ratios were low (generally <1) and regenerated N uptake was high relative to the other stations (Fig. 3.11a and d). Under favourable nutrient and light conditions, diatoms will typically consume NO_3^- over NH_4^+ as i) NO_3^- is usually present in substantially higher concentrations than NH_4^+ and ii) the lower surface area-to-volume ratio of (larger) diatoms makes it harder for them to compete with smaller cells for a less abundant resource (i.e., NH_4^+) (Probyn and Painting, 1985; Koike et al., 1986; Lomas and Glibert, 1999; Karsh et al., 2003). The average $Si:NO_3^-$ depletion ratio of 1.0 ± 0.2 at LCIS can therefore be attributed almost entirely to diatoms. When total N uptake is considered, the Si:N depletion ratios decrease to 0.3 ± 0.1, indicating the consumption of three-times more N than $Si(OH)_4$. We attribute this decline to regenerated N uptake by *P. antarctica*, a phytoplankton group that is known to preferentially consume NH_4^+ when it is available due to the lower energy and iron requirements of NH_4^+ assimilation (El-Sayed and Taguchi, 1981; Dortch, 1990; Jacques, 1991; Goeyens et al., 1995; Priddle et al., 1998; Stefels and Van Leeuwe, 1998).

We can also use the $NO_3^-:PO_4^{3-}$ depletion ratios to better understand the iron conditions and relative importance of *P. antarctica* versus diatoms in generating the observed nutrient depletion ratios. *P. antarctica* are known to consume NO_3^- and PO_4^{3-} in a ratio of ~20:1, while for iron-replete diatoms, this ratio is <14:1 (Arrigo et al. 1999; Smith and Asper 2001; Garcia et al. 2018). At LCIS, the $NO_3^-:PO_4^{3-}$ depletion ratio averaged 14.7 ± 2.9, consistent with a dominant role for iron-replete diatoms. However, variability in the $NO_3^-:PO_4^{3-}$ depletion ratios was observed among the LCIS stations (with ratios ranging from 11 to 20), which can be explained by local variations in phytoplankton community composition. At stations where large diatoms were dominant (e.g., L10, where diatoms contributed 6.47 x 10^{-3} pg C mL^{-1} to biomass while *P. antarctica* only contributed 0.07 x 10^{-3} pg C mL^{-1}), the $NO_3^-:PO_4^{3-}$ depletion ratios were low (13.0 ± 0.6; Fig. 3.11b). In contrast, at the stations where *P. antarctica* were numerically dominant (e.g., L6; where *P. antarctica* constituted 90% of the microphytoplankton) and contributed more to biomass (0.17 x 10^{-3} pg C mL^{-1}), elevated $NO_3^-:PO_4^{3-}$ depletion ratios were measured (20.4 ± 0.3; Fig. 3.11b; Table 3.1). Furthermore, high rates of NH_4^+ uptake were measured at LCIS, equivalent to and at times greater than the coincident NO_3^- uptake rates (Fig. 3.6; Table 3.2) , particularly at the stations with the highest relative abundance of *P. antarctica*. In general, the relative contribution of diatoms versus *P. antarctica* therefore appears to control the nutrient depletion ratios on a variety of scales in the Weddell Sea.

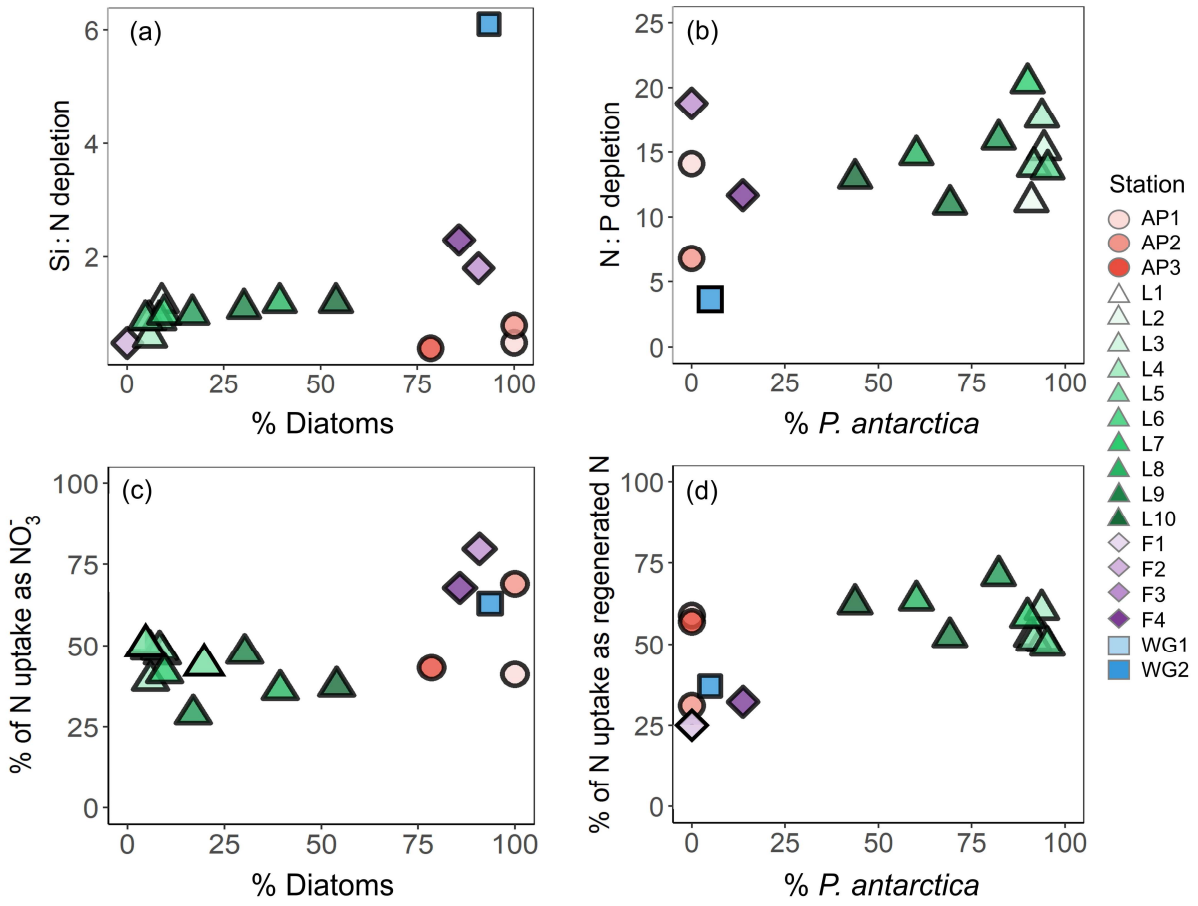


Figure 3.11. Scatterplots of (a) the Si:N depletion ratio (i.e., $Si(OH)_4$-to-total N depletion) versus the % diatom abundance, (b) N:P depletion ratio (i.e., total N-to-PO_4^{3-} depletion) versus the % *P. antarctica* abundance, (c) % of total N (i.e., NO_3^- + NH_4^+ + urea) assimilated as NO_3^- versus the % diatom abundance, and (d) % of total N assimilated as regenerated N (i.e., NH_4^+ + urea) versus the % *P. antarctica* abundance at each station.

Drivers of phytoplankton community composition: Phytoplankton community composition and the variations therein have implications for the biological carbon pump, both directly (diatoms sink more rapidly than smaller and/or non-ballasted phytoplankton; Treguer and Jacques 1992; De Baar et al. 2005; Boyd et al. 2007) and indirectly (NO_3^- consumption is quantitatively related to carbon export; Dugdale and Goering 1967; Eppley and Peterson 1979). Above, we have discussed the role of phytoplankton community composition in controlling productivity and upper ocean nutrient cycling. Below, we discuss the processes that may have caused *P. antarctica* to dominate over diatoms at LCIS, and vice versa at the other Weddell Sea stations.

At LCIS, a coastal sensible heat polynya persisted throughout the sampling period. The opening of such polynyas along the eastern AP is linked to the occurrence of warm, föhn winds that originate over the continent and blow over the AP, influencing the coastal north-western Weddell Sea (Cape et al., 2014).

Föhn winds drive the offshore movement of sea-ice, which initiates the opening of polynyas that persist because the winds are warm, thus hindering the formation of new sea-ice (Cape et al., 2014). The development of coastal sensible heat polynyas results in relatively deep mixed layers and a weakly stratified water column. The polynya at LCIS opened in late November, approximately two months prior to our sampling. At this time (i.e., the beginning of the growing season), motile *P. antarctica* cells likely dominated the phytoplankton community as *P. antarctica* are low-light specialists compared to other Antarctic phytoplankton (Goffart et al., 2000; Alderkamp et al., 2012; Delmont et al., 2014). This notion is supported by the generally low phytoplankton cell counts (for both flow cytometry and net-tow samples) and high relative abundance of *P. antarctica* compared to diatoms at the stations along the ice shelf where WW had recently upwelled (e.g., L3; Fig. 3.9a, d, e and B5). As the mixed layer shoaled into the summer and light limitation was alleviated, a diatom bloom would have been initiated and *P. antarctica* would have formed colonies (Schoemann et al., 2005) – indeed, the presence of *P. antarctica* colonies and diatom chains at the time of our sampling in January is evidence that the water column was well stratified (Goffart et al. 2000). As the season progressed, diatoms would have outcompeted *P. antarctica* and come to dominate the phytoplankton community. At the stations sampled later in the season (e.g., L10; Fig. 3.9e), the relative abundance of diatoms versus *P. antarctica* was higher than at the stations occupied two weeks earlier (e.g., L5; Fig. 3.9e). Diatoms have a lower iron and higher light requirement than *P. antarctica* and thus tend to thrive once the *P. antarctica* bloom declines, when the water column has stratified and they can access the lower concentrations of residual iron (Strzepek et al., 2011). That said, iron is likely perennially high at LCIS in summer as it is near-continuously supplied to surface waters by sea-ice melt and upwelling of WW along the ice shelf (Klunder et al., 2014). The elevated iron concentrations would allow the diatoms to grow rapidly on the available NO_3^- once the mixed layer had shoaled enough to alleviate light limitation, contributing to their capacity to outcompete other phytoplankton.

At the other (non-LCIS) sampling sites, diatoms dominated the phytoplankton community. We hypothesize that at the beginning of the growing season, melting sea-ice alleviated light- and, to a lesser extent, iron limitation, providing favourable conditions for diatom growth. At the same time, the generally lower iron concentrations characteristic of open Weddell Sea surface waters may have selected against *P. antarctica* (Strzepek et al., 2011). Previous studies conducted in the Ross Sea observed large diatom blooms associated with the receding ice-edge and concluded that bloom formation was favoured by the rapid stabilization of the water column from meltwater inputs (Goffart et al. 2000; Sedwick et al. 2000). Regions of the Weddell Sea that undergo rapid stratification due to sea-ice melt will likely also experience large diatom blooms. We thus conclude that the dominance of diatoms over *P. antarctica* at the non-LCIS stations was influenced by local hydrodynamic processes that rapidly induce water column stability, and increase light availability (e.g., in areas of recent sea-ice melt). By contrast, *P. antarctica* dominates under low-light, such as in the deep mixed layers that

initially characterize coastal polynyas. Eventually, diatoms will succeed *P. antarctica* in these polynyas as conditions become favourable for their growth.

3.4.2. Carbon export potential across the Weddell Sea

Previous f-ratio estimates for the summertime Weddell Sea range from 0.18 to 0.83 (Koike et al. 1986; Rönner et al. 1983; Nelson et al. 1987; Smith and Nelson 1990; Goeyens 1991; Goeyens et al. 1995). Using equations 3.4a and 3.4b, we calculate euphotic zone-integrated f-ratios that range from 0.32 to 0.91 (excluding urea uptake) and 0.30 to 0.84 (including urea uptake). The lowest f-ratios occurred at LCIS (f-ratio$_{(\text{excluding urea})}$ = 0.50 ± 0.09 and f-ratio$_{(\text{including urea})}$ = 0.47 ± 0.08) and the highest at FIS (f-ratio$_{(\text{excluding urea})}$ = 0.78 ± 0.1 and f-ratio$_{(\text{including urea})}$ = 0.73 ± 0.09) (Fig. 3.8; Table 3.2). We note that urea uptake may have been stimulated at the stations where it was measured given the quantity of ^{15}N-urea added (0.1 μM) relative to the ambient urea concentrations (average of 0.2 ± 0.1 μM; Fig. B2; section B3 in Appendix B); if so, regenerated production could be overestimated at all stations since we extrapolated the average measured contribution of urea-to-total-N uptake (8 ± 6%) to the stations at which ρurea was not measured (eq. 3.7). The f-ratio estimates excluding and including urea uptake thus represent an upper and lower bound, respectively, on the fraction of potentially exportable carbon. That said, accounting for urea uptake decreased the average f-ratio by very little, from 0.57 ± 0.15 to 0.52 ± 0.14.

Estimates of the f-ratio and carbon export potential can be complicated by euphotic zone nitrification, which supplies regenerated rather than new NO_3^- to phytoplankton. Failing to account for this regenerated N flux can lead to an overestimation of carbon export potential (Yool et al. 2007; Mdutyana et al. 2020). At all stations, the euphotic zone rates of $V_{NO_2^-}$ were low (undetectable to 9.5 nM d^{-1}, average of 0.6 ± 1.4 nM d^{-1}; Fig. 3.7b) and correcting the f-ratio for these rates (eq. 3.4) had a minimal effect (average decrease of 2 ± 6%). The largest decrease was observed at WG1 where the highest euphotic zone-integrated rates of $V_{NO_2^-}$ were measured (f-ratio$_{(\text{excluding urea})}$ decreased from 0.60 to 0.47 and f-ratio$_{(\text{including urea})}$ decreased from 0.49 to 0.39; Table 3.2).

The low rates of euphotic zone nitrification are consistent with the previous (limited) data available for the summertime OOZ and CCSZ of the Southern Ocean. For example, Mdutyana et al. (2020) measured euphotic zone rates of NO_2^- and NH_4^+ oxidation in summer at FIS and in the OOZ just north of the WG (56°S 0°E) that were below detection. Summertime studies of euphotic zone NH_4^+ oxidation in the Ross and Scotia Seas also report low rates, of 6-8.9 nM d^{-1} and 0.4-5.8 nM d^{-1}, respectively (Olson, 1981). We conclude that, as expected, the high-light and generally low-NH_4^+ conditions of the summertime Weddell Sea inhibited euphotic zone nitrification, and that the slow growing-nitrifiers were probably also outcompeted by phytoplankton for NH_4^+ (Ward 1985; 2005; Smith et al. 2014; Zakem et al. 2018).

Classifying NO_3^- uptake as new production and equating it to carbon export potential is thus reasonable for the summertime Weddell Sea.

Although the highest f-ratios were estimated for the FIS stations, the highest rates of ρNO_3^- were observed at LCIS and along the AP (Fig. 3.8; Table 3.2). FIS was thus characterised by the highest carbon export potential relative to NPP, while the N cycle data imply that the absolute potential carbon export flux was highest at LCIS and the AP. The maximum extent of nutrient depletion was also observed at LCIS (NO_3^- depletion of 57-428 mmol m^{-2} and PO_4^{3-} depletion of 5.8-18.7 mmol m^{-2}). Assuming Redfield C:N and C:P stoichiometry of 6.63:1 and 106:1, respectively, the seasonal NO_3^- depletion equates to a carbon export flux of 0.4-2.8 mol C m^{-2} and the PO_4^{3-} depletion to 0.6-2.0 mol C m^{-2}. Alternately, multiplying ρNO_3^- by the length of time that the coastal polynya had been open (30 November until the date of sampling; Table 3.1) yields an estimate for net seasonal NO_3^- uptake of 59-428 mmol m^{-2} and carbon export flux of 0.4-2.8 mol C m^{-2} at LCIS, remarkably similar to the estimates derived from seasonal NO_3^- depletion. Our estimates of carbon export potential are, however, on the low end of those reported previously for the CCSZ and MIZ of the Weddell Sea (e.g., estimates for January/February range from 2.4-4.9 mol C m^{-2}; Rönner et al. 1983; Hoppema et al. 2000; 2007). Given the high-light and nutrient- and iron-replete conditions encountered at LCIS, one might thus have expected higher f-ratios and estimates of carbon export potential (i.e., NO_3^- depletion), raising the question of the possible limitations thereon.

Throughout the Weddell Sea, NH_4^+ and urea uptake were coupled with substrate availability, while NO_3^- uptake was not. Instead, NO_3^- uptake appeared to vary with light (see above) and as a function of the ambient NH_4^+ concentration (Fig. 3.12a). At LCIS where NH_4^+ was elevated throughout the mixed layer at all stations, NO_3^- uptake and NO_3^- depletion decreased with increasing NH_4^+ (Fig. 3.12), which we attribute to NH_4^+ inhibition of NO_3^- uptake (Goeyens et al., 1995). By contrast, at the non-LCIS stations, NO_3^- depletion and ambient NH_4^+ concentration showed a positive relationship, consistent with NO_3^--fuelled phytoplankton growth being followed by intense remineralization and grazing, both of which can yield elevated NH_4^+ (Rönner et al. 1983; El-Sayed 1984; Semeneh et al. 1998).

Previous studies conducted in MIZ and CCSZ of the Weddell Sea have shown that NH_4^+ concentrations $\geq$0.5 µM can inhibit NO_3^- uptake, particularly by diatoms, resulting in phytoplankton (including diatoms) preferentially consuming NH_4^+ over NO_3^-. For example, Goeyens et al. (1995) observed a Weddell Sea phytoplankton community dominated by diatoms prior to NH_4^+ accumulation, but once surface waters became enriched in NH_4^+, diatom dominance ceased. The authors concluded that diatoms were unable to bloom despite the elevated NO_3^- concentrations because of the inhibitory effect of NH_4^+, while non-siliceous, smaller phytoplankton species flourished because their preferred N source is NH_4^+. In our study, although NH_4^+ inhibition of ρNO_3^- apparently occurred at LCIS (Fig. 3.12), ρNO_3^- was on

average as high as ρNH_4^+ and was never zero (Table 3.2) – in other words, the elevated ambient NH_4^+ concentrations did not prevent NO_3^- uptake even though it appears to have slowed it. We propose that the mixed community of diatoms and *P. antarctica* present at the time of our sampling meant that diatoms were able to assimilate mainly NO_3^- while *P. antarctica* consumed the NH_4^+, preventing this reduced N form from accumulating to fully inhibitory concentrations. While the reliance of *P. antarctica* on NH_4^+ over NO_3^- represents a missed opportunity for carbon export given that these phytoplankton are known to fix up to 50% more carbon than diatoms per mole of PO_4^{3-} consumed (Arrigo et al., 1999), that the diatoms were able to proliferate in the face of elevated NH_4^+ may have partly compensated for this. Earlier in the season when NH_4^+ concentrations were negligible, it is likely that the f-ratios at LCIS were >0.5 and comparable to those estimated for the FIS stations, as observed at Larsen A and B in early summer (Goeyens et al., 1995; Cape et al., 2014). We conclude that elevated NH_4^+ may have weakened carbon export potential at LCIS in January/February 2019 through its effect on whole-community NO_3^- uptake. Carbon export may have been further inhibited later in the season as NH_4^+ concentrations continued to increase following remineralisation of the phytoplankton bloom, coupled with the seasonal decrease in daylight that is expected to shift the phytoplankton community to proportionally higher NH_4^+ dependence (Lourey et al., 2003; Philibert et al., 2015; Glibert et al., 2016; Deary, 2020; Smart et al., 2020).

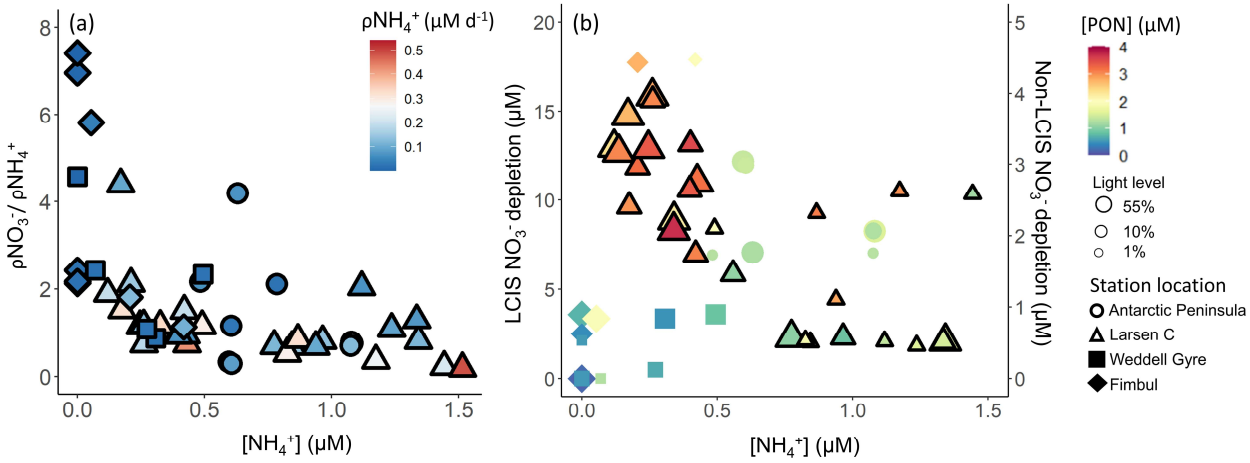


Figure 3.12. (a) NO_3^- uptake normalised to NH_4^+ uptake as a function of NH_4^+ concentration and b) NO_3^- depletion versus NH_4^+ concentration. The symbols in panel (a) are coloured by NH_4^+ uptake rate (ρNH_4^+) and in panel (b) by PON concentration. In panel (b), the symbol size indicates the incubation light level, NO_3^- depletion at LCIS corresponds with the left y-axis, and NO_3^- depletion at all other ("non-LCIS") stations corresponds with the right y-axis.

3.4.3. Broader biogeochemical implications at LCIS

LCIS is a region of deep-water formation, such that the biogeochemical properties of ASW influence those of MWDW and the bottom waters. Our data indicate significant net depletion of nutrients from ASW over the summer growing season. These nutrients would have been converted to organic matter that was either consumed by zooplankton or exported from the euphotic zone to be decomposed by heterotrophic bacteria, in the water column or on the shelf, or consumed by the benthic community. The subsurface remineralisation of organic matter acts to increase the CO_2 and nutrient reservoir of WW and shelf waters (ISW and HSSW; both precursors of CDW). Some portion of this CO_2 is effluxed to the atmosphere when WW upwells along the front of the ice shelf, while the remainder will be mixed into MWDW and eventually transferred to the bottom waters where it will be stored for hundreds of years (Ito et al. 2010). Exported organic matter that escapes water-column and on-shelf remineralization settles on the seafloor where a small fraction is buried and thus removed from the ocean-atmosphere system, while the bulk of the organic matter is consumed by the benthic community and ultimately converted back to CO_2 (Isla et al., 2006, 2011; Pineda-Metz et al., 2019). The CO_2 and nutrients recycled by the benthos may be resupplied to the surface during upwelling, whereupon remineralized CO_2 can escape to the atmosphere. Biological activity and nutrient drawdown at LCIS, and the limitations thereon, thus affect the CO_2 and nutrient content of the bottom waters, as well as the energy supply to the benthos and the extent to which CO_2 is removed from the atmosphere on climate-relevant timescales. The $Si(OH)_4$:NO_3^-:PO_4^{3-} ratio at depth at LCIS (average of 2:1:0.07 below 150 m) implicates diatoms as the main biological driver of nutrient conditions in MWDW, and by extension the bottom waters, throughout the Weddell Sea. Although the dominance of *P. antarctica* in early and mid-summer does not appear to affect the nutrient properties of MWDW, it may influence its CO_2 content. *P. antarctica* consume approximately twice as much carbon per mole of PO_4^{3-} as diatoms, and the colonial forms have been observed to rapidly sink out of the water column, thereby transporting large quantities of carbon to depth (Arrigo et al., 2000; Ditullio et al., 2000). The dominance of *P. antarctica* at LCIS may thus be important for carbon storage in MWDW and the bottom waters, as well as for the transport of organic matter to the benthos.

As SSTs rise and sea-ice melts, a shift from *P. antarctica*- to diatom-dominated phytoplankton blooms is expected because diatoms flourish in areas of recent sea-ice melt (Boyd and Doney 2002; Arrigo and van Dijken 2003; Petrou et al. 2016; Ferreira et al. 2020). Our results are consistent with this floristic shift hypothesis. For example, at L10 where recent sea-ice melt (Fig. 3.2a and c) had increased water column stratification, a different phytoplankton community was observed compared to the other LCIS stations, with diatoms dominating over *P. antarctica* (Fig. 3.9). By contrast, at other LCIS stations, *P. antarctica* dominated the biomass due to the low light conditions caused by the deep MLDs that initially characterize coastal polynyas. Given the anomalously high carbon-to-nutrient content of *P. antarctica*, a shift to diatom-dominated phytoplankton blooms may negatively affect the export and storage of

carbon in MWDW and the bottom waters. However, rising SSTs will also lead to increased glacial and ice shelf melt, further stratifying the adjacent water column and increasing the iron supply (Petrou et al., 2016). It is projected that these conditions will favour blooms of heavily-silicified diatom species that are known to sink rapidly out of the mixed layer or, if consumed, their frustules are expected to survive the gut passages of copepods, potentially resulting in increased carbon export (Assmy et al., 2013). However, this increase is unlikely to be two-fold that presently contributed by *P. antarctica*. Additionally, the sinking shells of heavily-silicified diatoms have at times been observed to be devoid of organic carbon (Smetacek, 2000; Assmy et al., 2013), which would further decrease the carbon export potential of diatoms compared to colonial *P. antarctica.* In net, the expected floristic shift may lead to decreased carbon export at the ice shelves, subsequently decreasing the carbon content of the MWDW formed at LCIS and/or the food supply to the benthos. Further investigation of the drivers of phytoplankton community composition is required to validate these hypotheses, particularly with regards to the response of Antarctic phytoplankton to warming, as well as to how changes in the surface ecosystem are transferred to and reflected in the biogeochemistry of bottom waters and benthic ecosystem functioning.

3.5. Conclusions

We investigated the summertime productivity of understudied regions of the Weddell Sea, including LCIS, along with the potential importance of different phytoplankton groups for biomass production, nutrient consumption, and carbon export potential. Our data show that mixed-layer nutrient depletion ratios are determined by the dominant phytoplankton group. The lowest Si:N and highest N:P depletion ratios were observed at LCIS where *P. antarctica* was dominant, while the highest Si:N and lowest N:P depletion ratios occurred at FIS and in the WG where diatoms dominated. The variability in phytoplankton community composition appears to have been largely driven by mechanisms controlling water column stratification. *P. antarctica* are low-light specialists and proliferated at LCIS due to the deep mixed layers that occurred early in the season, while diatoms succeeded at stations where the mixed layer was shallow, induced by sea-ice melt. Not only does the observed relationship between phytoplankton community composition and the nutrient depletion ratios have implications for the stoichiometry of the deep-water nutrient reservoir, but it likely also has consequences for carbon export and storage (Brzezinski et al. 2003; Weber and Deutsch 2010).

Although the waters adjacent to LCIS were characterized by the highest NO_3^- uptake rates, they also yielded the lowest f-ratios. We attribute these f-ratios to a degree of NH_4^+ inhibition of NO_3^- uptake, which translates to a missed opportunity for carbon export (Cochlan and Bronk, 2003) and potentially, decreased long-term storage in bottom waters, particularly since neither NO_3^- nor iron appeared to be limiting at the time of our sampling. Additional investigation is required to ascertain the persistence of NH_4^+ inhibition in the Antarctic CCSZ, particularly in regions of deep-water formation (e.g., at FRIS).

Furthermore, given the prediction that the Weddell Sea's upper water column will become more stratified with climate change (Pörtner et al., 2014; Sallée et al., 2013; Stammerjohn et al., 2012), it is essential that we improve our understanding of the physical and chemical drivers of phytoplankton community composition and function if we are to better predict changes to ocean carbon cycling and drawdown via the biological carbon pump.

3.6. References

Alderkamp, A.-C., Kulk, G., Buma, A. G. J., Visser, R. J. W., Dijken, G. L. Van, Mills, M. M., and Arrigo, K. R.: The effect of iron limitation on the photophysiology of Phaeocystis Antarctica (Prymnesiophyceae) and Fragilariopsis Cylindrus (Bacillariophyceae) under dynamic irradiance, J. Phycol., 48, 45–59, https://doi.org/10.1111/J.1529-8817.2011.01098.X, 2012.

Altabet, M. A. and Francois, R.: Nitrogen isotope biogeochemistry of the Antarctic polar frontal zone at 170°W, Deep. Res. Part II Top. Stud. Oceanogr., 48, 4247–4273, https://doi.org/10.1016/S0967-0645(01)00088-1, 2001.

Arrigo, K. R., Robinson, D. H., Worthen, D. L., Dunbar, R. B., DiTullio, G. R., VanWoert, M., and Lizotte, M. P.: Phytoplankton community structure and the drawdown of nutrients and CO2 in the Southern Ocean, Science (80-.)., 283, 365–367, https://doi.org/10.1126/science.283.5400.365, 1999.

Arrigo, K. R., DiTullio, G. R., Dunbar, R. B., Robinson, D. H., VanWoert, M., Worthen, D. L., and Lizotte, M. P.: Phytoplankton taxonomic variability in nutrient utilization and primary production in the Ross Sea, J. Geophys. Res. Ocean., 105, 8827–8846, https://doi.org/10.1029/1998jc000289, 2000.

Arrigo, K. R. and van Dijken, G. L.: Phytoplankton dynamics within 37 Antarctic coastal polynya systems, J. Geophys. Res. Ocean., 108, https://doi.org/10.1029/2002jc001739, 2003.

Arrigo, K. R., van Dijken, G., and Long, M.: Coastal Southern Ocean: A strong anthropogenic CO2 sink, Geophys. Res. Lett., 35, 1–6, https://doi.org/10.1029/2008GL035624, 2008.

Arteaga, L. A., Boss, E., Behrenfeld, M. J., Westberry, T. K., and Sarmiento, J. L.: Seasonal modulation of phytoplankton biomass in the Southern Ocean, Nat. Commun. 2020 111, 11, 1–10, https://doi.org/10.1038/s41467-020-19157-2, 2020.

Assmy, P., Smetacek, V., Montresor, M., Klaas, C., Henjes, J., Strass, V. H., Arrieta, J. M., Bathmann, U., Berg, G. M., Breitbarth, E., Cisewski, B., Friedrichs, L., Fuchs, N., Herndl, G. J., Jansen, S., Krägefsky, S., Latasa, M., Peeken, I., Röttgers, R., Scharek, R., Schüller, S. E., Steigenberger, S., Webb, A., and Wolf-Gladrow, D.: Thick-shelled, grazer-protected diatoms decouple ocean carbon and silicon cycles in the iron-limited Antarctic Circumpolar Current., Proc. Natl. Acad. Sci. U. S. A., 110, 20633–8, https://doi.org/10.1073/pnas.1309345110, 2013.

Bendschneider, K., Robinson, R. J., Margeson, J. H., Suggs, J. C., Midgett, M. R., Method, C. R., Dussin, R., Curchitser, E. N., Stock, C. A., Van Oostende, N., Galán, A., Zirbel, M. J., Saldías, G. S., Chan, F., Letelier, R., Najjar, G., Sarmiento, J. L., Xi, S., Scientific, T., Berelson, W. M., McManus, J., Coale, K. H., Johnson, K. S., Kilgore, T., Burdige, D., Pilskaln, C., Flohr, A., Van Der Plas, A. K., Emeis, K. C., Mohrholz, V., and Rixen, T.: A New Spectrophotometric Method for the Determination of Nitrite in Sea Water, J. Mar. Res., 11, 0–1, https://doi.org/10.1357/0022240963213673, 2020.

Berges, J. A. and Mulholland, M. R.: Enzymes and Nitrogen Cycling, 1385–1444 pp., https://doi.org/10.1016/B978-0-12-372522-6.00032-3, 2008.

Böhlke, J. K. and Coplen, T. B.: Interlaboratory comparison of reference materials for nitrogenisotope-ratio measurements, 1995.

Böhlke, J. K., Mroczkowski, S. J., and Coplen, T. B.: Oxygen isotopes in nitrate: New reference materials for 18O: 17O: 16O measurements and observations on nitrate-water equilibration., Rapid Commun. Mass Spectrom., 17, 1835–1846, 2003.

Boyd, P. W. and Doney, S. C.: Modelling regional responses by marine pelagic ecosystems to global climate change, Geophys. Res. Lett., 29, 53-1-53–4, https://doi.org/10.1029/2001gl014130, 2002.

Boyd, P. W.: Ironing out algal issues in the Southern Ocean, Nature, 304, 396–397, 2004.

Boyd, P. W., Jickells, T., Law, C. S., Blain, S., Boyle, E. A., Buesseler, K. O., Coale, K. H., Cullen, J. J., De Baar, H. J. W., Follows, M., Harvey, M., Lancelot, C., Levasseur, M., Owens, N. P. J., Pollard, R., Rivkin, R. B., Sarmiento, J., Schoemann, V., Smetacek, V., Takeda, S., Tsuda, A., Turner, S., and Watson, A. J.: Mesoscale iron enrichment experiments 1993-2005: Synthesis and future directions, Science (80-.)., 315, 612–617, https://doi.org/10.1126/science.1131669, 2007.

Boyd, P. W., Doney, S. C., Strzepek, R., Dusenberry, J., Lindsay, K., and Fung, I.: Climate-mediated changes to mixed-layer properties in the Southern Ocean: assessing the phytoplankton response, 5, 847–864, https://doi.org/10.5194/bg-5-847-2008, 2008.

Boyd, P. W. and Ellwood, M. J.: The biogeochemical cycle of iron in the ocean, Nat. Geosci., 3, 675–682, https://doi.org/10.1038/ngeo964, 2010.

Brennecke, W.: Die ozeanographischen Arbeiten der Deutschen Antarktischen Expedition 1911-12, Aus dem Arciv der Deutchen Seewarte, 39, 1–216, 1921.

Brzezinski, M. A., Dickson, M. L., Nelson, D. M., and Sambrotto, R.: Ratios of Si, C and N uptake by microplankton in the Southern Ocean, Deep. Res. Part II Top. Stud. Oceanogr., 50, 619–633, https://doi.org/10.1016/S0967-0645(02)00587-8, 2003.

Cape, M. R., Vernet, M., Kahru, M., and Spreen, G.: Polynya dynamics drive primary production in the Larsen A and B embayments following ice shelf collapse, J. Geophys. Res. Ocean., 119, 572–594, https://doi.org/10.1002/2013JC009441, 2014.

Carvalho, F., Kohut, J., Oliver, M. J., and Schofield, O.: Defining the ecologically relevant mixed-layer depth for Antarctica's coastal seas, Geophys. Res. Lett., 44, 338–345, https://doi.org/10.1002/2016GL071205, 2017.

Cochlan, W. P. and Bronk, D. A.: Effects of ammonium on nitrate utilization in the Ross Sea, Antarctica: Implications for *f*-ratio estimates, 78, 159–178, https://doi.org/10.1029/078ars10, 2003.

Cota, G. F., Smith, W. O., Nelson, D. M., Muench, R. D., and Gordon, L. I.: Nutrient and biogenic particulate distributions, primary productivity and nitrogen uptake in the Weddell-Scotia Sea marginal ice zone during winter, J. Mar. Res., 50, 155–181, https://doi.org/10.1357/002224092784797764, 1992.

De Baar, H. J. W., Boyd, P. W., Coale, K. H., Landry, M. R., Tsuda, A., Assmy, P., Bakker, D. C. E., Bozec, Y., Barber, R. T., Brzezinski, M. A., Buesseler, K. O., Boyé, M., Croot, P. L., Gervais, F., Gorbunov, M. Y., Harrison, P. J., Hiscock, W. T., Laan, P., Lancelot, C., Law, C. S., Levasseur, M., Marchetti, A., Millero, F. J., Nishioka, J., Nojiri, Y., Van Oijen, T., Riebesell, U., Rijkenberg, M. J. A., Saito, H., Takeda, S., Timmermans, K. R., Veldhuis, M. J. W., Waite, A. M., and Wong, C.-S.:

Synthesis of iron fertilization experiments: From the Iron Age in the Age of Enlightenment, J. Geophys. Res., 110, 9–16, https://doi.org/10.1029/2004JC002601, 2005.

De Jong, J., Schoemann, V., Lannuzel, D., Croot, P., De Baar, H., and Tison, J. L.: Natural iron fertilization of the Atlantic sector of the Southern Ocean by continental shelf sources of the Antarctic Peninsula, J. Geophys. Res. Biogeosciences, 117, https://doi.org/10.1029/2011JG001679, 2012.

Deary, A.: A high-resolution study of the early- to late-summer progression in primary production and carbon export potential in the Atlantic Southern Ocean Supervisor : Dr Sarah Fawcett, 2020.

Delmont, T. O., Hammar, K. M., Ducklow, H. W., Yager, P. L., and Post, A. F.: Phaeocystis antarctica blooms strongly influence bacterial community structures in the Amundsen Sea polynya, Front. Microbiol., 5, 1–13, https://doi.org/10.3389/fmicb.2014.00646, 2014.

DeVries, T.: The Oceanic Anthropogenic CO2 Sink: Storage, Air-Sea Fluxes, and Transports over the Industrial Era, Global Biogeochem. Cycles, 28, 631–647, 2014.

Diamond, D.: QuikChem Method 10-114-21-1-B: Silicate by flow injection analysis., 1994.

Dinniman, M. S., St-Laurent, P., Arrigo, K. R., Hofmann, E. E., and Dijken, G. L. van: Analysis of Iron Sources in Antarctic Continental Shelf Waters, J. Geophys. Res. Ocean., 125, e2019JC015736, https://doi.org/10.1029/2019JC015736, 2020.

Ditullio, G. R., Grebmeier, J. M., Arrigo, K. R., and Lizotte, M. P.: Rapid and early export of Phaeocystis antarctica blooms in the Ross Sea , Antarctica, 404, 1996–1999, 2000.

Dortch, Q.: The interaction between ammonium and nitrate uptake in phytoplankton, Mar. Ecol. Prog. Ser., 61, 183–201, https://doi.org/10.3354/meps061183, 1990.

Dowdeswell, J., Shears, J., Batchelor, C., Christie, F., Rack, W., Montelli, A., Evans, J., Dowdeswell, E., Ottesen, D., Fawcett, S., Bornman, T., Hutchinson, K., Audh, R., Burger, J., Flynn, R., Henry, T., Luyt, H., Smith, S., Spence, K., Woodall, L., Taylor, M., Frinault, B., Bekker, A., Zu, L., van Zilj, C., Matthee, J., and Makgabutlane, M.: The Weddell Sea Expedition 2019: Cruise Scientific Report, https://doi.org/https://doi.org/10.17863/CAM.58103, 2019.

Dubelaar, G. B. J. and Jonker, R. R.: Flow cytometry as a tool for the study of phytoplankton, Sci. Mar., 64, 135–156, https://doi.org/10.3989/scimar.2000.64n2135, 2000.

Dugdale, R. C. and Goering, J. J.: Uptake of New and Regenerated Forms of Nitrogen in Primary Productivity, Limnol. Oceanogr., 12, 196–206, https://doi.org/10.4319/lo.1967.12.2.0196, 1967.

Dugdale, R. C. and Wilkerson, F. P.: The use of 15N to measure nitrogen uptake in eutrophic experimental considerations1 t2, 3, 1986.

Eicken, H.: The role of sea ice in structuring Antarctic ecosystems, in: Weddell Sea Ecology, 3–13, 1993.

El-Sayed, S.: Productivity of the Antarctic Waters — A Reappraisal, in: Marine Phytoplankton and Productivity. Lecture Notes on Coastal and Estuarine Studies., edited by: O., H.-H., L., B., and R., G., Springer Berlin Heidelberg, 19–34, 1984.

El-Sayed, S. Z. and Taguchi, S.: Primary production and standing crop of phytoplankton along the ice-

edge in the Weddell Sea, Deep Sea Res. Part A, Oceanogr. Res. Pap., 28, 1017–1032, https://doi.org/10.1016/0198-0149(81)90015-7, 1981.

Eppley, R. W., Peterson, B.: Particulate organic matter flux and planktonic new production in the deep ocean, Nature, 282, 677–680, 1979.

Fahrbach, E., Rohardt, G., Schröder, M., and Strass, V.: Transport and structure of the weddell gyre, Ann. Geophys., 12, 840–855, https://doi.org/10.1007/s00585-994-0840-7, 1994.

Fahrbach, E., Rohardt, G., Scheele, N., Schroder, M., Strass, V., and Wisotzki, A.: Formation and discharge of deep and bottom water in the northwestern Weddell Sea, J. Mar. Res., 53, 515–538, https://doi.org/10.1357/0022240953213089, 1995.

Ferreira, A., Costa, R. R., Dotto, T. S., Kerr, R., Tavano, V. M., Brito, A. C., Brotas, V., Secchi, E. R., and Mendes, C. R. B.: Changes in Phytoplankton Communities Along the Northern Antarctic Peninsula: Causes, Impacts and Research Priorities, Front. Mar. Sci., 7, https://doi.org/10.3389/fmars.2020.576254, 2020.

Finkel, Z. V., Quigg, A., Raven, J. A., Reinfelder, J. R., Schofield, O. E., and Falkowski, P. G.: Irradiance and the elemental stoichiometry of marine phytoplankton, Limnol. Oceanogr., 51, 2690–2701, https://doi.org/10.4319/LO.2006.51.6.2690, 2006.

Franck, V. M., Brzezinski, M. A., Coale, K. H., and Nelson, D. M.: Iron and silicic acid concentrations regulate Si uptake north and south of the Polar Frontal Zone in the Pacific Sector of the Southern Ocean, Deep. Res. Part II Top. Stud. Oceanogr., 47, 3315–3338, https://doi.org/10.1016/S0967-0645(00)00070-9, 2000.

Fripiat, F., Sigman, D. M., Fawcett, S. E., Rafter, P. A., Weigand, M. A., and Tison, J.-L.: New insights into sea ice nitrogen biogeochemical dynamics from the nitrogen isotopes, Global Biogeochem. Cycles, 28, 115–130, https://doi.org/10.1002/2013GB004729, 2014.

Fripiat, F., Meiners, K. M., Vancoppenolle, M., Papadimitriou, S., Thomas, D. N., Ackley, S. F., Arrigo, K. R., Carnat, G., Cozzi, S., Delille, B., Dieckmann, G. S., Dunbar, R. B., Fransson, A., Kattner, G., Kennedy, H., Lannuzel, D., Munro, D. R., Nomura, D., Rintala, J. M., Schoemann, V., Stefels, J., Steiner, N., and Tison, J. L.: Macro-nutrient concentrations in Antarctic pack ice: Overall patterns and overlooked processes, 5, https://doi.org/10.1525/elementa.217, 2017.

Fripiat, F., Martínez-García, A., Marconi, D., Fawcett, S., Kopf, S., Luu, V., Rafter, P., Zhang, R., Sigman, D., and Haug, G.: Nitrogen isotopic contraints on nutrient transport to the upper ocean, Nat. Geosci., 2021.

Frölicher, T. L., Sarmiento, J. L., Paynter, D. J., Dunne, J. P., Krasting, J. P., and Winton, M.: Dominance of the Southern Ocean in anthropogenic carbon and heat uptake in CMIP5 models, J. Clim., 28, 862–886, 2015.

Garcia, N. S., Sexton, J., Riggins, T., Brown, J., Lomas, M. W., and Martiny, A. C.: High variability in cellular stoichiometry of carbon, nitrogen, and phosphorus within classes of marine eukaryotic phytoplankton under sufficient nutrient conditions, Front. Microbiol., 9, 1–10,

https://doi.org/10.3389/fmicb.2018.00543, 2018.
Gill, A. E.: Circulation and bottom water production in the Weddell Sea, Deep. Res. Oceanogr. Abstr., 20, 111–140, https://doi.org/10.1016/0011-7471(73)90048-X, 1973.
Gleitz, M., Michiel, M. R., Thomas, D. N., Dieckmann, G. S., and Millero, F. J.: Comparison of summer and winter inorganic carbon, oxygen and nutrient concentrations in Antarctic sea ice brine, Mar. Chem., 51, 81–91, https://doi.org/10.1016/0304-4203(95)00053-T, 1995.
Glibert, P. M., Wilkerson, F. P., Dugdale, R. C., Raven, J. A., Dupont, C. L., Leavitt, P. R., Parker, A. E., Burkholder, J. M., and Kana, T. M.: Pluses and minuses of ammonium and nitrate uptake and assimilation by phytoplankton and implications for productivity and community composition, with emphasis on nitrogen-enriched conditions, Limnol. Oceanogr., 61, 165–197, https://doi.org/10.1002/lno.10203, 2016.
Goeyens, L.: Ammonium regeneration in the Scotia-Weddell Confluence area during spring 1988, Mar. Ecol. Prog. Ser., 78, 241–252, https://doi.org/10.3354/meps078241, 1991.
Goeyens, L., Tréguer, P., Baumann, M. E. M., Baeyens, W., and Dehairs, F.: The leading role of ammonium in the nitrogen uptake regime of Southern Ocean marginal ice zones, J. Mar. Syst., 6, 345–361, https://doi.org/10.1016/0924-7963(94)00033-8, 1995.
Goffart, A., Catalano, G., and Hecq, J. H.: Factors controlling the distribution of diatoms and Phaeocystis in the Ross Sea, J. Mar. Syst., 27, 161–175, https://doi.org/10.1016/S0924-7963(00)00065-8, 2000.
Gonfiantini, R.: Stable isotope reference samples for geochemical and hydrological investigations., Rep. Advis. Group, Vienna., 1984.
Gordon, A. L., Huber, B. A., Hellmer, H. H., & Ffield, A.: Deep and bottom water of the Weddell Sea's western rim., Science (80-.)., 265, 95–97, 1993.
Granger, J. and Sigman, D. M.: Removal of nitrite with sulfamic acid for nitrate N and O isotope analysis with the denitrifier method, Rapid Commun. Mass Spectrom., 23, 3753–3762, https://doi.org/10.1002/rcm.4307, 2009.
Grasshoff, K.: Methods of seawater analysis, Weinheim and New York: Verlag Chemie, 1976.
Green, S. E. and Sambrotto, R. N.: Plankton community structure and export of C, N, P and Si in the Antarctic Circumpolar Current, Deep. Res. Part II Top. Stud. Oceanogr., 53, 620–643, https://doi.org/10.1016/j.dsr2.2006.01.022, 2006.
Gruber, N., Clement, D., Carter, B. R., Feely, R. A., Van Heuven, S., and Hoppema, M.: The oceanic sink for anthropogenic CO2 from 1994 to 2007, Science (80-.)., 363, 1193–1199, 2019.
Henley, S. F., Tuerena, R. E., Annett, A. L., Fallick, A. E., Meredith, M. P., Venables, H. J., Clarke, A., and Ganeshram, R. S.: Macronutrient supply, uptake and recycling in the coastal ocean of the west Antarctic Peninsula, Deep. Res. Part II Top. Stud. Oceanogr., 139, 58–76, https://doi.org/10.1016/j.dsr2.2016.10.003, 2017.
Holmes, R. M., Aminot, A., Kerouel, R., Hooker, B. A., and Peterson, B. J.: A simple and precise

method for measuring ammonium in marine and freshwater ecosystems, https://doi.org/10.1139/cjfas-56-10-1801, 1999.

Hoppema, M. and Goeyens, L.: Redfield behavior of carbon, nitrogen, and phosphorus depletions in Antarctic surface water, Limnol. Oceanogr., 44, 220–224, https://doi.org/10.4319/lo.1999.44.1.0220, 1999.

Hoppema, M., Stoll, M. H. C., and De Baar, H. J. W.: Co2 in the Weddell Gyre and Antarctic Circumpolar Current: Austral autumn and early winter, Mar. Chem., 72, 203–220, https://doi.org/10.1016/S0304-4203(00)00082-7, 2000a.

Hoppema, M., Goeyens, L., and Fahrbach, E.: Intense nutrient removal in the remote area off Larsen Ice Shelf (Weddell Sea), Polar Biol., 23, 85–94, https://doi.org/10.1007/s003000050012, 2000b.

Hoppema, M.: Weddell Sea is a globally significant contributor to deep-sea sequestration of natural carbon dioxide, Deep. Res. Part I Oceanogr. Res. Pap., 51, 1169–1177, https://doi.org/10.1016/j.dsr.2004.02.011, 2004.

Hoppema, M., Middag, R., de Baar, H., Fahrbach, E., van Weerlee, E., and Thomas, H.: Whole season net community production in the Weddell Sea, Polar Biol., 31, 101–111, 2007.

Hoppema, M., Bakker, K., MAC van Heuven, S., van Ooijen, J. C., and de Baar, H. J.: Distributions, trends and inter-annual variability of nutrients along a repeat section through the Weddell Sea (1996-2011), https://doi.org/10.1016/j.marchem.2015.08.007, 2015.

Hutchins, D. A. and Bruland, K. W.: Iron-limited growth and Si:N ratios in a costal upwelling regime, Nature, 393, 561–564, 1998.

Hutchinson, K., Deshayes, J., Sallee, J. B., Dowdeswell, J. A., de Lavergne, C., Ansorge, I., Luyt, H., Henry, T., and Fawcett, S. E.: Water Mass Characteristics and Distribution Adjacent to Larsen C Ice Shelf, Antarctica, J. Geophys. Res. Ocean., 125, 0–2, https://doi.org/10.1029/2019JC015855, 2020.

Isla, E., Rossi, S., Palanques, A., Gili, J. M., Gerdes, D., and Arntz, W.: Biochemical composition of marine sediment from the eastern Weddell Sea (Antarctica): High nutritive value in a high benthic-biomass environment, J. Mar. Syst., 60, 255–267, https://doi.org/10.1016/J.JMARSYS.2006.01.006, 2006.

Isla, E., Gerdes, D., Rossi, S., Fiorillo, I., Sañé, E., Gili, J.-M., and Arntz, W. E.: Biochemical characteristics of surface sediments on the eastern Weddell Sea continental shelf, Antarctica: is there any evidence of seasonal patterns?, Polar Biol. 2011 348, 34, 1125–1133, https://doi.org/10.1007/S00300-011-0973-6, 2011.

Ito, T., Woloszyn, M., and Mazloff, & M.: Anthropogenic carbon dioxide transport in the Southern Ocean driven by Ekman flow, 463, https://doi.org/10.1038/nature08687, 2010.

Jacobs, S. S.: The Antarctic slope front, Antarct. JUS, 21, 123–124, 1986.

Jacobs, S. S.: On the nature and significance of the Antarctic Slope Front, Mar. Chem., 35, 9–24, https://doi.org/10.1016/S0304-4203(09)90005-6, 1991.

Jacques, G.: Is the concept of new production—regenerated production valid for the Southern Ocean?,

Mar. Chem., 35, 273–286, https://doi.org/10.1016/S0304-4203(09)90022-6, 1991.
Jennings, J. C., Gordon, L. I., and Nelson, D. M.: Nutrient depletion indicates high primary productivity in the Weddell Sea, Nature, 309, 51–54, https://doi.org/10.1038/309051a0, 1984.
Kana, T. M. and Glibert, P. M.: Effect of irradiances up to 2000 μE m-2 s-1 on marine Synechococcus WH7803-I. Growth, pigmentation, and cell composition, Deep Sea Res. Part A, Oceanogr. Res. Pap., 34, 479–495, https://doi.org/10.1016/0198-0149(87)90001-X, 1987.
Kaprelyants, A. S. and Kell, D. B.: Dormancy in stationary-phase cultures of Micrococcus luteus: flow cytometric analysis of starvation and resuscitation, 1Applied Environ. Microbiol., 59, 3187–3196, 1993.
Karsh, K. L., Trull, T. W., Lourey, M. J., and Sigman, D. M.: Relationship of nitrogen isotope fractionation to phytoplankton size and iron availability during the Southern Ocean Iron RElease Experiment (SOIREE), Limnol. Oceanogr., 48, 1058–1068, https://doi.org/10.4319/lo.2003.48.3.1058, 2003.
Keffer, T. and Holloway, G.: Estimating Southern Ocean eddy flux of heat and salt from satellite altimetry, Nature, 332, 624–626, https://doi.org/10.1038/332624a0, 1988.
Keller, D. P., Kriest, L., Koeve, W., and Oschlies, A.: Southern Ocean biological impacts on global ocean oxygen, Geophys. Res. Lett., 43, 6469–6477, 2016.
Kerr, R., Mata, M. M., Mendes, C. R. B., and Secchi, E. R.: Northern Antarctic Peninsula: a marine climate hotspot of rapid changes on ecosystems and ocean dynamics, Deep. Res. Part II Top. Stud. Oceanogr., 149, 4–9, https://doi.org/10.1016/j.dsr2.2018.05.006, 2018.
Klunder, M. B., Laan, P., Middag, R., De Baar, H. J. W., and van Ooijen, J. C.: Dissolved iron in the Southern Ocean (Atlantic sector), Deep. Res. Part II Top. Stud. Oceanogr., 58, 2678–2694, https://doi.org/10.1016/j.dsr2.2010.10.042, 2011.
Klunder, M. B., Laan, P., De Baar, H. J. W., Middag, R., Neven, I., and Van Ooijen, J.: Dissolved Fe across the Weddell Sea and Drake Passage: impact of DFe on nutrient uptake, 11, 651–669, https://doi.org/10.5194/bg-11-651-2014, 2014.
Koike, I., Holm-Hansen, O., and Biggs, D.: Inorganic nitrogen metabolism by Antarctic phytoplankton with special reference to ammonium cycling, Mar. Ecol. Prog. Ser., 30, 105–116, https://doi.org/10.3354/meps030105, 1986.
Lannuzel, D., Schoemann, V., de Jong, J., Chou, L., Delille, B., Becquevort, S., and Tison, J. L.: Iron study during a time series in the western Weddell pack ice, Mar. Chem., 108, 85–95, https://doi.org/10.1016/j.marchem.2007.10.006, 2008.
Le Corre, P. and Minas, H.: Distributions et évolution des éléments nutritifs dans le secteur indien de l'Océan Antarctique en Wn de période estivale, Oceanol. Acta, 6, 365–381, 1983.
Leblanc, K., Arístegui, J., Armand, L., Assmy, P., Beker, B., Bode, A., Breton, E., Cornet, V., Gibson, J., Gosselin, M. P., Kopczynska, E., Marshall, H., Peloquin, J., Piontkovski, S., Poulton, A. J., Quéguiner, B., Schiebel, R., Shipe, R., Stefels, J., Van Leeuwe, M. A., Varela, M., Widdicombe, C.,

and Yallop, M.: A global diatom database- A bundance, biovolume and biomass in the world ocean, Earth Syst. Sci. Data, 4, 149–165, https://doi.org/10.5194/ESSD-4-149-2012, 2012.

Llort, J., Lévy, M., Sallée, J.-B., and Tagliabue, A.: Onset, intensification, and decline of phytoplankton blooms in the Southern Ocean, J. Mar. Sci., 72, 1971–1984, https://doi.org/10.1093/icesjms/fsv053, n.d.

Locarnini, R. A., Whitworth, T., and Nowlin, W. D.: The importance of the Scotia Sea on the outflow of Weddell Sea Deep Water, J. Mar. Res., 51, 135–153, https://doi.org/10.1357/0022240933223846, 1993.

Lomas, M. W. and Glibert, P. M.: Interactions between NH4/+ and NO3/- uptake and assimilation: Comparison of diatoms and dinoflagellates at several growth temperatures, Mar. Biol., 133, 541–551, https://doi.org/10.1007/s002270050494, 1999.

Lourey, M. J., Trull, T. W., and Sigman, D. M.: Sensitivity of δ15N of nitrate, surface suspended and deep sinking particulate nitrogen to seasonal nitrate depletion in the Southern Ocean, Global Biogeochem. Cycles, 17, 1–18, https://doi.org/10.1029/2002gb001973, 2003.

Martin, J. H., Gordon, R. M., and Fitzwater, S. E.: Iron Limitation, Limnol. Oceanogr., 36, 1793–1802, 1991.

Martínez-García, A., Sigman, D. M., Ren, H., Anderson, R. F., Straub, M., Hodell, D. A., Jaccard, S. L., Eglinton, T. I., and Haug, G. H.: Iron Fertilization of the Subantarctic Ocean During the Last Ice Age, 2014.

Martiny, A. C., Pham, C. T. A., Primeau, F. W., Vrugt, J. A., Moore, J. K., Levin, S. A., and Lomas, M. W.: Strong latitudinal patterns in the elemental ratios of marine plankton and organic matter, Nat. Geosci., https://doi.org/10.1038/NGEO1757, 2013.

Mathot, S., Smith, W. O., Carlson, C. A., Garrison, D. L., Gowing, M. M., and Vickers, C. L.: Carbon partitioning within phaeocystis antarctica (prymnesiophyceae) colonies in the ross sea, antarctica, J. Phycol., 36, 1049–1056, https://doi.org/10.1046/j.1529-8817.2000.99078.x, 2000.

McIlvin, M. R. and Casciotti, K. L.: Technical updates to the bacterial method for nitrate isotopic analyses, Anal. Chem., 83, 1850–1856, https://doi.org/10.1021/ac1028984, 2011.

Mdutyana, M., Thomalla, S. J., Philibert, R., Ward, B. B., and Fawcett, S. E.: The Seasonal Cycle of Nitrogen Uptake and Nitrification in the Atlantic Sector of the Southern Ocean, Global Biogeochem. Cycles, 34, 1–29, https://doi.org/10.1029/2019GB006363, 2020.

Moisan, T. A. and Mitchell, B. G.: Photophysiological acclimation of Phaeocystis antarctica Karsten under light limitation, Limnol. Oceanogr., 44, 247–258, https://doi.org/10.4319/LO.1999.44.2.0247, 1999.

Mosseri, J., Quéguiner, B., Armand, L., and Cornet-Barthaux, V.: Impact of iron on silicon utilization by diatoms in the Southern Ocean: A case study of Si/N cycle decoupling in a naturally iron-enriched area, Deep. Res. Part II Top. Stud. Oceanogr., 55, 801–819, https://doi.org/10.1016/j.dsr2.2007.12.003, 2008.

Muench, R. D. and Gordon, A. L.: Circulation and transport of water along the western Weddell Sea

margin, J. Geophys. Res., 100, 18503–18515, https://doi.org/10.1029/95jc00965, 1995.
Nelson, M., Smith, O., Gordon, I., and Huber, A.: nutrient, 92, 7181–7190, 1987.
Nicholls, K. W., Pudsey, C. J., and Morris, P.: Summertime water masses off the northern Larsen C Ice Shelf, Antarctica, Geophys. Res. Lett., 31, 2–5, https://doi.org/10.1029/2004GL019924, 2004.
Nicholls, K. W., Østerhus, S., Makinson, K., Gammelsrød, T., and Fahrbach, E.: Ice-ocean processes over the continental shelf of the Southern Weddell Sea, Antarctica: A review, Rev. Geophys., 47, 1–23, https://doi.org/10.1029/2007RG000250, 2009.
Nissen, C. and Vogt, M.: Factors controlling the competition between Phaeocystis and diatoms in the Southern Ocean in the Southern Ocean, Biogeosciences Discuss., 1–39, https://doi.org/10.5194/bg-2019-488, 2021.
Olson, R. J.: Differential photoinhibition of marine nitrifying bacteria: a possible mechanism for the formation of the primary nitrite maximum, J. Mar. Res., 39, 227–238, 1981.
Orsi, A. H., Nowlin, W. D., and Whitworth, T.: On the circulation and stratification of the Weddell Gyre, Deep. Res. Part I, 40, 169–203, https://doi.org/10.1016/0967-0637(93)90060-G, 1993.
Orsi, A. H., Whitworth, T., and Nowlin, W. D.: On the meridional extent and fronts of the Antarctic Circumpolar Current, Deep. Res. Part I, 42, 641–673, https://doi.org/10.1016/0967-0637(95)00021-W, 1995.
Park, M. G., Yang, S. R., Kang, S.-H., Chung, K. H., and Shim, J. H.: Phytoplankton biomass and primary production in the marginal ice zone of the northwestern Weddell Sea during austral summer, Polar Biol. 1999 214, 21, 251–261, https://doi.org/10.1007/S003000050360, 1999.
Parsons, T. R., Maita, Y., and Lalli, C. M.: A manual of chemical and biological methods for seawater analysis, 1984.
Paulsen, M. L., Riisgaard, K., Thingstad, T. F., John, M. S., and Nielsen, T. G.: Winter-spring transition in the subarctic Atlantic: Microbial response to deep mixing and pre-bloom production., Aquat. Microb. Ecol., 76, 49–49, 2015.
Peng, X., Fuchsman, C. A., Jayakumar, A., Oleynik, S., Martens-Habbena, W., Devol, A. H., and Ward, B. B.: Ammonia and nitrite oxidation in the eastern tropical North Pacific, Glob. Biogeochem. Cycles2, 29, 2034–2049, 2015.
Petrou, K., Kranz, S. A., Trimborn, S., Hassler, C. S., Ameijeiras, S. B., Sackett, O., Ralph, P. J., and Davidson, A. T.: Southern Ocean phytoplankton physiology in a changing climate, J. Plant Physiol., 203, 135–150, https://doi.org/10.1016/j.jplph.2016.05.004, 2016.
Philibert, R., Waldron, H., and Clark, D.: A geographical and seasonal comparison of nitrogen uptake by phytoplankton in the Southern Ocean, Ocean Sci., 11, 251–267, https://doi.org/10.5194/OS-11-251-2015, 2015.
Pineda-Metz, S. E. A., Isla, E., and Gerdes, D.: Benthic communities of the Filchner Region (Weddell Sea, Antarctica), Mar. Ecol. Prog. Ser., 628, 37–54, https://doi.org/10.3354/MEPS13093, 2019.
Pörtner, H. O., Karl, D. M., Boyd, P. W., Cheung, W. W., Lluch-Cota, S. E., Nojiri, Y., and Et, A.:

Ocean systems, in: Impacts, Adaptation, and Vulnerability. Part A: Global and Sectoral Aspects. Contribution of Working Group II to the Fifth Assessment Report of the Intergovernmental Panel on Climate Change, edited by: Field, C. B. and Et, A., Cambridge University Press, 411–484, 2014.

Priddle, J., Boyd, I. L., Whitehouse, M. J., Murphy, E. J., and Croxall, J. P.: Estimates of Southern Ocean primary production - Constraints from predator carbon demand and nutrient drawdown, in: Journal of Marine Systems, 275–288, https://doi.org/10.1016/S0924-7963(98)00043-8, 1998.

Probyn, T. A. and Painting, S. J.: Nitrogen uptake by size-fractionated phytoplankton populations in Antarctic surface waters1, Limnol. Oceanogr., 30, 1327–1332, https://doi.org/10.4319/LO.1985.30.6.1327, 1985.

Ragueneau, O., Tréguer, P., Leynaert, A., Anderson, R. F., Brzezinski, M. A., DeMaster, D. J., Dugdale, R. C., Dymond, J., Fischer, G., François, R., Heinze, C., Maier-Reimer, E., Martin-Jézéquel, V., Nelson, D. M., and Quéguiner, B.: A review of the Si cycle in the modern ocean: Recent progress and missing gaps in the application of biogenic opal as a paleoproductivity proxy, Glob. Planet. Change, 26, 317–365, https://doi.org/10.1016/S0921-8181(00)00052-7, 2000.

Revilla, M., Alexander, J., and Glibert, P. M.: Urea analysis in coastal waters: Comparison of enzymatic and direct methods, Limnol. Oceanogr. Methods, 3, 290–299, https://doi.org/10.4319/lom.2005.3.290, 2005.

Rönner, U., Sörensson, F., and Holm-Hansen, O.: Nitrogen assimilation by phytoplankton in the Scotia Sea, Polar Biol., 2, 137–147, https://doi.org/10.1007/BF00448963, 1983.

Sallée, J. B., Shuckburgh, E., Bruneau, N., Meijers, A. J., Bracegirdle, T. J., and Wang, Z.: Assessment of Southern Ocean mixed-layer depths in CMIP5 models: Historical bias and forcing response, J. Geophys. Res. Ocean., 118, 1845–1862, 2013.

Santoro, A. E., Sakamoto, C. M., Smith, J. M., Plant, J. N., Gehman, A. L., Worden, A. Z., Johnson, K. S., Francis, C. A., and Casciotti, K. L.: Measurements of nitrite production in and around the primary nitrite maximum in the central California Current, 10, 7395–7410, https://doi.org/10.5194/bg-10-7395-2013, 2013.

Sarmiento, J., Toggweiler, J.: A new model for the role of the oceans in determining atmospheric P CO2., Nature, 308, 621–624, https://doi.org/https://doi.org/10.1038/308621a0, 1984.

Sarmiento, J. L., Gruber, N., Brzezinski, M. A., and Dunne, J. P.: High-latitude controls of thermocline nutrients and low latitude biological productivity, Nature, 427, 56–60, https://doi.org/10.1038/nature10605, 2004.

Saxberg, B. E. H. and Kowalski, B. R.: Generalized Standard Addition Method, Anal. Chem., 51, 1031–1038, https://doi.org/10.1021/ac50043a059, 1979.

Scharek, R., Smetacek, V., Fahrbach, E., Gordon, L. I., Rohardt, G., and Moore, S.: The transition from winter to early spring in the eastern Weddell Sea, Antarctica: Plankton biomass and composition in relation to hydrography and nutrients, Deep. Res. Part I, 41, 1231–1250, https://doi.org/10.1016/0967-0637(94)90042-6, 1994.

Schodlok, M. P., Hellmer, H. H.,&Beckmann, A.: On the transport, variability and origin of densewatermasses crossing the South Scotia Ridge.e, Deep Sea Res. II Trop. Stud. Oceanogr., 49, 4807–4825, 2002.

Schoemann, V., Becquevort, S., Stefels, J., Rousseau, V., and Lancelot, C.: Phaeocystis blooms in the global ocean and their controlling mechanisms: A review, J. Sea Res., 53, 43–66, https://doi.org/10.1016/j.seares.2004.01.008, 2005.

Schofield, O., Miles, T., Alderkamp, A. C., Lee, S. H., Haskins, C., Rogalsky, E., Sipler, R., Sherrell, R. M., and Yager, P. L.: In situ phytoplankton distributions in the Amundsen Sea Polynya measured by autonomous gliders, 3, 1–17, https://doi.org/10.12952/journal.elementa.000073, 2015.

Schröder, M., Hellmer, H. H., and Absy, J. M.: On the near-bottom variability in the northwestern Weddell Sea, Deep. Res. Part II Top. Stud. Oceanogr., 49, 4767–4790, https://doi.org/10.1016/S0967-0645(02)00158-3, 2002.

Sedwick, P. N., Di Tullio, G. R., and Mackey, D. J.: Iron and manganese in the Ross Sea, Seasonal iron limitation in Antarctic, J. Geophys. Res. Ocean., 105, 11321–11336, https://doi.org/10.1029/2000JC000256, 2000.

Semeneh, M., Dehairs, F., Elskens, M., Baumann, M. E. M., Kopczynska, E. E., Lancelot, C., and Goeyens, L.: Nitrogen uptake regime and phytoplankton community structure in the Atlantic and Indian sectors of the Southern Ocean, J. Mar. Syst., 17, 159–177, https://doi.org/10.1016/S0924-7963(98)00036-0, 1998.

SI, R., T, T., DW, C., and JG, G.: Primary productivity and nutrient utilization ratios in the Pacific sector of the Southern Ocean based on seasonal changes in seawater chemistry, Deep Sea Res. Part I Oceanogr. Res. Pap., 45, 1211–1234, 1998.

Sigman, D. M. and Boyle[2], E. A.: Glacial/interglacial variations in atmospheric carbon dioxide, NATURE, 2000.

Sigman, D. M., Casciotti, K. L., Andreani, M., Barford, C., Galanter, M., and Böhlke, J. K.: A bacterial method for the nitrogen isotopic analysis of nitrate in seawater and freshwater, Anal. Chem., 73, 4145–4153, https://doi.org/10.1021/ac010088e, 2001.

Sigman, D. M., Hain, M. P., and Haug, G. H.: The polar ocean and glacial cycles in atmospheric CO 2 concentration, Nature, 466, https://doi.org/10.1038/nature09149, 2010.

Smart, S. M., Fawcett, S. E., Ren, H., Schiebel, R., Tompkins, E. M., Martínez-García, A., Stirnimann, L., Roychoudhury, A., Haug, G. H., and Sigman, D. M.: The Nitrogen Isotopic Composition of Tissue and Shell-Bound Organic Matter of Planktic Foraminifera in Southern Ocean Surface Waters, Geochemistry, Geophys. Geosystems, 21, 1–29, https://doi.org/10.1029/2019GC008440, 2020.

Smetacek, V.: The giant diatom dump, Nat. 2000 4066796, 406, 574–575, https://doi.org/10.1038/35020665, 2000.

Smetacek, V., Assmy, P., and Henjes, J.: The role of grazing in structuring Southern Ocean pelagic ecosystems and biogeochemical cycles, Antarct. Sci., 16, 541–558,

https://doi.org/10.1017/S0954102004002317, 2004.

Smith, J. M., Chavez, F. P., and Francis, C. A.: Ammonium Uptake by Phytoplankton Regulates Nitrification in the Sunlit Ocean, PLoS One, 9, 108173, https://doi.org/10.1371/journal.pone.0108173, 2014.

Smith, W. 0. and Nelson, D. M.: Phytoplankton growth and new production in the Weddell Sea marginal ice zone in the austral spring and autumn, Limnol. Oceanogr., 35, 809–821, https://doi.org/10.4319/lo.1990.35.4.0809, 1990.

Smith, W. O. and Asper, V. L.: The influence of phytoplankton assemblage composition on biogeochemical characteristics and cycles in the southern Ross Sea, Antarctica, Deep. Res. Part I Oceanogr. Res. Pap., 48, 137–161, https://doi.org/10.1016/S0967-0637(00)00045-5, 2001.

Spiridonov, V. A., Nöthig, E. M., Schröder, M., and Wisotzki, A.: The onset of biological winter in the eastern Weddell Gyre (Antarctica) planktonic community, J. Mar. Syst., 9, 211–230, https://doi.org/10.1016/S0924-7963(95)00049-6, 1996.

Stammerjohn, S., Massom, R., Rind, D., and Martinson, D.: Regions of rapid sea ice change: An inter-hemispheric seasonal comparison, Geophys. Res. Lett., 39, L06501, 2012.

Stefels, J. and Van Leeuwe, M. A.: Effects of iron and light stress on the biochemical composition of antarctic Phaeocystis sp. (Prymnesiophyceae). I. Intracellular DMSP concentrations, J. Phycol., 34, 486–495, https://doi.org/10.1046/j.1529-8817.1998.340486.x, 1998.

Strickland, J. D. H. and Parsons, T. R.: A practical handbook of seawater analysis, Bull. Fish. Res. Board Canada, 167, 81–86, 1968.

Strzepek, R. F., Maldonado, M. T., Hunter, K. A., Frew, R. D., and Boyd, P. W.: Adaptive strategies by Southern Ocean phytoplankton to lessen iron limitation: Uptake of organically complexed iron and reduced cellular iron requirements, Limnol. Oceanogr., 56, 1983–2002, https://doi.org/10.4319/lo.2011.56.6.1983, 2011.

Sunda, W. G. and Huntsman, S. A.: Interrelated influence of iron, light and cell size on marine phytoplankton growth, Nature, 390, 389–392, https://doi.org/10.1038/37093, 1997.

Sunda, W. G. and Huntsman, S. A.: High iron requirement for growth, photosynthesis, and low-light acclimation in the coastal cyanobacterium Synechococcus bacillaris, Front. Microbiol., 6, 561, 2015.

Takeda, S.: Influence of iron availability on nutrient consumption ratio, Nature, 393, 774–777, 1998.

Talley, L. D., Pickard, G. L., Emery, W. J., and Swift, J. H.: Southern Ocean, Descr. Phys. Oceanogr., 437–471, https://doi.org/10.1016/b978-0-7506-4552-2.10013-7, 2011.

Taylor, B. W., Keep, C. F., Hall, R. O., Koch, B. J., Tronstad, L. M., Flecker, A. S., and Ulseth, A. J.: Improving the fluorometric ammonium method: matrix effects, background fluorescence, and standard additions, J. North Am. Benthol. Soc., 26, 167–177, https://doi.org/10.1899/0887-3593(2007)26[167:ITFAMM]2.0.CO;2, 2007.

Treguer, P. and G, J.: Review Dynamics of nutrients and phytoplankton, and fluxes of carbon, nitrogen and silicon in the Antarctic Ocean, edited by: Hempel, G., Springer Berlin Heidelberg, 1992.

Tréguer, P., Bowler, C., Moriceau, B., Dutkiewicz, S., Gehlen, M., Aumont, O., Bittner, L., Dugdale, R., Finkel, Z., Iudicone, D., Jahn, O., Guidi, L., Lasbleiz, M., Leblanc, K., Levy, M., and Pondaven, P.: Influence of diatom diversity on the ocean biological carbon pump, Nat. Geosci., https://doi.org/10.1038/s41561-017-0028-x, 2017.

Vernet, M., Geibert, W., Hoppema, M., Brown, P. J., Haas, C., Hellmer, H. H., Jokat, W., Jullion, L., Mazloff, M., Bakker, D. C. E., Brearley, J. A., Croot, P., Hattermann, T., Hauck, J., Hillenbrand, C. D., Hoppe, C. J. M., Huhn, O., Koch, B. P., Lechtenfeld, O. J., Meredith, M. P., Naveira Garabato, A. C., Nöthig, E. M., Peeken, I., Rutgers van der Loeff, M. M., Schmidtko, S., Schröder, M., Strass, V. H., Torres-Valdés, S., and Verdy, A.: The Weddell Gyre, Southern Ocean: Present Knowledge and Future Challenges, Rev. Geophys., 57, 623–708, https://doi.org/10.1029/2018RG000604, 2019.

Vogt, M., O'Brien, C., Peloquin, J., Schoemann, V., Breton, E., Estrada, M., Gibson, J., Karentz, D., Van Leeuwe, M. A., Stefels, J., Widdicombe, C., and Peperzak, L.: Global marine plankton functional type biomass distributions: <i>Phaeocystis</i> spp., Earth Syst. Sci. Data, 4, 107–120, https://doi.org/10.5194/essd-4-107-2012, 2012.

Volk, T. and Hoffert, M. I.: Ocean Carbon Pumps: Analysis of Relative Strengths and Efficiencies in Ocean-Driven Atmospheric CO2 Changes, in: Geophysical Monograph Series, edited by: Sundquist, E. T. and Broecker, W. S., 1985.

Ward, B. B.: Light and substrate concentration relationships with marine ammonium assimilation and oxidation rates, Mar. Chem., 16, 301–316, https://doi.org/10.1016/0304-4203(85)90052-0, 1985.

Ward, B. B.: Temporal variability in nitrification rates and related biogeochemical factors in Monterey Bay, California, USA, Mar. Ecol. Prog. Ser., 292, 97–109, https://doi.org/10.3354/meps292097, 2005.

Weber, T. S. and Deutsch, C.: Ocean nutrient ratios governed by plankton biogeography, https://doi.org/10.1038/nature09403, 2010a.

Weber, T. S. and Deutsch, C.: Ocean nutrient ratios governed by plankton biogeography, Nature, 467, 550–554, https://doi.org/10.1038/nature09403, 2010b.

Whitworth, T. and Nowlin, W. D.: Water Masses and Currents of the Southern Ocean at the Greenwich Meridian, JOURNAL OF GEOPHYSICAL RESEARCH, 6462–6476 pp., https://doi.org/10.1029/JC092iC06p06462, 1987.

Yool, A., Martin, A. P., Fernández, C., and Clark, D. R.: The significance of nitrification for oceanic new production, https://doi.org/10.1038/nature05885, n.d.

Zakem, E. J., Al-Haj, A., Church, M. J., Van Dijken, G. L., Dutkiewicz, S., Foster, S. Q., Fulweiler, R. W., Mills, M. M., and Follows, M. J.: Ecological control of nitrite in the upper ocean, Nat. Commun., 9, https://doi.org/10.1038/s41467-018-03553-w, 2018.

Appendix B: Summertime productivity and carbon export potential in the Weddell Sea, with a focus on the waters adjacent to Larsen C Ice Shelf

B1. Carbon content of the identified Antarctic diatom species

Light microscopy was used to identify the diatom cells to the lowest taxonomic classification possible. Due to unforeseen circumstances, we were unable to the measure the size and carbon content of individual diatoms. We therefore used the average size (μm) and carbon content (pg C cell^{-1}) for the diatom species identified in this study as determined by Leblanc et al. (2012) for the high-latitude Southern Ocean (50 – 70°S) (Table B1).

Table B1. Average carbon content (pg C cell^{-1}) assigned to the various diatom species identified via light microscopy, taken from Leblanc et al. (2012) for waters between 50 and 70°S. "–" indicates no available data.

Diatom species	Average carbon content (pg C cell^{-1})
Actinocyclis actinochilus	13575
Amphiprora kufferathi	2115
Amphora sp.	4
Asteromphalus hookeri	1893
Bacteriastrum	2376
Banquisia belgicae	-
Berkeleya rutilans	-
Chaetoceros atlanticus	463
Chaetoceros brevis/neglectus	395
Chaetoceros bulbosa	-
Chaetoceros castracanei	3247
Chaetoceros concavicornis	883
Chaetoceros convolutus	321
Chaetoceros curvatus	388
Chaetoceros debilis	355
Chaetoceros decipiens	1079
Chaetoceros dichaeta	800
Chaetoceros flexuosus	138
Chaetoceros hendeyi	404
Chaetoceros peruvianus	404
Chaetoceros simplex	254
Chaetoceros tortissimus	205
Cocconeis spp	505
Corethron pennatum	317
Coscinodiscus asteromphalus	95958
Coscinodiscus bouvet	22195
Cylindrotheca closterium	300
Dactyliosolen	9039
Entomoneis paludosa	1499

Table B1. *continued*

Diatom species	Average carbon content (pg C cell^{-1})
Ephemera planamembranacea	723
Eucampia antarctica var antarctica	1231
Eucampia antarctica var recta	1231
Fragilariopsis curta	55
Fragilariopsis kerguelensis	283
Fragilariopsis long	243
Fragilariopsis pseudonana	26
Fragilariopsis rhombica	189
Fragilariopsis richerii	243
Fragilariopsis small	26
Gyrosigma sp	5694
Haslea spp	748
Leptocylindrus mediterraneus	1450
Manguinea fusiformis	1114
Membraneis challengeri	12162
Navicula directa	2006
Navicula sp.	1999
Neocalyptrella sp	-
Nitzschia australis	4422
Nitzschia lecontei	4422
Nitzschia medioconstricta	4422
Nitzschia sicula	135
Nitzschia sp.	4422
Nitzschia stellata	4422
Odontella litigosa	4722
Odontella weisflogii	4722
Pinnularia sp	2918
Plagiotropus gaussii	3230
Pleurosigma directum	5050
Proboscia alata	2202
Proboscia inermis	3278
Proboscia sp.	2202
Pseudo-nitzschia sp1	32
Pseudo-nitzschia sp2	32
Pseudo-nitzschia subcurvata	24
Rhizosolenia sp.	3798
Rhizosolenia imbricata	2238
Thalassionema nitzschoides	115
Thalassiosira large	2476
Thalassiosira gracilis	319
Thalassiosira lentignosa	4047
Thalassiosira small	42
Thalassiosira very large	7934
Thalassiothrix antarctica	2456
Trichotoxon reinboldii	4708

B2. Flow cytometric identification of phytoplankton populations

Flow cytometry was used to identify smaller (typically <15 µm) phytoplankton populations at all stations (Fig. 3.1). The size-class of each cell was determined based on forward scatter area (FSC-A) relative to the FSC-A of 2.8 µm and 20 µm beads (Fig. B1a). Once categorised as picoplankton (<2.8 µm), nanoplankton (2.8-20 µm) or microplankton (>20 µm), the cells were further subdivided into six populations based on their phycoerythrin (PE) relative to their chlorophyll-a fluorescence (Fig. B1b).

Synechococcus (Syn) contain high concentrations of PE and relatively low chlorophyll-a (Marie et al., 2005). We identified two Syn populations, with one population characterized by a lower PE content (Syn 2) than the other (Syn 1; Fig. B1b). In contrast to the other phytoplankton groups, the Syn populations were not identified from their size but from their PE vs. chlorophyll-a fluorescence characteristics only. This is because, as Fig. B1a shows, the Syn populations were associated with FSC-A values that overlapped with the pico- and nanoplankton size-classes. This signature is an artefact of Syn having a high ratio of photosystem I to photosystem II compared to other phytoplankton, which increases the electron chain activity, leading to an increase in the emission spectrum and low excitation of the Syn populations (Kaprelyants and Kell, 1993; Sunda and Huntsman, 2015).

The picoeukaryotes (PicoEuk), nanoeukaryotes (NanoEuk 1 and 2), and microeukaryotes (MicroEuk) were initially identified from their FSC-A relative to the FSC-A of the 2.8 µm and 20 µm beads (Fig. B1a). Additionally, PicoEuk and NanoEuk were characterized by intermediate chlorophyll-a and low PE fluorescence relative to the other phytoplankton groups investigated here (Fig. B1b). The PicoEuk and NanoEuk 2 populations fluoresced similarly, with their only discerning factor being size, while the NanoEuk 1 population had relatively higher PE and chlorophyll-a fluorescence than both the PicoEuk and NanoEuk 2 populations. The MicroEuk population had high PE fluorescence and variable chlorophyll-a fluorescence.

To determine the average biovolume of each phytoplankton group, six spherical beads of varying diameters (ranging from 1-15 µm) were run on the flow cytometer. The resulting calibration curve of FSC-A versus volume was used to estimate the biovolume of the PicoEuk, NanoEuk, and MicroEuk populations (Fig. B1c; Table B2). Due to the anomalous FSC-A of the Syn populations, the average Syn biovolume was taken from literature (1 μm^3; Kana and Glibert, 1987; Paulsen et al., 2015).

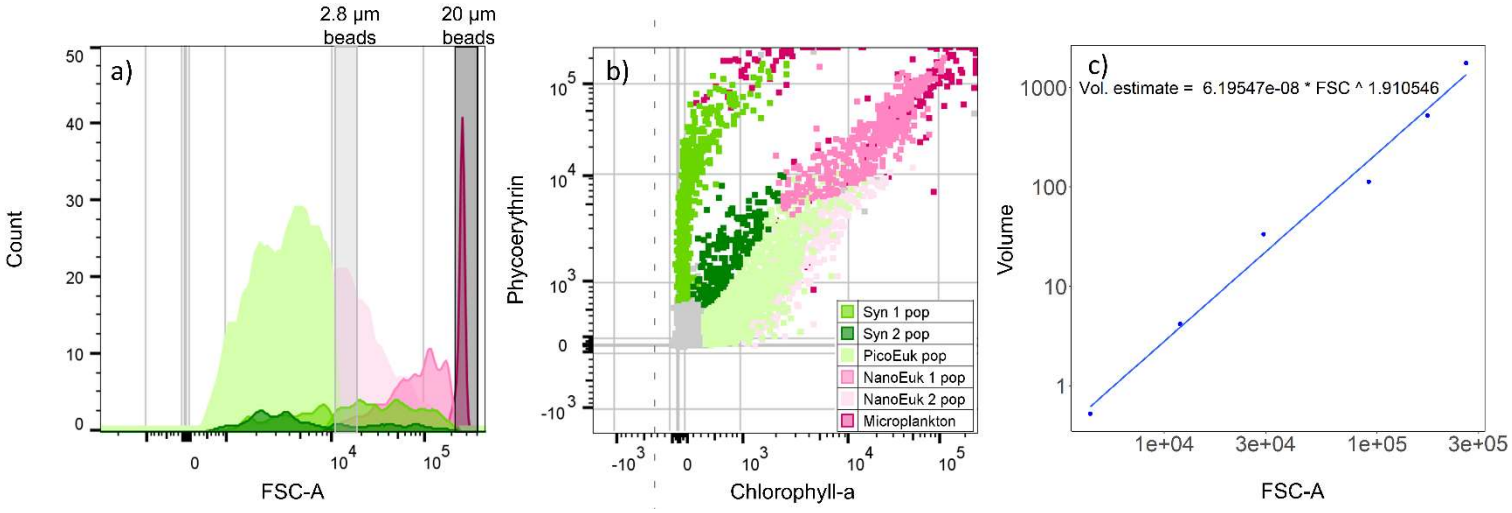


Figure B1. Example (a) histogram of relative cell size as inferred from forward scatter area (FSC-A) and (b) cytogram of phycoerythrin (PE) (i.e., orange) fluorescence versus chlorophyll-a (i.e., red) fluorescence, showing the Weddell Sea populations that were identified using flow cytometry. The populations identified the include: Synechococcus (Syn 1 and Syn 2), picoeukaryotes (PicoEuk), nanoeukaryotes (NanoEuk 1 and NanoEuk 2), and microeukaryotes (MicroEuk). Panel (c) shows the calibration curve generated from beads of various sizes that was used to infer the biovolume of the different phytoplankton groups. The grey vertical bars in panel (a) indicate the FSC-A of the 2.8 µm (light grey) and 20 µm beads (dark grey). The grey data in panel (b) show background noise and detritus.

Table B2. Average biovolumes assigned to the various phytoplankton populations identified using flow cytometry. Due to the anomalous FSC-A of the Synechococcus populations, the average Syn 1 and Syn 2 biovolumes were set to 1 µm^3 (Kana and Glibert, 1987; Paulsen et al., 2015).

Phytoplankton group	Average biovolume (µm^3)
Synechococcus 1	1
Synechococcus 2	1
Picoeukaryotes	0.7 ± 0.3
Nanoeukaryotes 1	159 ± 69
Nanoeukaryotes 2	52 ± 26
Microeukaryotes	1300 ± 29

B3. Including urea uptake in estimates of total N uptake

If NPP is mainly supported by NO_3^- and NH_4^+ and phytoplankton growth is balanced, then the total N uptake rate (i.e., $\rho N_x = \rho NO_3^- + \rho NH_4^+$) at each station multiplied by the Redfield C:N ratio (6.63) should approximate NPP at that station (e.g., Peng et al., 2018, Mdutyana et al., 2020). For the summertime Weddell Sea, NPP was generally well-accounted for by $\rho NO_3^- + \rho NH_4^+$ only, with N uptake × 6.63 even exceeding NPP at some of the AP and WG stations ($\rho NO_3^- + \rho NH_4^+ = 142 \pm 234\%$ of NPP on average; Fig. B2, black symbols). At some of the stations where urea uptake was directly measured (i.e., at LCIS and WG1), ρurea may have been stimulated (i.e., in the cases where total N uptake (= $\rho NO_3^- + \rho NH_4^+ +$ ρurea) × 6.63 exceeds NPP; Fig. B2, grey symbols), likely due to the low ambient concentrations of urea-N present in the euphotic zone at the time of sampling (average of 0.2 ± 0.1 μM; Fig. 3.3.3b and Table 3.1). Nonetheless, we cannot discount the possibility of urea supporting some fraction of NPP, which has implications for estimating carbon export potential given that urea is a regenerated N form. At the stations where urea uptake was measured (11 out of 19), ρurea accounted for 8 ± 6% of total N uptake. We thus estimated urea uptake at the stations where ρurea was not directly measured by multiplying $\rho NO_3^- + \rho NH_4^+$ by 0.08 (see section 3.3.3.4; eq. 3.7). If anything, this will lead to an underestimate of the f-ratio and carbon export potential.

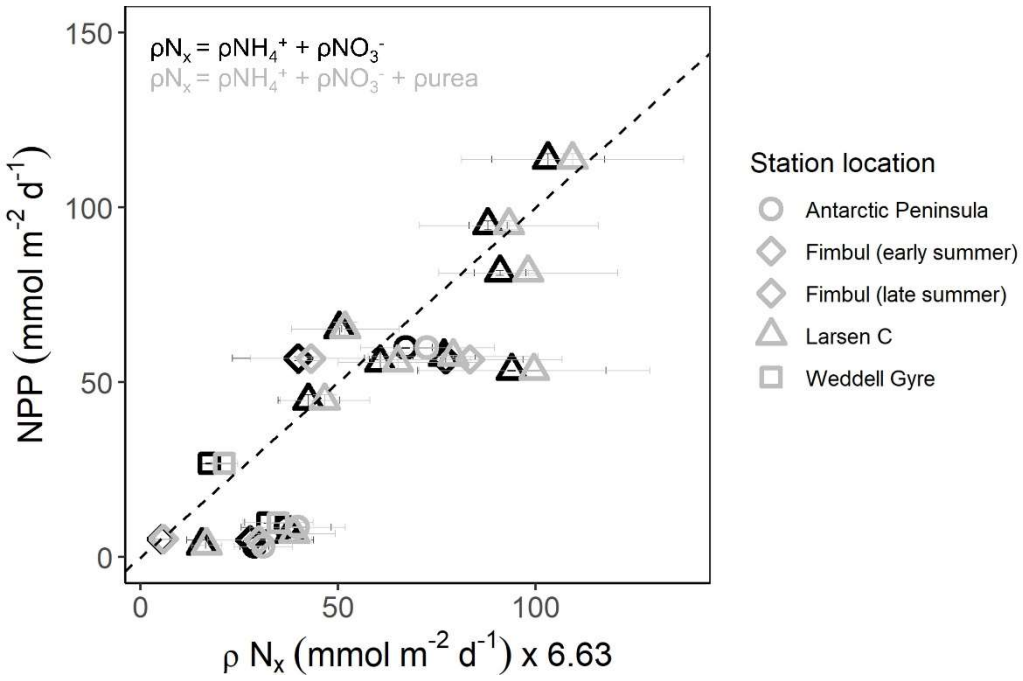


Figure B2. Euphotic zone-integrated rates of NPP and total N uptake (ρN_x) × 6.63. The black symbols represent $\rho N_x = \rho NO_3^- + \rho NH_4^+$ and the grey symbols show $\rho N_x = \rho NO_3^- + \rho NH_4^+ +$ ρurea. The dashed line represents the 1:1 line on which the data points are expected to fall if all N sources supporting NPP are accounted for. Error (± 1 SE) has been propagated according to standard statistical practices.

B4. Multiple dimension statistical analyses

To confirm the relationship of the phytoplankton community to their environment, we performed a Non-metric Multidimensional Scaling (NMDS) and Canonical Correspondence Analysis (CCA) using data from all stations.

NMDS (Fig. B3a) is an indirect gradient analysis approach that produces an ordination based on a distance or dissimilarity matrix using Bray-Curtis distance. The NMDS was used to visualise the community composition differences between sites and samples (data were square-root transformed, Bray-Curtis dissimilarity, 999 permutations using Canoco 5). The LCIS and FIS sites were similar to each other and different from the AP and WG sites. AP3 emerged as an outlier, likely due to the very low species diversity and phytoplankton abundance at that station.

The CCA (Fig. B3b) summarizes the variation in species composition explained by the environmental variables. Monte Carlo permutation tests (499 permutations) were performed to assess the significance of the canonical axes. The environmental variables considered in the analysis are plotted as arrows originating from the centre of the graph. The origin represents the mean value of each variable, and the arrow represents an increase in the value of that variable. The distance between the symbols approximates the dissimilarity of their species composition as measured by their chi-square distance. Prior to the analysis, co-linearity among possible predictor variables was assessed using variance inflation factors (VIF), with VIFs > 5 deemed co-linear (Zuur et al., 2009, 2010). Therefore, salinity, density, oxygen and PO_4^{3-} were omitted from the analysis. The CCA uses the same species data as plotted in the NMDS but shows the species distribution as constrained by the environmental variables. The AP and WG stations were characterized by higher-than-average temperature (and urea concentrations, although this relationship was less significant). Stations L6, L10, and F3 were characterized by lower-than-average temperature and PAR (consistent with recent sea ice melt and deep MLDs). Station F4 was characterized by higher-than-average PAR and NO_2^- and NO_3^- concentrations, and lower-than-average temperature and NH_4^+ and $Si(OH)_4$ concentrations. The LCIS stations to the left of the centre of Fig. B3b (i.e., L1, L2, L4, and L7) were characterized by lower-than-average NO_3^-, NO_2^-, and PAR (likely due to elevated biomass at these stations) and elevated concentrations of NH_4^+ and $Si(OH)_4$.

The NMDS and CCA confirm that the LCIS stations were statistically different from the AP and WG stations, as indicated by the observed variability in the Si:N:P depletion ratios and the dominant phytoplankton groups (i.e., *P. antarctica* at LCIS and diatoms at the AP and WG stations) between the station locations. The LCIS stations were generally characterized by elevated NH_4^+ and urea concentrations (Fig. 3.3a and b), the result of increased heterotrophy and an upregulated microbial loop, and high $Si(OH)_4$ concentrations (Fig. 3.3e), likely the result of low $Si(OH)_4$ uptake by a phytoplankton

community consisting of a low abundance of diatoms (Fig. 3.9). Furthermore, the lowest Si:N and highest N:P depletion ratios were observed at LCIS (consistent with *P. antarctica* dominance), while the highest Si:N and lowest N:P depletion ratios occurred at FIS and in the WG (consistent with diatom dominance; Fig. 3.4 and 3.11; Table 3.1). The variability in phytoplankton community composition appears to have been largely driven by the mechanisms controlling water column stratification, as discussed at length in the main text.

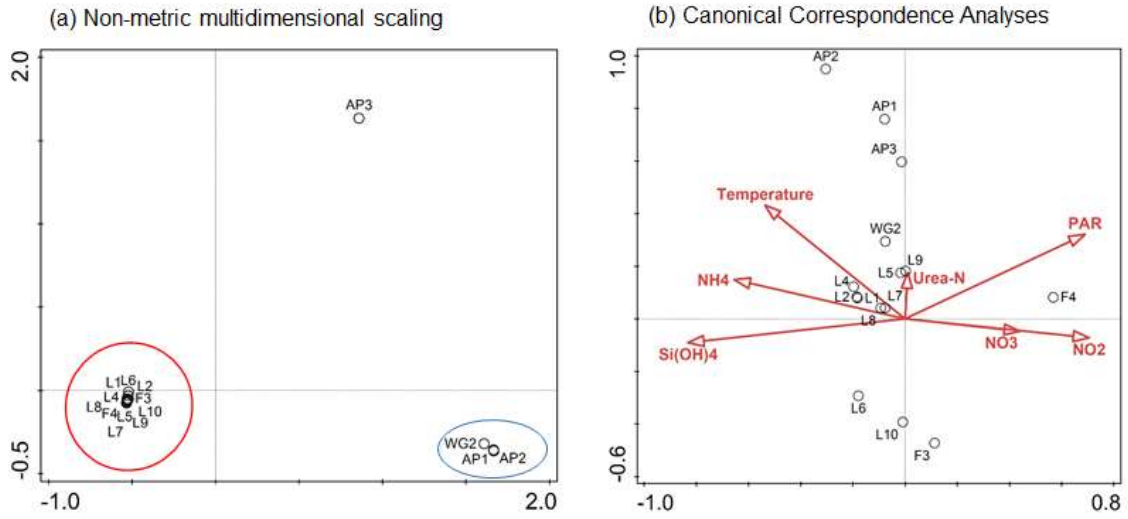


Figure B3. (a) NMDS analysis of the variability in phytoplankton community composition among stations and (b) CCA ordination of phytoplankton species constrained by environmental variables, visualized as a biplot with sampling stations labeled (see Fig. 3.3.1 for station positions).

B5. Apparent effect of temperature on NPP and N uptake

The euphotic zone-averaged rates of NPP and N uptake (μM d^{-1}) generally increased with increasing sea surface temperature (SST) across our study region (Fig. B4a-d). Antarctic phytoplankton growth rates are known to be temperature-sensitive, with very low temperatures limiting cellular metabolic rates (Neori and Holm-Hansen, 1982). However, while the transport rates measured here were positively correlated with SST, the specific rates of carbon fixation and N uptake (d^{-1}; both proxies for growth rate) showed no such relationship (Fig. B4e), suggesting that the phytoplankton community was adapted to the low *in situ* temperatures (Bracher et al., 1999). The observed increase in NPP and N uptake with SST can instead be explained by the observed increase in biomass (i.e., POC and PON) with SST (Fig. B4f; because transport rate = specific rate × biomass). Given this observation, we propose that SST can be used as a measure of time, particularly at LCIS where the stations are very close together, with warmer SSTs indicating "older" surface waters and cooler SST evincing recently upwelled WW. The higher rates of NPP and N uptake in the warm surface waters can be attributed to phytoplankton having experienced favourable growth conditions for an extended period such that

biomass has accumulated, while in cold, newly-upwelled waters, little phytoplankton growth has occurred.

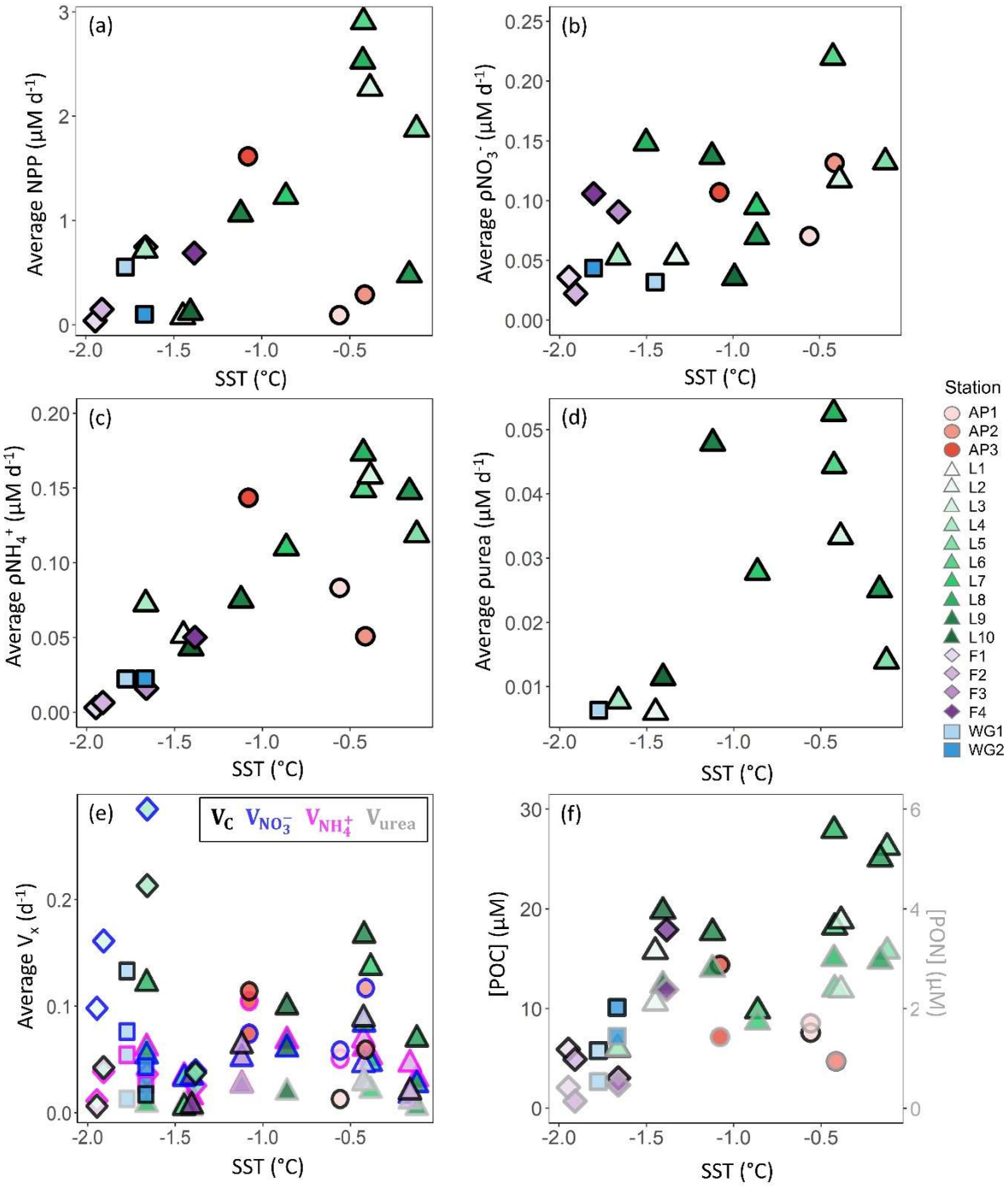


Figure B4. Average euphotic zone rates of (a) net primary production (NPP), (b) NO_3^- uptake (ρNO_3^-), (c) NH_4^+ uptake (ρNH_4^+), and (d) urea uptake (ρurea) as a function of sea surface temperature (SST), as well as the (e) specific rates of NPP, NO_3^-, NH_4^+, and urea uptake (V_X) and (f) concentrations of POC (black outline; left y-axis) and PON (grey outline; right y-axis) versus SST. The symbol outline colours in panel (e) denote the specific uptake rates of carbon (black), NO_3^- (blue), NH_4^+ (pink), and urea (grey).

B6. Upwelling of Winter Water along LCIS

At LCIS, localised "pockets" of cool, saline surface waters were present along the ice shelf front (Fig. B5a-b). This is due to the upwelling of winter water (WW; the source water mass to the surface) at the ice shelf. From the oxygen content of these surface waters, we deduce that these waters were recently upwelled – their oxygen concentrations were low (and below saturation) compared to the other stations (Fig. B5c-d), such that these cool, saline surface waters cannot be attributed to another physical process (e.g., sea-ice melt). Furthermore, the oxygen concentrations in the mixed layer at these stations were contiguous with underlying WW, while the other stations at LCIS (i.e., the "non-upwelling" stations) exhibited an increase in oxygen concentration towards the surface (Fig. B5d) due to gaseous exchange with the atmosphere and phytoplankton and sea-ice algae growth.

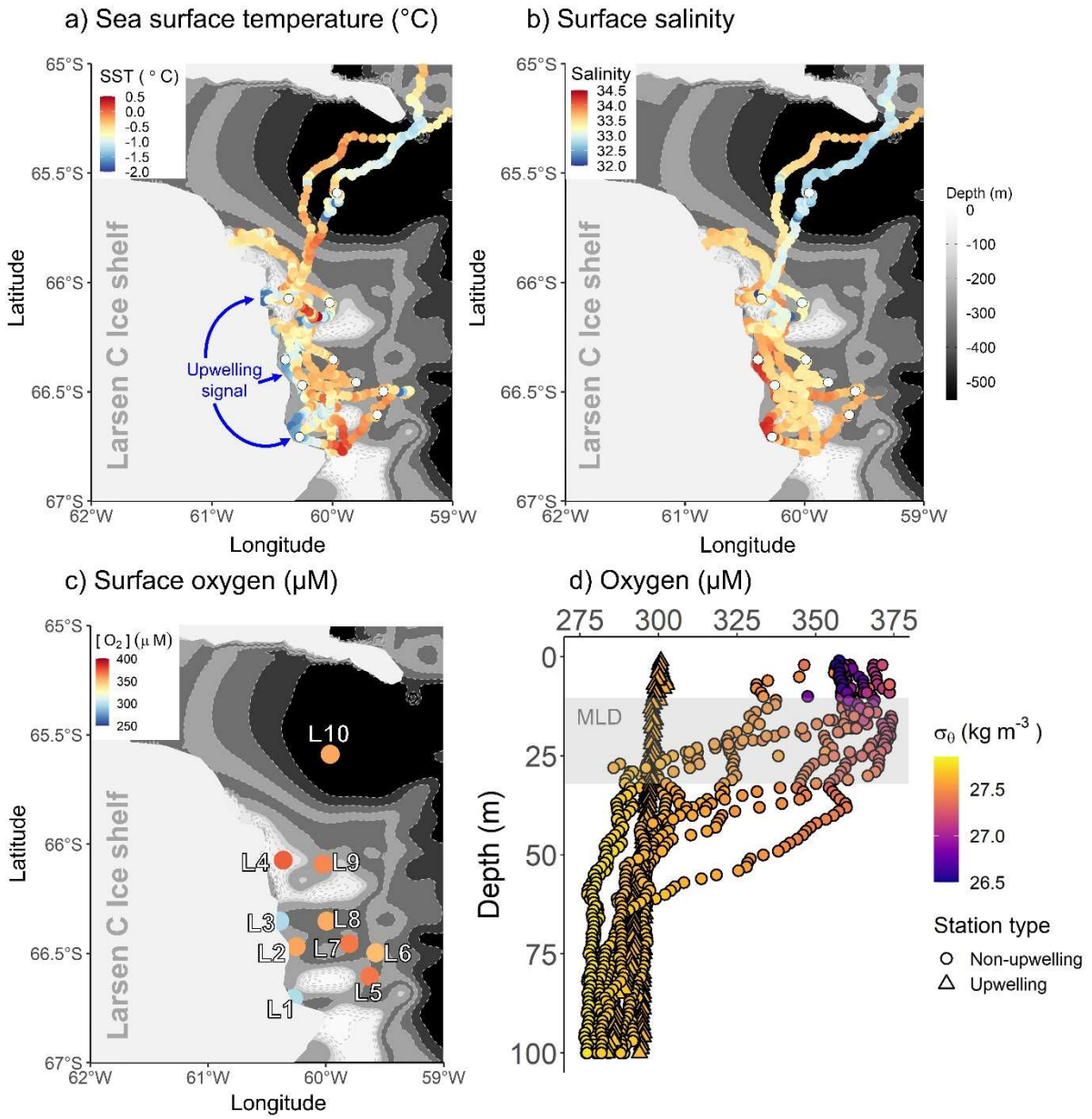


Figure B5. Maps of (a) SST, (b) sea surface salinity, and (c) surface oxygen concentrations and (d) depth profiles of oxygen concentrations in the region of LCIS at the time of sampling. SST and salinity data were acquired from the underway (~7 m inflow) ferrybox, while the oxygen concentrations were measured via the oxygen sensor on the CTD profiler, calibrated against discrete seawater samples measured for dissolved oxygen by Winkler titration (Carpenter, 1965; Grasshoff et al., 1983; Hutchinson et al., 2020). The symbols in panel (d) are coloured by potential density (σ_θ), with the circles indicating the "non-upwelling" stations and the triangles the upwelling stations. The grey box in panel (d) indicates the average mixed layer depth (MLD) ± 1 SD across the stations at LCIS (n=10). The bathymetry data in panels (a-c) were taken from ETOPO1 (NOAA National Geophysical Data Center, 2009).

Chapter 4: Phytoplankton group-specific contributions to carbon export potential across the summertime Weddell Sea

Abstract

The Weddell Sea represents a point of origin where water masses form and exchange with the atmosphere, thereby setting the physical and chemical conditions of much of the global ocean. At Larsen C Ice Shelf (LCIS) in the western Weddell Sea, deep water masses form and subduct, transferring CO_2 to the ocean interior where it remains sequestered for 100s to 1000s of years. The shallow continental shelf and summertime glacial- and sea-ice melt at LCIS alleviate phytoplankton iron and light limitation, fuelling large blooms that drive a strong biological carbon pump. To investigate the potential role of small (<20 μm) Weddell Sea phytoplankton for carbon export, we measured the $^{15}N/^{14}N$ of four flow cytometrically-sorted phytoplankton groups (namely *Synechococcus,* picoeukaryotes, nanoeukaryotes, and cryptophytes) at LCIS, the Antarctic Peninsula (AP), and in the southwestern Weddell Gyre (WG). Phytoplankton growth fuelled by nitrate (NO_3^-) yields particulate organic nitrogen (PON) biomass that is high in $^{15}N/^{14}N$ relative to PON supported by regenerated N sources (e.g., ammonium (NH_4^+) and urea); as such, measurements of phytoplankton $^{15}N/^{14}N$ can be used to infer the dominant N form fuelling their growth, with implications for estimating their contributions to carbon export potential. Across the Weddell Sea, *Synechococcus* numerically dominated the phytoplankton community while the nanoplankton (2.7-20 μm; particularly cryptophytes) contributed most to biomass and N uptake. The dominance of the cryptophytes can be explained by the extremely shallow mixed layers observed across the Weddell Sea (average of 16 ± 7 m) since this group possesses photoprotective pigments while the diatoms and/or *Phaeocystis antarctica* that previously dominated the region do not. At LCIS, the $^{15}N/^{14}N$ of the flow-sorted phytoplankton groups was high compared to the AP and WG stations yet the lowest proportional NO_3^- dependence was estimated for all LCIS phytoplankton groups (average of 51 ± 19% vs. 71 ± 11% and 63 ± 8% at the AP and WG stations), except *Synechococcus*. The lower NO_3^- dependence at LCIS may be partly due to NH_4^+ inhibition, with the NO_3^- dependence of the picoeukaryotes, nanoeukaryotes and cryptophytes decreasing with increasing rates of regenerated N uptake. Although the phytoplankton community relied near equally on NO_3^- and NH_4^+, the carbon export flux was likely high because of elevated phytoplankton biomass present at LCIS. In contrast, the phytoplankton at the AP and WG stations consumed proportionally more NO_3^- than the groups present at LCIS, but the lower biomass and rates of productivity in these waters would have yielded a far lower carbon export flux. Our data show that across the Weddell Sea, new versus regenerated N uptake and carbon export are controlled by various factors, and although the phytoplankton community at LCIS experienced some NH_4^+ inhibition of NO_3^- uptake, it is nonetheless a region characterised by a strong biological pump where ~50% of the elevated phytoplankton productivity is potentially exported.

Table of acronyms and symbols

Acronym (units)	Full description
AP	Antarctic Peninsula
LCIS	Larsen C Ice Shelf
WG	Weddell Gyre
ASW	Antarctic Surface Water
WW	Winter Water
CCSZ	Coastal and Continental Shelf Zone
MIZ	Marginal Ice Zone
OOZ	Open Ocean Zone
MLD (m)	Mixed layer depth
Z_{eu} (m)	Euphotic zone depth
FACS	Fluorescence activated cell sorting
PON (μM)	Particulate organic nitrogen
PON_{bulk} (μM)	Particulate organic nitrogen concentration of the bulk phytoplankton community
$PON_{picoplankton}$ (μM)	Particulate organic nitrogen concentration of the picoplankton
$PON_{nanoplankton}$ (μM)	Particulate organic nitrogen concentration of the nanoplankton
$PON_{microplankton}$ (μM)	Particulate organic nitrogen concentration of the microplankton
PON_{phyto} (μM)	The summed particulate organic nitrogen concentration of all flow-sorted phytoplankton populations
PON_{Syn} (μM)	Particulate organic nitrogen concentration of Synechococcus
$PON_{P.euk}$ (μM)	Particulate organic nitrogen concentration of the picoeukaryotes
$PON_{N.euk}$ (μM)	Particulate organic nitrogen concentration of the nanoeukaryotes
PON_{Crypto} (μM)	Particulate organic nitrogen concentration of the cryptophytes
RNC (%)	Relative nitrogen contribution
$\delta^{15}N_{NO_3^-}$ (‰)	δ^{15}N of nitrate and nitrite
$\delta^{15}N_{NO_3^- WW}$ (‰)	δ^{15}N of nitrate and nitrite in winter water (the source water mass)
$\delta^{15}N_{NH_4^+}$ (‰)	δ^{15}N of ammonium
$\delta^{15}N_{new}$ (‰)	δ^{15}N of new nitrogen
$\delta^{15}N_{regenerated}$ (‰)	δ^{15}N of regenerated nitrogen
$\delta^{15}N_{bulk\ PON}$ (‰)	δ^{15}N of the bulk phytoplankton community
$\delta^{15}N_{picoplankton}$ (‰)	δ^{15}N of the picoplankton
$\delta^{15}N_{nanoplankton}$ (‰)	δ^{15}N of the nanoplankton
$\delta^{15}N_{microplankton}$ (‰)	δ^{15}N of the microplankton
$\delta^{15}N_{phyto}$ (‰)	δ^{15}N of flow-sorted phytoplankton groups

Acronym (units)	Full description
$\delta^{15}N_{Syn}$ (‰)	$\delta^{15}N$ of Synechococcus
$\delta^{15}N_{P.euk}$ (‰)	$\delta^{15}N$ of the picoeukaryotes
$\delta^{15}N_{N.euk}$ (‰)	$\delta^{15}N$ of the nanoeukaryotes
$\delta^{15}N_{Crypto}$ (‰)	$\delta^{15}N$ of the cryptophytes
ρNO_3^- (µmol m^{-2} hr^{-1})	Absolute rate of nitrate uptake
$\rho NO_3^-{}_{bulk}$ (µmol m^{-2} hr^{-1})	Absolute rate of nitrate uptake by the bulk phytoplankton community
$\rho NO_3^-{}_{pico}$ (µmol m^{-2} hr^{-1})	Absolute rate of nitrate uptake by the picoplankton
$\rho NO_3^-{}_{nano}$ (µmol m^{-2} hr^{-1})	Absolute rate of nitrate uptake by the nanoplankton
$\rho NO_3^-{}_{micro}$ (µmol m^{-2} hr^{-1})	Absolute rate of nitrate uptake by the microplankton
ρNH_4^+ (µmol m^{-2} hr^{-1})	Absolute rate of ammonium uptake
$\rho NH_4^+{}_{bulk}$ (µmol m^{-2} hr^{-1})	Absolute rate of ammonium uptake by the bulk phytoplankton community
$\rho NH_4^+{}_{pico}$ (µmol m^{-2} hr^{-1})	Absolute rate of ammonium uptake by the picoplankton
$\rho NH_4^+{}_{nano}$ (µmol m^{-2} hr^{-1})	Absolute rate of ammonium uptake by the nanoplankton
$\rho NH_4^+{}_{micro}$ (µmol m^{-2} hr^{-1})	Absolute rate of ammonium uptake by the microplankton
ρurea (µmol m^{-2} hr^{-1})	Absolute rate of urea uptake
$\rho urea_{bulk}$ (µmol m^{-2} hr^{-1})	Absolute rate of urea uptake by the bulk phytoplankton community
$\rho urea_{pico}$ (µmol m^{-2} hr^{-1})	Absolute rate of urea uptake by the picoplankton
$\rho urea_{nano}$ (µmol m^{-2} hr^{-1})	Absolute rate of urea uptake by the nanoplankton
$\rho urea_{micro}$ (µmol m^{-2} hr^{-1})	Absolute rate of urea uptake by the microplankton
ρN_{reg} (µmol m^{-2} hr^{-1})	Absolute rate of regenerated nitrogen (i.e., ρNH_4^+ + ρurea) uptake
$\rho N_{reg\ bulk}$ (µmol m^{-2} hr^{-1})	Absolute rate of regenerated nitrogen uptake by the bulk phytoplankton community
$\rho N_{reg\ pico}$ (µmol m^{-2} hr^{-1})	Absolute rate of regenerated nitrogen uptake by the picoplankton
$\rho N_{reg\ nano}$ (µmol m^{-2} hr^{-1})	Absolute rate of regenerated nitrogen uptake by the nanoplankton
$\rho N_{reg\ micro}$ (µmol m^{-2} hr^{-1})	Absolute rate of regenerated nitrogen uptake by the microplankton
f_{new}	Fraction of new nitrogen consumed (i.e., NO_3^- dependence)
f-ratio	Flux ratio, equal to the proportion of primary productivity fuelled by NO_3^- uptake
$f\text{-}ratio_{phyto}$	the f-ratio of the total flow-sorted phytoplankton community
$f\text{-}ratio_{PON}$	the f-ratio of the bulk phytoplankton community estimated using the PON measurements
$f\text{-}ratio_{rates}$	f-ratio of the phytoplankton community estimated using either the bulk or size-fractionated absolute rates of nitrogen uptake
$f\text{-}ratio_{bulk}$	f-ratio of the bulk phytoplankton community estimated using the bulk absolute rates of nitrogen uptake
$f\text{-}ratio_{pico}$	f-ratio of the picoplankton estimated using the picoplankton absolute rates of nitrogen uptake
$f\text{-}ratio_{nano}$	f-ratio of the nanoplankton estimated using the nanoplankton absolute rates of nitrogen uptake
$f\text{-}ratio_{micro}$	f-ratio of the microplankton estimated using the microplankton absolute rates of nitrogen uptake

4.1. Introduction

The Southern Ocean plays a fundamental role in global biogeochemical cycles, supplying as much as ~85% of the global ocean's nutrients (Keffer and Holloway, 1988; Sarmiento et al., 2004; Fripiat et al., 2021). The Southern Ocean's Weddell Sea is a particularly important region for atmospheric CO_2 removal due to the formation of deep-water masses at Larsen C Ice Shelf (LCIS) and Filchner-Rönne Ice Shelf (FRIS) (Gordon et al., 1993; Schröder et al., 2002; Schodlok et al., 2002). Here, deep waters upwell to the surface and undergo various physical and chemical modifications as they interact with the atmosphere (Muench and Gordon, 1995; Talley et al., 2011). The modified waters subsequently sink into the ocean interior and flow northwards, thereby setting the physicochemical conditions of the deep global ocean. Although the ice shelves are a key component of the Southern Ocean's CO_2 sink, the perennially harsh sea-ice conditions that persist in the Weddell Sea, particularly in the vicinity of LCIS, have limited our knowledge of phytoplankton bloom dynamics in these waters, and thus of the biological carbon removal that occurs coincident with deep-water mass formation.

In the Southern Ocean, nitrate (NO_3^-; an essential macronutrient) is never fully consumed due to phytoplankton being co-limited by iron and light availability (Martin et al., 1991; Sunda and Huntsman, 1997). On an annual basis, phytoplankton growth that is fuelled by newly upwelled NO_3^- (termed "new production") is balanced by the export of sinking organic matter (including carbon) into the ocean interior (i.e., "export production"; Dugdale and Goering, 1967; Eppley and Peterson, 1979). By contrast, phytoplankton growth supported by nitrogen (N) forms such as ammonium (NH_4^+) and urea that are recycled in the surface mixed layer (termed "regenerated production") results in no net removal of CO_2 to depth.

Experiments involving ^{15}N-labelled tracers are frequently used to estimate carbon export potential, as these experiments allow for the direct measurement of the uptake rates of new and regenerated N by phytoplankton (e.g., Chapters 2 and 3). Measurements of bulk particulate organic nitrogen (PON) isotopes have also been used to estimate proportional NO_3^- dependence, and thus carbon export potential, of the bulk phytoplankton community (e.g., Karsh et al., 2003; Lourey et al., 2003). This approach leverages the idea that phytoplankton that predominantly assimilate NO_3^- have a higher biomass $\delta^{15}N$ (defined, in permil (‰) vs. N_2 in air, as $\left(\frac{(^{15}N/N)_{sample}}{(^{15}N/^{14}N)_{standard}} - 1\right) \times 1000$) than phytoplankton that assimilate regenerated N forms because NO_3^- upwelled from depth has a higher $\delta^{15}N$ (≥5‰) than N regenerated in the mixed layer (~0‰; Altabet, 1988; Sigman et al., 1999; Fawcett et al., 2011, 2014; Treibergs et al., 2014; Sigman and Fripiat, 2019). The $\delta^{15}N$ of PON can therefore be used to estimate the relative NO_3^- dependence of the phytoplankton community (Fawcett et al. 2011; 2014), providing an estimate of the quantity of newly-produced organic carbon that is potentially exported from the mixed layer (e.g., Eppley and Peterson, 1979). However, the bulk PON pool includes detritus

and heterotrophic material in addition to the active phytoplankton community. It is also susceptible to heterotrophic degradation and remineralisation, which are fractionating processes that generally increase the $\delta^{15}N$ of the PON pool (Trull et al., 2001; Lourey et al., 2003; Smart et al., 2020). Carbon export potential estimated using the $\delta^{15}N$ of bulk PON may therefore be over/underestimated depending on the proportion of material that is not actively photosynthesising phytoplankton. To overcome this limitation, the photoautotrophic component of the bulk PON pool needs to be isolated before its $\delta^{15}N$ is measured (Fawcett et al., 2011, 2014; Treibergs et al., 2014). This can be achieved using flow cytometry, specifically fluorescence-activated cell sorting (FACS), which separates the non-photosynthetic material (i.e., detritus, bacteria) from the active phytoplankton, after which the $\delta^{15}N$ of specific groups of phytoplankton can be measured and their role in the biological pump evaluated (Fawcett et al., 2011, 2014; Treibergs et al., 2014).

The biological pump acts to transfer CO_2 to the isolated waters of the deep ocean, lowering the atmospheric concentration of this greenhouse gas. The high macronutrient-low chlorophyll state of the Southern Ocean represents a "leak" in the global ocean's biological pump since by consuming NO_3^- more completely, Antarctic phytoplankton could theoretically lower atmospheric CO_2. Indeed, a more efficient biological pump at high latitudes is a leading hypothesis for the decrease in atmospheric CO_2 that characterised the ice ages (Sigman and Boyle, 2000; Sigman et al., 2010). Understanding the controls on biological NO_3^- utilization in the modern Antarctic Ocean, which includes the roles of different phytoplankton groups, is central to our understanding of its outsized role in setting atmospheric CO_2 today and in the past, and in absorbing CO_2 in the future (Sarmiento and Toggweiler, 1984).

Across the Weddell Sea, the phytoplankton community is generally thought to be dominated by either *Phaeocystis antarctica* or diatoms, with the dominance of the one group over the other driven mainly by mixed-layer light conditions (Nissen and Vogt, 2021). *P. antarctica* are low-light specialists, generally dominating in regions with deep mixed layers such as coastal polynyas, while diatoms prefer high-light conditions and thus proliferate in the marginal ice zone (MIZ) and coastal and continental shelf zone (CCSZ) following recent sea-ice- and/or glacial melt (Moisan and Mitchell, 1999; Arrigo et al., 1999; Goffart et al., 2000; Nissen and Vogt, 2021). However, recent studies along the Antarctic Peninsula (AP) have shown that rapid warming (2-3°C in surface waters over the last 50 years; King, 1994; Smith, 1994; Stark, 1994; Steig et al., 2009; Saba et al., 2014) and the associated sea-ice- and glacial melt has increased upper ocean stratification (Petrou et al., 2016), resulting in extremely shallow (<15 m) and relatively fresh mixed layers and a coincident shift from *P. antarctica* and/or diatom dominance to elevated cryptophyte abundances (Mendes et al., 2012; Kerr et al., 2018; Ferreira et al., 2020; Mendes et al., 2018a, 2023). This shift is hypothesised to be due to cryptophytes having photoprotective carotenoids, which protect them from the high UV radiation associated with shallow mixed layers while other phytoplankton groups generally sustain damage to their photosynthetic

apparatus (Mendes et al., 2018a, 2023). The shift from *P. antarctica* and/or diatoms to cryptophytes has implications for carbon export. Diatoms (and to some extent *P. antarctica*) are associated with elevated rates of carbon export while cryptophytes may act to upregulate the microbial loop as they decrease the mean size of the phytoplankton community (Kerr et al., 2018; Ferreira et al., 2020).

Although the phytoplankton community across the Weddell Sea is generally thought to be dominated by large cells (>20 μm; Vernet et al., 2019), recent studies from the western AP and open Southern Ocean have shown the importance of smaller cells (<20 μm) for productivity and carbon export (Huang et al., 2012; Lin et al., 2017; Chapter 2). Given the importance of the Weddell Sea for setting the biogeochemical conditions of the Southern and global oceans, this study aimed to investigate the importance of small cells for new, regenerated, and export production. To this end, we measured the $\delta^{15}N$ of four flow cytometry-sorted phytoplankton groups (namely *Synechococcus*, picoeukaryotes (0.3-2.7 μm), nanoeukaryotes (2.7-20 μm), and cryptophytes) at 17 stations in the western Weddell Sea. From these measurements, we estimate the NO_3^- dependence (relative to total N uptake) of the different phytoplankton groups and by extension, their potential contributions to carbon export. We interpret these results in the context of coincident measurements of regional hydrography, macronutrient concentrations, ^{15}N tracer-derived N uptake rates, and phytoplankton community composition.

4.2. Methods

4.2.1. Study site and hydrography

Sampling was conducted in austral summer 2018/2019 during the Weddell Sea Expedition onboard the R/V *SA Agulhas II* (Fig. 4.1; Table 4.1). A total of 17 stations were sampled in the western Weddell Sea and are categorised based on their geographic position as either Antarctic Peninsula (AP), Larsen C Ice Shelf (LCIS), or Weddell Gyre (WG) stations. Hydrographic data were collected using a Seabird conductivity-temperature-depth (CTD) profiler equipped with a photosynthetically active radiation (PAR) sensor. Density (sigma-theta; σ_θ) was derived from temperature, salinity, and pressure and was used to identify the water masses in the Weddell Sea during the sampling period as well at the mixed layer depth (MLD) at each station, which was determined as the depth of maximum Brunt-Väisälä Frequency (Schofield et al., 2015).

Seawater was collected from discrete depths using a rosette of twenty-four 12 L Niskin bottles. At each CTD station, seawater samples for nutrient analysis and N (as nitrate+nitrite (NO_3^-+NO_2^-) and NH_4^+) isotopes were collected throughout the water column. Samples for phytoplankton taxonomy and N isotopes of size-fractionated particulate organic nitrogen (PON) and specific phytoplankton groups were taken from a number of depths of interest (see below), selected based on the vertical profiles of temperature, chlorophyll *a* fluorescence, and PAR measured during the CTD down casts.

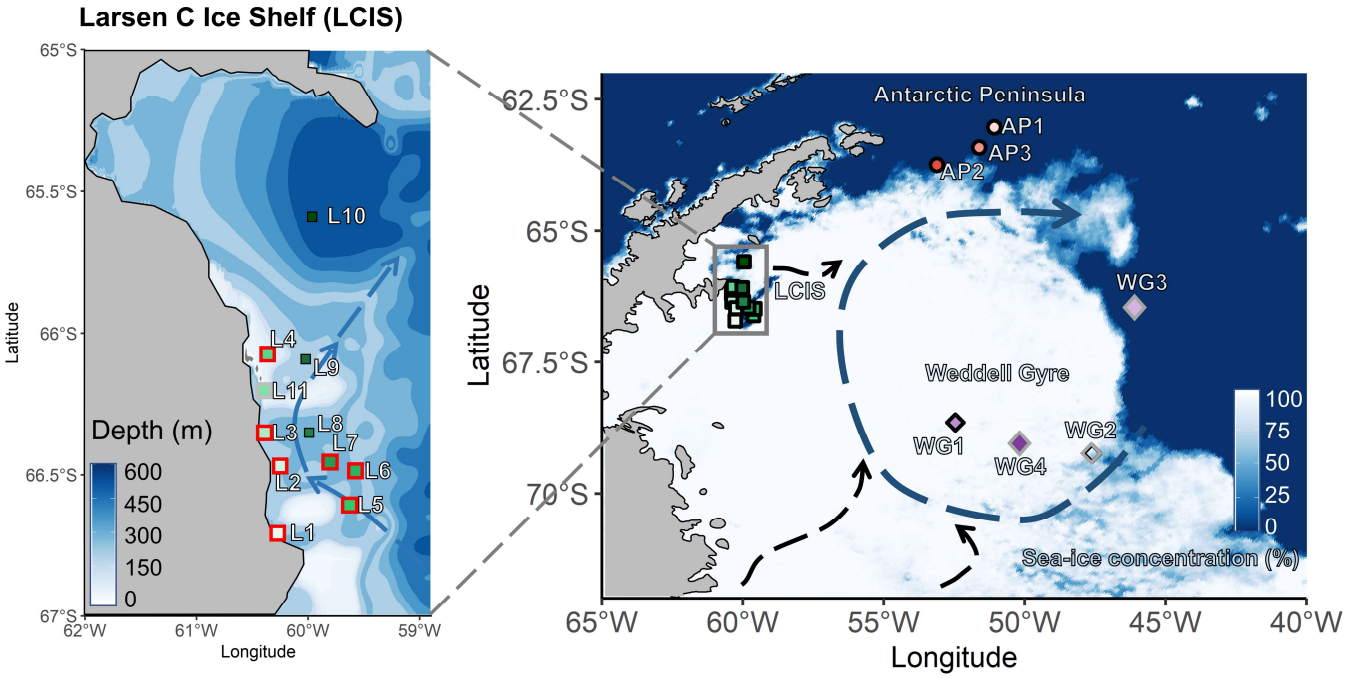


Figure 4.1. Maps of the Weddell Sea and Larsen C Ice Shelf (LCIS; insert) showing the position of the stations sampled during the Weddell Sea Expedition in January-February 2019. The symbols and colours represent the different regions of the Weddell Sea that were sampled (red circle – Antarctic Peninsula, green square – Larsen C Ice Shelf, purple diamond – Weddell Gyre). The symbols outlined in red indicate the stations where size-fractionated rates of nitrogen uptake were measured, in black where bulk rates of nitrogen uptake were measured (Chapter 3), and in grey where only samples for fluorescence-activated cell sorting (FACS) were collected (Table 4.1). At station WG2, denoted by the empty symbol, no FACS samples were collected. The dark blue cyclonic arrow in the main panel indicates the Weddell Gyre and the black dashed lines indicate the input of modified deep-water masses from LCIS and Filchner-Rönne Ice Shelf (FRIS; Gordon et al., 1993; Schröder et al. , 2002; Schodlok et al., 2002). The hypothesized circulation at LCIS (Nicholls et al., 2004; Hutchinson et al., 2020) is represented by the light blue dashed arrow in the insert. The 3.125 km sea-ice concentration data from 31 January 2019 shown in the main panel were taken from ftp://ftp-projects.cen.uni-hamburg.de/seaice/AMSR2/3.125km (last access: 29 September 2021), and the bathymetry data (insert) were taken from ETOPO1 (NOAA National Geophysical Data Center, 2009).

Table 4.1. Station information for all stations occupied in the Weddell Sea in January-February 2019. The mixed layer depth (MLD) and euphotic zone depth (Z_{eu}; the 1% light level) measured at each station are also provided. The stations where FACS samples were collected, and nitrogen uptake experiments (as bulk and size-fractionated) were conducted at each station in this chapter and in Chapter 3 are indicated in the table.

Station position	Station	Sampling date	MLD (m)	Z_{eu} (m)	Samples collected		
					FACS	Size-fractionated N uptake	Bulk N uptake
AP Average	**AP**		**23 ± 8**	**45 ± 9**			
Antarctic Peninsula	AP1	09/01/2019	23	35	x		x
Antarctic Peninsula	AP2	09/01/2019	30	50	x		x
Antarctic Peninsula	AP3	09/01/2019	15	50	x		x
LCIS Average	**LCIS**		**12 ± 5**	**29 ± 9**			
Larsen C	L1	22/01/2019	8.5	33	x	x	x
Larsen C	L2	20/01/2019	14	25	x	x	x
Larsen C	L3	11/01/2019	7	50	x	x	x
Larsen C	L4	14/01/2019	24	22	x	x	x
Larsen C	L5	15/01/2019	10	25	x	x	x
Larsen C	L6	13/01/2019	17.5	30	x	x	x
Larsen C	L7	22/01/2019	8.5	25	x	x	x
Larsen C	L8	23/01/2019	11	-	x		x
Larsen C	L9	19/01/2019	12	22	x		x
Larsen C	L10	24/01/2019	14	14	x		x
Larsen C	L11	10/01/2019	10	25	x		
WG Average	**WG**		**19 ± 3**	**90 ± 14**			
Weddell Gyre	WG1	14/02/2019	20	100	x		x
Weddell Gyre	WG2	15/02/2019	20	80			x
Weddell Gyre	WG3	29/01/2019	15	-	x		
Weddell Gyre	WG4	24/01/2019	20	80	x		

4.2.2. Nutrient analysis

NO_3^-+NO_2^- concentrations were measured using a Lachat QuickChem flow injection analysis platform following published auto-analysis protocols (Diamond, 1994; Grasshoff, 1976) in a configuration with a detection limit of 0.1 µM. Duplicate samples were measured for NO_3^-+NO_2^- on different days, and the standard deviation for duplicates was ≤0.5 µM, with a lower standard deviation for lower concentration samples. Aliquots of a certified reference material (JAMSTEC; Lot CG) were analysed during all autoanalyzer and manual runs to ensure measurement accuracy.

NH_4^+ concentrations were measured shipboard following the fluorometric method of Holmes et al. (1999) using a Turner Designs Trilogy Laboratory fluorometer equipped with a UV module. The detection limit was 0.05 µM and the standard deviation for duplicate samples was ≤0.1 µM. The matrix effect (ME) that results from the calibration of seawater samples to Milli Q water standards was calculated using the standard addition method (Saxberg and Kowalski, 1979). All samples were corrected for the ME, which was always <10% and typically ≤5%.

Urea-N (hereafter, urea) concentrations were measured via the colourimetric method of Revilla et al. (2005) using a Thermo Scientific Genesis 30 Visible spectrophotometer equipped with either a 1 cm- or 5 cm pathlength cell. The detection limit was 0.05 µM and the standard deviation for duplicate samples was ≤0.05 µM.

4.2.3. Seawater nitrate isotopes

Seawater samples for NO_3^-+NO_2^- isotopes ($\delta^{15}N_{NO_3^-}$) were collected in 60 mL high density polyethylene (HDPE) bottles that were rinsed with sample water three times prior to being filled. Samples were stored frozen at -20°C until they were shipped to the University of California, Davis for analysis. Prior to shipping and analysis, all NO_3^- isotope samples were filtered using a clean 0.2 µm syringe filter. The $\delta^{15}N_{NO_3^-}$ was measured via the "denitrifier-isotope ratio mass spectrometer (IRMS)" method. Briefly, denitrifying bacteria lacking a terminal nitrous oxide (N_2O) reductase enzyme quantitatively convert sample NO_3^- (and NO_2^-) to N_2O (Sigman et al., 2001). The N_2O was then measured using a Thermo Delta V Plus IRMS and purpose-built on-line N_2O extraction and purification system (Sigman et al., 2001; Casciotti et al., 2002; McIlvin and Casciotti, 2010). To calibrate the sample isotope ratios after IRMS analysis, certified NO_3^- isotope reference materials dissolved in high purity Milli Q water were included in all batch analyses. These included IAEA-NO_3^-, potassium nitrate with a $\delta^{15}N$ of 4.7 ± 0.2‰ vs. N_2 air (Gonfiantini, 1984), and USGS34, potassium nitrate with a $\delta^{15}N$ of 1.8 ± 0.1‰ vs. N_2 air (Böhlke et al., 2003). All samples were run in duplicate, with a precision of ≤0.1‰.

4.2.4. Seawater ammonium isotopes

Seawater samples for NH_4^+ isotopes ($\delta^{15}N_{NH_4^+}$) were collected in 250 mL low density polyethylene (LDPE) bottles that were rinsed three times with sample water before being filled. Samples were then "fixed" with 0.1 mL of 2 M HCl to achieve a final pH of ~4 to ensure that any ammonia (NH_3) gas was converted to dissolved NH_4^+. Thereafter, samples were stored frozen at -20°C until analysis at the University of Connecticut. The $\delta^{15}N_{NH_4^+}$ was measured for all samples with NH_4^+ concentrations ≥1 µM by the conversion of NH_4^+ to NO_2 using hypobromite (Zhang et al., 2007) followed by the reduction of NO_2 to N_2O by the addition of a 1:1 sodium azide and acetic acid buffer solution (McIlvin and Altabet, 2005). The N_2O was then measured using a Thermo Delta V Plus IRMS and purpose-built on-line N_2O extraction and purification system (Sigman et al., 2001; McIlvin and Casciotti, 2010). To calibrate the sample isotope ratios after IRMS analysis, certified NH_4^+ isotope reference materials dissolved in high purity Milli Q water were included in all batch analyses. These included IAEA-N1 ($\delta^{15}N$ = 0.4 ± 0.2‰ versus N_2 in air), IAEA-N2 ($\delta^{15}N$ = 20.3 ± 0.2‰ versus N_2 in air), and USGS-25 ($\delta^{15}N$ = -30.4 ± 0.4‰ versus N_2 in air) (Böhlke et al., 1993). All samples were run in duplicate, with a precision of ≤0.2‰.

4.2.5. Phytoplankton taxonomy

At all stations, samples for flow cytometry (typically cells ≤20 µm) were collected at the three depths to which 55%, 10%, and 1% of surface PAR penetrated. Samples were collected in 50 mL centrifuge tubes and immediately fixed with 10 µL of 25% 0.2 µm filtered glutaraldehyde. The samples were stored in the dark at 4°C until analysis. Additionally, microphytoplankton samples were collected between the surface and 30 m using a HYDRO-BIOS conical plankton net with a mesh size of 55 µm. Samples were transferred from the net cod-end to 50 mL centrifuge tubes and immediately fixed with 10 µL of 25% 0.2 µm filtered glutaraldehyde. The microphytoplankton samples were stored in the dark at room temperature until analysis.

The flow cytometry samples were analysed using a BD LSR II SORP flow cytometer with a blue-red-green laser configuration and the microphytoplankton cells were analysed via light and scanning electron microscopy. The cells identified and enumerated using flow cytometry and microscopy were categorized as per Flynn et al. (2021) (Chapter 3).

4.2.6. Bulk and size-fractionated PON concentration and $\delta^{15}N$

Water samples for N isotope analysis of bulk and size-fractionated (as picoplankton – 0.3-2.7 µm, nanoplankton – 2.7-20 µm, and microplankton – >20 µm) PON were collected from five euphotic zone depths during each hydrocast. At each depth, 2 L of seawater was collected and filtered onto a Milli Q rinsed 20 µm nylon mesh filter, and 0.5 L each onto ashed (combusted at 450°C for 6 hours) 0.3 µm-

(Sterlitech GF-75) and 2.7 µm (Sterlitech Grade-D) glass-fibre filters. Each 20 µm nylon filter was transferred to a 50 mL centrifuge tube where the particles were resuspended in 0.2 µm filtered seawater. The resuspended material was then filtered onto a clean ashed 2.7 µm filter. After filtration, the glass fibre filters were folded in half using ethanol-cleaned forceps and stored in ashed foil envelopes at -80°C. For analysis, the filters were dried for 24 hrs at 40°C and then folded into tin cups. Samples were analysed using a Delta V Plus IRMS coupled to a Flash 1112 Series Elemental Analyser with a detection limit of 1 µg N. Blanks (unused combusted filters) and laboratory standards (Choc and Valine) calibrated to certified IAEA reference materials were run after every five samples, and were used to calibrate the sample measurements to N_2 in air.

The PON concentration of the different size-classes was calculated by subtraction as follows:

$$PON_{picoplankton} = PON_{0.3\ \mu m} - PON_{2.7\ \mu m} \quad (4.1)$$

$$PON_{nanoplankton} = PON_{2.7\ \mu m} - PON_{20\ \mu m} \quad (4.2)$$

with the $PON_{0.3\ \mu m}$ equating to the PON_{bulk} and the $PON_{20\ \mu m}$ to the $PON_{microplankton}$.

The $\delta^{15}N$ of the different size-classes was calculated using a two-end member mixing model as follows:

$$\delta^{15}N_{picoplankton} = \frac{(\delta^{15}N_{0.3\ \mu m} \times PON_{0.3\ \mu m}) - (\delta^{15}N_{2.7\ \mu m} \times PON_{2.7\ \mu m})}{PON_{0.3\ \mu m} - PON_{2.7\ \mu m}} \quad (4.3)$$

$$\delta^{15}N_{nanoplankton} = \frac{(\delta^{15}N_{2.7\ \mu m} \times PON_{2.7\ \mu m}) - (\delta^{15}N_{20\ \mu m} \times PON_{20\ \mu m})}{PON_{2.7\ \mu m} - PON_{20\ \mu m}} \quad (4.4)$$

with the $\delta^{15}N_{0.3\ \mu m}$ equating to the $\delta^{15}N_{bulk\ PON}$ and the $\delta^{15}N_{20\ \mu m}$ to the $\delta^{15}N_{microplankton}$.

4.2.7. Phytoplankton group-specific concentration and $\delta^{15}N$

Seawater samples for phytoplankton group-specific N isotopes (hereafter, "flow-sorted groups") were collected from three euphotic zone depths (representing the 55%, 10%, and 1% light levels). Duplicate 2 L bottles of seawater were taken from each depth of interest and filtered through a clean polycarbonate (PC) membrane filter with a pore size of 0.4 µm under gentle vacuum. After filtration, the PC filters were transferred to 5 mL cryovials to which ~4 mL of 0.2 µm filtered seawater and 100 µL of glutaraldehyde were added in order to resuspend the cells from the filters and preserve them. The cryovials were subsequently stored in the fridge for 1-4 hours, then frozen at -80°C pending analysis.

Ashore, the samples were analysed using the coupled flow cytometry-N isotope protocol (Fawcett et al., 2011, 2014; Treibergs et al., 2014). All FACS took place at the University of Cape Town Flow Cytometry Core Facility using a BD FACSJazz™ Cell Sorter equipped with a 488 nm blue laser. Vials

were thawed in the dark and gently shaken to dislodge cells from filters and re-suspended cells were filtered through a 70 μm mesh to remove (rare) large particles that may have clogged the flow cytometer. Samples were sorted for four populations identified from cytograms of chlorophyll *a* (i.e., red) fluorescence versus phycoerythrin (PE; i.e., orange) fluorescence and relative size determined by forward-scatter (FSC) (Fig. C1; Flynn et al., 2021): *Synechococcus* (Syn), picoeukaryotes (P. euk; 1-2.7μm), cryptophytes (Crypto), and nanoeukaryotes (N. euk; >2.5 μm). Briefly, *Synechococcus* had high concentrations of PE and relatively low chlorophyll *a* compared to the other populations (Marie et al., 2005). The picoeukaryote and nanoeukaryote populations were identified by their intermediate chlorophyll *a* and low PE fluorescence relative to the cryptophytes, which had higher chlorophyll *a* and PE fluorescence (Fig. C1a). Because we could only sort four populations synchronously, and given that we needed to sort enough cells to make a robust N isotope measurement (i.e., at least 3 nmoles of N), some of the populations identified in Chapter 3 (Flynn et al., 2021) were combined for sorting purposes (Fig. 3.9a-c and Fig. 4.4a-c). The populations Syn 1 and Syn 2 were grouped as one large *Synechococcus* population, and NanoEuk 1 and MicroEuk were grouped together and reclassified as cryptophytes, noting that the number of MicroEuk cells (i.e., cells ≥20 μm) was at least two orders of magnitude lower than that of NanoEuk 1.

The PON of the flow-sorted phytoplankton populations was converted to NO_3^- using the persulfate oxidation method of Knapp et al. (2005) as modified by Fawcett et al. (2014) and Van Oostende et al. (2017). Briefly, flow-sorted particles were filtered onto ashed 0.3 μm GF-75 filters, then transferred to recently combusted (500°C for 6 hours) 4 mL borosilicate glass Wheaton vials to which 2 mL of persulfate oxidizing reagent (POR) was added. POR was also added to vials containing blank ashed GF-75 filters plus varying amounts of two L-glutamic acid isotope standards, USGS-40 ($\delta^{15}N$ = -4.5 ± 0.1‰) and USGS-41a ($\delta^{15}N$ = 47.6 ± 0.1‰) (Qi et al., 2003), which allowed for the quantification of the N content and $\delta^{15}N$ of the procedural blank. The POR was made by dissolving 2 g of NaOH and 2 g of five-times recrystallized, methanol-rinsed potassium persulfate in 100 mL of high purity Milli Q water. After POR addition, the vials were autoclaved at 121°C for 55 mins on a slow-vent setting. Sample pH was then lowered to 5-8 and vials were centrifuged at 3000 rpm for 10 mins to separate residual GF-75 from the liquid sample, which was transferred to a fresh combusted Wheaton vial. The concentration of the oxidized NO_3^- was then measured via chemiluminescent analysis (Garside, 1982; Braman and Hendrix, 1989) using a NO_x analyzer (Teledyne T200) with custom-built front-end and its $\delta^{15}N$ was analysed using the denitrifier method (see section 4.2.3) in the University of Cape Town Marine Biogeochemistry Lab using a Thermo Delta V Plus IRMS interfaced with a custom-built online N_2O extraction and purification system (Sigman et al. 2001; Weigand et al. 2016). The precision of the full collection/flow cytometry/N isotope protocol is ~0.4‰ (Fawcett et al., 2011, 2014).

To correct the sample measurements for the POR+GF-75 blank, a two-end member mixing model was used:

$$\delta^{15}N_{\text{phyto group}} = \frac{(\delta^{15}N_{\text{measured}} \times PON_{\text{measured}}) - (\delta^{15}N_{\text{blank}} \times PON_{\text{blank}})}{PON_{\text{measured}} - PON_{\text{blank}}} \quad (4.5)$$

where the $\delta^{15}N_{measured}$ is the $\delta^{15}N$ of each sorted sample plus blank measured via IRMS, $\delta^{15}N_{blank}$ is the $\delta^{15}N$ of the POR+GF-75 blank, estimated using the vials containing blank filters plus varying amounts of glutamic acid standard (i.e., blank+standard) following Montoya (2008). PON_{blank} is the PON concentration of the POR+GF-75 blank measured using the NO_x analyzer, and $PON_{measured}$ is the PON concentration of the sample plus blank measured using the NO_x analyzer.

While $PON_{measured} - PON_{POR\ blank}$ provides a measure of the phytoplankton group PON captured by the FACS sorts, the water-column PON concentration represented by each phytoplankton group at the time of sampling (i.e., $PON_{phyto\ group}$) was quantified using separate flow cytometry samples that were collected coincident with the FACS samples (see section 4.2.5). For each population identified in these samples, the average biovolume was calculated as per Flynn et al. (2021) and converted to particulate organic carbon (POC) using phytoplankton group-specific carbon conversion factors (Table 4.2). The POC content of the various phytoplankton groups (i.e., $POC_{phyto\ group}$) was then converted to $PON_{phyto\ group}$ using the Redfield C:N ratio of 6.63:1. The in situ $PON_{phyto\ group}$ concentrations were estimated in this way because the samples taken for simple counting flow cytometry more quantitatively represent the amount of biomass present in the water column. The flow-sorted PON estimates, by contrast, are likely biased low because we take a very conservative approach in gating the FACS populations to ensure the accuracy of the subsequent N isotope measurements.

Table 4.2. Average biovolume and carbon content assigned to the different phytoplankton populations identified using flow cytometry (Flynn et al., 2021). Due to the anomalous forward scatter of the *Synechococcus* populations, the average biovolume of Syn was set to 1 μm^3 (Kana and Glibert, 1987; Paulsen et al., 2015; Flynn et al., 2021; see Chapter 3 section B2 for details). The carbon content values for each population were taken from literature (as indicated in the "Reference" column).

Population	Average biovolume (μm^3)	Carbon conversion factor (fg C μm^{-3})	Reference
Crypto	730 ± 663	220	Mullin et al. (1966); Booth (1988); Paulsen et al. (2015)
N.euk	53 ± 0.3	220	Mullin et al. (1966); Booth (1988); Paulsen et al. (2015)
P.euk	0.7 ± 0.3	220	Mullin et al. (1966); Booth (1988); Paulsen et al. (2015)
Syn	1*	250	Kana & Glibert (1987); Paulsen et al. (2015)

4.2.8. Size-fractionated ρNO_3^-, ρNH_4^+, and ρurea uptake rates

Simulated *in situ* experiments were conducted to determine the size-fractionated (as picoplankton – 0.3-2.7 µm, nanoplankton – 2.7-20 µm, and microplankton – 20-200 µm) rates of NO_3^-, NH_4^+, and urea uptake (i.e., ρNO_3^-, ρNH_4^+, and ρurea) at 7 of the 11 LCIS stations (stations outlined in red in Fig. 4.1 insert). Seawater was collected at three euphotic zone depths (representing the 55%, 10%, and 1% light depths, as per the flow-sorted samples) and pre-screened through a 200 µm mesh to remove large grazers. Duplicate 1 L and 2 L bottles were collected for each N species (a total of 12 bottles per depth) and were amended with either 1 µM ^{15}N-NO_3^-, 0.05 µM ^{15}N-NH_4^+, or 0.1 µM ^{15}N-urea (i.e., yielding an ^{15}N enrichment of ~5-10% of the assumed ambient concentrations). Bottles were incubated on deck for 4-6 hours in a custom build incubator equipped with neutral density filters to mimic the relevant light levels and cooled with running surface water (ship's intake at ~7 m). Experiments were terminated via filtration onto either ashed 0.3 µm (Sterlitech GF-75) filters, ashed 2.7 µm (Sterlitech Grade-D) filters, or Milli Q rinsed 20 µm nylon mesh. The 20 µm nylon filters were transferred to 50 mL centrifuge tubes where the particles were resuspended in 0.2 µm filtered seawater. The resuspended material was then filtered onto an ashed 2.7 µm Grade-D filter. After filtration, the filters were folded in half using ethanol-cleaned forceps and stored in ashed foil envelopes at -80°C pending analysis.

The size-fractionated uptake rate filters were prepared and analysed in the same way as the bulk and size-fractionated PON filters (section 4.2.6). The specific uptake rates of NO_3^-, NH_4^+, and urea uptake ($V_{NO_3^-}, V_{NH_4^+}, V_{urea}$; hr^{-1}) were calculated according to eq. 2 in Dugdale and Wilkerson (1986) and the absolute uptake rates (ρNO_3^-, ρNH_4^+, and ρurea; nM hr^{-1}) were then calculated by multiplying $V_{NO_3^-}, V_{NH_4^+}$, and V_{urea} by the measured PON concentrations (Dugdale and Wilkerson, 1986; eq. 3). As for the PON (section 4.2.6), ρNO_3^-, ρNH_4^+, and ρurea for the different size-classes were calculated by subtraction.

4.2.9. Phytoplankton group-specific and total community nitrate dependence

The $\delta^{15}N$ of phytoplankton biomass (i.e., $\delta^{15}N_{phyto}$ or $\delta^{15}N_{PON}$) is set by the $\delta^{15}N$ of the N forms (either new or regenerated N) assimilated by the phytoplankton (Altabet, 1988; Fawcett et al., 2011, 2014; Treibergs et al., 2014; Sigman and Fripiat, 2019). The $\delta^{15}N$ of phytoplankton can therefore be described by a two-end member mixing model:

$$\delta^{15}N_x = \delta^{15}N_{new}(f_{new}) + \delta^{15}N_{regenerated}(f_{regenerated}) \quad (4.6)$$

where $\delta^{15}N_x$ is either $\delta^{15}N_{PON}$ or $\delta^{15}N_{phyto}$, $\delta^{15}N_{new}$ and $\delta^{15}N_{regenerated}$ are the $\delta^{15}N$ of the new and regenerated N assimilated by the phytoplankton, and f_{new} and $f_{regenerated}$ are the fraction of phytoplankton

growth fuelled by new and regenerated N, with $f_{new} + f_{regenerated} = 1$ (Fawcett et al., 2011). The fraction of new N consumed (i.e., NO_3^- dependence) can therefore be computed as:

$$f_{new} = \frac{\delta^{15}N_x - \delta^{15}N_{regenerated}}{\delta^{15}N_{new} - \delta^{15}N_{regenerated}} \quad (4.7)$$

We assume that the $\delta^{15}N_{regenerated}$ was well represented by the $\delta^{15}N_{NH_4^+}$, as NH_4^+ was the most abundant form of regenerated N present during the study (Fig. 4.2c-d). Moreover, given the isotope effects associated with the metabolic pathways that yield regenerated N (NH_4^+ and urea), the $\delta^{15}N$ of urea should be similar to that of regenerated NH_4^+. Our measured values of $\delta^{15}N_{NH_4^+}$ are consistent with estimates of $\delta^{15}N_{NH_4^+}$ from previous Southern Ocean studies (Lourey et al., 2003; Smart et al. 2015), noting that $\delta^{15}N_{NH_4^+}$ is very seldom directly measured. $\delta^{15}N_{NH_4^+}$ averaged -0.9 ± 0.3‰ at LCIS and -2.4 ± 0.3‰ at the AP stations (Table 4.3). Due to the low NH_4^+ concentrations at the WG stations, $\delta^{15}N_{NH_4^+}$ could not be measured; we use the LCIS $\delta^{15}N_{NH_4^+}$ average for these stations given its consistency with previous estimates. Since phytoplankton appear to assimilate NH_4^+ with little-to-no isotopic fractionation when NH_4^+ concentrations are <5 μM (Hoch et al., 1993; Pennock et al., 1996; Liu et al., 2013), we conclude that $\delta^{15}N_{regenerated} = \delta^{15}N_{NH_4^+}$.

We assume that NO_3^- was the only new N form assimilated by Weddell Sea phytoplankton, which is reasonable given that rates of N_2 fixation and atmospheric N deposition are negligible in the Weddell Sea (Vernet et al., 2019 and references therein). To estimate the $\delta^{15}N_{new}$ (i.e., the $\delta^{15}N$ of the NO_3^- consumed), we use the Rayleigh model, which describes the unidirectional transformation of reactant into product (i.e., the assimilation of NO_3^- into PON) that proceeds with a constant isotope effect ($\varepsilon_{assimilation}$) under conditions where the reactant NO_3^- is not resupplied (e.g., by vertical mixing) or lost (e.g., exported; Mariotti et al., 1981). In the summertime Southern Ocean, the Rayleigh model generally describes the N isotope dynamics of NO_3^- well, as NO_3^- is predominantly supplied to surface waters during deep winter mixing and consumed in spring and summer (i.e., the phytoplankton growth season), with little to no resupply during the growth season due to the mixed layer being well stratified (Sigman et al., 1999). The Rayleigh model describes the isotopic evolution of the reactant NO_3^- pool, the instantaneously formed product (i.e., PON) pool, and the accumulated product pool as:

$$\delta^{15}N_{reactant} = \delta^{15}N_{source} - \varepsilon_{assimilation} \times \ln(F) \quad (4.8)$$

$$\delta^{15}N_{instantaneous} = \delta^{15}N_{reactant} - \varepsilon_{assimilation} \quad (4.9)$$

$$\delta^{15}N_{accumulated} = \delta^{15}N_{source} + \varepsilon_{assimilation} \frac{F \times \ln(F)}{1-F} \quad (4.10)$$

where $\delta^{15}N_{source}$ is the initial $\delta^{15}N$ of the source NO_3^- supplied to the mixed layer during winter (i.e., $\delta^{15}N_{NO_3^-}$ of winter water (WW)), F is the fraction of NO_3^- supplied during winter mixing that remains in the water column at the time of sampling (i.e., $\frac{NO_3^- \text{ measured}}{NO_3^- \text{ WW}}$), and $\delta^{15}N_{reactant}$ is the $\delta^{15}N$ of NO_3^- measured at each depth at the time of sampling (i.e., $\delta^{15}N_{NO_3^- \text{ measured}}$). $\varepsilon_{assimilation}$ is the isotope effect of NO_3^- assimilation (Table 4.3), which was estimated as:

$$\varepsilon_{assimilation} = \frac{\delta^{15}N_{NO_3^- \text{ WW}} - \delta^{15}N_{NO_3^- \text{ measured}}}{\ln(F)} \quad (4.11)$$

The value of $\varepsilon_{assimilation}$ derived using equation 4.11 was assumed to apply to all phytoplankton populations and size fractions except *Synechococcus*. The $\varepsilon_{assimilation}$ is determined by two processes: 1) the ε imparted during the transport of NO_3^- into (ε_{uptake}) and out of (ε_{efflux}) the cell (which is generally small) and 2) the reduction of NO_3^- to NO_2^- by NO_3^- reductase, which imparts a signification ε (ε_{NR} >25‰) (Karsh et al., 2014). The $\varepsilon_{assimilation}$ observed in the environment depends on the quantity of cellular NO_3^- that is effluxed from the cell relative to that which was initially taken up (R), as follows: $\varepsilon_{assimilation} = \varepsilon_{uptake} + R(\varepsilon_{NR} - \varepsilon_{efflux})$ (Francois et al., 1993; Needoba et al., 2004; Granger et al., 2004, 2010; Karsh et al., 2014). The plasticity in the $\varepsilon_{assimilation}$ observed for eukaryotes is due to the presence of vacuoles in these cells, which can maintain NO_3^- homeostasis (i.e., the ratio of efflux to uptake can vary significantly) (Needoba et al., 2004). The lack of vacuoles in prokaryotes precludes NO_3^- storage and thus regulates the quantity of NO_3^- that can be assimilated and reduced by these cells, resulting in a lower $\varepsilon_{assimilation}$ as less NO_3^- is effluxed (Needoba et al., 2004). The $\varepsilon_{assimilation}$ for *Synechococcus* was set to 3.9‰, the value estimated from a batch culture of *Synechococcus* sp. WH8102 (Granger et al., 2010).

Table 4.3. End-members used for the Rayleigh model. The $\delta^{15}N_{NO_3^-\ WW}$ is the average $\delta^{15}N_{NO_3^-}$ of winter water (WW; the source to the Weddell Sea mixed layer), $\delta^{15}N_{NH_4^+}$ is the average $\delta^{15}N_{NH_4^+}$ measured at the Antarctic Peninsula (AP) and Larsen C Ice Shelf (LCIS) stations, and $\varepsilon_{assimilation}$ is the isotope effect associated with NO_3^- uptake (eq. 4.11). At LCIS, the same end-members were used for all stations as the $\delta^{15}N_{NO_3^-\ WW}$ was homogenous among stations and the phytoplankton community composition was similar among stations.

Station	$\delta^{15}N_{NO3\ WW}$ (‰)	$\delta^{15}N_{NH4}$ (‰)	$\varepsilon_{assimilation}$
AP1	5.1 ± 0.03	-2.4 ± 0.3	5.7
AP2	5.1 ± 0.2	-2.4 ± 0.3	5.8
AP3	5.3 ± 0.02	-2.4 ± 0.3	5.5
Larsen C Ice Shelf	5.2 ± 0.1	-0.9 ± 0.3	4.1
WG3	4.9 ± 0.03	-0.9 ± 0.3	3.9
WG1	4.8 ± 0.1	-0.9 ± 0.3	3.7
WG4	4.8 ± 0.01	-0.9 ± 0.3	3.7

The $\delta^{15}N_{instantaneous}$ is the $\delta^{15}N_{PON}$ or $\delta^{15}N_{phyto}$ produced at a particulate moment during NO_3^- assimilation while the $\delta^{15}N_{accumulated}$ is the sum of all the PON produced since NO_3^- assimilation began (Mariotti et al., 1981). The $\delta^{15}N_{instantaneous}$ and $\delta^{15}N_{accumulated}$ thus both theoretically provide an estimate of the $\delta^{15}N$ of the NO_3^- consumed (i.e., $\delta^{15}N_{new}$).

If all the PON produced between the time of sampling and the start of the growth season had been exported from the mixed layer, then the $\delta^{15}N_{instantaneous}$ would best approximate $\delta^{15}N_{new}$. However, phytoplankton biomass is known to accumulate in the surface mixed layer during the growth season in the Southern Ocean (e.g., Goeyens et al., 1998), which is consistent with our relatively high measured PON concentrations (see section 4.3.2 below). By contrast, if no PON had been exported, then the $\delta^{15}N_{accumulated}$ would best approximate $\delta^{15}N_{new}$. However, if a significant portion of the PON was exported, as would be expected since sampling occurred ~3-months after the initiation of the spring bloom (Flynn et al., 2021), then neither $\delta^{15}N_{instantaneous}$ nor $\delta^{15}N_{accumulated}$ will accurately approximate $\delta^{15}N_{new}$. To estimate the amount of PON exported, we compare the $[NO_3^-]_{WW}$ (which represents the $[NO_3^-]$ available to phytoplankton immediately following winter recharge) to the concentration of N measured in the mixed layer at the time of sampling (i.e., $[NO_3^-]$ + $[NH_4^+]$ + [urea] + [PON]; since NH_4^+, urea and PON were ultimately produced from $NO_3^-{}_{WW}$). Assuming mass balance, the difference between these two concentrations approximates the quantity of N exported from the mixed layer since the beginning of the growth season:

$$PON_{export} = [NO_3^-]_{WW} - ([NO_3^-] + [NH_4^+] + [urea] + [PON])_{measured} \quad (4.12)$$

Using eq. 4.12, we estimate that 0-60% of the PON was exported between the start of the growth season and the time of sampling; therefore, neither $\delta^{15}N_{instantaneous}$ nor $\delta^{15}N_{accumulated}$ can be used to approximate $\delta^{15}N_{new}$. Instead, $\delta^{15}N_{new}$ can be estimated by integrating the $\delta^{15}N_{instantaneous}$ over the concentration of PON, NH_4^+, and urea present in the mixed layer at the time of sampling (Mirkin, 2023) as these pools represent consumed $NO_3^-{}_{WW}$ that had not been exported. We modify eq. 4.9 as follows:

$$\delta^{15}N_{reactant\ sampling} = \delta^{15}N_{source} - \varepsilon_{assimilation} \times \ln \frac{([NO_3^-]+[NH_4^+]+[urea]+[PON_x])_{measured}}{[NO_3^-{}_{WW}]} \quad (4.13)$$

where $\delta^{15}N_{reactant\ sampling}$ is the theoretical $\delta^{15}N_{NO_3^-}$ at the concentration of total N (i.e., measured NO_3^-, NH_4^+, urea, and PON) present in the surface mixed layer at the time of sampling, $\frac{([NO_3^-]+[NH_4^+]+[urea]+[PON_x])_{measured}}{[NO_3^-{}_{WW}]}$ is the fraction of the NO_3^- supplied in winter that remained at the time of sampling (F in eq. 4.8), and PON_x is either $PON_{size\text{-}class}$ or PON_{phyto}.

We can then modify eq. 4.10 to estimate $\delta^{15}N_{new}$ as follows:

$$\delta^{15}N_{new} = \delta^{15}N_{reactant\ sampling} + \varepsilon_{assimilation}\left(\frac{F_{measured} \times \ln(F_{measured})}{1-F_{measured}}\right) \quad (4.14)$$

where $F_{measured}$ is the fraction of $NO_3^-{}_{WW}$ remaining in the surface mixed layer at the time of sampling after accounting for export:

$$F_{measured} = \frac{[NO_3^-]_{measured}}{([NO_3^-]+[NH_4^+]+[urea]+[PON_x])_{measured}} \quad (4.15)$$

We note that if $\delta^{15}N_{new}$ was well approximated by either the instantaneous or accumulated product, our definition of $\delta^{15}N_{new}$ would still return the correct values for $\delta^{15}N_{instantaneous}$ or $\delta^{15}N_{accumulated}$.

4.2.10. Bulk, size-fractionated, and flow-sorted phytoplankton community f-ratios and potential contributions to carbon export

The f-ratio of the total flow-sorted phytoplankton community ($f\text{-}ratio_{phyto}$) was estimated as follows:

$$f\text{-}ratio_{phyto} = \sum(f_{new} \times RNC)_{population} \quad (4.16)$$

where f_{new} was estimated for each flow-sorted phytoplankton group using eq. 4.7 and RNC is the relative nitrogen contribution per sorted population, calculated as:

$$\mathrm{RNC} = \frac{\mathrm{PON_{phyto\ group}}}{\mathrm{PON_{phyto}}} \tag{4.17}$$

where PON_{phyto} is the sum of the PON concentrations of each phytoplankton population (i.e., PON_{Crypto} + $PON_{N.euk}$ + $PON_{P.euk}$ + PON_{Syn}), and $PON_{phyto\ group}$ is the PON concentration of each individual phytoplankton group. For example, at AP1 the RNC of the cryptophytes = $\frac{0.49\ \mu M}{0.51\ \mu M} = 0.95$.

Using the f-ratio of the total flow-sorted phytoplankton community (eq. 4.16), the contribution of each phytoplankton group to carbon export potential (i.e., new production; Dugdale and Goering, 1967) was estimated as follows:

$$\text{contribution to carbon export potential (\%)} = \frac{f_{new} \times \mathrm{RNC}}{\text{f-rat}_{\ \mathrm{phyto}}} \tag{4.18}$$

where f_{new} was estimated for each flow-sorted phytoplankton group using eq. 4.8, RNC is the relative nitrogen contribution per sorted population, and f-ratio_{phyto} is the f-ratio of the total flow-sorted phytoplankton community estimated using eq. 4.16. For example, the cryptophyte contribution to carbon export potential at AP1 = $\frac{0.85 \times 95\%}{0.84} = 96\%$.

Using the absolute N uptake rates (i.e., ρNx; section 4.2.8), the f-ratio of the bulk (f-ratio_{bulk}) and size-fractionated (f-ratio_{pico}, f-ratio_{nano}, f-ratio_{micro}) community was calculated as:

$$\text{f-ratio}_x = \frac{(\rho NO_3^-)_x}{(\rho NO_3^-)_x + (\rho NH_4^+)_x + (\rho \mathrm{urea})_x} \tag{4.19}$$

where x represents the bulk community, picoplankton, nanoplankton or microplankton.

4.3. Results

4.3.1. Hydrography and biogeochemical conditions

Across the study region, Antarctic Surface Water (ASW; upper ~50 m) was generally warmer and fresher than the underlying winter water (WW), the ultimate source water to the mixed layer (Fig. 3.2b; Chapter 3), resulting in these waters being less dense than WW (Fig. 4.2a). At the AP stations, low interstation variability was observed in ASW density. In the WG, the ASW at the eastern-most station (WG3) had a lower density than the other stations (27.2 ± 0.06 versus 27.6 ± 0.01 kg m^{-3}), likely due to

recent sea-ice melt given that this station had 0% sea-ice cover while stations WG1 and WG4 had 100% sea-ice cover (Fig. 4.1). At LCIS, the density of ASW ranged from 26.8-27.7 kg m^{-3} (Fig. 4.2a). The large variability in the temperature and salinity, and thus density, of ASW at LCIS was the result of various physical processes. For example, along the ice-shelf front, the recent upwelling of WW led to cool, saline waters being present in the surface at stations L1 and L3 (average density of 27.4 ± 0.13 kg m^{-3}). Conversely, recent sea-ice melt at stations L5 and L10 decreased the salinity of ASW, yielding the lower densities observed at these stations (26.9 ± 0.04 kg m^{-3}).

The mixed layer depth (MLD) was strongly controlled by salinity at all stations, and was always shallower than the euphotic zone depth (Z_{eu}; Table 4.1). The deepest MLDs were observed along the AP (average of 23 ± 8 m) while the shallowest MLDs occurred at LCIS (12 ± 5 m), particularly at the stations where recent sea-ice melt had occurred. The deepest Z_{eu} were observed at the WG stations (average of 90 ± 14 m) and the shallowest at LCIS (average of 29 ± 9 m). The rates of NPP and N uptake were therefore integrated to the Z_{eu} rather than the MLD as we assume that the phytoplankton were active to the depth of 1% PAR (Flynn et al., 2021).

Throughout the euphotic zone, the NO_3^- concentrations decreased as $\delta^{15}N_{NO_3^-}$ increased between the Z_{eu} and the surface (Fig. 4.2b and 4.2e) due to the assimilation of NO_3^- by phytoplankton (Sigman et al. 1999). The lowest mixed-layer NO_3^- concentrations (average of 13.9 ± 4.6 µM) and highest $\delta^{15}N_{NO_3^-}$ (average of 8.3 ± 1.4‰) were measured at LCIS while the highest mixed-layer NO_3^- concentrations (average of 26.7 ± 1.5 µM) and lowest $\delta^{15}N_{NO_3^-}$ (average of 5.2 ± 0.1‰) were measured at the WG stations. The average $\delta^{15}N_{NO_3^-}$ of WW varied regionally, with the highest $\delta^{15}N_{NO_3^-\,WW}$ measured at the LCIS and AP stations (average of 5.2 ± 0.1‰ and 5.2 ± 0.1‰, respectively) and the lowest in the WG (average of 4.8 ± 0.1‰).

Mixed-layer NH_4^+ concentrations were high at LCIS and along the AP (average of 0.5 ± 0.4 µM and 0.8 ± 0.2 µM, respectively) and were low in the WG (average of 0.1 ± 0.1 µM; Fig. 4.2c). NH_4^+ concentrations generally reached local maxima near Z_{eu} (average of 0.7 ± 0.3 µM and 1.0 ± 0.3 µM for the AP and LCIS stations, respectively), rapidly decreasing to below detection below Z_{eu}. The elevated NH_4^+ concentrations at LCIS and at a surface underway station near the AP stations could be measured for $\delta^{15}N_{NH_4^+}$ (Fig. 4.2f). The $\delta^{15}N_{NH_4^+}$ ranged between -6.6‰ and 2.3‰, and was fairly uniform throughout the upper water column at each station. Interestingly, the $\delta^{15}N_{NH_4^+}$ was ~1.5‰ lower near the AP than at LCIS (median of -2.4 ± 0.3‰ versus -0.9 ± 0.2‰), as was the $\delta^{15}N_{bulk\ PON}$ (euphotic-zone average of -2.2 ± 3.1‰ at the AP versus 3.0 ± 2.8‰ at the LCIS and WG stations; Fig. 4.2g).

The urea concentrations were generally low in the surface, increasing with depth to reach a local maximum near Z_{eu}, similar to NH_4^+ (Fig. 4.2d). The mixed-layer urea concentrations were lowest at the WG stations (0.05 ± 0.05 µM) and highest at LCIS (average of 0.2 ± 0.1 µM), albeit with considerable variability (range of 0-0.47 µM); the highest mixed-layer urea concentrations were measured at L7 (average of 0.4 ± 0.1 µM) and the lowest at L11 (average of 0.06 ± 0.02 µM). The large range was likely due to variability in the processes that produce urea (e.g., bacterial excretion; Berges and Mulholland, 2008).

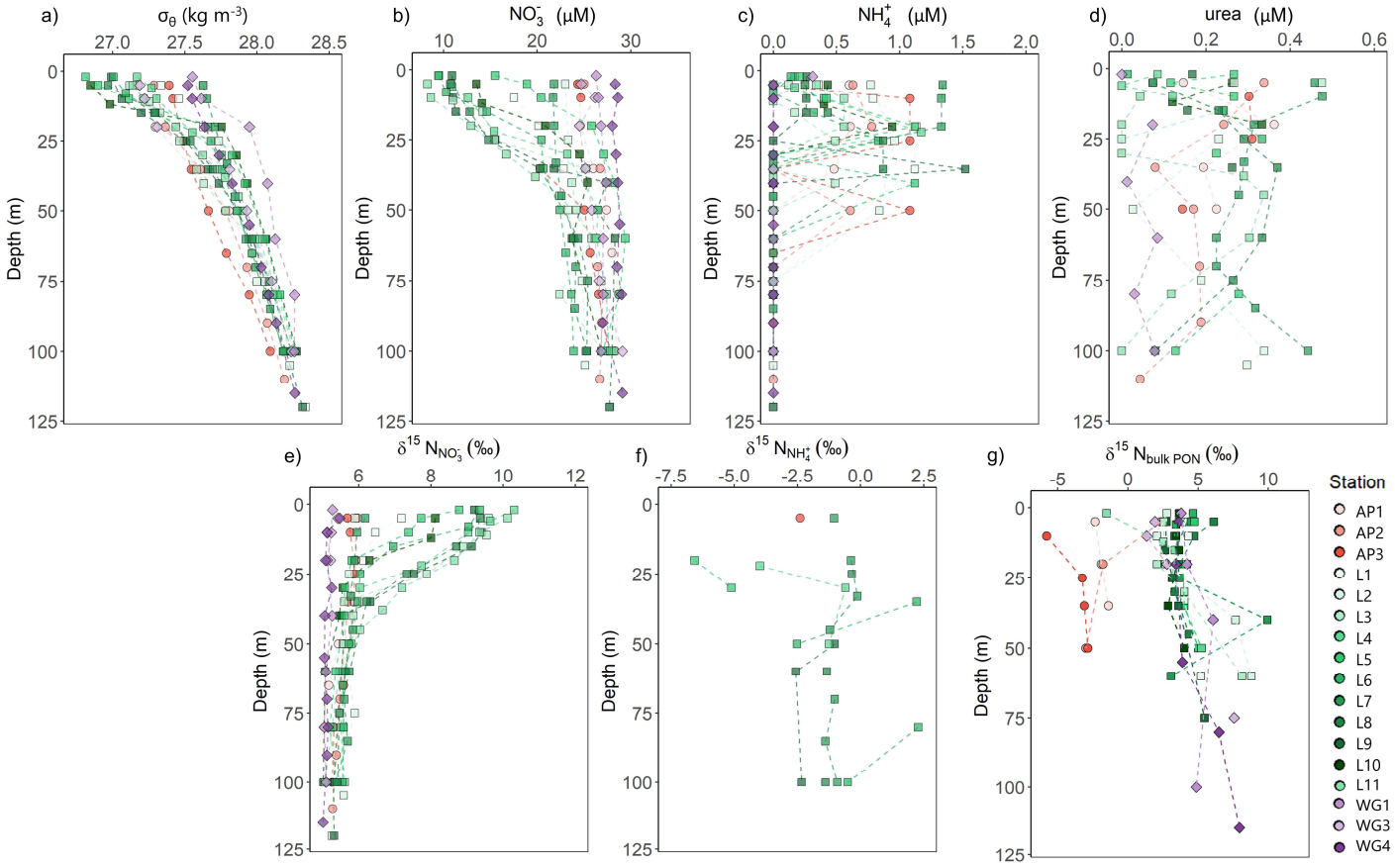


Figure 4.2. Depth profiles (0-125 m) of a) sigma-theta (σ_θ), b) nitrate concentrations ($[NO_3^-]$), c) ammonium concentrations ($[NH_4^+]$), d) urea concentrations ([urea]), e) $\delta^{15}N_{NO_3^-}$, f) $\delta^{15}N_{NH_4^+}$ and g) $\delta^{15}N_{PON}$ of the bulk particulate organic nitrogen (PON) pool. The $\delta^{15}N_{NH_4^+}$ could not be measured at all stations and depths because the NH_4^+ concentrations were too low; in panel f, we show all available data. The different hydrographic regions are represented by different symbols and colours (red circles – Antarctic Peninsula, green square – Larsen C Ice Shelf, purple diamond – Weddell Gyre) and the stations are represented by different colours. Note the difference in the x-axis among panels.

4.3.2. Phytoplankton biomass and community composition

The PON concentrations were generally highest in the surface and rapidly decreased to below detection just below the Z_{eu} (Fig. 4.3). The highest euphotic-zone averaged PON concentrations were measured at LCIS (3.3 ± 1.6 μM) and the lowest at the WG stations (0.4 ± 0.2 μM). At the stations where PON was size-fractionated, nanoplankton contributed most to total PON (73 ± 14%), while the picoplankton and microplankton contributions were similar (15 ± 7% and 14 ± 14%, respectively).

The average difference between the bulk PON (PON_{bulk}) and summed flow-sorted PON (PON_{phyto}) concentrations was 1.1 ± 1.6 μM, which can be explained by the different size ranges captured by the two measurements (i.e., the flow-sorted populations were generally <20 μm while the bulk PON included material >20 μm). As per the PON_{bulk}, the highest PON_{phyto} was measured at LCIS (1.5 ± 1.1 μM) and the lowest at the WG stations (0.7 ± 0.4 μM). Although *Synechococcus* was numerically dominant (average relative abundance of flow cytometrically counted cells of 54 ± 21%; Fig. 4.4a-b), except at stations L11, L5, and L6 where picoeukaryotes had the highest relative abundance (44 ± 14%), the PON_{phyto} was dominated by nanoplankton-sized cryptophytes at all stations (92 ± 5%), with the nanoeukaryotes making the second largest contribution to PON_{phyto} (8 ± 5%). The low contribution of *Synechococcus* and picoeukaryotes to PON_{phyto} (0.3 ± 0.2% and 0.1 ± 0.2%, respectively) was due to their small cell biovolume (1 μm^3 and 0.7 ± 0.3 μm^3, respectively) compared to the nanoeukaryotes and cryptophytes (53 ± 0.3 μm^3 and 730 ± 663 μm^3, respectively; Table 4.2).

The microplankton community, characterised via microscopy (Flynn et al. 2021), was dominated by diatoms at the AP stations (91 ± 11%) while *Phaeocystis antarctica* was most abundant at all the LCIS stations (81 ± 18%; Fig. 4.4d-e). The LCIS stations with cooler mixed-layer temperatures had a higher abundance of *P. antarctica* (e.g., stations L1 and L3) relative to those with warmer mixed layers (likely sampled later in the bloom; Flynn et al., 2021) where generally higher abundances of diatoms were observed (e.g., station L10). Although *P. antarctica* was abundant at LCIS, due to the smaller size and carbon content of these cells relative to diatoms (Mathot et al., 2000; Leblanc et al., 2012), they contributed less to total carbon (Fig. 4.4f). For example, at station L3, *P. antarctica* contributed 0.1×10^{-3} pg C mL^{-1} (6394×10^{-3} cells mL^{-1}) versus the 22 diatom species present (402×10^{-3} cells mL^{-1}) that contributed 0.3×10^{-3} pg C mL^{-1} (Leblanc et al., 2012)

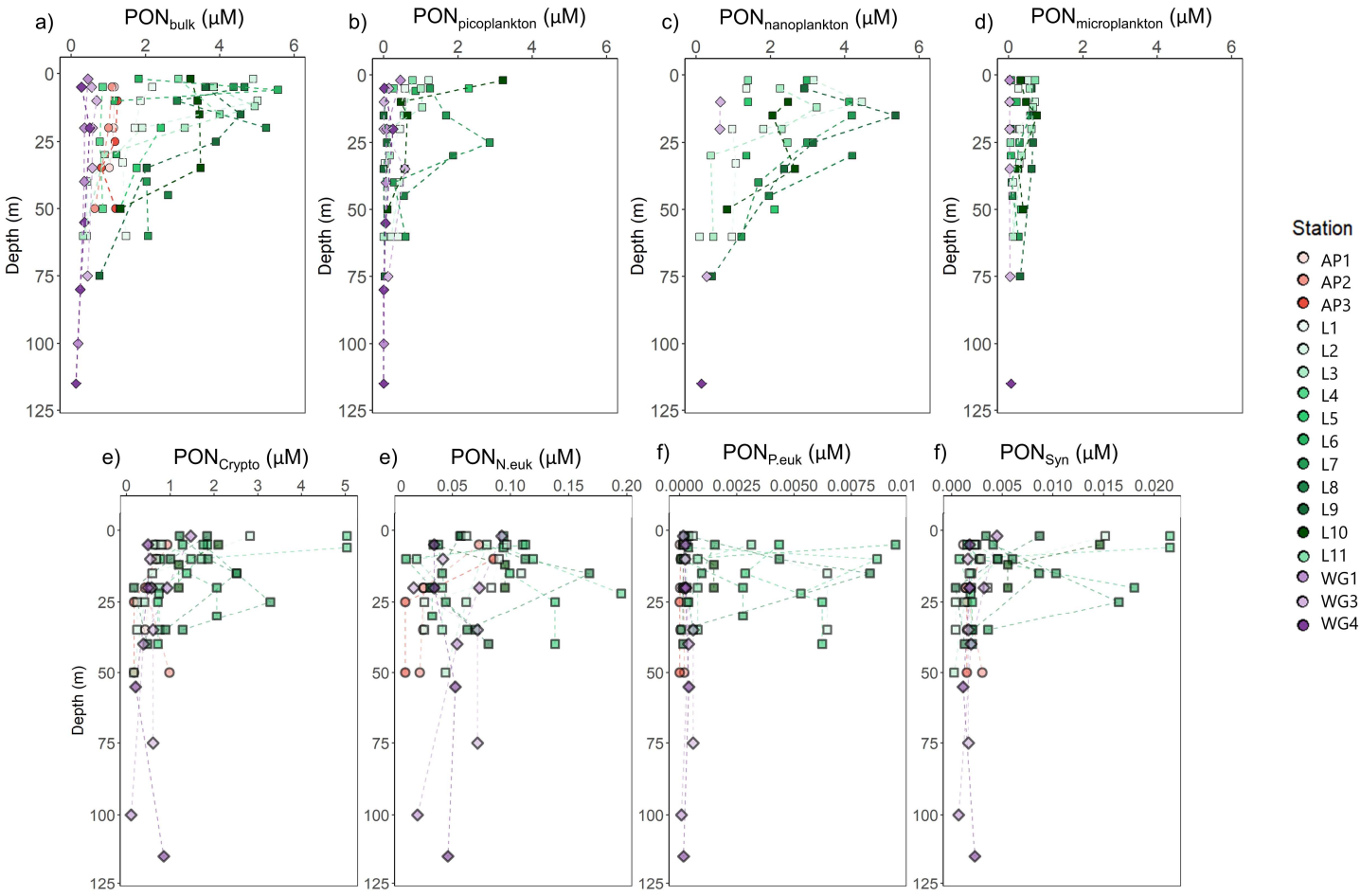


Figure 4.3. Depth profiles (0-125 m) of the particulate organic nitrogen (PON) concentrations measured or estimated for the a) bulk phytoplankton community (PON_{bulk}), b) picoplankton ($PON_{picoplankton}$), c) nanoplankton ($PON_{nanoplankton}$), d) microplankton ($PON_{microplankton}$), e) cryptophytes (PON_{Crypto}), f) nanoeukaryotes ($PON_{N.euk}$), g) picoeukaryotes ($PON_{P.euk}$) and h) *Synechococcus* (PON_{Syn}). Note the difference in the x-axis among panels.

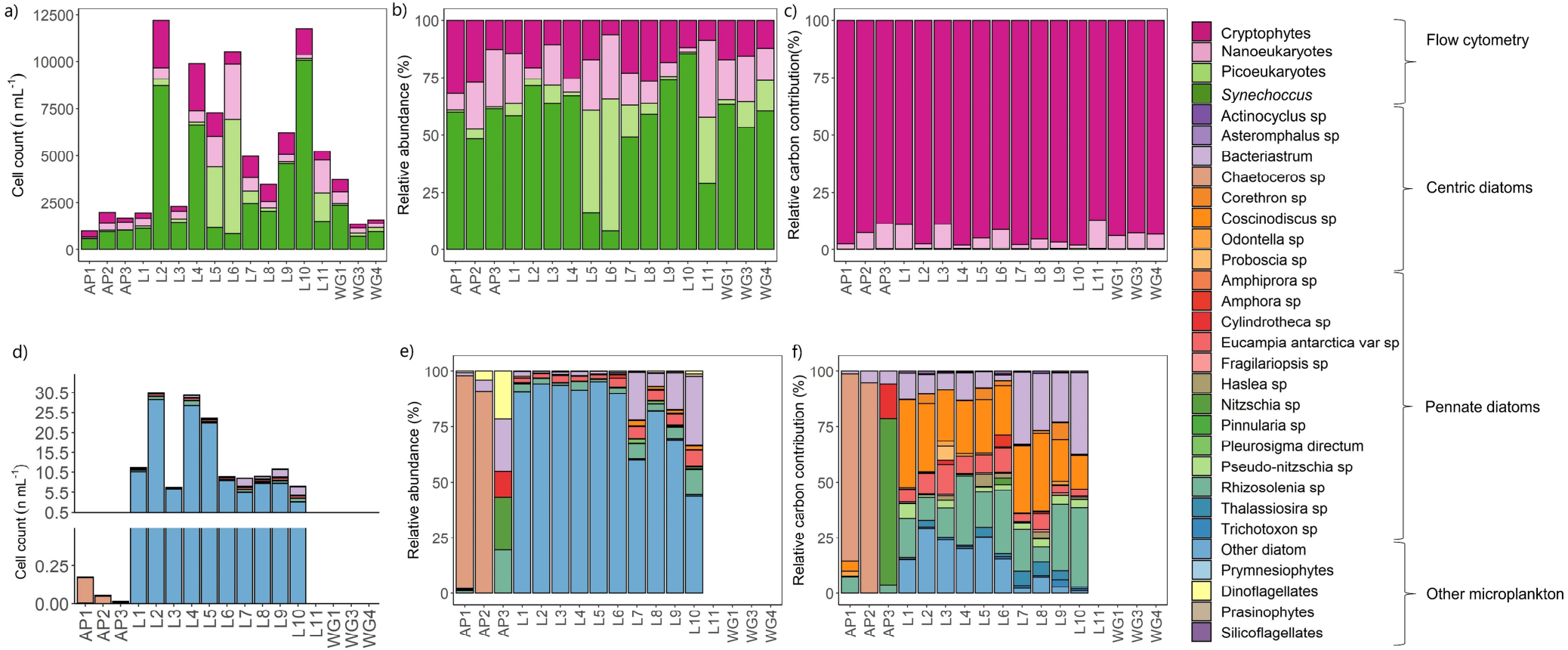


Figure 4.4. The (a,d) cell counts, (b,e) relative abundance and (c,f) relative carbon contribution of all phytoplankton groups identified via (a-c) flow cytometric analysis of surface samples and (d-f) microscopic analysis of plankton net tow samples. The stations are labelled on the x-axis. Where there are no bars in panels (d-f), no data are available. The carbon biomass estimates in panel (f) are for *Phaeocystis antarctica* and the diatom species only. Note that this figure is a slightly amended version of Fig. 3.9 in Chapter 3 (Figure 9 in Flynn et al., 2021).

4.3.3. $\delta^{15}N$ of PON and phytoplankton populations

On average, the $\delta^{15}N_{bulk\ PON}$ was highest at the WG stations (4.5 ± 2.0‰) and lowest at the AP stations (-2.2 ± 2.1‰; Fig. 4.3g and 4.5a). At LCIS where the highest PON_{bulk} concentrations were measured, $\delta^{15}N_{bulk\ PON}$ averaged 3.7 ± 1.7‰. PON was size-fractionated at all the LCIS and WG stations; however, the PON captured on the 2.7 µm and 20 µm filters was at times too low for accurate analysis of its $\delta^{15}N$, which is why there are no $\delta^{15}N$ data for some size classes in Fig. 4.5b-d. The highest $\delta^{15}N_{picoplankton}$, $\delta^{15}N_{nanoplankton}$, and $\delta^{15}N_{microplankton}$ were measured at the WG stations (average of 4.5 ± 2.4‰, 4.1 ± 1.7‰, and 5.2‰ (n=1), respectively), while the lowest $\delta^{15}N_{picoplankton}$, $\delta^{15}N_{nanoplankton}$, and $\delta^{15}N_{microplankton}$ were measured at LCIS (average of 4.0 ± 2.9‰, 3.0 ± 1.4‰, and 3.7 ± 1.7‰, respectively). The highest variability in the $\delta^{15}N_{bulk\ PON}$, $\delta^{15}N_{picoplankton}$, $\delta^{15}N_{nanoplankton}$, and $\delta^{15}N_{microplankton}$ of all size classes was observed among stations at LCIS (which could simply be due to the far greater number of stations sampled at LCIS compared to the other regions).

The highest $\delta^{15}N_{phyto}$ were measured at LCIS (average of 0.7 ± 1.2‰, 0.8 ± 1.2‰, 1.1 ± 1.2‰, and 0.8 ± 1.3‰ for the cryptophytes, nanoeukaryotes, picoeukaryotes, and *Synechococcus*, respectively; Fig. 4.5e-h, Table 4.4) where the euphotic zone NO_3^- concentrations were lowest and $\delta^{15}N_{NO_3^-}$ was highest compared to WW. Conversely, the lowest $\delta^{15}N_{phyto}$ were measured at the AP stations (average of -0.5 ± 0.5‰, -0.9 ± 1.3‰, 0.0 ± 0.5‰, and -0.8 ± 1.2‰ for cryptophytes, nanoeukaryotes, picoeukaryotes, and *Synechococcus*, respectively), coincident with low $\delta^{15}N_{bulk\ PON}$ and $\delta^{15}N_{NH_4^+}$. At LCIS, the picoeukaryotes had the highest $\delta^{15}N_{phyto}$ (average of 1.1 ± 1.2‰) and the cryptophytes had the lowest (average of 0.7 ± 1.2‰). Variability was high among the LCIS stations, with some having a low $\delta^{15}N_{phyto}$ for all phytoplankton groups (e.g., L7) and others a high $\delta^{15}N_{phyto}$ for all groups (e.g., L10), while there were still other stations where some groups had a high $\delta^{15}N_{phyto}$ and others a low $\delta^{15}N_{phyto}$ (e.g., L5 where the picoeukaryotes had a $\delta^{15}N$ of 4‰ and the cryptophytes had a $\delta^{15}N$ of 1.3‰).

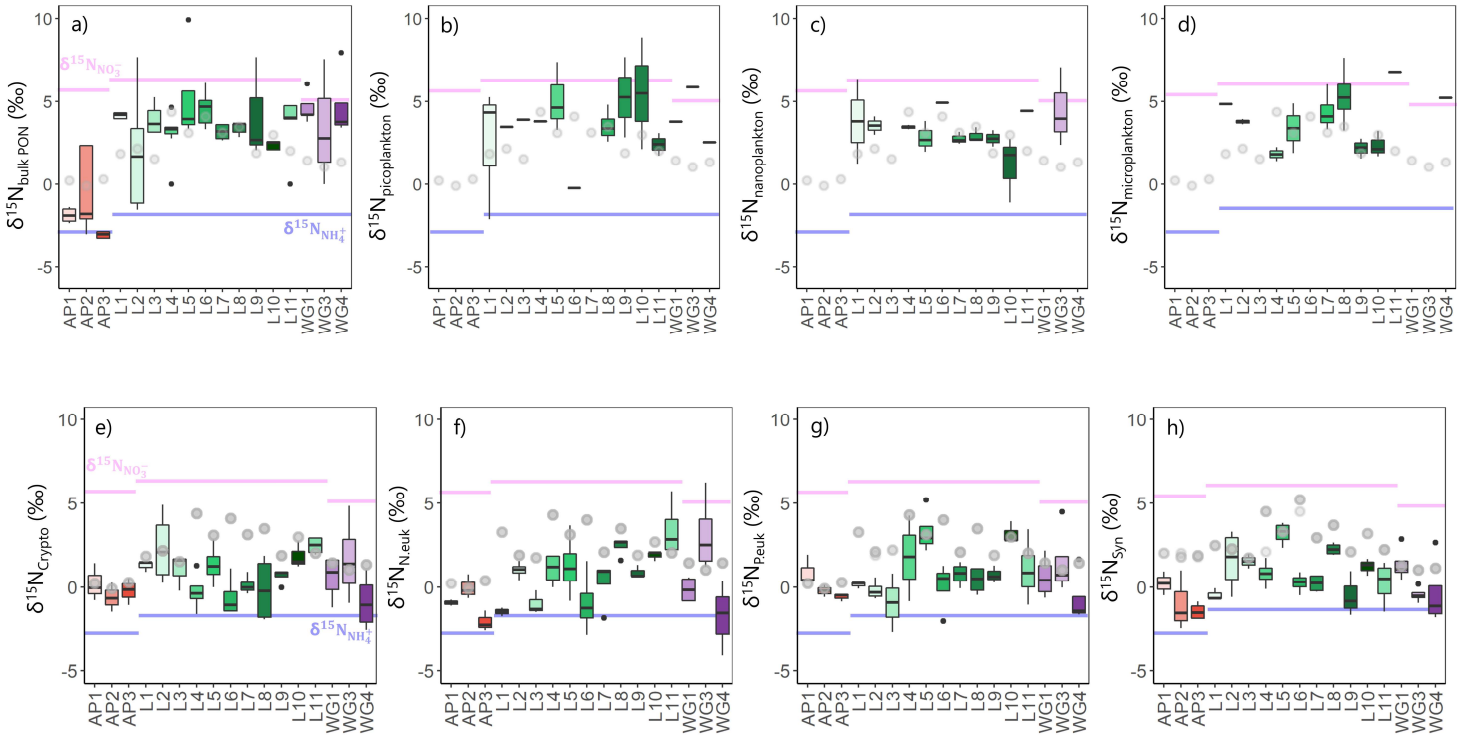


Figure 4.5. Boxplots showing the median mixed-layer δ¹⁵N of the a) bulk PON ($\delta^{15}N_{bulk\ PON}$), b) picoplankton PON ($\delta^{15}N_{picoplankton}$), c) nanoplankton PON ($\delta^{15}N_{nanoplankton}$), d) microplankton PON ($\delta^{15}N_{microplankton}$), e) cryptophytes ($\delta^{15}N_{Crypto}$), f) nanoeukaryotes ($\delta^{15}N_{N.euk}$), g) picoeukaryotes ($\delta^{15}N_{P.euk}$) and h) Synechococcus ($\delta^{15}N_{Syn}$). The stations are labeled on the x-axis. The pink line indicates the average $\delta^{15}N_{NO_3^-\ WW}$ (i.e., the source NO_3^-) and the blue line shows the average $\delta^{15}N_{NH_4^+}$ used in our calculations. The grey dots indicate the theoretical $\delta^{15}N_{new}$ at each station, estimated using the Rayleigh model (eq. 4.14).

Table 4.4. Depth-weighted mixed-layer average PON concentrations, $\delta^{15}N$ and the estimated extent of NO_3^- dependence for the bulk and size-fractionated PON community, and flow-sorted phytoplankton populations at each station. The values in the brackets are the SD of the regional averages.'-' indicates where no data are available.

	Phytoplankton size-class/group	Antarctic Peninsula	AP1	AP2	AP3	Larsen C Ice Shelf	L1	L2	L3	L4	L5	L6	L7	L8	L9	L10	L11	Weddell Gyre	WG1	WG3	WG4
PON (μM)	Bulk	**1.0** (0.1)	1.1	0.9	1.1	**3.6** (1.3)	2.0	3.4	0.8	3.7	5.4	3.8	4.1	3.3	5.0	4.4	3.8	**0.5** (0.1)	0.4	0.6	0.4
	Picoplankton	-	-	-	-	**0.8** (0.6)	0.5	0.7	0.3	0.4	1.5	-	0.0	1.8	0.6	1.0	1.1	**0.1** (0.1)	0.2	0.0	0.1
	Nanoplankton	-	-	-	-	**2.7** (1.2)	1.4	1.4	-	3.0	4.2	-	4.1	2.5	3.8	2.8	1.4	**0.6**	-	0.6	-
	Microplankton	-	-	-	-	**0.4** (0.3)	0.3	0.7	-	0.1	0.6	-	0.6	0.4	0.6	0.6	0.1	**0.0** (0.0)	0.0	0.0	-
PON (nM)	Crypto	**517.9** (299.3)	485.6	832.0	236.1	**1402.3** (835.5)	843.7	729.9	1513.3	372.8	1016.3	2713.4	979.8	1562.2	2890.4	2056.2	747.0	**459.1** (183.7)	294.0	598.5	624.3
	N.euk	**23.3** (4.1)	25.0	26.4	18.6	**71.3** (27.0)	80.4	41.5	62.0	67.4	44.7	125.6	104.5	45.7	58.2	94.1	59.8	**41.3** (12.9)	36.0	61.7	46.6
	P.euk	**0.1** (0.1)	0.0	0.2	0.0	**2.0** (1.6)	0.3	1.0	1.3	0.3	1.1	2.3	5.0	3.0	0.6	3.0	4.3	**0.2** (0.2)	0.2	0.5	0.3
	Syn	**1.9** (0.6)	1.4	2.5	1.6	**4.8** (3.3)	3.1	2.0	8.8	1.0	2.7	5.5	2.0	10.8	7.8	6.8	2.6	**1.6** (0.3)	1.3	1.7	1.9
$\delta^{15}N$ (‰)	Bulk	**-2.1** (1.5)	-1.9	-0.8	-3.7	**3.4** (1.2)	4.1	0.9	3.4	4.0	3.8	5.4	2.7	3.5	2.4	2.5	4.7	**3.4** (1.3)	4.7	2.0	3.6
	Picoplankton	-	-	-	-	**2.1** (3.8)	1.1	-6.6	3.9	3.8	5.3	-	-2.1	3.4	2.8	6.3	3.1	**-4.8** (1.8)	-6.7	-4.6	-3.2
	Nanoplankton	-	-	-	-	**3.2** (1.6)	6.4	4.1	-	3.3	2.0	-	2.6	2.7	2.5	0.8	4.4	**3.2**	-	3.2	-
	Microplankton	-	-	-	-	**4.0** (1.8)	4.8	3.9	-	2.2	1.9	-	4.9	6.3	2.2	2.7	6.8	-	-	-	
	Crypto	**-0.5** (0.5)	-0.4	-1.0	-0.1	**0.7** (1.2)	1.2	1.3	1.3	-0.8	1.3	-1.0	-0.3	-0.4	0.5	2.2	2.8	**-0.3** (1.7)	1.2	0.8	-1.9
	N.euk	**-0.9** (1.3)	-0.9	0.3	-2.2	**0.8** (1.2)	-0.8	1.2	-0.7	0.9	0.7	0.2	-0.6	2.5	1.1	1.8	2.8	**-0.6** (1.8)	0.4	2.0	-1.5
	P.euk	**0.0** (0.5)	0.5	-0.1	-0.5	**1.1** (1.2)	0.2	0.1	0.4	1.3	4.0	0.5	0.4	0.4	1.3	2.9	0.5	**0.3** (1.0)	1.3	0.6	-0.6
	Syn	**-0.8** (1.2)	0.5	-1.2	-1.8	**0.8** (1.3)	-0.6	0.9	1.6	1.1	3.6	0.0	0.0	2.2	-0.7	1.5	-0.3	**0.5** (1.7)	2.1	-0.7	-1.0
NO_3^- dependence (%)	Bulk	**26** (4)	29	23	-	**74** (14)	-	-	49	68	-	91	70	75	85	79	-	**73** (25)	-	56	91
	Picoplankton	-	-	-	-	**67** (27)	-	87	89	75	73	5	-	74	75	55	-	-	-	-	-
	Nanoplankton	-	-	-	-	**70** (9)	-	66	-	77	69	-	76	56	82	65	-	-	-	-	-
	Microplankton	-	-	-	-	**58** (17)	-	75	-	-	32	-	74	67	47	53	-	-	-	-	-
	Crypto	**72** (12)	85	61	69	**52** (22)	81	61	29	25	42	33	31	45	58	75	88	**63** (13)	54	79	57
	N.euk	**61** (28)	60	89	34	**55** (20)	-	61	31	40	34	40	41	70	67	74	91	**46** (14)	36	-	56
	P.euk	**76** (10)	-	84	69	**51** (25)	46	23	75	34	96	29	40	27	41	85	66	**55** (12)	46	63	-
	Syn	**37** (30)	70	27	14	**43** (22)	17	46	89	39	60	17	26	53	25	53	51	**35** (34)	72	28	6

4.3.4. Size-fractionated N uptake ratios

Size-fractionated uptake rates of ρNO_3^-, ρNH_4^+, and ρurea were measured at seven of the 17 stations where flow-sorted samples were collected (Fig. 4.1 insert; Fig. 4.6). At these stations, regenerated N (i.e., NH_4^+ + urea) was the dominant N source utilised by the phytoplankton, with bulk community rates of regenerated N uptake (i.e., ρNH_4^+ + ρurea) that were ~1.5-times the bulk community ρNO_3^- (263 ± 180 μmol m^{-2} hr^{-1} versus 187 ± 113 μmol m^{-2} hr^{-1}). The highest euphotic-zone integrated uptake rates, for all N species, were observed at stations L2 and L7, and the lowest at L1 and L3 where the upwelling of WW had recently occurred. The nanoplankton contributed most to ρNO_3^-, ρNH_4^+, and ρurea (64 ± 18%, 76 ± 15%, and 62 ± 15%, respectively) followed by the picoplankton (26 ± 14%, 16 ± 20% and 31 ± 13%, respectively), while the microplankton made a low, albeit not insignificant, contribution to ρNO_3^-, ρNH_4^+, and ρurea (10 ± 10%, 8 ± 5%, and 7 ±5%, respectively).

In Chapter 3 (Flynn et al., 2021), we concluded that *P. antarctica* preferentially consumed regenerated N while the diatoms preferentially consumed NO_3^-. The discrepancy between that conclusion and the observations presented in this chapter, where nanoplankton dominate the biomass and rates of N uptake, shows how the addition of size-fractionated uptake rates may provide further insights into the functioning of the phytoplankton community. However, the conclusion drawn in Chapter 3 may not be incorrect. At LCIS, the high abundance and carbon content of *P. antarctica* and the various large diatom species versus the small cells (e.g., nanoeukaryotes) means that they are likely to be disproportionately important for biogeochemical cycling (e.g., driving changes in nutrient depletion ratios) and for carbon export. It is also likely that some of the diatom cells identified via microscopy were nanoplankton-sized (e.g., *Bacteriastrum, Chaetoceros* spp., *Fragilariopsis* spp.), with the high biomass in the water column (which clogged the net) and/or the presence of these diatoms as large chains (e.g., *Chaetoceros* spp.) resulting in them being captured in the microplankton net. Furthermore, *P. antarctica* (mainly found in its colonial form) and microplankton diatoms (the dominant diatoms observed during this study) were likely under sampled by the Niskin bottles such that the microplankton were underrepresented in the size-fractionated uptake rate experiments. The size-fractionated PON concentrations may suffer from the same methodological bias.

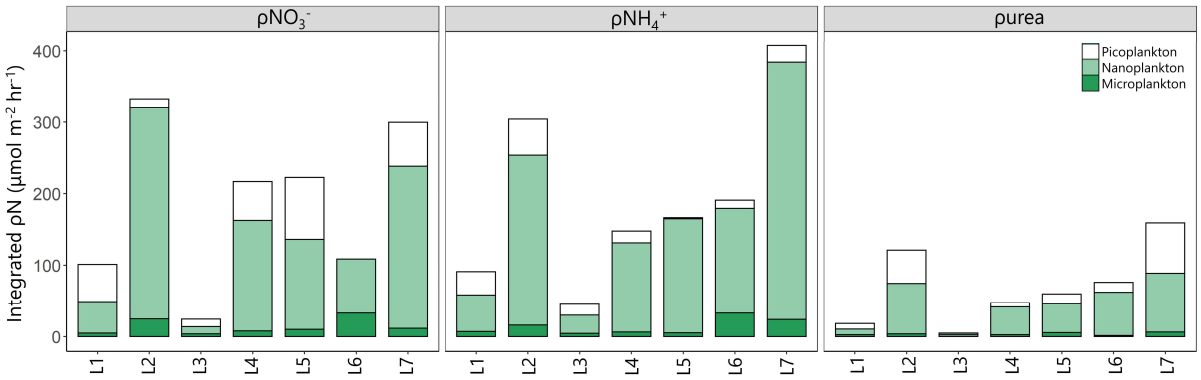


Figure 4.6. Euphotic-zone integrated size-fractionated uptake rates of a) nitrate uptake (ρNO_3^-), b) ammonium uptake (ρNH_4^+) and c) urea uptake (ρurea) at LCIS. The stations are labeled on the x-axis. The different shadings indicate the different phytoplankton size-classes (white – picoplankton, opaque – nanoplankton, solid – microplankton).

4.3.5. NO_3^- dependence of the different phytoplankton size-classes and groups

The NO_3^- dependence (i.e., a measure of the f-ratio derived from a two end-member isotope mixing model; eq. 4.7) of each phytoplankton size-class or group (Fig. 4.7; Table 4.4) provides insights into their potential contribution to carbon export (in a mass balance sense; Dugdale and Goering 1967). The highest regionally-averaged NO_3^- dependence for the bulk phytoplankton community (derived from the bulk PON data; Table 4.4) was estimated for the LCIS and WG stations (average of 74 ± 14% and 74 ± 25%, respectively), while the lowest was estimated along the AP (average of 26 ± 4%). The NO_3^- dependence of the pico-, nano-, and microplankton was only estimated at certain LCIS stations (Fig. 4.7b-d; Table 4.4) due to the issue of low PON concentrations at the other LCIS and WG stations (see above), which can introduce significant error into such estimates (i.e., yielding NO_3^- dependence estimates <0% or >100%). The highest size-class specific NO_3^- dependence was estimated for the nanoplankton (average of 70 ± 9%), with the picoplankton NO_3^- dependence averaging 67 ± 27% and the microplankton 58 ± 17%.

On average, the cryptophytes had the highest NO_3^- dependence at all stations (average of 59 ± 20%), while *Synechococcus* had the lowest (average of 38 ± 21%). The cryptophytes, nanoeukaryotes, and picoeukaryotes had the highest NO_3^- dependence at the AP stations (average of 72 ± 10%, 61 ± 30%, and 76 ± 10%, respectively), while *Synechococcus* had the highest NO_3^- dependence at LCIS (average of 43 ± 20%). The cryptophytes and picoeukaryotes had the lowest NO_3^- dependence at LCIS (average of 52 ± 20% and 51 ± 30%, respectively), while the nanoeukaryotes and *Synechococcus* had the lowest NO_3^- dependence at the WG stations (average of 46 ± 10% and 35 ± 30%, respectively). At the AP stations, the NO_3^- dependence of all phytoplankton groups decreased shoreward, coincident with an increase in the NH_4^+ concentration and decrease in $\delta^{15}N_{bulk\ PON}$ and $\delta^{15}N_{phyto}$.

The highest f-ratio$_{phyto}$ (eq. 4.16) was estimated at the AP stations (average of 0.71 ± 0.11, decreasing shoreward from 0.84 to 0.65) while the f-ratio$_{phyto}$ at the WG stations averaged 0.63 ± 0.08. The lowest regionally-averaged f-ratio$_{phyto}$ was estimated for the LCIS stations (0.50 ± 0.19), although variability was high. For example, at station L11 the f-ratio$_{phyto}$ was 0.78 while at the adjacent station (L4), the f-ratio$_{phyto}$ was the lowest (0.27) estimated for all stations.

The f-ratio was also estimated for the bulk phytoplankton community and the three size-classes using the N uptake rates (f-ratio$_{rates}$; Fig. 4.8a; Table 4.5; eq. 4.19). The bulk community f-ratios (f-ratio$_{bulk}$) indicate that primary production was predominantly fuelled by regenerated N at most stations (average f-ratio$_{bulk}$ of 0.52 ± 0.15, 0.41 ± 0.11 and 0.39 for the AP, LCIS and WG stations, respectively). Contrary to the NO_3^- dependences estimated from the $\delta^{15}N_{phyto}$ measurements at LCIS, the f-ratios estimated from the size-fractionated N uptake rates indicate that the picoplankton (which includes the picoeukaryotes and *Synechococcus*) relied most on NO_3^- (average f-ratio$_{pico}$ of 0.70 ± 0.17), which is consistent with the picoplankton f-ratio$_{PON}$ estimates (average of 0.67 ± 0.27). The nano- and microplankton had similar NO_3^- dependences (average f-ratio$_{nano}$ of 0.37 ± 0.10 and average f-ratio$_{micro}$ of 0.41 ± 0.07), 10-15% lower than the LCIS f-ratio estimates suggested by the NO_3^- dependence of the flow-sorted nanoeukaryotes and cryptophytes, and 20-30% lower than the f-ratio$_{PON}$ estimated for the nano- and microplankton size fractions.

Table 4.5. Depth-weighted mixed-layer averaged f-ratios (i.e., the proportion of NO_3^- consumed by the phytoplankton) estimated for the bulk phytoplankton community using the PON_{bulk} measurements (f-ratio$_{PON\ bulk}$; eq. 4.7), all flow-sorted phytoplankton groups (f-ratio$_{phyto}$; eq. 4.16) and for the bulk phytoplankton community using the bulk nitrogen uptake rates (f-ratio$_{rates\ bulk}$; eq. 4.19) for each station, and contribution of each flow-sorted phytoplankton group to carbon export potential (eq. 4.18).

Station	f-ratio$_{PON\ bulk}$	f-ratio$_{phyto}$	f-ratio$_{rates\ bulk}$	Contribution to carbon export potential (%)			
				Crypto	N.euk	P.euk	Syn
Antarctic Peninsula	0.26 ± 0.04	0.71 ± 0.11	0.52 ± 0.15	94.6 ± 3.4	5.2 ± 3.3	0.1 ± 0.1	0.1 ± 0.1
AP1	0.29	0.84	0.38	95.8	4.0	-	0.2
AP2	0.23	0.64	0.67	90.8	9.0	0.1	0.1
AP3	-	0.65	0.50	97.2	2.7	0.0	0.1
Larsen C Ice Shelf	0.74 ± 0.14	0.50 ± 0.19	0.42 ± 0.11	92.6 ± 5.3	7.6 ± 4.9	0.2 ± 0.3	0.3 ± 0.2
L1	-	0.70	0.47	99.9	-	0.0	0.1
L2	-	0.60	0.45	90.5	9.1	0.2	0.2
L3	0.49	0.31	0.25	83.5	15.8	0.1	0.6
L4	0.68	0.27	0.57	87.5	11.9	0.2	0.4
L5	-	0.42	0.49	91.3	7.5	1.0	0.1
L6	0.91	0.33	0.29	97.9	1.6	0.2	0.2
L7	0.70	0.31	0.35	97.4	2.3	0.1	0.3
L8	0.75	0.47	0.30	91.2	8.4	0.1	0.3
L9	0.85	0.59	0.57	87.5	12.3	0.0	0.1
L10	0.79	0.75	0.42	94.1	5.4	0.1	0.4
L11	-	0.78	-	98.3	1.3	0.2	0.2
Weddell Gyre	0.74 ± 0.25	0.63 ± 0.1	0.39	91.6 ± 8.6	12.3 ± 7.3	0.1 ± 0.1	0.2 ± 0.3
WG1	0.56	0.55	0.39	92.4	7.1	0.0	0.5
WG3	-	0.70	-	99.8	-	0.1	0.1
WG4	0.91	0.65	-	82.6	17.4	-	0.0

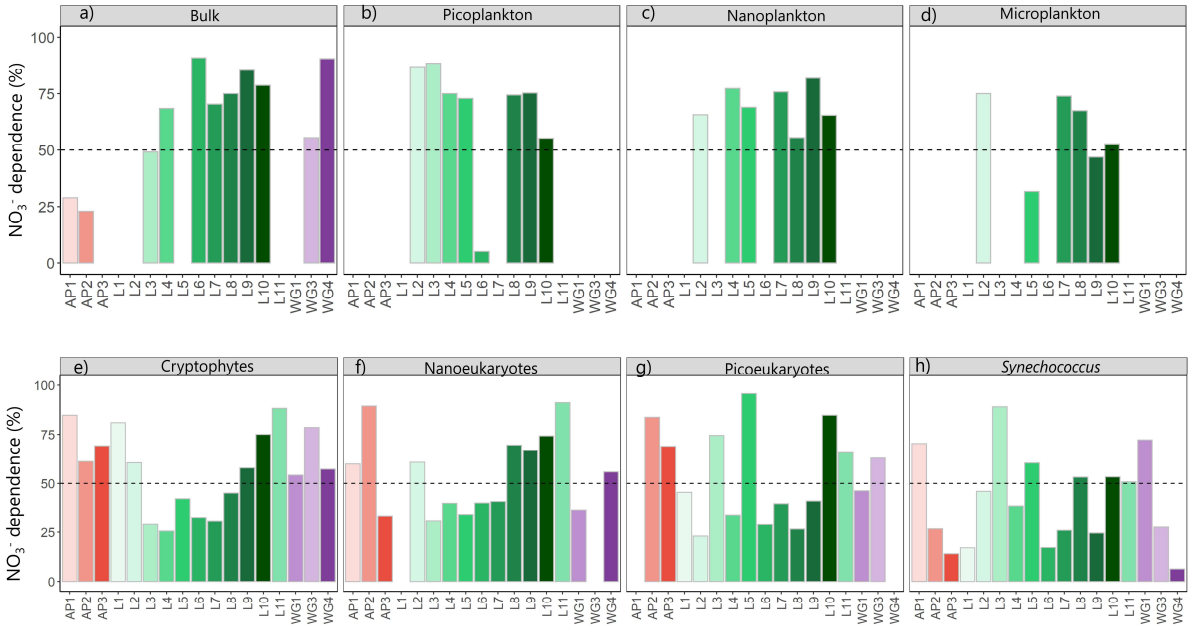


Figure 4.7. The estimated fraction of NO_3^- (versus regenerated nitrogen) dependence of a) the bulk phytoplankton community, b) picoplankton, c) nanoplankton, d) microplankton, e) cryptophytes, f) nanoeukaryotes, g) picoeukaryotes and h) *Synechococcus*. The stations are labeled on the x-axis. The dashed black line indicates a nitrate dependence of 50%.

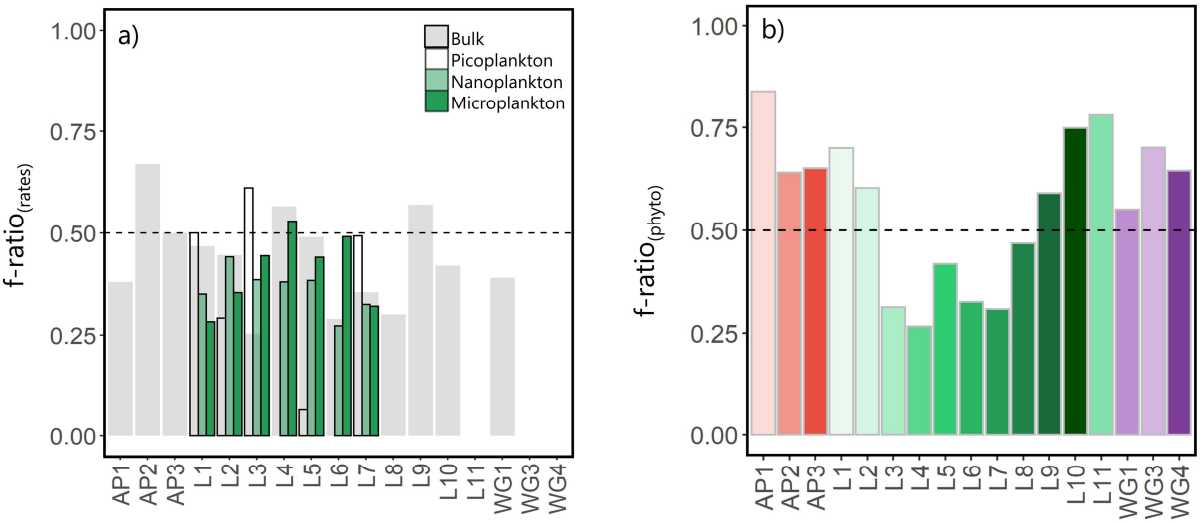


Figure 4.8. Estimates of the f-ratio calculated using a) size-fractionated nitrogen uptake rate data (eq. 4.19) and bulk nitrogen uptake rate data (Chapter 3) and b) measurements of flow-sorted phytoplankton $\delta^{15}N$ (eq. 4.16). The stations are labeled on the x-axis. The dashed black line indicates a f-ratio of 0.5. In panel (a) the different shadings indicate the different phytoplankton size-class f-ratios (transparent – picoplankton, opaque – nanoplankton, solid – microplankton) and the grey bar denotes the bulk phytoplankton f-ratio. Where there are no bars in panel (a), no data are available. Note that this panel (a) is a slightly amended version of Figure 3.8 in Chapter 3 (Figure 8 in Flynn et al., 2021).

4.4. Discussion

Across the summertime Weddell Sea, the $\delta^{15}N_{phyto}$ was generally lower at the open ocean zone (OOZ) stations (i.e., in the WG) than at the MIZ and CCSZ stations, with the highest $\delta^{15}N_{phyto}$ observed at LCIS (Fig. 4.5, Table 4.4). As such, it can be assumed that the phytoplankton community at LCIS was more productive than the community in the OOZ. This supposition is consistent with the findings of previous summertime studies from the region, which employed different methods (e.g., ^{15}N-uptake rate experiments) to estimate rates of net primary production in the CCSZ that were ~5-times higher than in the OOZ (El-Sayed and Taguchi, 1981; Smith and Nelson, 1990; Myung Gil et al., 1999; Flynn et al., 2021). The CCSZ of the Weddell Sea is thus clearly a highly productive region, with the waters near LCIS supporting a thriving phytoplankton community due to the elevated water-column stratification and high iron availability, both the result of sea-ice melt and glacial run-off (Petrou et al., 2016). That said, our data suggest that the phytoplankton community at LCIS were generally less proportionally dependent on NO_3^- (average f-ratio$_{phyto}$ <50%) than the communities at the AP and WG stations. Below, we examine the possible drivers of the inter- and intra-regional differences in phytoplankton community composition, the NO_3^- dependence of the different phytoplankton groups, and the implications for carbon export potential.

4.4.1. Phytoplankton community composition in the summertime Weddell Sea

The phytoplankton community of the summertime Weddell Sea was numerically dominated by *Synechococcus* (Fig. 4.4a-b). However, the small size of *Synechococcus* meant that their contribution to total phytoplankton biomass was low. Instead, the less abundant, larger nanoplankton (predominantly cryptophytes) dominated both the flow-sorted phytoplankton biomass (<20 μm) and the rates of productivity (Fig. 4.3c, 4.3e, 4.4c and 4.6), while the total biomass was variably made up of cryptophytes, diatoms, and *P. antarctica* (Fig. 4.4). This observation is consistent with previous work showing that phytoplankton blooms in the Antarctic CCSZ and MIZ are generally dominated by *P. antarctica*, diatoms, and/or cryptophytes (Garibotti et al., 2005; Trimborn et al., 2015), with the relative abundance of the different groups driven by various physicochemical conditions, predominantly light and iron availability (Arrigo et al., 1999, 2010; Mendes et al., 2013).

The dominance of cryptophytes was likely the result of sampling taking place late in the growth season, prior to which the spring and early-summer phytoplankton community would have been dominated by *P. antarctica* at LCIS and diatoms at the AP and WG stations (Moisan and Mitchell, 1999; Arrigo et al., 1999; Goffart et al., 2000; Nissen and Vogt, 2021). At LCIS, thick sea-ice conditions persist year-round. In spring, warm Föhn winds originating over the AP initiate the formation of a coastal sensible heat polynya that is present throughout the growth season (Cape et al., 2014). When the polynya first opens, it is characterised by deep mixed layers and a weakly stratified water column, which should favour the growth of motile *P. antarctica* cells since this species is a low-light specialist compared to

other Antarctic phytoplankton (Goffart et al., 2000; Alderkamp et al., 2012; Delmont et al., 2014). However, *P. antarctica* has a high iron requirement, limiting its geographic distribution to iron replete regions such as the waters adjacent to LCIS (Strzepek et al., 2011). The idea that *P. antarctica* dominate in weakly stratified, iron replete mixed layers is supported by the low cell counts (for both flow cytometry and microscopy) and higher abundance of *P. antarctica* and nanoeukaryotes (likely consisting of motile *P. antarctica* and small diatoms) compared to cryptophytes and microplankton-sized diatoms at the ice-shelf stations where the upwelling of WW had recently occurred (i.e., L1 and L3; Fig. 4.4).

As the season progresses, light limitation in the polynya is alleviated as the water column stratifies due to the sensible heating of surface waters. As the mixed layer shoals and light becomes replete, *P. antarctica* initiate colony formation (Schoemann et al., 2005) and microplankton-sized diatoms bloom as they are generally better adapted to high-light conditions (Goffart et al., 2000; Nissen and Vogt, 2021). We thus propose that mixed-layer shoaling prior to our sampling shifted the phytoplankton community from motile *P. antarctica* cells to diatoms and colonial *P. antarctica*. Indeed, at the stations where the mixed layer was shallowest (e.g., L10), diatoms had a higher abundance and contribution to biomass (Fig. 4.4f). Although there was a shift from *P. antarctica* to diatoms as the mixed layer shoaled, cryptophytes still dominated the phytoplankton biomass. The extremely shallow MLD and Z_{eu} at LCIS (average of 12 ± 5 m and 29 ± 9 m, respectively) likely selected for the growth of cryptophytes over diatoms and *P. antarctica* because cryptophytes contain photoprotective carotenoids that allow them to thrive under high-light conditions (Mendes et al., 2018b, 2023). In contrast, although diatoms are generally well adapted to high light, they may experience some amount of damage to their photosynthetic apparatus under extremely high light conditions (Mendes et al., 2018b, 2023), which would have inhibited their growth in the shallow mixed layers at LCIS. The notion that light exerted a control on the abundance of the cryptophytes is consistent with the observation that the highest cryptophyte cell counts and PON concentrations were observed at the LCIS stations with the shallowest MLD and Z_{eu} (e.g., L7; Fig. 4.4). Furthermore, the N uptake experiments indicate that the nanoplankton contributed most to N uptake at the surface (average of 70 ± 24% for total N uptake at ~5 m; Fig. C3), with their contribution decreasing towards the Z_{eu} (average of 62 ± 20% at the 1% light level). This trend evidences the inhibiting effect of high light on the other phytoplankton groups, which is reduced with depth, allowing for increased competition for resources among the different groups.

At the other (non-LCIS) stations, the spring and early-summer phytoplankton community was likely dominated by diatoms as rapid sea-ice melt provided favourable growth conditions for this phytoplankton group by rapidly alleviating light and, to some extent, iron limitation (Klunder et al., 2011). Coincidently, the generally low iron availability in the open Weddell Sea (Klunder et al., 2011, 2014) likely inhibited the growth of *P. antarctica*, which has a high iron requirement (Strzepek et al.,

2011). The dominance of cryptophytes later in the season at the AP and WG stations was, however, not due to the same physicochemical drivers. At the time of sampling, iron and light in the WG co-limited phytoplankton productivity, as indicated by the elevated $Si(OH)_4$-to-NO_3^- depletion ratios (>>2:1; Flynn et al., 2021) and deep Z_{eu} (average of 90 ± 14 m). The low iron and light conditions likely favoured the growth of nanoplankton-sized cryptophytes over microplankton-sized diatoms. Smaller cells generally have a lower light and absolute nutrient requirement because of their larger surface area-to-volume ratio (Edwards et al., 2012 and references therein), which may have allowed the cryptophytes to outcompete the large diatoms for the low concentrations of available iron. In contrast, along the AP, light and iron were generally replete (average Z_{eu} of 45 ± 9 m and $Si(OH)_4$-to-NO_3^- depletion ratios of ~1:1; Flynn et al., 2021). Here, elevated mixed layer temperatures (average of -0.9 ± 0.3°C versus -1.5 ± 0.4°C at the WG stations) drove increased sea-ice melt which favoured the growth of cryptophytes over diatoms, similar to the situation at LCIS. Indeed, recent work has shown a general secular shift in the phytoplankton community along the AP from diatom- to cryptophyte dominance, coincident with the warming of ASW and increased stratification of the mixed layer (Mendes et al., 2013, 2018a, 2023, b; Kerr et al., 2018). Although diatoms generally thrive in shallow mixed layers (Vernet et al., 2008; Costa et al., 2020), the enhanced warming of ASW along the AP shoals the mixed layer to such an extent that diatoms can become light inhibited, thus allowing the cryptophytes (with their photoprotective carotenoids) to dominate (Mendes et al., 2018b, 2023). We thus conclude that local hydrodynamic processes that yield extremely shallow mixed layers (such as at LCIS and along the AP) or deep mixed layers coincident with low iron concentrations (as in the WG) selects for cryptophytes over diatoms and/or *P. antarctica* in the summertime Weddell Sea.

4.4.2. The role of community composition in modulating carbon export

In the Southern Ocean, microplankton-sized diatoms are generally thought, and have to some extent been observed, to contribute disproportionately to carbon export (both directly via sinking and indirectly through their high reliance on NO_3^-) (Tréguer et al., 2017; Dugdale and Goering 1967; Eppley and Peterson, 1979). However, recent studies have shown that the role of nanoplankton in carbon export has been overlooked (Cassar et al., 2015; Leblanc et al., 2018; Juranek et al., 2020) and that this size class may be important for carbon export in the Southern Ocean (e.g., Chapter 2). To investigate the contribution of small cells (<20 µm) to carbon export potential, we estimated the NO_3^- dependence (i.e., approximated by f_{new}; eq. 4.7) of each phytoplankton size-class and group (Fig. 4.7 and 4.8; Table 4.4 and 4.5). These results are discussed in detail below.

Drivers of the nitrate dependence of the various phytoplankton groups

The extent to which the different phytoplankton groups relied on NO_3^- versus regenerated N was on average lower at the LCIS and WG stations and higher at the AP stations compared to that of the bulk phytoplankton community (Fig. 4.7 and 4.8; Table 4.4). In addition, the NO_3^- dependence inferred for

the different size-classes at LCIS was generally higher than that of the sorted phytoplankton groups associated with each size-class. For example, the NO_3^- dependence of the picoplankton averaged 67 ± 27%, yet the picoplankton-sized *Synechococcus* and picoeukaryotes apparently relied on NO_3^- for 38 ± 21% and 55 ± 23% of their N, respectively. This discrepancy between the size-fractionated PON and phytoplankton-specific NO_3^- dependence is likely due to the phytoplankton-specific estimates only accounting for the actively growing phytoplankton, while the estimates based on the PON data include the growing phytoplankton community (including microplankton in the case of PON_{bulk}), heterotrophs, and detritus. The $\delta^{15}N$ of detritus is expected to be high compared to the live photoautotrophic biomass (Fawcett et al. 2011) as bacterial decomposition preferentially removes ^{14}N (Deniro and Epstein, 1981; Macko et al., 1986; Silfer et al., 1992; Checkley and Miller, 1989), raising the $\delta^{15}N$ of the residual detrital pool (Möbius, 2013). As such, the inclusion of detritus in PON samples is likely to bias the $\delta^{15}N$ – and thus the inferred NO_3^- dependence – to higher values. The presence of heterotrophs (as either bacteria or zooplankton) within the bulk PON pool will also affect the $\delta^{15}N_{bulk\ PON}$, either raising or decreasing it. Heterotrophic bacteria have been shown to be low in $\delta^{15}N$ (<0‰; Fawcett et al., 2011), noting that these measurements are limited and were made in the subtropical ocean. In contrast, zooplankton have a high $\delta^{15}N$ as they preferentially excrete ^{14}N-NH_4^+, raising the $\delta^{15}N$ of their biomass (Checkley and Miller, 1989). The contribution of heterotrophic bacteria to the PON pool will therefore likely lower the $\delta^{15}N_{PON\ bulk}$ while that of zooplankton will raise the $\delta^{15}N_{bulk\ PON}$. The phytoplankton-specific estimates are not subject to these limitations because detrital and heterotrophic material is excluded during flow cytometric sorting. We thus focus hereafter on the flow-sorted results and do not further interpret the PON-based data.

We propose that at LCIS, variability in the NO_3^- dependence of the different phytoplankton groups was predominantly driven by NH_4^+ and/or temperature (Fig. 4.9). Interestingly, an inverse relationship was observed between the mixed-layer average NH_4^+ concentrations and temperature, with higher NH_4^+ concentrations coinciding with lower temperatures (Fig. 4.10a). Initially, this relationship appears confounding, particularly since in Chapter 3 it was deduced based on the observation that the mixed-layer PON concentrations increased with increasing temperature, that mixed-layer temperature can be used as a proxy for water-mass age. One might thus expect higher NH_4^+ concentrations to coincide with higher PON concentrations and warmer temperatures (i.e., in older surface waters where the phytoplankton bloom had progressed the furthest) because enhanced heterotrophic consumption and remineralisation of phytoplankton biomass, which typically occurs later in a bloom, should increase mixed-layer NH_4^+ (Semeneh et al., 1998). To explain the opposite trend observed at LCIS we suggest that the mixed-layer NH_4^+ concentrations are indicative of the amount of NH_4^+ consumed rather than the quantity produced (i.e., lower NH_4^+ concentrations are the result of enhanced NH_4^+ consumption; Flynn et al., 2021). We further conclude that in newly upwelled waters (e.g., at station L3), the phytoplankton community showed the highest relative NO_3^- dependence (noting that this estimate is not

indicative of the total quantity of NO_3^- consumed, but rather the proportion of NO_3^- uptake compared to total N consumption) due to the low availability of NH_4^+ (mixed-layer average concentration of 0.1 ± 0.03 μM), as well as the elevated iron and light availability, which should favour NO_3^- assimilation (Lannuzel et al., 2008). As the surface waters aged and the bloom progressed, there was a shift towards regenerated N consumption, made favourable by an increase in the availability of NH_4^+ (i.e., a higher NH_4^+ supply, which need not manifest in a higher ambient NH_4^+ concentration) and possibly a decline in iron (Fig. 4.10).

Although the highest $\delta^{15}N_{phyto}$ was measured at LCIS, the NO_3^- dependence of the cryptophytes, nanoeukaryotes, and picoeukaryotes was estimated to be low at these stations compared to the AP and WG stations (Fig. 4.7; Table 4.4). The low NO_3^- dependence of these phytoplankton groups coincided with high rates of regenerated N uptake (Fig. 4.10f). These results, coupled with the lower mixed-layer NH_4^+ concentrations in older surface waters, provides evidence that as the availability of NH_4^+ increased later in the growth season, the phytoplankton community shifted towards greater reliance on regenerated N. However, the high NH_4^+ availability did not completely inhibit NO_3^- uptake, as has been observed elsewhere (Goeyens et al., 1995). At LCIS, the NO_3^- dependence of all phytoplankton groups and the rates of NO_3^- uptake were not zero (Fig. 4.6 and 4.7), indicating that the phytoplankton community was still able to consume NO_3^-. For the same region, Flynn et al. (2021) found using measurements of NO_3^- and NH_4^+ uptake, that the total phytoplankton community continued to consume NO_3^- even in the presence of elevated NH_4^+ concentrations. The authors hypothesized that *P. antarctica* was predominantly consuming NH_4^+ while the diatom community continued to assimilate NO_3^- given that under favourable growth conditions (i.e., high light and iron availability), diatoms are known to prefer NO_3^- even when ambient NH_4^+ is high (Probyn and Painting, 1985; Koike et al., 1986; Lomas and Glibert, 1999; Karsh et al., 2003). However, the flow-sorted data suggest that all the LCIS phytoplankton groups continued consuming some NO_3^- even as the ambient NH_4^+ increased to potentially inhibitory concentrations (average NO_3^- dependence of 51 ± 24% at $[NH_4^+]$ >0.5 μM). It is possible that NH_4^+ had only recently become inhibitory (i.e., over the last few days), which would not have been well reflected in the $\delta^{15}N_{phyto}$ measurements as they integrate phytoplankton N consumption over a few weeks. As such, phytoplankton could have been consuming very little NO_3^- at the time of our sampling while their $\delta^{15}N_{phyto}$ still reflected past NO_3^- dependence. We conclude that the elevated NH_4^+ concentrations present at LCIS partially inhibited NO_3^--based phytoplankton growth, with the ^{15}N-tracer-derived N uptake rates providing the best measure of the instantaneous NO_3^- dependence of the different phytoplankton groups and the phytoplankton-specific data yielding a more integrated estimate.

In contrast to the LCIS stations, the NO_3^- dependence of the phytoplankton groups at the AP1 and WG stations was controlled by light availability, although the shoreward decrease in NO_3^- dependence at the

AP may have been due to an increase in NH_4^+ availability (Fig. 4.9 and circles in Fig. 4.10b-e). AP1 and the WG stations were characterised by the deepest MLD and Z_{eu} (Table 4.1), likely causing the phytoplankton community at these stations to be somewhat light limited. Under conditions of light limitation, phytoplankton will preferentially use regenerated N sources over NO_3^- because they are more energetically efficient to assimilate (El-Sayed and Taguchi, 1981; Dortch, 1990; Jacques, 1991; Goeyens et al., 1995; Priddle et al., 1998; Stefels and Van Leeuwe, 1998). Indeed, at the WG station with the deepest MLD (i.e., WG1), the phytoplankton relied more heavily on regenerated N than at the station with the shallowest MLD (i.e., WG3; Table 4.4; Fig. 4.7e-h). Furthermore, unlike at LCIS, the NH_4^+ concentrations increased with increasing PON concentrations at the AP and WG stations (Fig. 4.10a), indicating that NH_4^+ was in net being produced, via the consumption (by zooplankton) and remineralisation (by bacteria) of the phytoplankton bloom (Rönner et al., 1983; El-Sayed, 1984; Semeneh et al., 1998). The generally low PON concentrations at AP1 and the WG stations therefore limited the availability of regenerated N at these stations, restricting regenerated N uptake and resulting in the generally high NO_3^- dependence of the different phytoplankton groups. The shoreward increase in the mixed-layer NH_4^+ concentrations along the AP is consistent with this interpretation, indicating that all phytoplankton groups increased their reliance on regenerated N relative to NO_3^- as NH_4^+ availability increased (Fig. 4.10b-e). We conclude that light and NH_4^+ availability played a central role in controlling the extent of NO_3^- dependence of all phytoplankton groups in the Weddell Sea in late summer.

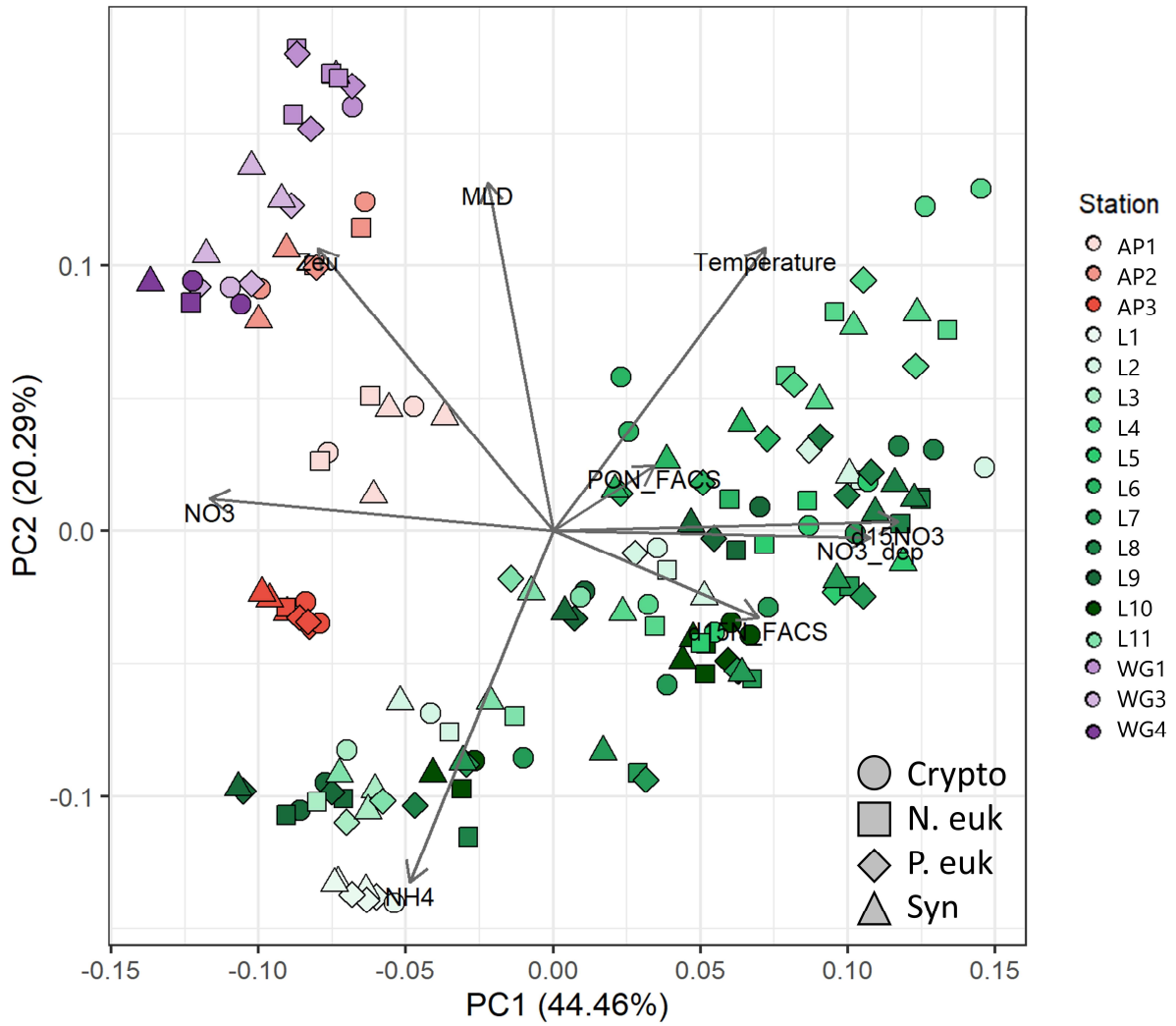


Figure 4.9. Principal component analysis (PCA) of the variability in the extent of NO_3^- dependence by the different flow-sorted phytoplankton groups constrained by various environmental variables and visualized as a biplot. The points are coloured by station (red – Antarctic Peninsula, green – Larsen C Ice Shelf, purple – Weddell Gyre) and the different phytoplankton groups are denoted by symbols (circle – cryptophytes, square – nanoeukaryotes, diamond – picoeukaryotes, triangle – *Synechococcus*). The variables used in the PCA are as follows: MLD – mixed layer depth, Zeu – euphotic zone depth, NO3 – nitrate concentration, NH4 – ammonium concentration, d15N_FACS – $\delta^{15}N_{phyto}$, NO3_dep – the fraction of nitrate consumed (i.e., $[NO_3^-]_{measured}/[NO_3^-]_{ww}$), d15NO3 – $\delta^{15}N_{NO_3^-}$, PON_FACS – PON concentration of the different flow-sorted phytoplankton groups, Temperature – the measured temperature.

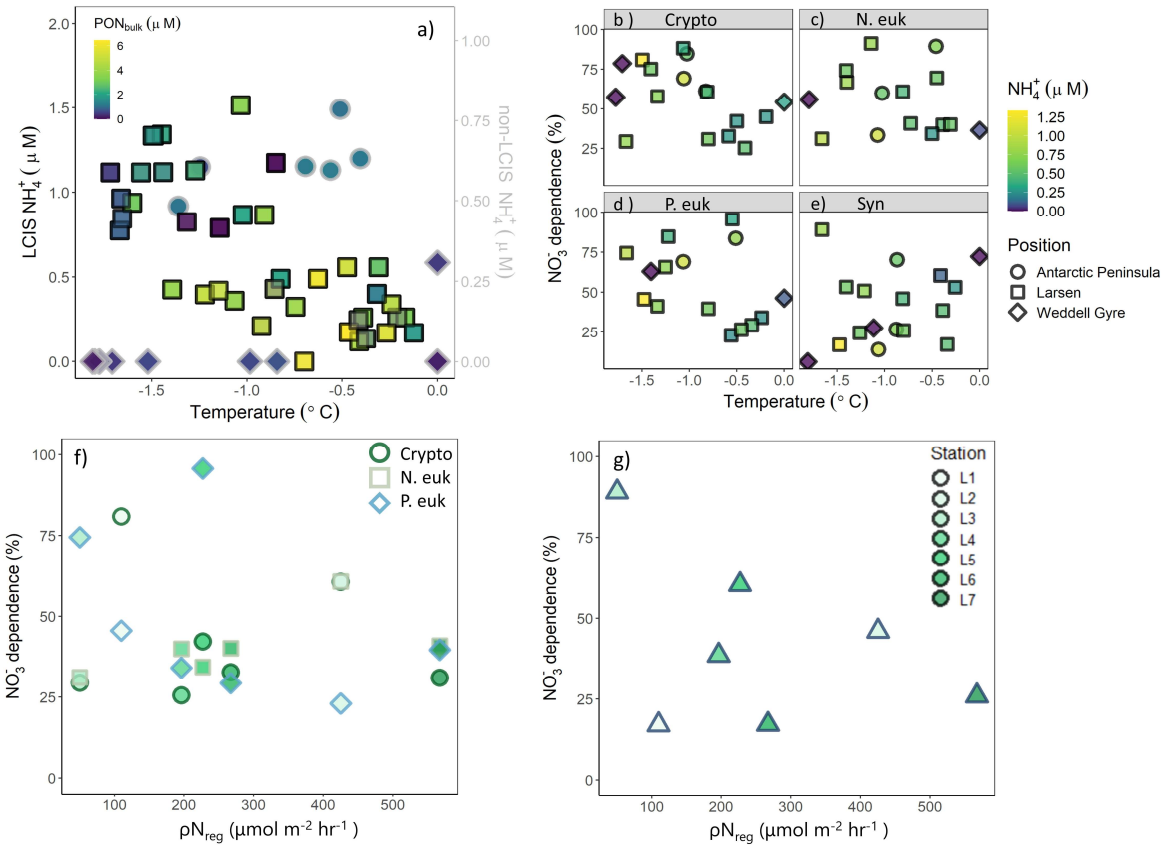


Figure 4.10. Scatterplots of a) mixed-layer NH_4^+ concentration versus mixed-layer temperature, NO_3^- dependence versus temperature for the b) cryptophytes, c) nanoeukaryotes, d) picoeukaryotes and e) *Synechococcus*, and euphotic-zone integrated NO_3^- dependence versus ρN_{reg} (i.e., integrated bulk rates of regenerated N uptake) versus of f) the cryptophytes, nanoeukaryotes and picoeukaryotes and g) *Synechococcus*. The symbols in panel (a) are coloured by the bulk PON concentration, in panels (b-e) by NH_4^+ concentration and in (f-g) by station. The symbols in panels (a-e) denote the different hydrographic regions (circle – Antarctic Peninsula, square – Larsen C Ice Shelf, diamond – Weddell Gyre) and in panel (f-g), the different phytoplankton groups (dark green circle – cryptophytes, light green square – nanoeukaryotes, light blue diamond – picoeukaryotes, dark blue triangle – *Synechococcus*). In panel (a), the NH_4^+ concentrations at LCIS corresponds with the left y-axis and the NH_4^+ concentrations at the other ("non-LCIS") stations corresponds with the right y-axis.

Carbon export potential inferred from phytoplankton reliance on NO_3^-

The phytoplankton-specific NO_3^- dependence estimates can be used to compute the f-ratio of the total flow-sorted phytoplankton community (f-ratio$_{phyto}$; eq. 4.16). These values were on average 10% higher (range of 0.31-0.84, average of 0.56 ± 0.18; Table 4.5) than the ^{15}N tracer-derived estimates (f-ratio$_{tracer}$) for the same sampling period (Fig. 4.8; Table 4.5; Flynn et al., 2021), likely because of the different time-scales represented by the $\delta^{15}N_{phyto}$ (days to weeks) versus ^{15}N tracer-derived (instantaneous) data as well as the exclusion of heterotrophic and detrital material from the $\delta^{15}N_{phyto}$ measurements. Although the f-ratio$_{phyto}$ estimates were higher than the f-ratio$_{tracer}$ estimates, similar trends were observed, with the highest f-ratios estimated for the AP and WG stations and the lowest at LCIS (Fig. 4.8). As for the extent of NO_3^- dependence of the different phytoplankton groups, this pattern can be largely attributed to the elevated NH_4^+ availability at LCIS compared to at the AP and WG stations.

The f-ratio$_{phyto}$ was strongly driven by the NO_3^- dependence of the cryptophytes because of the dominant contribution of this phytoplankton group to total biomass; indeed, in as mass balance sense, the cryptophytes were responsible for an average of 85 ± 6% of the potentially exportable carbon represented by the <20 μm cells. In contrast, the most abundant phytoplankton groups, the picoeukaryotes and *Synechococcus,* made the lowest contribution to carbon export potential (<0.6%; Table 4.5). The difference between the contribution of the cryptophytes versus picoplankton (i.e., picoeukaryotes and *Synechococcus*) evidences the role of cell size in carbon export potential. The small size of the picoplankton (<1 μm^3) results in their low contribution to carbon export as they 1) have a low cellular carbon content, 2) will sink slowly, and 3) are generally associated with conditions of nutrient recycling, contributing to the microbial loop (Basu and Mackey, 2018). By contrast, the cryptophytes were the largest flow-sorted phytoplankton group (average biovolume of 730 ± 663 μm^3; Table 4.2) and although we assumed the same carbon content per μm^3 as for the other cells, their larger size resulted in a high contribution to biomass and carbon export potential. The larger size of the cryptophytes likely also means that their direct contribution to the sinking flux (and thus carbon export) was high compared to *Synechococcus,* picoeukaryotes, and nanoeukaryotes because they were less likely to be grazed by microzooplankton (the dominant grazers of small phytoplankton; Smetacek et al., 2004).

Based on the euphotic-zone integrated NO_3^- depletions (Chapter 3; eq. 3.1), we can directly estimate the amount of carbon export associated with the flow-sorted phytoplankton groups. The seasonal NO_3^- depletion (i.e., from the point of maximum winter recharge to the time of sampling) ranged from 16-428 mmol m^{-2}. Assuming a Redfieldian C:N stoichiometry of 6.63:1, the seasonal NO_3^- depletion equates to a carbon export flux of 0.1-2.8 mol C m^{-2}. Using the NO_3^- dependence of the different flow-sorted phytoplankton groups and their contributions to carbon export potential, we estimate the direct contribution of each group to this carbon export flux. Assuming that conditions were only favourable

for cryptophyte growth ~2 weeks prior to sampling (Mendes et al., 2013), we estimate that 0.04-0.56 mol C m^{-2} was exported during the cryptophyte growth period (7-33% of the seasonal carbon export). By contrast, the relatively small contribution of the other phytoplankton groups to biomass resulted in these groups having a low contribution to the seasonal carbon export (0-14%). For example, *Synechococcus* accounted for 0.01-1.2 mmol C m^{-2} which constitutes 0-0.3% of the seasonal carbon export flux. It is likely that *P. antarctica* and/or diatom blooms accounted for a large portion of the seasonal carbon export prior to the cryptophyte bloom as these groups are known to contribute significantly to carbon export (Arrigo et al., 2000; Ditullio et al., 2000; Tréguer et al., 2017). Furthermore, the shift in the phytoplankton community from *P. antarctica* and/or diatoms to cryptophytes over the growth season coincided with increasing reliance on regenerated N, which partially inhibited biological carbon export and CO_2 removal across the Weddell Sea.

4.4.3. The nitrate dependence of *Synechococcus*: biogeochemical implications at LCIS

Synechococcus are a cosmopolitan phytoplankton group and have been observed to reach higher abundances in the nutrient-rich high latitudes than in the oligotrophic oceans (Partensky et al., 1999; Van Oostende et al., 2017b). The ubiquity of this group has resulted in its N nutrition being extensively studied, with *Synechococcus* known to assimilate both new and regenerated N sources (Glibert et al., 1986; Paerl, 1991; Lindell et al., 1998; Collier et al., 1999; Moore et al., 2002; Fuller et al., 2003). However, culture and $\delta^{15}N_{phyto}$-based studies have shown that *Synechococcus* has a preference for regenerated N (Glibert and Ray, 1990; Lindell and Post, 2001; Fawcett et al., 2011a, 2014; Treibergs et al., 2014). Interestingly, the present study shows that at LCIS, the NO_3^- dependence of *Synechococcus* generally increased with increasing mixed-layer temperatures under conditions of apparently high regenerated N availability, as indicated by the bulk ρN_{reg} uptake rates, while the NO_3^- dependence of the cryptophytes, nanoeukaryotes, and picoeukaryotes decreased (Fig. 4.10b-g). This result is consistent with a recent study by Forrer (2021) showing that in the Subantarctic Southern Ocean, *Synechococcus* had a high NO_3^- dependence (>70%) even under conditions of high NH_4^+ availability (1.9 ± 1.3 μM). The unexpected increase in *Synechococcus'* NO_3^- dependence with increasing mixed-layer temperatures and NH_4^+ concentrations may be due to a number of factors. Below, we discuss the potential implications of iron and temperature for *Synechococcus'* ability to consume NO_3^- over regenerated N.

Synechococcus thrived in the surface waters at LCIS, with this group's relative abundance decreasing towards the Z_{eu} (Fig. C2), similar to observations from the subtropics and Subantarctic (Durand et al., 2001; Treibergs et al., 2014; Forrer, 2021). This observation can be explained by the high light requirement of *Synechococcus* because of its high ratio of photosystem I to photosystem II compared to other phytoplankton groups; as such, the growth of *Synechococcus* is limited in low light regions (e.g., at the Z_{eu}; Glover et al., 1987; Prezelinl et al., 1989; Moore et al., 1998; Sunda and Huntsman, 2015). Furthermore, *Synechococcus* needs considerable iron because of the higher iron requirements

associated with photosystem I (12 atoms of iron) relative to photosystem II (2-3 atoms of iron; Raven, 1990; Brand, 1991; Wilhelm et al., 1996); as such, its growth is generally reduced in iron limited regions (Sunda and Huntsman, 2015). The high light and iron conditions that characterised the late-summer waters adjacent to LCIS thus provided ideal conditions for the growth of *Synechococcus*. However, the NO_3^- dependence of *Synechococcus* varied at LCIS (ranged from 17% to 89%), indicating that something other than light and iron availability influenced the preference of *Synechococcus* for new versus regenerated N.

At LCIS, the mixed-layer temperatures ranged by almost 2°C (from -1.7°C to 0°C) and a generally positive relationship was observed between the NO_3^- dependence of *Synechococcus* and temperature (Fig. 4.10e). In oligotrophic and coastal regions, the abundance of *Synechococcus* has been shown to strongly positively correlate with temperature (Agawin et al., 1998; Li and Dickie, 2001; Tsai et al., 2008). The increase in the NO_3^- dependence of *Synechococcus* with increasing temperature may therefore be explained by the organism's physiology. At low temperatures, *Synechococcus* has been observed to be unable to reach its maximum growth rates (Agawin et al., 1998; Chen et al., 2014). When it is cold, *Synechococcus* may thus preferentially consume NH_4^+ even if light and macro- and micro-nutrients are replete, as reduced N assimilation requires less energy, which can instead be used for other purposes (such as growth). In the Weddell Sea, as the season progressed and ASW warmed, grazing and remineralisation increased, enhancing the supply of NH_4^+ to the mixed layer at LCIS. The increased NH_4^+ flux partially inhibited NO_3^- uptake by the cryptophytes, nanoeukaryotes, and picoeukaryotes but did not appear to inhibit NO_3^- uptake by *Synechococcus* (Fig. 4.10). We hypothesize that their small size and low biomass resulted in *Synechococcus* being outcompeted by the larger phytoplankton groups for the available NH_4^+. Although small cells have a higher nutrient affinity, larger cells are able to achieve higher maximum nutrient uptake rates, which may have allowed them to more efficiently acquire NH_4^+ as it was produced, assuming the flux was large (Sommer, 1984; Edwards et al., 2012). At the same time, the high iron and light conditions that characterised LCIS during the sampling period may have allowed for the persistence of *Synechococcus*, with elevated competition for NH_4^+ resulting in *Synechococcus* increasing their reliance on NO_3^- as the growth season progressed.

The apparent shift of *Synechococcus* from regenerated N to NO_3^- dependence with the warming of ASW may have implications for carbon export potential at LCIS and in other regions of the Antarctic CCSZ where ASW is warming and iron and light are replete. Recent studies have shown that the warming of ASW is shifting the phytoplankton community from predominantly diatoms to cryptophytes (Kerr et al., 2018; Mendes et al., 2018b, 2023). This shift results in a net decrease in the size spectrum of the phytoplankton assemblage which may enhance microbial activity via the sloppy feeding of zooplankton, thereby decreasing carbon export potential (Rodríguez et al., 2002; Ducklow et al., 2013). The shift towards cryptophytes may also drive a shift in the zooplankton community from mainly krill

to predominantly salp (e.g., Ducklow et al., 2006; Montes-Hugo et al., 2009; Mendes et al., 2013), which may offset the decrease in carbon export potential as salp faecal pellets are faster-sinking than those of krill and have been estimated to make a large contribution to carbon export (Pakhomov et al., 2002; Phillips et al., 2009). The proliferation of *Synechococcus* with its elevated reliance on NO_3^- may be hypothesized to partially mitigate the potential decrease in carbon export. However, we show that even when *Synechococcus* growth is predominantly supported by NO_3^- (e.g., at L5), this group contributes <0.6% to total carbon export potential such that even if it becomes considerably more abundant, it is unlikely to influence biological carbon export at LCIS or in other regions of the Antarctic CCSZ. Nonetheless, further investigation into the drivers of phytoplankton community composition and N nutrition is required, particularly as the ocean warms, given the implications for carbon export, the biogeochemistry of deep-water masses (such as those formed at LCIS), and trophic interactions.

4.5. Conclusion

We estimated the NO_3^- dependence of four flow-sorted phytoplankton groups (<20 μm) in understudied regions of the Weddell Sea and evaluated the importance of each group for biomass and carbon export potential. Our data show that cryptophytes dominated the phytoplankton biomass across the region, with the relative importance of cryptophytes versus *P. antarctica* and diatoms driven by the extremely shallow late-summer mixed layers that characterised most stations. Cryptophytes contain photoprotective carotenoid pigments, which allows this group to proliferate in these shallow mixed layers where conditions are damaging to other phytoplankton groups (Mendes et al., 2018b, 2023). The dominance of cryptophytes over *P. antarctica* and diatoms has consequences for carbon export and storage, particularly at LCIS where deep water-mass formation occurs (Kerr et al., 2018).

Although the phytoplankton community was most productive at LCIS (Chapter 3; Flynn et al., 2021), it was the region characterised by the lowest f-ratios and NO_3^- dependence of the various flow-sorted phytoplankton groups. We attribute this to partial NH_4^+ inhibition of NO_3^- uptake, which amounts to a missed opportunity for carbon export (Cochlan and Bronk, 2003) and CO_2 storage in bottom waters, particularly since light, iron, and macronutrients were not limiting at the time of sampling. Given that the surface waters of the Weddell Sea, particularly along the AP and in the vicinity of ice shelves, will become increasingly stratified with the warming of ASW and increased glacial and/or sea-ice melt (Pörtner et al., 2014; Sallée et al., 2013; Stammerjohn et al., 2012; Petrou et al., 2016; Kerr et al., 2018), better understanding the physicochemical drivers of phytoplankton community composition and their role in carbon export in these waters is imperative.

4.6. References

Agawin, N. S. R., Duarte, C. M., and Agusti, S.: MARINE ECOLOGY PROGRESS SERIES Growth and abundance of Synechococcus sp. in a Mediterranean Bay: seasonality and relationship with temperature, Mar. Ecol. Prog. Ser., 170, 45–53, 1998.

Alderkamp, A.-C., Kulk, G., Buma, A. G. J., Visser, R. J. W., Dijken, G. L. Van, Mills, M. M., and Arrigo, K. R.: The effect of iron limitation on the photophysiology of Phaeocystis Antarctica (Prymnesiophyceae) and Fragilariopsis Cylindrus (Bacillariophyceae) under dynamic irradiance, J. Phycol., 48, 45–59, https://doi.org/10.1111/J.1529-8817.2011.01098.X, 2012.

Altabet, M. A.: Variations in nitrogen isotopic composition between sinking and suspended particles: implications for nitrogen cycling and particle transformation in the open ocean, Deep Sea Res. Part A, Oceanogr. Res. Pap., 35, 535–554, https://doi.org/10.1016/0198-0149(88)90130-6, 1988.

Arrigo, K. R., Robinson, D. H., Worthen, D. L., Dunbar, R. B., DiTullio, G. R., VanWoert, M., and Lizotte, M. P.: Phytoplankton community structure and the drawdown of nutrients and CO2 in the Southern Ocean, Science (80-.)., 283, 365–367, https://doi.org/10.1126/science.283.5400.365, 1999.

Arrigo, K. R., DiTullio, G. R., Dunbar, R. B., Robinson, D. H., VanWoert, M., Worthen, D. L., and Lizotte, M. P.: Phytoplankton taxonomic variability in nutrient utilization and primary production in the Ross Sea, J. Geophys. Res. Ocean., 105, 8827–8846, https://doi.org/10.1029/1998jc000289, 2000.

Arrigo, K. R., Mills, M. M., Kropuenske, L. R., Van Dijken, G. L., Alderkamp, A. C., and Robinson, D. H.: Photophysiology in two major southern ocean phytoplankton taxa: Photosynthesis and growth of phaeocystis antarctica and fragilariopsis cylindrus under different irradiance levels, Integr. Comp. Biol., 50, 950–966, https://doi.org/10.1093/icb/icq021, 2010.

Berges, J. A. and Mulholland, M. R.: Enzymes and Nitrogen Cycling, 1385–1444 pp., https://doi.org/10.1016/B978-0-12-372522-6.00032-3, 2008.

Böhlke, J. K., Gwinn, C. J., and Coplen, T. B.: New reference materials for nitrogen-isotope-ratio measurements, Geostand. Newsl., 17, 159–164, 1993.

Böhlke, J. K., Mroczkowski, S. J., and Coplen, T. B.: Oxygen isotopes in nitrate: New reference materials for 18O: 17O: 16O measurements and observations on nitrate-water equilibration., Rapid Commun. Mass Spectrom., 17, 1835–1846, 2003.

Braman, R. S. and Hendrix, S. A.: Nanogram Nitrite and Nitrate Determination in Environmental and Biological Materials by Vanadium(III) Reduction with Chemiluminescence Detection, Anal. Chem., 61, 2715–2718, https://doi.org/10.1021/ac00199a007, 1989.

Brand, L. E.: Minimum iron requirements of marine phytoplankton and the implications for the biogeochemical control of new production, Limnol. Oceanogr., 36, 1756–1771, https://doi.org/10.4319/LO.1991.36.8.1756, 1991.

Cape, M. R., Vernet, M., Kahru, M., and Spreen, G.: Polynya dynamics drive primary production in the Larsen A and B embayments following ice shelf collapse, J. Geophys. Res. Ocean., 119, 572–594, https://doi.org/10.1002/2013JC009441, 2014.

Cassar, N., Wright, S. W., Thomson, P. G., Trull, T. W., Westwood, K. J., De Salas, M., Davidson, A., Pearce, I., Davies, D. M., and Matear, R. J.: The relation of mixed-layer net community production to phytoplankton community composition in the Southern Ocean, Global Biogeochem. Cycles, 29, 446–462, https://doi.org/10.1002/2014GB004936, 2015.

Checkley, D. M. and Miller, C. A.: Nitrogen isotope fractionation by oceanic zooplankton, Deep Sea Res. Part A. Oceanogr. Res. Pap., 36, 1449–1456, https://doi.org/10.1016/0198-0149(89)90050-2, 1989.

Chen, B., Liu, H., Huang, B., and Wang, J.: Temperature effects on the growth rate of marine picoplankton, Mar. Ecol. Prog. Ser., 505, 37–47, https://doi.org/10.3354/MEPS10773, 2014.

Cochlan, W. P. and Bronk, D. A.: Effects of ammonium on nitrate utilization in the Ross Sea, Antarctica: Implications for *f*-ratio estimates, 78, 159–178, https://doi.org/10.1029/078ars10, 2003.

Collier, J. L., Brahamsha, B., and Palenik, B.: The marine cyanobacterium Synechococcus sp. WH7805 requires urease (urea amidohydrolase, EC 3.5.1.5) to utilize urea as a nitrogen source: Molecular-genetic and biochemical analysis of the enzyme, 145, 447–459, https://doi.org/10.1099/13500872-145-2-447/CITE/REFWORKS, 1999.

Costa, R. R., Mendes, C. R. B., Tavano, V. M., Dotto, T. S., Kerr, R., Monteiro, T., Odebrecht, C., and Secchi, E. R.: Dynamics of an intense diatom bloom in the Northern Antarctic Peninsula, February 2016, Limnol. Oceanogr., 65, 2056–2075, https://doi.org/10.1002/LNO.11437, 2020.

Delmont, T. O., Hammar, K. M., Ducklow, H. W., Yager, P. L., and Post, A. F.: Phaeocystis antarctica blooms strongly influence bacterial community structures in the Amundsen Sea polynya, Front. Microbiol., 5, 1–13, https://doi.org/10.3389/fmicb.2014.00646, 2014.

Deniro, M. J. and Epstein, S.: Influence of diet on the distribution of nitrogen isotopes in animals, Geochim. Cosmochim. Acta, 45, 341–351, https://doi.org/10.1016/0016-7037(81)90244-1, 1981.

Diamond, D.: QuikChem Method 10-114-21-1-B: Silicate by flow injection analysis., 1994.

Ditullio, G. R., Grebmeier, J. M., Arrigo, K. R., and Lizotte, M. P.: Rapid and early export of Phaeocystis antarctica blooms in the Ross Sea , Antarctica, 404, 1996–1999, 2000.

Dortch, Q.: The interaction between ammonium and nitrate uptake in phytoplankton, Mar. Ecol. Prog. Ser., 61, 183–201, https://doi.org/10.3354/meps061183, 1990.

Ducklow, H. W., Baker, K., Martinson, D. G., Quetin, L. B., Ross, R. M., Smith, R. C., Stammerjohn, S. E., Vernet, M., and Fraser, W.: Marine pelagic ecosystems: the West Antarctic Peninsula, Philos. Trans. R. Soc. B Biol. Sci., 362, 67–94, https://doi.org/10.1098/RSTB.2006.1955, 2006.

Ducklow, H. W., Fraser, W. R., Meredith, M. P., Stammerjohn, S. E., Doney, S. C., Martinson, D. G., Sailley, S. F., Schofield, O. M., Steinberg, D. K., Venables, H. J., and Amsler, C. D.: West Antarctic peninsula: An ice-dependent coastal marine ecosystem in transition, 26, 190–203, https://doi.org/10.5670/OCEANOG.2013.62, 2013.

Dugdale, R. C. and Goering, J. J.: Uptake of New and Regenerated Forms of Nitrogen in Primary Productivity, Limnol. Oceanogr., 12, 196–206, https://doi.org/10.4319/lo.1967.12.2.0196, 1967.

Dugdale, R. C. and Wilkerson, F. P.: The use of 15N to measure nitrogen uptake in eutrophic experimental considerations1 t2, 3, 1986.

Durand, M. D., Olson, R. J., and Chisholm, S. W.: Phytoplankton population dynamics at the Bermuda Atlantic Time-series station in the Sargasso Sea, Deep Sea Res. Part II Top. Stud. Oceanogr., 48, 1983–2003, https://doi.org/10.1016/S0967-0645(00)00166-1, 2001.

Edwards, K. F., Thomas, M. K., Klausmeier, C. A., and Litchman, E.: Allometric scaling and taxonomic variation in nutrient utilization traits and maximum growth rate of phytoplankton, Limnol. Oceanogr., 57, 554–566, https://doi.org/10.4319/LO.2012.57.2.0554, 2012.

El-Sayed, S. Z. and Taguchi, S.: Primary production and standing crop of phytoplankton along the ice-edge in the Weddell Sea, Deep Sea Res. Part A, Oceanogr. Res. Pap., 28, 1017–1032, https://doi.org/10.1016/0198-0149(81)90015-7, 1981.

Eppley, R. W., Peterson, B.: Particulate organic matter flux and planktonic new production in the deep ocean, Nature, 282, 677–680, 1979.

Fawcett, S. E., Lomas, M. W., Casey, J. R., Ward, B. B., and Sigman, D. M.: Assimilation of upwelled nitrate by small eukaryotes in the Sargasso Sea, Nat. Geosci., 4, 717–722, https://doi.org/10.1038/ngeo1265, 2011a.

Fawcett, S. E., Lomas, M. W., Casey, J. R., Ward, B. B., and Sigman, D. M.: Assimilation of upwelled nitrate by small eukaryotes in the Sargasso Sea, Nat. Geosci., 4, 717–722, https://doi.org/10.1038/ngeo1265, 2011b.

Fawcett, S. E., Lomas, M. W., Ward, B. B., and Sigman, D. M.: Global Biogeochemical Cycles production in the Sargasso Sea, Global Biogeochem. Cycles, 28, 86–102, https://doi.org/10.1002/2013GB004579.Received, 2014.

Ferreira, A., Costa, R. R., Dotto, T. S., Kerr, R., Tavano, V. M., Brito, A. C., Brotas, V., Secchi, E. R., and Mendes, C. R. B.: Changes in Phytoplankton Communities Along the Northern Antarctic Peninsula: Causes, Impacts and Research Priorities, Front. Mar. Sci., 7, https://doi.org/10.3389/fmars.2020.576254, 2020.

Flynn, R. F., Bornman, T. G., Burger, J. M., Smith, S., Spence, K. A. M., and Fawcett, S. E.: Summertime productivity and carbon export potential in the Weddell Sea, with a focus on the waters adjacent to Larsen C Ice Shelf, 18, 6031–6059, https://doi.org/10.5194/BG-18-6031-2021, 2021.

Forrer, H.: Toward an improved understanding of the Southern Ocean ' s biological pump : Phytoplankton group-specific contributions to nitrogen and carbon cycling across the Subantarctic Indian Ocean Supervisor : Dr Sarah Fawcett, 2021.

Francois, R., Bacon, M. P., Altabet, M. A., and Labeyrie, L. D.: Glacial/interglacial changes in sediment rain rate in the SW Indian Sector of subantarctic Waters as recorded by 230Th, 231Pa, U, and δ15N, Paleoceanography, 8, 611–629, https://doi.org/10.1029/93PA00784, 1993.

Fripiat, F., Martínez-García, A., Marconi, D., Fawcett, S., Kopf, S., Luu, V., Rafter, P., Zhang, R., Sigman, D., and Haug, G.: Nitrogen isotopic contraints on nutrient transport to the upper ocean, Nat.

Geosci., 2021.

Fuller, N. J., Marie, D., Partensky, F., Vaulot, D., Post, A. F., and Scanlan, D. J.: Clade-specific 16S ribosomal DNA oligonucleotides reveal the predominance of a single marine synechococcus clade throughout a stratified water column in the red sea, Appl. Environ. Microbiol., 69, 2430–2443, https://doi.org/10.1128/AEM.69.5.2430-2443.2003/ASSET/D086534F-5DC3-4AFA-A316-4F02BC7DB6F3/ASSETS/GRAPHIC/AM0532044007.JPEG, 2003.

Garibotti, I. A., Vernet, M., Smith, R. C., and Ferrario, M. E.: Interannual variability in the distribution of the phytoplankton standing stock across the seasonal sea-ice zone west of the Antarctic Peninsula, J. Plankton Res., 27, 825–843, https://doi.org/10.1093/PLANKT/FBI056, 2005.

Garside, C.: A chemiluminescent technique for the determination of nanomolar concentrations of nitrate and nitrite in seawater, Mar. Chem., 11, 159–167, https://doi.org/10.1016/0304-4203(82)90039-1, 1982.

Glibert, P. M. and Ray, R. T.: Different patterns of growth and nitrogen uptake in two clones of marine Synechococcus spp., Mar. Biol., 107, 273–280, https://doi.org/10.1007/BF01319826/METRICS, 1990.

Glibert, P. M., Kana, T. M., Olson, R. J., Kirchman, D. L., and Alberte, R. S.: Clonal comparisons of growth and photosynthetic responses to nitrogen availability in marine Synechococcus spp, J. Exp. Mar. Bio. Ecol., 101, 199–208, https://doi.org/10.1016/0022-0981(86)90050-X, 1986.

Glover, H. E., Keller, M. D., and Spinrad, R. W.: The effects of light quality and intensity on photosynthesis and growth of marine eukaryotic and prokaryotic phytoplankton clones, J. Exp. Mar. Bio. Ecol., 105, 137–159, https://doi.org/10.1016/0022-0981(87)90168-7, 1987.

Goeyens, L., Tréguer, P., Baumann, M. E. M., Baeyens, W., and Dehairs, F.: The leading role of ammonium in the nitrogen uptake regime of Southern Ocean marginal ice zones, J. Mar. Syst., 6, 345–361, https://doi.org/10.1016/0924-7963(94)00033-8, 1995.

Goeyens, L., Semeneh, M., Baumann, M. E. M., Elskens, M., Shopova, D., and Dehairs, F.: Phytoplanktonic nutrient utilisation and nutrient signature in the Southern Ocean, J. Mar. Syst., 17, 143–157, https://doi.org/10.1016/S0924-7963(98)00035-9, 1998.

Goffart, A., Catalano, G., and Hecq, J. H.: Factors controlling the distribution of diatoms and Phaeocystis in the Ross Sea, J. Mar. Syst., 27, 161–175, https://doi.org/10.1016/S0924-7963(00)00065-8, 2000.

Gonfiantini, R.: Stable isotope reference samples for geochemical and hydrological investigations., Rep. Advis. Group, Vienna., 1984.

Gordon, A. L., Huber, B. A., Hellmer, H. H., & Ffield, A.: Deep and bottom water of the Weddell Sea's western rim., Science (80-.)., 265, 95–97, 1993.

Granger, J., Sigman, D. M., Needoba, J. A., and Harrison, P. J.: Coupled nitrogen and oxygen isotope fractionation of nitrate during assimilation by cultures of marine phytoplankton, Limnol. Oceanogr., 49, 1763–1773, https://doi.org/10.4319/LO.2004.49.5.1763, 2004.

Granger, J., Sigman, D. M., Rohde, M. M., Maldonado, M. T., and Tortell, P. D.: N and O isotope

effects during nitrate assimilation by unicellular prokaryotic and eukaryotic plankton cultures, Geochim. Cosmochim. Acta, 74, 1030–1040, https://doi.org/10.1016/J.GCA.2009.10.044, 2010.

Grasshoff, K.: Methods of seawater analysis, Weinheim and New York: Verlag Chemie, 1976.

Hoch, M. P., Fogel, M. L., and Kirchman, D. L.: Isotope fractionation during ammonium uptake by marine microbial assemblages, 12, 113–127, https://doi.org/10.1080/01490459409377977, 1993.

Holmes, R. M., Aminot, A., Kerouel, R., Hooker, B. A., and Peterson, B. J.: A simple and precise method for measuring ammonium in marine and freshwater ecosystems, https://doi.org/10.1139/cjfas-56-10-1801, 1999.

Huang, K., Ducklow, H., Vernet, M., Cassar, N., and Bender, M. L.: Export production and its regulating factors in the West Antarctica Peninsula region of the Southern Ocean, Global Biogeochem. Cycles, 26, 2005, https://doi.org/10.1029/2010GB004028, 2012.

Hutchinson, K., Deshayes, J., Sallee, J. B., Dowdeswell, J. A., de Lavergne, C., Ansorge, I., Luyt, H., Henry, T., and Fawcett, S. E.: Water Mass Characteristics and Distribution Adjacent to Larsen C Ice Shelf, Antarctica, J. Geophys. Res. Ocean., 125, 0–2, https://doi.org/10.1029/2019JC015855, 2020.

Jacques, G.: Is the concept of new production—regenerated production valid for the Southern Ocean?, Mar. Chem., 35, 273–286, https://doi.org/10.1016/S0304-4203(09)90022-6, 1991.

Juranek, L. W., White, A. E., Dugenne, M., Henderikx Freitas, F., Dutkiewicz, S., Ribalet, F., Ferrón, S., Armbrust, E. V., and Karl, D. M.: The Importance of the Phytoplankton “Middle Class” to Ocean Net Community Production, Global Biogeochem. Cycles, 34, e2020GB006702, https://doi.org/10.1029/2020GB006702, 2020.

Kana, T. M. and Glibert, P. M.: Effect of irradiances up to 2000 μE m-2 s-1 on marine Synechococcus WH7803-I. Growth, pigmentation, and cell composition, Deep Sea Res. Part A, Oceanogr. Res. Pap., 34, 479–495, https://doi.org/10.1016/0198-0149(87)90001-X, 1987.

Karsh, K. L., Trull, T. W., Lourey, M. J., and Sigman, D. M.: Relationship of nitrogen isotope fractionation to phytoplankton size and iron availability during the Southern Ocean Iron RElease Experiment (SOIREE), Limnol. Oceanogr., 48, 1058–1068, https://doi.org/10.4319/lo.2003.48.3.1058, 2003.

Karsh, K. L., Trull, T. W., Sigman, D. M., Thompson, P. A., and Granger, J.: The contributions of nitrate uptake and efflux to isotope fractionation during algal nitrate assimilation, Geochim. Cosmochim. Acta, 132, 391–412, https://doi.org/10.1016/j.gca.2013.09.030, 2014.

Keffer, T. and Holloway, G.: Estimating Southern Ocean eddy flux of heat and salt from satellite altimetry, Nature, 332, 624–626, https://doi.org/10.1038/332624a0, 1988.

Kerr, R., Mata, M. M., Mendes, C. R. B., and Secchi, E. R.: Northern Antarctic Peninsula: a marine climate hotspot of rapid changes on ecosystems and ocean dynamics, Deep. Res. Part II Top. Stud. Oceanogr., 149, 4–9, https://doi.org/10.1016/j.dsr2.2018.05.006, 2018.

Klunder, M. B., Laan, P., Middag, R., De Baar, H. J. W., and van Ooijen, J. C.: Dissolved iron in the Southern Ocean (Atlantic sector), Deep. Res. Part II Top. Stud. Oceanogr., 58, 2678–2694,

https://doi.org/10.1016/j.dsr2.2010.10.042, 2011.

Klunder, M. B., Laan, P., De Baar, H. J. W., Middag, R., Neven, I., and Van Ooijen, J.: Dissolved Fe across the Weddell Sea and Drake Passage: Impact of DFe on nutrient uptake, 11, 651–669, https://doi.org/10.5194/bg-11-651-2014, 2014.

Knapp, A. N., Sigman, D. M., and Lipschultz, F.: N isotopic composition of dissolved organic nitrogen and nitrate at the Bermuda Atlantic Time-series Study site, Global Biogeochem. Cycles, 19, 1–15, https://doi.org/10.1029/2004GB002320, 2005.

Koike, I., Holm-Hansen, O., and Biggs, D.: Inorganic nitrogen metabolism by Antarctic phytoplankton with special reference to ammonium cycling, Mar. Ecol. Prog. Ser., 30, 105–116, https://doi.org/10.3354/meps030105, 1986.

Lannuzel, D., Schoemann, V., de Jong, J., Chou, L., Delille, B., Becquevort, S., and Tison, J. L.: Iron study during a time series in the western Weddell pack ice, Mar. Chem., 108, 85–95, https://doi.org/10.1016/j.marchem.2007.10.006, 2008.

Leblanc, K., Arístegui, J., Armand, L., Assmy, P., Beker, B., Bode, A., Breton, E., Cornet, V., Gibson, J., Gosselin, M. P., Kopczynska, E., Marshall, H., Peloquin, J., Piontkovski, S., Poulton, A. J., Quéguiner, B., Schiebel, R., Shipe, R., Stefels, J., Van Leeuwe, M. A., Varela, M., Widdicombe, C., and Yallop, M.: A global diatom database- A bundance, biovolume and biomass in the world ocean, Earth Syst. Sci. Data, 4, 149–165, https://doi.org/10.5194/ESSD-4-149-2012, 2012.

Leblanc, K., Quéguiner, B., Diaz, F., Cornet, V., Michel-Rodriguez, M., Durrieu De Madron, X., Bowler, C., Malviya, S., Thyssen, M., Grégori, G., Rembauville, M., Grosso, O., Poulain, J., De Vargas, C., Pujo-Pay, M., and Conan, P.: Nanoplanktonic diatoms are globally overlooked but play a role in spring blooms and carbon export, Nat. Commun. 2018 91, 9, 1–12, https://doi.org/10.1038/s41467-018-03376-9, 2018.

Li, W. K. W. and Dickie, P. M.: Monitoring Phytoplankton, Bacterioplankton, and Virioplankton in a Coastal Inlet (Bedford Basin) by Flow Cytometry, https://doi.org/10.1002/1097-0320(20010701)44:3<236::AID-CYTO1116>3.0.CO;2-5, 2001.

Lin, Y., Cassar, N., Marchetti, A., Moreno, C., Ducklow, H., and Li, Z.: Specific eukaryotic plankton are good predictors of net community production in the Western Antarctic Peninsula, Sci. Reports 2017 71, 7, 1–11, https://doi.org/10.1038/s41598-017-14109-1, 2017.

Lindell, D. and Post, A. F.: Ecological Aspects of ntcA Gene Expression and Its Use as an Indicator of the Nitrogen Status of Marine Synechococcus spp., Appl. Environ. Microbiol., 67, 3340–3349, https://doi.org/10.1128/AEM.67.8.3340-3349.2001/ASSET/DAB3DEE9-DB5F-4E2D-8676-112B2C13E39E/ASSETS/GRAPHIC/AM0810457008.JPEG, 2001.

Lindell, D., Padan, E., and Post, A. F.: Regulation of ntcA expression and nitrite uptake in the marine Synechococcus sp. strain WH 7803, J. Bacteriol., 180, 1878–1886, https://doi.org/10.1128/JB.180.7.1878-1886.1998/ASSET/17649FC6-11C6-4B93-947D-1C90A344D2A4/ASSETS/GRAPHIC/JB0781268009.JPEG, 1998.

Liu, K. K., Kao, S. J., Chiang, K. P., Gong, G. C., Chang, J., Cheng, J. S., and Lan, C. Y.: Concentration dependent nitrogen isotope fractionation during ammonium uptake by phytoplankton under an algal bloom condition in the Danshuei estuary, northern Taiwan, Mar. Chem., 157, 242–252, https://doi.org/10.1016/J.MARCHEM.2013.10.005, 2013.

Lomas, M. W. and Glibert, P. M.: Interactions between NH4/+ and NO3/- uptake and assimilation: Comparison of diatoms and dinoflagellates at several growth temperatures, Mar. Biol., 133, 541–551, https://doi.org/10.1007/s002270050494, 1999.

Lourey, M. J., Trull, T. W., and Sigman, D. M.: Sensitivity of δ15N of nitrate, surface suspended and deep sinking particulate nitrogen to seasonal nitrate depletion in the Southern Ocean, Global Biogeochem. Cycles, 17, 1–18, https://doi.org/10.1029/2002gb001973, 2003.

Macko, S. A., Estep, M. L. F., Engel, M. H., and Hare, P. E.: Kinetic fractionation of stable nitrogen isotopes during amino acid transamination, Geochim. Cosmochim. Acta, 50, 2143–2146, https://doi.org/10.1016/0016-7037(86)90068-2, 1986.

Marie, D., Pierre, U., Curie, M., Simon, N., and Vaulot, D.: Algae Culturing Techniques Chapter 17: Phytoplankton Cell Counting by Flow Cytometry, 1–15, 2005.

Mariotti, A., Germon, J. C., Hubert, P., Kaiser, P., Letolle, R., Tardieux, A., and Tardieux, P.: Experimental determination of nitrogen kinetic isotope fractionation: Some principles; illustration for the denitrification and nitrification processes, Plant Soil, 62, 413–430, https://doi.org/10.1007/BF02374138/METRICS, 1981.

Martin, J. H., Gordon, R. M., and Fitzwater, S. E.: Iron Limitation, Limnol. Oceanogr., 36, 1793–1802, 1991.

Mcilvin, M. R. and Casciotti, K. L.: Fully automated system for stable isotopic analyses of dissolved nitrous oxide at natural abundance levels, Limnol. Oceanogr. Methods, 8, 54–66, https://doi.org/10.4319/LOM.2010.8.54, 2010.

McIlvin, M. R. and Altabet, M. A.: Chemical conversion of nitrate and nitrite to nitrous oxide for nitrogen and oxygen isotopic analysis in freshwater and seawater, Anal. Chem., 77, 5589–5595, https://doi.org/10.1021/AC050528S, 2005.

Mendes, C. R. B., de Souza, M. S., Garcia, V. M. T., Leal, M. C., Brotas, V., and Garcia, C. A. E.: Dynamics of phytoplankton communities during late summer around the tip of the Antarctic Peninsula, Deep. Res. Part I Oceanogr. Res. Pap., 65, 1–14, https://doi.org/10.1016/j.dsr.2012.03.002, 2012.

Mendes, C. R. B., Tavano, V. M., Leal, M. C., de Souza, M. S., Brotas, V., and Garcia, C. A. E.: Shifts in the dominance between diatoms and cryptophytes during three late summers in the Bransfield Strait (Antarctic Peninsula), Polar Biol., 36, 537–547, https://doi.org/10.1007/s00300-012-1282-4, 2013.

Mendes, C. R. B., Tavano, V. M., Kerr, R., Dotto, T. S., Maximiano, T., and Secchi, E. R.: Impact of sea ice on the structure of phytoplankton communities in the northern Antarctic Peninsula, Deep. Res. Part II Top. Stud. Oceanogr., 149, 111–123, https://doi.org/10.1016/j.dsr2.2017.12.003, 2018a.

Mendes, C. R. B., Tavano, V. M., Dotto, T. S., Kerr, R., de Souza, M. S., Garcia, C. A. E., and Secchi,

E. R.: New insights on the dominance of cryptophytes in Antarctic coastal waters: A case study in Gerlache Strait, Deep. Res. Part II Top. Stud. Oceanogr., 149, 161–170, https://doi.org/10.1016/j.dsr2.2017.02.010, 2018b.

Mendes, C. R. B., Costa, R. R., Ferreira, A., Jesus, B., Tavano, V. M., Dotto, T. S., Leal, M. C., Kerr, R., Islabão, C. A., Franco, A. de O. da R., Mata, M. M., Garcia, C. A. E., and Secchi, E. R.: Cryptophytes: an emerging algal group in the rapidly changing Antarctic Peninsula marine environments, Glob. Chang. Biol., https://doi.org/10.1111/GCB.16602, 2023.

Möbius, J.: Isotope fractionation during nitrogen remineralization (ammonification): Implications for nitrogen isotope biogeochemistry, Geochim. Cosmochim. Acta, 105, 422–432, https://doi.org/10.1016/J.GCA.2012.11.048, 2013.

Moisan, T. A. and Mitchell, B. G.: Photophysiological acclimation of Phaeocystis antarctica Karsten under light limitation, Limnol. Oceanogr., 44, 247–258, https://doi.org/10.4319/LO.1999.44.2.0247, 1999.

Montes-Hugo, M., Doney, S. C., Ducklow, H. W., Fraser, W., Martinson, D., Stammerjohn, S. E., and Schofield, O.: Recent changes in phytoplankton communities associated with rapid regional climate change along the western Antarctic Peninsula, Science (80-.)., 323, 1470–1473, https://doi.org/10.1126/SCIENCE.1164533/SUPPL_FILE/MONTES-HUGO_SOM.PDF, 2009.

Montoya, J. P.: Nitrogen Stable Isotopes in Marine Environments, Nitrogen Mar. Environ., 1277–1302, https://doi.org/10.1016/B978-0-12-372522-6.00029-3, 2008.

Moore, L. R., Rocap, G., and Chisholm, S. W.: Physiology and molecular phylogeny of coexisting Prochlorococcus ecotypes, Nat. 1998 3936684, 393, 464–467, https://doi.org/10.1038/30965, 1998.

Moore, L. R., Post, A. F., Rocap, G., and Chisholm, S. W.: Utilization of different nitrogen sources by the marine cyanobacteria Prochlorococcus and Synechococcus, Limnol. Oceanogr., 47, 989–996, https://doi.org/10.4319/LO.2002.47.4.0989, 2002.

Muench, R. D. and Gordon, A. L.: Circulation and transport of water along the western Weddell Sea margin, J. Geophys. Res., 100, 18503–18515, https://doi.org/10.1029/95jc00965, 1995.

Myung Gil, P., Sung Ryull, T., Sung-Ho, K., Kyung Ho, C., and Jae Hyung, S.: Phytoplankton biomass and primary production in the marginal ice zone of the northwestern Weddell Sea during austral summer, Polar Biol., 21, 251–261, 1999.

Needoba, J. A., Sigman, D. M., and Harrison, P. J.: THE MECHANISM OF ISOTOPE FRACTIONATION DURING ALGAL NITRATE ASSIMILATION AS ILLUMINATED BY THE 15 N/ 14 N OF INTRACELLULAR NITRATE 1, J. Phycol, 40, 517–522, https://doi.org/10.1111/j.1529-8817.2004.03172.x, 2004.

Nicholls, K. W., Pudsey, C. J., and Morris, P.: Summertime water masses off the northern Larsen C Ice Shelf, Antarctica, Geophys. Res. Lett., 31, 2–5, https://doi.org/10.1029/2004GL019924, 2004.

Nissen, C. and Vogt, M.: Factors controlling the competition between <i>Phaeocystis</i> and diatoms in the Southern Ocean and implications for carbon export fluxes, 18, 251–283,

https://doi.org/10.5194/BG-18-251-2021, 2021.

Van Oostende, N., Fawcett, S. E., Marconi, D., Lueders-Dumont, J., Sabadel, A. J. M., Woodward, E. M. S., Jönsson, B. F., Sigman, D. M., and Ward, B. B.: Variation of summer phytoplankton community composition and its relationship to nitrate and regenerated nitrogen assimilation across the North Atlantic Ocean, Deep Sea Res. Part I Oceanogr. Res. Pap., 121, 79–94, https://doi.org/10.1016/J.DSR.2016.12.012, 2017a.

Van Oostende, N., Fawcett, S. E., Marconi, D., Lueders-Dumont, J., Sabadel, A. J. M., Woodward, E. M. S., Jönsson, B. F., Sigman, D. M., and Ward, B. B.: Variation of summer phytoplankton community composition and its relationship to nitrate and regenerated nitrogen assimilation across the North Atlantic Ocean, Deep. Res. Part I Oceanogr. Res. Pap., https://doi.org/10.1016/j.dsr.2016.12.012, 2017b.

Paerl, H. W.: Ecophysiological and Trophic Implications of Light-Stimulated Amino Acid Utilization in Marine Picoplankton, Appl. Environ. Microbiol., 57, 473–479, https://doi.org/10.1128/AEM.57.2.473-479.1991, 1991.

Pakhomov, E. A., Froneman, P. W., and Perissinotto, R.: Salp/krill interactions in the Southern Ocean: spatial segregation and implications for the carbon flux, Deep Sea Res. Part II Top. Stud. Oceanogr., 49, 1881–1907, https://doi.org/10.1016/S0967-0645(02)00017-6, 2002.

Partensky, F., Blanchot, J., and Vaulot, D.: DifferentiaI distribution and ecology of Prochlorococcus and Synechococcus in oceanic waters: a review, Bull. l'Institut océanographique, 1999.

Paulsen, M. L., Riisgaard, K., Thingstad, T. F., John, M. S., and Nielsen, T. G.: Winter-spring transition in the subarctic Atlantic: Microbial response to deep mixing and pre-bloom production., Aquat. Microb. Ecol., 76, 49–49, 2015.

Pennock, J. R., Velinsky, D. J., Ludlam, J. M., Sharp, J. H., and Fogel, M. L.: Isotopic fractionation of ammonium and nitrate during uptake by Skeletonema costatum: Implications for δ15N dynamics under bloom conditions, Limnol. Oceanogr., 41, 451–459, https://doi.org/10.4319/LO.1996.41.3.0451, 1996.

Petrou, K., Kranz, S. A., Trimborn, S., Hassler, C. S., Ameijeiras, S. B., Sackett, O., Ralph, P. J., and Davidson, A. T.: Southern Ocean phytoplankton physiology in a changing climate, J. Plant Physiol., 203, 135–150, https://doi.org/10.1016/j.jplph.2016.05.004, 2016.

Phillips, B., Kremer, P., and Madin, L. P.: Defecation by Salpa thompsoni and its contribution to vertical flux in the Southern Ocean, Mar. Biol., 156, 455–467, https://doi.org/10.1007/S00227-008-1099-4/TABLES/7, 2009.

Pörtner, H. O., Karl, D. M., Boyd, P. W., Cheung, W. W., Lluch-Cota, S. E., Nojiri, Y., and Et, A.: Ocean systems, in: Impacts, Adaptation, and Vulnerability. Part A: Global and Sectoral Aspects. Contribution of Working Group II to the Fifth Assessment Report of the Intergovernmental Panel on Climate Change, edited by: Field, C. B. and Et, A., Cambridge University Press, 411–484, 2014.

Prezelinl, B. B., Glover2, H. E., Hovenl, D., and Steinbergl, H. A. ~: Blue-green light effects on light-limited rates of photosynthesis: relationship to pigmentation and productivity estimates for

Synechococcus populations from the Sargasso Sea, 54, 121–136, 1989.

Priddle, J., Boyd, I. L., Whitehouse, M. J., Murphy, E. J., and Croxall, J. P.: Estimates of Southern Ocean primary production - Constraints from predator carbon demand and nutrient drawdown, in: Journal of Marine Systems, 275–288, https://doi.org/10.1016/S0924-7963(98)00043-8, 1998.

Probyn, T. A. and Painting, S. J.: Nitrogen uptake by size-fractionated phytoplankton populations in Antarctic surface waters1, Limnol. Oceanogr., 30, 1327–1332, https://doi.org/10.4319/LO.1985.30.6.1327, 1985.

Qi, H., Coplen, T. B., Geilmann, H., Brand, W. A., and Böhlke, J. K.: Two new organic reference materials for δ13C and δ15N measurements and a new value for the δ13C of NBS 22 oil, Rapid Commun. Mass Spectrom., 17, 2483–2487, https://doi.org/10.1002/RCM.1219, 2003.

RAVEN, J. A.: Predictions of Mn and Fe use efficiencies of phototrophic growth as a function of light availability for growth and of C assimilation pathway, New Phytol., 116, 1–18, https://doi.org/10.1111/J.1469-8137.1990.TB00505.X, 1990.

Revilla, M., Alexander, J., and Glibert, P. M.: Urea analysis in coastal waters: Comparison of enzymatic and direct methods, Limnol. Oceanogr. Methods, 3, 290–299, https://doi.org/10.4319/lom.2005.3.290, 2005.

Rodríguez, J., Jiménez-Gómez, F., Blanco, J. M., and Figueroa, F. L.: Physical gradients and spatial variability of the size structure and composition of phytoplankton in the Gerlache Strait (Antarctica), Deep Sea Res. Part II Top. Stud. Oceanogr., 49, 693–706, https://doi.org/10.1016/S0967-0645(01)00119-9, 2002.

Saba, G. K., Fraser, W. R., Saba, V. S., Iannuzzi, R. A., Coleman, K. E., Doney, S. C., Ducklow, H. W., Martinson, D. G., Miles, T. N., Patterson-Fraser, D. L., Stammerjohn, S. E., Steinberg, D. K., and Schofield, O. M.: Winter and spring controls on the summer food web of the coastal West Antarctic Peninsula, Nat. Commun. 2014 51, 5, 1–8, https://doi.org/10.1038/ncomms5318, 2014.

Sallée, J. B., Shuckburgh, E., Bruneau, N., Meijers, A. J., Bracegirdle, T. J., and Wang, Z.: Assessment of Southern Ocean mixed-layer depths in CMIP5 models: Historical bias and forcing response, J. Geophys. Res. Ocean., 118, 1845–1862, 2013.

Sarmiento, J., Toggweiler, J.: A new model for the role of the oceans in determining atmospheric P CO2., Nature, 308, 621–624, https://doi.org/https://doi.org/10.1038/308621a0, 1984.

Sarmiento, J. L., Gruber, N., Brzezinski, M. A., and Dunne, J. P.: High-latitude controls of thermocline nutrients and low latitude biological productivity, Nature, 427, 56–60, https://doi.org/10.1038/nature10605, 2004.

Saxberg, B. E. H. and Kowalski, B. R.: Generalized Standard Addition Method, Anal. Chem., 51, 1031–1038, https://doi.org/10.1021/ac50043a059, 1979.

Schodlok, M. P., Hellmer, H. H., and Beckmann, A.: On the transport, variability and origin of dense water masses crossing the South Scotia Ridge, Deep. Res. Part II Top. Stud. Oceanogr., 49, 4807–4825, https://doi.org/10.1016/S0967-0645(02)00160-1, 2002.

Schoemann, V., Becquevort, S., Stefels, J., Rousseau, V., and Lancelot, C.: Phaeocystis blooms in the global ocean and their controlling mechanisms: a review, J. Sea Res., 53, 43–66, https://doi.org/10.1016/j.seares.2004.01.008, 2005.

Schofield, O., Miles, T., Alderkamp, A. C., Lee, S. H., Haskins, C., Rogalsky, E., Sipler, R., Sherrell, R. M., and Yager, P. L.: In situ phytoplankton distributions in the Amundsen Sea Polynya measured by autonomous gliders, 3, 1–17, https://doi.org/10.12952/journal.elementa.000073, 2015.

Schröder, M., Hellmer, H. H., & Absy, J. M.: On the near-bottom variability in the northwestern Weddell Sea., Deep. Res. Part II Top. Stud. Oceanogr., 49, 4767–4790, 2002.

Semeneh, M., Dehairs, F., Fiala, M., Elskens, M., and Goeyens, L.: Seasonal variation of phytoplankton community structure and nitrogen uptake regime in the Indian Sector of the Southern Ocean, Polar Biol., 20, 259–272, https://doi.org/10.1007/s003000050302, 1998.

Sigman, D. M. and Boyle[2], E. A.: Glacial/interglacial variations in atmospheric carbon dioxide, NATURE, 2000.

Sigman, D. M. and Fripiat, F.: Nitrogen isotopes in the ocean, in: Encyclopedia of Ocean Sciences, Elsevier Inc., 263–278, https://doi.org/10.1016/B978-0-12-409548-9.11605-7, 2019.

Sigman, D. M., Bernard, C., Hastings, M. G., Sigman, D. M., Casciotti, K. L., Andreani, M., Barford, C., Galanter, M., and Bo, J. K.: A Bacterial Method for the Nitrogen Isotopic Analysis of Nitrate in Seawater and Freshwater A Bacterial Method for the Nitrogen Isotopic Analysis of Nitrate in Seawater and Freshwater, 73, 4145–4153, https://doi.org/10.1021/ac010088e, 2001.

Sigman, D. M., Hain, M. P., and Haug, G. H.: The polar ocean and glacial cycles in atmospheric CO 2 concentration, https://doi.org/10.1038/nature09149, 2010.

Sigman, O. M., Altabet, M. A., McCorkle, D. C., Francois, R., and Fischer, G.: The δ15N of nitrate in the southern ocean: Consumption of nitrate in surface waters, Global Biogeochem. Cycles, 13, 1149–1166, https://doi.org/10.1029/1999GB900038, 1999.

Silfer, J. A., Engel, M. H., and Macko, S. A.: Kinetic fractionation of stable carbon and nitrogen isotopes during peptide bond hydrolysis: Experimental evidence and geochemical implications, Chem. Geol. Isot. Geosci. Sect., 101, 211–221, https://doi.org/10.1016/0009-2541(92)90003-N, 1992.

Smart, S. M., Fawcett, S. E., Ren, H., Schiebel, R., Tompkins, E. M., Martínez-García, A., Stirnimann, L., Roychoudhury, A., Haug, G. H., and Sigman, D. M.: The Nitrogen Isotopic Composition of Tissue and Shell-Bound Organic Matter of Planktic Foraminifera in Southern Ocean Surface Waters, Geochemistry, Geophys. Geosystems, 21, e2019GC008440, https://doi.org/10.1029/2019GC008440, 2020.

Smetacek, V., Assmy, P., and Henjes, J.: The role of grazing in structuring Southern Ocean pelagic ecosystems and biogeochemical cycles, Antarct. Sci., 16, 541–558, https://doi.org/10.1017/S0954102004002317, 2004.

Smith, W. 0. and Nelson, D. M.: Phytoplankton growth and new production in the Weddell Sea marginal ice zone in the austral spring and autumn, Limnol. Oceanogr., 35, 809–821,

https://doi.org/10.4319/lo.1990.35.4.0809, 1990.
Sommer, U.: The paradox of the plankton: Fluctuations of phosphorus availability maintain diversity of phytoplankton in flow-through cultures1, Limnol. Oceanogr., 29, 633–636, https://doi.org/10.4319/LO.1984.29.3.0633, 1984.
Stammerjohn, S., Massom, R., Rind, D., and Martinson, D.: Regions of rapid sea ice change: An inter-hemispheric seasonal comparison, Geophys. Res. Lett., 39, L06501, 2012.
Stefels, J. and Van Leeuwe, M. A.: Effects of iron and light stress on the biochemical composition of antarctic Phaeocystis sp. (Prymnesiophyceae). I. Intracellular DMSP concentrations, J. Phycol., 34, 486–495, https://doi.org/10.1046/j.1529-8817.1998.340486.x, 1998.
Steig, E. J., Schneider, D. P., Rutherford, S. D., Mann, M. E., Comiso, J. C., and Shindell, D. T.: Warming of the Antarctic ice-sheet surface since the 1957 International Geophysical Year, Nat. 2009 4577228, 457, 459–462, https://doi.org/10.1038/nature07669, 2009.
Strzepek, R. F., Maldonado, M. T., Hunter, K. A., Frew, R. D., and Boyd, P. W.: Adaptive strategies by Southern Ocean phytoplankton to lessen iron limitation: Uptake of organically complexed iron and reduced cellular iron requirements, Limnol. Oceanogr., 56, 1983–2002, https://doi.org/10.4319/lo.2011.56.6.1983, 2011.
Sunda, W. G. and Huntsman, S. A.: Interrelated influence of iron, light and cell size on marine phytoplankton growth, Nature, 390, 389–392, https://doi.org/10.1038/37093, 1997.
Sunda, W. G. and Huntsman, S. A.: High iron requirement for growth, photosynthesis, and low-light acclimation in the coastal cyanobacterium Synechococcus bacillaris, Front. Microbiol., 6, 561, 2015.
Talley, L. D., Pickard, G. L., Emery, W. J., and Swift, J. H.: Southern Ocean, Descr. Phys. Oceanogr., 437–471, https://doi.org/10.1016/b978-0-7506-4552-2.10013-7, 2011.
Tréguer, P., Bowler, C., Moriceau, B., Dutkiewicz, S., Gehlen, M., Aumont, O., Bittner, L., Dugdale, R., Finkel, Z., Iudicone, D., Jahn, O., Guidi, L., Lasbleiz, M., Leblanc, K., Levy, M., and Pondaven, P.: Influence of diatom diversity on the ocean biological carbon pump, Nat. Geosci., https://doi.org/10.1038/s41561-017-0028-x, 2017.
Treibergs, L. A., Fawcett, S. E., Lomas, M. W., and Sigman, D. M.: Nitrogen isotopic response of prokaryotic and eukaryotic phytoplankton to nitrate availability in Sargasso Sea surface waters, Limnol. Oceanogr., 59, 972–985, https://doi.org/10.4319/lo.2014.59.3.0972, 2014.
Trimborn, S., Hoppe, C. J. M., Taylor, B. B., Bracher, A., and Hassler, C.: Physiological characteristics of open ocean and coastal phytoplankton communities of Western Antarctic Peninsula and Drake Passage waters, Deep Sea Res. Part I Oceanogr. Res. Pap., 98, 115–124, https://doi.org/10.1016/J.DSR.2014.12.010, 2015.
Trull, T., Rintoul, S. R., Hadfield, M., and Abraham, E. R.: Circulation and seasonal evolution of polar waters south of Australia: implications for iron fertilization of the Southern Ocean, Deep Sea Res. Part II Top. Stud. Oceanogr., 48, 2439–2466, https://doi.org/10.1016/S0967-0645(01)00003-0, 2001.
Tsai, A. Y., Chiang, K. P., Chang, J., and Gong, G. C.: Seasonal variations in trophic dynamics of

nanoflagellates and picoplankton in coastal waters of the western subtropical Pacific Ocean, Aquat. Microb. Ecol., 51, 263–274, https://doi.org/10.3354/AME01196, 2008.
Vernet, M., Martinson, D., Iannuzzi, R., Stammerjohn, S., Kozlowski, W., Sines, K., Smith, R., and Garibotti, I.: Primary production within the sea-ice zone west of the Antarctic Peninsula: I—Sea ice, summer mixed layer, and irradiance, Deep Sea Res. Part II Top. Stud. Oceanogr., 55, 2068–2085, https://doi.org/10.1016/J.DSR2.2008.05.021, 2008.
Vernet, M., Geibert, W., Hoppema, M., Brown, P. J., Haas, C., Hellmer, H. H., Jokat, W., Jullion, L., Mazloff, M., Bakker, D. C. E., Brearley, J. A., Croot, P., Hattermann, T., Hauck, J., Hillenbrand, C. D., Hoppe, C. J. M., Huhn, O., Koch, B. P., Lechtenfeld, O. J., Meredith, M. P., Naveira Garabato, A. C., Nöthig, E. M., Peeken, I., Rutgers van der Loeff, M. M., Schmidtko, S., Schröder, M., Strass, V. H., Torres-Valdés, S., and Verdy, A.: The Weddell Gyre, Southern Ocean: Present Knowledge and Future Challenges, Rev. Geophys., 57, 623–708, https://doi.org/10.1029/2018RG000604, 2019.
Wilhelm, S. W., Maxwell, D. P., and Trick, C. G.: Growth, iron requirements, and siderophore production in iron-limited Synechococcus PCC 72, Limnol. Oceanogr., 41, 89–97, https://doi.org/10.4319/LO.1996.41.1.0089, 1996.
Zhang, L., Altabet, M. A., Wu, T., and Hadas, O.: Sensitive measurement of NH4+15N/ 14N (δ15NH4+) at natural abundance levels in fresh and saltwaters, Anal. Chem., 79, 5297–5303, https://doi.org/10.1021/AC070106D/SUPPL_FILE/AC070106DSI20070611_103247.PDF, 2007.

Appendix C: Phytoplankton group-specific contributions to carbon export potential across the summertime Weddell Sea

C1: Flow cytometric identification of phytoplankton populations

Flow cytometry was used to identify and sort phytoplankton groups (<20 μm) at all stations across the summertime Weddell Sea (Fig. 4.1, C1 and C2). The phytoplankton populations were identified as per Chapter 3 (appendix B), however, because we could only sort four populations synchronously, and given that we needed to sort enough cells to make a robust nitrogen (N) isotope measurement (i.e., at least 3 nmoles of N), some of the populations identified in Chapter 3 (Fig. B1) were combined for sorting purposes. The populations Syn 1 and Syn 2 were grouped as one large *Synechococcus* population, and NanoEuk 1 and MicroEuk were grouped together and reclassified as cryptophytes, noting that the number of MicroEuk cells (i.e., cells ≥20 μm) was at least two orders of magnitude lower than that of NanoEuk 1 (Fig. C1 and C2).

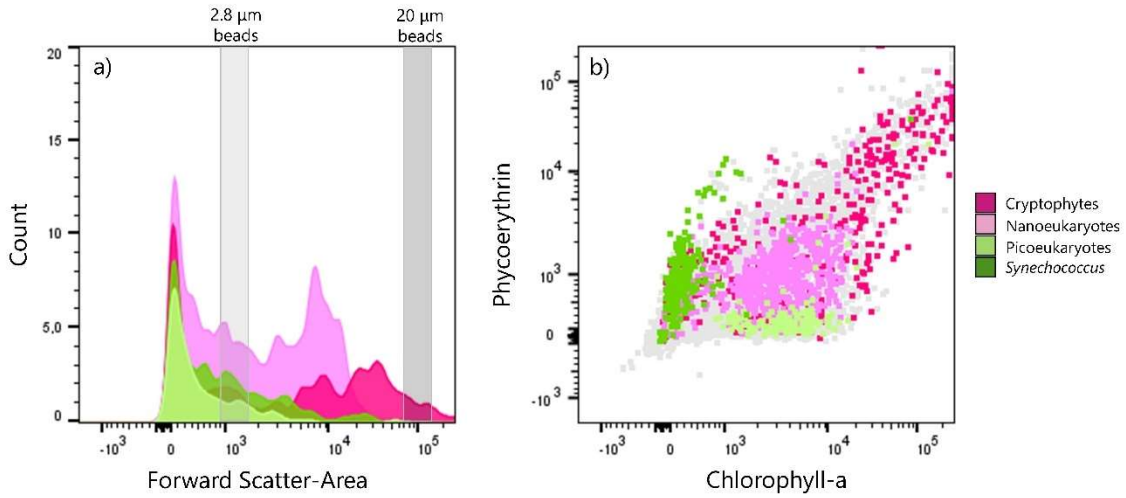


Figure C1. Example (a) histogram of relative cell size as inferred from forward scatter area (FSC-A) and (b) cytogram of phycoerythrin (PE) (i.e., orange) fluorescence versus chlorophyll *a* (i.e., red) fluorescence, showing the Weddell Sea populations that were identified using flow cytometry. The populations identified the include: *Synechococcus*, picoeukaryotes, nanoeukaryotes and cryptophytes. The grey vertical bars in panel (a) indicate the FSC-A of the 2.8 µm (light grey) and 20 µm beads (dark grey). The grey data in panel (b) show background noise and detritus.

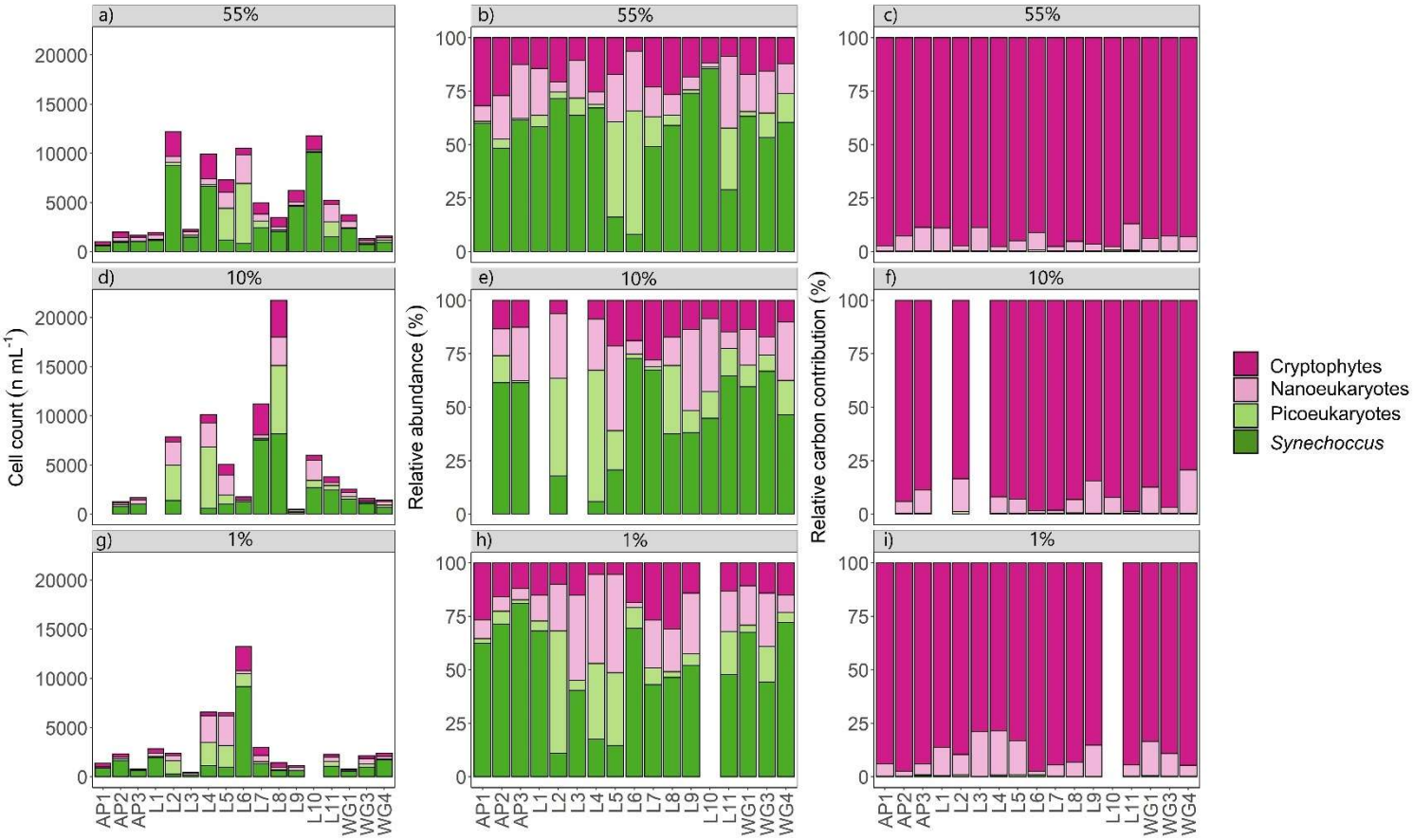


Figure C2. The (a,d,g) cell counts, (b,e,h) relative abundance and (c,f,i) relative carbon contribution of all phytoplankton groups identified via flow cytometric analysis at the 55% (surface; a-c), 10% (d-f) and 1% (base of the euphotic zone; g-i) light levels. The stations are labelled on the x-axis. Where there are no bars in panels (d-i), no data are available. The carbon biomass estimates in panels (c,f,i) were calculated using the average biovolume of each group (Flynn et al., 2021) and converted to particulate organic carbon (POC) using phytoplankton group-specific carbon conversion factors (Table 4.2).

C2: Size-fractionated rates of N uptake

Size-fractionated rates of nitrogen (N; as nitrate (NO_3^-), ammonium (NH_4^+) and urea) uptake were conducted at seven of the 17 fluorescence-activated cell sorting (FACS) stations (Fig. 4.1 insert (red outlined symbols) and C3). Throughout the euphotic zone, nanoplankton dominated N uptake, however, their relative contribution decreased between the surface (average contribution of 70 ± 24%) and the base of the euphotic zone (Z_{eu}; average contribution of 62 ± 20% at the 1% light level). This is somewhat consistent with the flow cytometry data, whereby the contribution of the nanoplankton (predominantly cryptophytes) to biomass decreased between the surface and Z_{eu}. This is likely due to the cryptophytes outcompeting the other phytoplankton groups within the surface, due to the inhibiting effect of high light on the other phytoplankton groups, which was reduced with depth, allowing for increased competition for resources among the different groups.

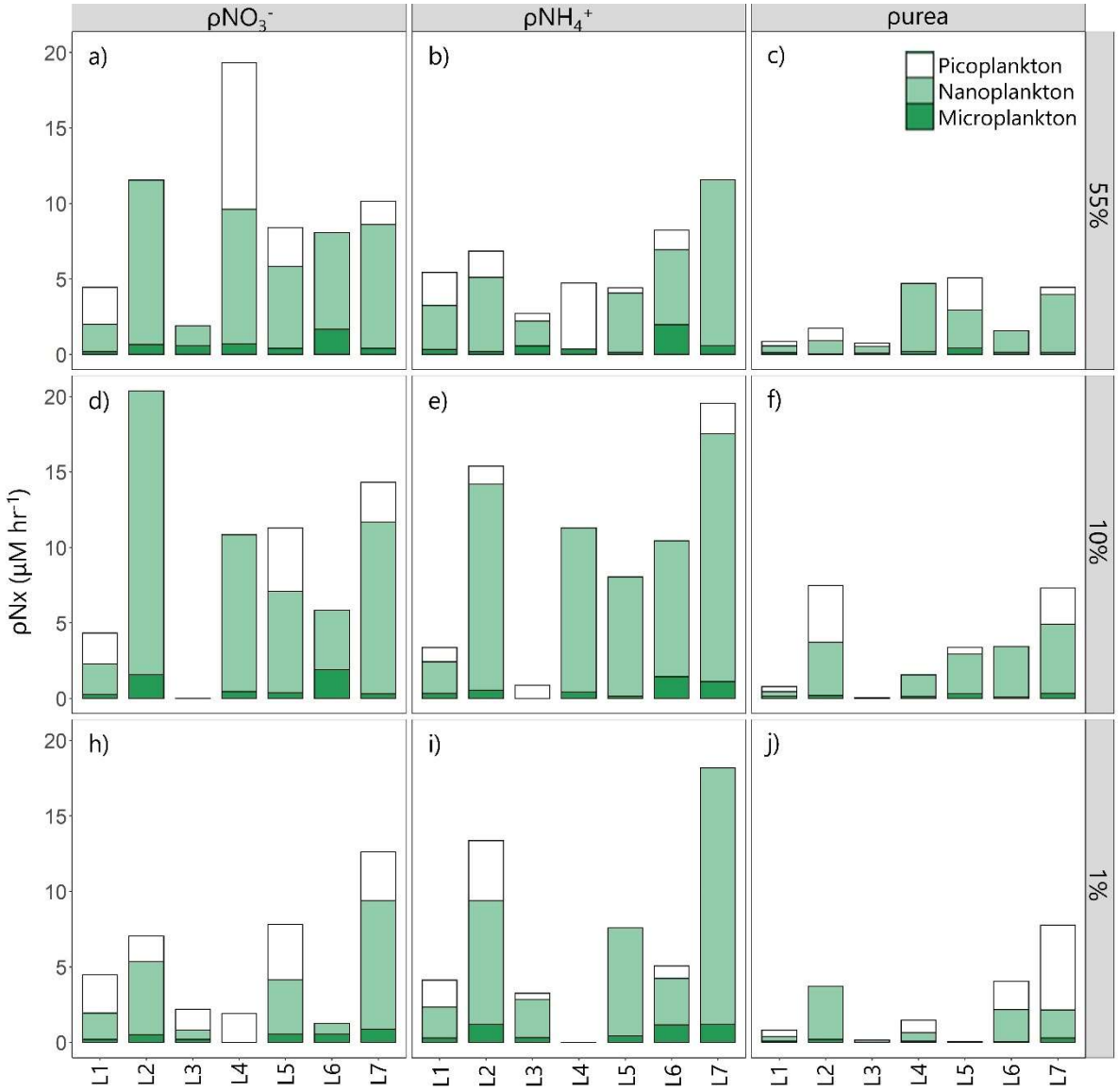


Figure C3. Size-fractionates rates of (a,d,h) nitrate uptake (ρNO_3^-), (b,e,i) ammonium uptake (ρNH_4^+) and (c,f.j) urea uptake (ρurea) throughout the euphotic zone. The stations are labelled on the x-axis and the euphotic zone depth on the y-axis. The different shading the different size-classes (white – picoplankton, opaque – nanoplankton, solid colour – microplankton).

Chapter 5: Conclusions and implications

Each data chapter (Chapters 2 through 4) of this thesis includes a detailed conclusions and implications section pertaining to the research presented therein. This concluding chapter will therefore not repeat these conclusions and implications in detail, but rather offer a summary of the main findings of this thesis and then use them to speculate, in the context of the existing literature, as to the potential impact of climate change on Southern Ocean phytoplankton community dynamics, as well as the implications thereof for productivity, higher trophic levels, and the Southern Ocean's biological carbon pump.

Throughout this thesis, I show how phytoplankton community composition in the Southern Ocean is driven by various bottom-up and top-down controls. The interplay between these drivers dictates the dominance of one group over another (e.g., *Phaeocystis antarctica* versus diatoms), influencing the functioning of the nitrogen cycle and the magnitude and efficiency of carbon export (both directly – via the sinking flux – and indirectly – *sensu* the new production paradigm).

I showed in Chapter 2 that in the springtime open Southern Ocean, iron and light availability were generally high, leading to the initiation of the spring bloom. The phytoplankton community and rates of net primary production (NPP) were dominated by nanoplankton, predominantly the diatom *Chaetoceros* spp., with the success of this genus attributable to its size duality (as both nanoplankton (individual cells) and microplankton (chains)), apparently low (Fe:carbon uptake ratio ~2 μmol mol^{-1}) and inelastic (unchanged with increasing nitrate (NO_3^-) dependence) iron requirement, and boom-and-bust lifestyle. The spring *Chaetoceros* bloom rapidly depleted the surface iron (and silicate ($Si(OH)_4$) in the SAZ) inventory, influencing the succeeding phytoplankton community composition and its role in the nitrogen cycle (likely predominantly consuming regenerated nitrogen) and carbon export.

In contrast to the perennially iron-limited region studied in Chapter 2, Chapters 3 and 4 focused on the Marginal Ice Zone (MIZ) and Coastal and Continental Shelf Zone (CCSZ) of the Weddell Sea, where iron concentrations are generally replete (Lannuzel et al., 2008; Klunder et al., 2011; De Jong et al., 2012; Klunder et al., 2014). In Chapter 3, I showed how phytoplankton community composition in this region was predominantly driven by mixed-layer stratification, with *P. antarctica* dominating under low-light conditions and diatoms under high-light conditions. I further showed how the dominance of *P. antarctica* versus diatoms drove changes in the mixed-layer nutrient ratios (i.e., $Si(OH)_4$:NO_3^- and NO_3^-:phosphate(PO_4^{3-})), which may impact the biogeochemistry of the deep water masses formed at Larsen C Ice Shelf (LCIS) in the western Weddell Sea.

In Chapters 3 and 4 (via the use of two different nitrogen isotope methods), I showed that although NPP was highest at LCIS compared to the other regions sampled across the Weddell Sea, NO_3^- uptake (and by association, carbon export potential) was inhibited by the elevated ammonium (NH_4^+) concentrations

(average of 0.6 ± 0.4 μM). This work shows that in iron-replete regions of the Southern Ocean, carbon export may be inhibited by environmental factors that are not accounted for. However, the extent to which NH_4^+ may inhibit carbon export potential, particularly later in the growth season as light and iron availability decrease and NH_4^+ availability increases, is still to be investigated.

Below, within the context of the main findings of this thesis, I consider some of the outstanding questions regarding how phytoplankton community composition might change in a warming climate and the potential implications of these changes for the biological carbon pump. A general consensus is that with climate change, NPP will increase in the Southern Ocean by ~50% due to the alleviation of light and iron limitation, along with the warming of surface waters (Leung et al., 2015; Fu et al., 2016; Henson et al., 2022). That said, the Southern Ocean will likely experience two major physical changes that will impact NPP and carbon export. In the Subantarctic (the combined Subantarctic Zone (SAZ) and Polar Frontal Zone (PFZ)), NPP will initially be enhanced as a result of increased iron supply due to increased atmospheric deposition from the surrounding land masses and the shoaling of the mixed layer due to an increase in the latent heat flux (Leung et al., 2015; Petrou et al., 2016; Deppeler and Davidson, 2017; Moore et al., 2018). Similarly, NPP will increase in the CCSZ and MIZ due to the warming of surface waters, which will enhance the rate of sea-ice- and glacial melt, increasing the surface iron supply and stratifying the mixed layer (Leung et al., 2015; Petrou et al., 2016; Deppeler and Davidson, 2017; Moore et al., 2018). In contrast, the open Antarctic Zone (OAZ), predominantly the region between 50°S and 65°S, will experience a decrease in NPP due to the strengthening of the westerly winds, which will decrease mixed-layer stratification and thus the mean light flux to phytoplankton (Leung et al., 2015; Petrou et al., 2016; Deppeler and Davidson, 2017; Moore et al., 2018).

As discussed in Chapters 3 and 4, the shoaling of mixed-layer in the CCSZ and MIZ generally shifts the phytoplankton community from *P. antarctica* dominance towards diatom and/or cryptophyte dominance as these phytoplankton groups bloom under well-stratified, high-light conditions (Goffart et al., 2000; Mendes et al., 2012, 2018a, 2023; Kerr et al., 2018; Ferreira et al., 2020). Although the rates of NPP may be higher in the CCSZ and MIZ following the alleviation of light – and to some extent, iron – limitation, the shift in community composition will have implications for the nutrient ratios in surface waters and for carbon export. *P. antarctica* consume more nitrogen (and carbon) relative to PO_3^{4-} than diatoms and cryptophytes (Hutchins and Bruland, 1998; Takeda, 1998; Arrigo et al., 1999; Ragueneau et al., 2000) and also have no requirement for $Si(OH)_4$. As such, a shift from *P. antarctica* to diatoms and/or cryptophytes may decrease the N:P and Si:N ratios of surface waters, influencing the nutrients available to the succeeding phytoplankton community (e.g., Chapter 3). In addition, *P. antarctica* are associated with higher rates of carbon export than diatoms and cryptophytes (Arrigo et al., 2000; DiTullio et al., 2000), and while diatoms are generally good carbon exporters, *P. antarctica*

fix approximately twice as much carbon relative to PO_4^{3-} consumed than diatoms, leading to *P. antarctica* making a disproportionate contribution to carbon export (Arrigo et al., 2000; DiTullio et al., 2000). In regions of the MIZ and CCSZ currently characterised by iron-replete conditions and deep mixed layers that favour the dominance of *P. antarctica*, such as in coastal polynyas, the stratification of the mixed layer and shift towards diatom dominance may decrease carbon export. Although earlier sea ice melt will shoal the mixed layer sooner than what is currently observed, the surface mixed layer may become subjected to increased winds earlier in the growth season which would drive longer periods of low light conditions. In regions of the MIZ and CCSZ characterised by iron-replete conditions, such as those at LCIS, the low light, high iron conditions shift the community from diatom to *P. antarctica* dominance. The shift from diatoms to *P. antarctica* dominance may offset the decrease in carbon export associated with the shift to diatom dominance as described above.

In regions currently characterised by well-stratified mixed layers, the increased stratification of surface waters will shift the community from *P. antarctica* and/or diatoms to cryptophyte dominance as cryptophytes are able to withstand particularly high UV radiation (Mendes et al., 2018b, 2023). The transition to cryptophyte dominance decreases the mean size of the phytoplankton community, which decreases the efficiency of zooplankton grazing, thereby enhancing microbial activity and potentially decreasing carbon export potential (Rodríguez et al., 2002; Ducklow et al., 2013). The shift from *P. antarctica* and/or diatoms to cryptophytes is also likely to drive a shift in the zooplankton community (e.g., Ducklow et al., 2006; Montes-Hugo et al., 2009; Mendes et al., 2013). Krill, the dominant zooplankton species in the CCSZ and MIZ of the Southern Ocean, preferentially consume diatoms (Meyer and El-Sayed, 1983) and are unable to graze on small phytoplankton (<10 μm; i.e., cryptophytes; Pakhomov et al., 2002). The shift towards cryptophyte dominance would thus likely shift the zooplankton community from krill to salp, as salps are non-selective, indiscriminate feeders and unlike krill, can graze on a large size range of phytoplankton (Pauli et al., 2021). Although cryptophytes generally cause an upregulation of the microbial loop because they cannot be efficiently grazed (Rodríguez et al., 2002; Ducklow et al., 2013), salp faecal pellets are faster-sinking than those of krill and other zooplankton and have been estimated to make a large contribution to the carbon flux (Pakhomov et al., 2002; Phillips et al., 2009). The increase in salp abundance may therefore partially counteract the decrease in carbon export associated with the shift towards cryptophyte dominance. A secular change in phytoplankton and zooplankton community composition will, however, have other implications for the food web, particularly higher trophic levels. Krill is a key-stone species in the Southern Ocean and forms the base of the food-chain that supports whales, seals and sea birds (Loeb et al., 1997). Changes in plankton community composition will therefore directly affect the structure and functioning of the ecosystem in the CCSZ and MIZ.

The OAZ is hypothesised to be the only region in the Southern Ocean where NPP will initially decrease due to increased wind-driven mixing, which will decrease light availability (Leung et al., 2015; Moore et al., 2018). The OAZ is currently characterised by perennial iron limitation (Klunder et al., 2011) and the phytoplankton community in this region consists of pico- and nanoflagellates and large, heavily-silicified diatom species (e.g., *Fragilariopsis*) that are able to store iron (Sunda and Huntsman, 1995; Hoffmann et al., 2006; Petrou et al., 2016; Deppeler and Davidson, 2017). The decrease in light availability in the summertime OAZ will continue to favour the growth of small flagellates as these cells have a high surface area-to-volume ratio, which allows them to leverage the low mean light flux to the mixed layer (Margalef, 1978; Edwards et al., 2012). Other phytoplankton groups that are well adapted to low iron- and light conditions may also persist. For example, as described in Chapter 2, phytoplankton such as *Chaetoceros* spp. may come to dominate in the OAZ at the onset of the phytoplankton growth season as they have a low iron requirement, and due to their nanoplankton size (as single cells), are able to proliferate under low-light conditions. However, the dominance of one phytoplankton group over another will be the result of multiple factors that are dependent on the ecological adaptions a specific group or species is able to undergo to cope with an increase in light limitation. The OAZ is currently a region of low carbon export due to the perennial iron limitation (Schlitzer, 2002; Smetacek et al., 2004) – the decrease in NPP due to increased light inhibition may further decrease carbon export in the OAZ (Deppeler and Davidson, 2017; Henley et al., 2020). The extent to which carbon export decreases will depend on the ability of small flagellates and particularly small diatoms (observed to be important for carbon export in the Southern Ocean; Chapter 2) to cope under low-light conditions.

NPP in the Subantarctic is expected to initially increase as iron and light limitation is reduced (Petrou et al., 2016; Deppeler and Davidson, 2017; Henley et al., 2020). However, the increased stratification of surface waters will ultimately lead to a decrease in NPP as the increase in mixed-layer stratification inhibits the upward supply of macronutrients (Deppeler and Davidson, 2017 and references therein). In addition, subtropical surface waters are expected to migrate southwards, which, along with an increase in the intrusion of eddies that supply warm, low-nutrient waters from the subtropics to the Subantarctic, will further stratify the surface waters in the northern region of the Subantarctic (McLeod et al., 2012; Constable et al., 2014; Deppeler and Davidson, 2017). Similar to in the OAZ, the decreased nutrient availability will shift the phytoplankton community towards smaller phytoplankton that are better adapted to low-nutrient conditions (Petrou et al., 2016). However, unlike the OAZ, the Subantarctic is currently a region of substantial carbon export (e.g., Chapter 2) and a decrease in the upward nutrient supply may decrease this flux (Moore et al., 2018). Lower nutrient availability in surface waters may drive the phytoplankton community to enhanced reliance on recycled nitrogen, similarly to in the oligotrophic gyres (Petrou et al., 2016). Although the rates of NPP may decrease, when macronutrients are supplied to surface waters (e.g., during storms), they will be rapidly consumed, such that a future

Subantarctic may be characterised by a more efficient (although weaker) biological carbon pump than it is today (Petrou et al., 2016; Deppeler and Davidson, 2017). The extent to which NPP and carbon export decrease in the Subantarctic will, however, depend on the extent to which the upward macronutrient supply is diminished, as this will ultimately regulate the productivity of the phytoplankton community if light and iron are replete (Boyd et al., 2000; Lancelot et al., 2000).

This thesis provides insights into how physical, chemical and biological drivers influence phytoplankton community composition and provide us with a sense of how the community might change as the climate warms. It is likely that nanoplankton will have an ecological advantage over other phytoplankton size-classes as they are able to outcompete microplankton under deplete nutrient and light conditions while concurrently escaping predation, unlike the picoplankton. The ability of Southern Ocean phytoplankton to adapt to environmental changes will ultimately determine the extent to which NPP and biological carbon export increase/decrease in a changing climate.

5.1. References

Arrigo, K. R., Robinson, D. H., Worthen, D. L., Dunbar, R. B., DiTullio, G. R., VanWoert, M., and Lizotte, M. P.: Phytoplankton community structure and the drawdown of nutrients and CO2 in the Southern Ocean, Science (80-.)., 283, 365–367, https://doi.org/10.1126/science.283.5400.365, 1999.

Arrigo, K. R., DiTullio, G. R., Dunbar, R. B., Robinson, D. H., VanWoert, M., Worthen, D. L., and Lizotte, M. P.: Phytoplankton taxonomic variability in nutrient utilization and primary production in the Ross Sea, J. Geophys. Res. Ocean., 105, 8827–8846, https://doi.org/10.1029/1998jc000289, 2000.

Boyd, P. W., Watson, A. J., Law, C. S., Abraham, E. R., Trull, T., Murdoch, R., Bakker, D. C. E., Bowie, A. R., Buesseler, K. O., Chang, H., Charette, M., Croot, P., Downing, K., Frew, R., Gall, M., Hadfield, M., Hall, J., Harvey, M., Jameson, G., LaRoche, J., Liddicoat, M., Ling, R., Maldonado, M. T., McKay, R. M., Nodder, S., Pickmere, S., Pridmore, R., Rintoul, S., Safi, K., Sutton, P., Strzepek, R., Tanneberger, K., Turner, S., Waite, A., and Zeldis, J.: A mesoscale phytoplankton bloom in the polar Southern Ocean stimulated by iron fertilization, Nature, 407, 695–702, https://doi.org/10.1038/35037500, 2000.

Constable, A. J., Melbourne-Thomas, J., Corney, S. P., Arrigo, K. R., Barbraud, C., Barnes, D. K. A., Bindoff, N. L., Boyd, P. W., Brandt, A., Costa, D. P., Davidson, A. T., Ducklow, H. W., Emmerson, L., Fukuchi, M., Gutt, J., Hindell, M. A., Hofmann, E. E., Hosie, G. W., Iida, T., Jacob, S., Johnston, N. M., Kawaguchi, S., Kokubun, N., Koubbi, P., Lea, M. A., Makhado, A., Massom, R. A., Meiners, K., Meredith, M. P., Murphy, E. J., Nicol, S., Reid, K., Richerson, K., Riddle, M. J., Rintoul, S. R., Smith, W. O., Southwell, C., Stark, J. S., Sumner, M., Swadling, K. M., Takahashi, K. T., Trathan, P. N., Welsford, D. C., Weimerskirch, H., Westwood, K. J., Wienecke, B. C., Wolf-Gladrow, D., Wright, S. W., Xavier, J. C., and Ziegler, P.: Climate change and Southern Ocean ecosystems I: how changes in physical habitats directly affect marine biota, Glob. Chang. Biol., 20, 3004–3025, https://doi.org/10.1111/GCB.12623, 2014.

De_Jong, J., Schoemann, V., Lannuzel, D., Croot, P., De Baar, H., and Tison, J. L.: Natural iron fertilization of the Atlantic sector of the Southern Ocean by continental shelf sources of the Antarctic Peninsula, J. Geophys. Res. Biogeosciences, 117, https://doi.org/10.1029/2011JG001679, 2012.

Deppeler, S. L. and Davidson, A. T.: Southern Ocean phytoplankton in a changing climate, Front. Mar. Sci., 4, https://doi.org/10.3389/fmars.2017.00040, 2017.

DiTullio, G. R., Grebmeier, J. M., Arrigo, K. R., Lizotte, M. P., Robinson, D. H., Leventer, A., Barry, J. P., VanWoert, M. L., and Dunbar, R. B.: Rapid and early export of Phaeocystis antarctica blooms in the Ross Sea, Antarctica, Nature, 404, 595–598, https://doi.org/10.1038/35007061, 2000.

Ducklow, H. W., Baker, K., Martinson, D. G., Quetin, L. B., Ross, R. M., Smith, R. C., Stammerjohn, S. E., Vernet, M., and Fraser, W.: Marine pelagic ecosystems: the West Antarctic Peninsula, Philos. Trans. R. Soc. B Biol. Sci., 362, 67–94, https://doi.org/10.1098/RSTB.2006.1955, 2006.

Ducklow, H. W., Fraser, W. R., Meredith, M. P., Stammerjohn, S. E., Doney, S. C., Martinson, D. G., Sailley, S. F., Schofield, O. M., Steinberg, D. K., Venables, H. J., and Amsler, C. D.: West Antarctic

Peninsula:, 26, 190–203, 2013.

Edwards, K. F., Thomas, M. K., Klausmeier, C. A., and Litchman, E.: Allometric scaling and taxonomic variation in nutrient utilization traits and maximum growth rate of phytoplankton, Limnol. Oceanogr., 57, 554–566, https://doi.org/10.4319/LO.2012.57.2.0554, 2012.

Ferreira, A., Costa, R. R., Dotto, T. S., Kerr, R., Tavano, V. M., Brito, A. C., Brotas, V., Secchi, E. R., and Mendes, C. R. B.: Changes in Phytoplankton Communities Along the Northern Antarctic Peninsula: Causes, Impacts and Research Priorities, Front. Mar. Sci., 7, https://doi.org/10.3389/fmars.2020.576254, 2020.

Fu, W., Randerson, J. T., and Moore, J. K.: Climate change impacts on net primary production (NPP) and export production (EP) regulated by increasing stratification and phytoplankton community structure in the CMIP5 models, 13, 5151–5170, https://doi.org/10.5194/bg-13-5151-2016, 2016.

Goffart, A., Catalano, G., and Hecq, J. H.: Factors controlling the distribution of diatoms and Phaeocystis in the Ross Sea, J. Mar. Syst., 27, 161–175, https://doi.org/10.1016/S0924-7963(00)00065-8, 2000.

Henley, S. F., Cavan, E. L., Fawcett, S. E., Kerr, R., Monteiro, T., Sherrell, R. M., Bowie, A. R., Boyd, P. W., Barnes, D. K. A., Schloss, I. R., Marshall, T., Flynn, R., and Smith, S.: Changing Biogeochemistry of the Southern Ocean and Its Ecosystem Implications, 1–31 pp., https://doi.org/10.3389/fmars.2020.00581, 2020.

Henson, S. A., Laufkötter, C., Leung, S., Giering, S. L. C., Palevsky, H. I., and Cavan, E. L.: Uncertain response of ocean biological carbon export in a changing world, Nat. Geosci. 2022 154, 15, 248–254, https://doi.org/10.1038/s41561-022-00927-0, 2022.

Hoffmann, L. J., Peeken, I., Lochte, K., Assmy, P., and Veldhuis, M.: Different reactions of Southern Ocean phytoplankton size classes to iron fertilization, Limnol. Oceanogr., 51, 1217–1229, https://doi.org/10.4319/lo.2006.51.3.1217, 2006.

Hutchins, D. A. and Bruland, K. W.: Iron-limited diatom growth and Si:N uptake ratios in a coastal upwelling regime, Nature, 393, 561–564, https://doi.org/10.1038/31203, 1998.

Kerr, R., Mata, M. M., Mendes, C. R. B., and Secchi, E. R.: Northern Antarctic Peninsula: a marine climate hotspot of rapid changes on ecosystems and ocean dynamics, Deep. Res. Part II Top. Stud. Oceanogr., 149, 4–9, https://doi.org/10.1016/j.dsr2.2018.05.006, 2018.

Klunder, M. B., Laan, P., Middag, R., De Baar, H. J. W., and van Ooijen, J. C.: Dissolved iron in the Southern Ocean (Atlantic sector), Deep. Res. Part II Top. Stud. Oceanogr., 58, 2678–2694, https://doi.org/10.1016/j.dsr2.2010.10.042, 2011.

Klunder, M. B., Laan, P., De Baar, H. J. W., Middag, R., Neven, I., and Van Ooijen, J.: Dissolved Fe across the Weddell Sea and Drake Passage: impact of DFe on nutrient uptake, 11, 651–669, https://doi.org/10.5194/bg-11-651-2014, 2014.

Lancelot, C., Hannon, E., Becquevort, S., Veth, C., and De Baar, H. J. W.: Modeling phytoplankton blooms and carbon export production in the Southern Ocean: Dominant controls by light and iron in

the Atlantic sector in Austral spring 1992, Deep. Res. Part I Oceanogr. Res. Pap., 47, 1621–1662, https://doi.org/10.1016/S0967-0637(00)00005-4, 2000.

Lannuzel, D., Schoemann, V., de Jong, J., Chou, L., Delille, B., Becquevort, S., and Tison, J. L.: Iron study during a time series in the western Weddell pack ice, Mar. Chem., 108, 85–95, https://doi.org/10.1016/j.marchem.2007.10.006, 2008.

Leung, S., Cabré, A., and Marinov, I.: A latitudinally banded phytoplankton response to 21st century climate change in the Southern Ocean across the CMIP5 model suite, 12, 5715–5734, https://doi.org/10.5194/bg-12-5715-2015, 2015.

Loeb, V., Siegel, V., Holm-Hansen, O., Hewitt, R., Fraser, W., Trivelpiece, W., and Trivelpiece, S.: Effects of sea-ice extent and krill or salp dominance on the Antarctic food web, Nat. 1997 3876636, 387, 897–900, https://doi.org/10.1038/43174, 1997.

Margalef, R.: Life-forms of phytoplankton Life-forms Phytoplankton Turbulence Dia toms Dinoftagellates Types biologiques Phytoplancton Turbulence Diatomées Dinoftagellés as survival alternatives in an unstable environment ABSTRACT RÉSUMÉ, Oceanol. Acta, 1, 1978.

McLeod, D. J., Hallegraeff, G. M., Hosie, G. W., and Richardson, A. J.: Climate-driven range expansion of the red-tide dinoflagellate Noctiluca scintillans into the Southern Ocean, J. Plankton Res., 34, 332–337, https://doi.org/10.1093/PLANKT/FBR112, 2012.

Mendes, C. R. B., de Souza, M. S., Garcia, V. M. T., Leal, M. C., Brotas, V., and Garcia, C. A. E.: Dynamics of phytoplankton communities during late summer around the tip of the Antarctic Peninsula, Deep. Res. Part I Oceanogr. Res. Pap., 65, 1–14, https://doi.org/10.1016/j.dsr.2012.03.002, 2012.

Mendes, C. R. B., Tavano, V. M., Leal, M. C., de Souza, M. S., Brotas, V., and Garcia, C. A. E.: Shifts in the dominance between diatoms and cryptophytes during three late summers in the Bransfield Strait (Antarctic Peninsula), Polar Biol., 36, 537–547, https://doi.org/10.1007/s00300-012-1282-4, 2013.

Mendes, C. R. B., Tavano, V. M., Kerr, R., Dotto, T. S., Maximiano, T., and Secchi, E. R.: Impact of sea ice on the structure of phytoplankton communities in the northern Antarctic Peninsula, Deep. Res. Part II Top. Stud. Oceanogr., 149, 111–123, https://doi.org/10.1016/j.dsr2.2017.12.003, 2018a.

Mendes, C. R. B., Tavano, V. M., Dotto, T. S., Kerr, R., de Souza, M. S., Garcia, C. A. E., and Secchi, E. R.: New insights on the dominance of cryptophytes in Antarctic coastal waters: A case study in Gerlache Strait, Deep. Res. Part II Top. Stud. Oceanogr., 149, 161–170, https://doi.org/10.1016/j.dsr2.2017.02.010, 2018b.

Mendes, C. R. B., Costa, R. R., Ferreira, A., Jesus, B., Tavano, V. M., Dotto, T. S., Leal, M. C., Kerr, R., Islabão, C. A., Franco, A. de O. da R., Mata, M. M., Garcia, C. A. E., and Secchi, E. R.: Cryptophytes: an emerging algal group in the rapidly changing Antarctic Peninsula marine environments, Glob. Chang. Biol., https://doi.org/10.1111/GCB.16602, 2023.

Meyer, M. A. and El-Sayed, S. Z.: Grazing of Euphausia superba Dana on natural phytoplankton populations, Polar Biol., 1, 193–197, https://doi.org/10.1007/BF00443187/METRICS, 1983.

Montes-Hugo, M., Doney, S. C., Ducklow, H. W., Fraser, W., Martinson, D., Stammerjohn, S. E., and

Schofield, O.: Recent changes in phytoplankton communities associated with rapid regional climate change along the western Antarctic Peninsula, Science (80-.)., 323, 1470–1473, https://doi.org/10.1126/SCIENCE.1164533/SUPPL_FILE/MONTES-HUGO_SOM.PDF, 2009.

Moore, K. J., Fu, W., Primeau, F., Britten, G. L., Lindsay, K., Long, M., Doney, S. C., Mahowald, N., Hoffman, F., and Randerson, J. T.: Sustained climate warming drives declining marine biological productivity, Science, 359, 113–1143, https://doi.org/10.1126/SCIENCE.AAO6379, 2018.

Pakhomov, E. A., Froneman, P. W., and Perissinotto, R.: Salp/krill interactions in the Southern Ocean: spatial segregation and implications for the carbon flux, Deep Sea Res. Part II Top. Stud. Oceanogr., 49, 1881–1907, https://doi.org/10.1016/S0967-0645(02)00017-6, 2002.

Pauli, N. C., Metfies, K., Pakhomov, E. A., Neuhaus, S., Graeve, M., Wenta, P., Flintrop, C. M., Badewien, T. H., Iversen, M. H., and Meyer, B.: Selective feeding in Southern Ocean key grazers—diet composition of krill and salps, Commun. Biol., 4, https://doi.org/10.1038/S42003-021-02581-5, 2021.

Petrou, K., Kranz, S. A., Trimborn, S., Hassler, C. S., Ameijeiras, S. B., Sackett, O., Ralph, P. J., and Davidson, A. T.: Southern Ocean phytoplankton physiology in a changing climate, J. Plant Physiol., 203, 135–150, https://doi.org/10.1016/j.jplph.2016.05.004, 2016.

Phillips, B., Kremer, P., and Madin, L. P.: Defecation by Salpa thompsoni and its contribution to vertical flux in the Southern Ocean, Mar. Biol., 156, 455–467, https://doi.org/10.1007/S00227-008-1099-4/TABLES/7, 2009.

Ragueneau, O., Tréguer, P., Leynaert, A., Anderson, R. F., Brzezinski, M. A., DeMaster, D. J., Dugdale, R. C., Dymond, J., Fischer, G., François, R., Heinze, C., Maier-Reimer, E., Martin-Jézéquel, V., Nelson, D. M., and Quéguiner, B.: A review of the Si cycle in the modern ocean: Recent progress and missing gaps in the application of biogenic opal as a paleoproductivity proxy, Glob. Planet. Change, 26, 317–365, https://doi.org/10.1016/S0921-8181(00)00052-7, 2000.

Rodríguez, J., Jiménez-Gómez, F., Blanco, J. M., and Figueroa, F. L.: Physical gradients and spatial variability of the size structure and composition of phytoplankton in the Gerlache Strait (Antarctica), Deep Sea Res. Part II Top. Stud. Oceanogr., 49, 693–706, https://doi.org/10.1016/S0967-0645(01)00119-9, 2002.

Schlitzer, R.: Carbon export fluxes in the Southern Ocean: results from inverse modeling and comparison with satellite-based estimates, Deep Sea Res. Part II Top. Stud. Oceanogr., 49, 1623–1644, https://doi.org/10.1016/S0967-0645(02)00004-8, 2002.

Smetacek, V., Assmy, P., and Henjes, J.: The role of grazing in structuring Southern Ocean pelagic ecosystems and biogeochemical cycles, Antarct. Sci., 16, 541–558, https://doi.org/10.1017/S0954102004002317, 2004.

Sunda, W. G. and Huntsman, S. A.: Iron uptake and growth limitation in oceanic and coastal phytoplankton, Mar. Chem., 50, 189–206, https://doi.org/10.1016/0304-4203(95)00035-P, 1995.

Takeda, S.: Influence of iron availability on nutrient consumption ratio, Nature, 393, 774–777, 1998.